

# Relativistic Distorted Wave Analysis of Neutrino-induced Strange Particle Production on Nuclei

by

Gashaw Bekele Adera

*Dissertation approved for the degree of Doctor of Philosophy in Physics  
in the Faculty of Science at Stellenbosch University*



Department of Physics,  
Stellenbosch University,  
Private Bag X1, Matieland 7602, South Africa.

Promoter:

Prof. B. I. S. van der Ventel  
Department of Physics  
Stellenbosch University

Co-Promoter:

Prof. D. R. Phillips  
Department of Physics and Astronomy  
Ohio University

December 2014

# Declaration

By submitting this dissertation electronically, I declare that the entirety of the work contained therein is my own, original work, that I am the sole author thereof (save to the extent explicitly otherwise stated), that reproduction and publication thereof by Stellenbosch University will not infringe any third party rights and that I have not previously in its entirety or in part submitted it for obtaining any qualification.

Date: December 2014

# Abstract

## Relativistic Distorted Wave Analysis of Neutrino-induced Strange Particle Production on Nuclei

G. B. Adera

*Department of Physics,  
Stellenbosch University,  
Private Bag X1, Matieland 7602, South Africa.*

Dissertation: PhD (Phys)

December 2014

In this dissertation, we study the neutrino-induced strangeness associated production on nuclei within the relativistic plane wave impulse approximation (RPWIA) and relativistic distorted wave impulse approximation (RDWIA) frameworks in the energy region between 1 and 3 GeV. The general theoretical description of the neutrino-nucleus interaction producing the exclusive channels is developed based the relativistic impulse approximation (RIA) scheme, which allows the embedding of the underlying elementary associated production process on a free nucleon inside the nuclear medium without significant alteration. The weak hadronic current amplitudes are calculated using a model-dependent evaluation of the elementary production vertex using the Born term approximation. The nuclear structure effects are taken into account via bound state wave functions of nucleons.

The differential cross section of RPWIA (RDWIA) model describing the exclusive reaction is constructed in the laboratory (center-of-momentum) frame; and the angular, missing momentum and energy distributions are presented for various nuclear targets under two kinematic settings. In the relativistic distorted wave analysis, special emphasis is placed on the kaon final state interaction (FSI) effects by turning the hyperon FSI off. The distorted wave functions are obtained by solving the Klein-Gordon equation containing the Kisslinger form of the relativistic optical potential. The numerical complexity introduced by the weak nuclear transition current containing the kaon distortion is addressed by employing the high performance computing (HPC) technique that calculates the RDWIA differential cross sections on a computer cluster.

The theoretical predictions of the two relativistic models are presented and also compared for the neutrino-induced charged-current (CC)  $K^+\Lambda$  production on a bound state neutron. The numerical results of the plane wave limit analysis of the production process on  $1s^{1/2}$  and  $1p^{3/2}$  orbitals of  $^{12}\text{C}$  show that the angular distributions are strongly forward peaked under both kinematic settings, whereas (specifically) under the quasifree setting the cross sections tend to mimic the missing momentum distribution of the bound nucleon inside the nucleus. The inclusion of the kaon FSI is found to considerably reduce the angular distributions of the CC  $K^+\Lambda$  production process on (i)  $^4\text{He}$ ,  $^{12}\text{C}$ ,  $^{16}\text{O}$  and  $^{40}\text{Ca}$  under quasifree kinematics, and (ii) the  $^{208}\text{Pb}$  under open kinematics.

# Uittreksel

## Relatiewistiese Vervormdegolf Analiese van Neutrino-geïnduseerde Vreemde Deeltjie Produksie vanaf Kerne

*(“Relativistic Distorted Wave Analysis of Neutrino-induced Strange Particle Production on Nuclei”)*

G. B. Adera

*Departement Fisika,  
Universiteit van Stellenbosch,  
Private Bag X1, Matieland 7602, South Africa.*

Proefskrif: PhD (Fis)

Desember 2014

In hierdie tesis word die produksie van vreemde deeltjies as gevolg van neutrino interaksies met kerne bestudeer binne die raamwerk van die relatiewistiese vlakgolf impuls benadering (RVGIB) en relatiewistiese vervormdegolf impuls benadering (RVVIB) in die energie gebied van 1 tot 3 GeV. Die onderliggende aanname is dat die reaksiekanale ontstaan as gevolg van die interaksie van die neutrino met 'n enkele nukleon binne die kern. Dit staan bekend as die relatiewistiese impuls benadering. Daar word dus aanvaar dat die elementêre reaksie onveranderd bly binne die kernmedium. Die hadroniese amplitudes vir die swak wisselwerking word bepaal deur gebruik te maak van die Born model by die verteks of interaksiepunt van die ooreenstemmende elementêre interaksie. Die effek van die kernstruktuur word beskryf deur gebruik te maak van gebonde-deeltjie golffunksies vir die nukleon in die kern.

Die differensiële kansvlak word in die laboratorium-assestelsel en massamiddelpunt-assestelsel bereken vir die RVGIB en RVVIB, respektiewelik. Die kansvlakke word bereken vir twee kinematiese opstellings vir 'n verskeidenheid van kerne. In die RVVIB word die klem geplaas op die kernvervorming spesifiek op die kaon. Die vervormdegolwe vir die kaon word bereken deur die Klein-Gordon vergelyking op te los deur gebruik te maak van die Kisslinger vorm van die relatiewistiese optiesw potensiaal. Die gevolglike toename in numeriese ingewikkeldheid vir die berekening van die kansvlak in die RVVIB word aangespreek deur gebruik te maak van parallele-programmeringstegnieke op 'n rekenaar-bondel.

Die teoretiese voorspellings van die twee modelle word vergelyk met die gelaaide-stroom (GS) produksie van 'n  $K^+\Lambda$ -paar op 'n gebonde neutron. Die numeriese resultate van die RVGIB vir die produksie vanaf die  $1s^{1/2}$  en  $1p^{3/2}$  orbitale van  $^{12}\text{C}$  wys dat die hoekverspreiding van die kansvlak 'n voorkeur toon vir klein waardes van die verstrooiingshoek vir albei kinematiese opstellings. Vir die kwasivrye opstelling is daar 'n egter ook duidelike verband tussen die kansvlak se hoekverspreiding en die momentumverspreiding van die gebonde nukleon in die kern. Die effek van die vervorming op die kaon is om die kansvlak vir die GS  $K^+\Lambda$ -paar aansienlik te verminder. Vir  $^4\text{He}$ ,  $^{12}\text{C}$ ,  $^{16}\text{O}$  en  $^{40}\text{Ca}$  is die vermindering die grootste vir die kwasievrye kinematiese opstelling en vir  $^{208}\text{Pb}$  is dit vir die oop kinematiese opstelling.

## Acknowledgements

I would like to express my sincere gratitude to Professor Brandon van der Ventel, without whose expertise, guidance and support, this dissertation could not have been a success. I am very grateful for his encouragement, concern and patience through the course of this research. I would like to extend my sincere appreciation to the Physics Department of Stellenbosch University and my colleagues in the nuclear physics group for playing important role in making this doctoral study such an educational and enjoyable experience. I would also like to thank Professor Daniel R. Phillips for being helpful in revising and polishing this manuscript. I am deeply indebted to my sister Ms. Mebrat Bekele Adera, whose spiritual guidance, fruitful prayers, and frequent encouragements have kept me going at times of despair and difficult circumstances. My special thanks also goes to the Postgraduate and International Office of Stellenbosch University for the postgraduate Merit bursary award during the extended period of my study. This work is funded by German Academic Exchange Service in association with Africa Institute for Mathematical Sciences under Code No.: A/10/02802.

# Dedications

*“For by him were all things created, that are in heaven, that are in earth, visible and invisible, whether they be thrones, or dominions, or principalities, or powers: all things were created by him, and for him.” - Col. 1:16; “I can do all things through Christ, who gives me strength.” - Phil. 4:13.*

*I dedicate this dissertation to*

- *the ancient of days, who has been with me through my ups and downs to help me make the impossible possible. To him be glory forever.*
- *my beloved, late mother Gete Yadeta, and late grandmother Sidise Sadeta, who shared their immense and precious love, wisdom, and care as I grew up. They shall live forever in my heart.*

# Contents

<b>Declaration</b>	<b>i</b>
<b>Abstract</b>	<b>ii</b>
<b>Uittreksel</b>	<b>iii</b>
<b>Acknowledgements</b>	<b>iv</b>
<b>Dedications</b>	<b>v</b>
<b>Contents</b>	<b>vi</b>
<b>List of Figures</b>	<b>viii</b>
<b>List of Tables</b>	<b>xiii</b>
<b>1 Introduction</b>	<b>1</b>
1.1 Background Information . . . . .	1
1.2 Outline of Dissertation . . . . .	4
<b>2 Preliminaries for Neutrino-induced Kaon-Hyperon Production on Nuclei.</b>	<b>5</b>
2.1 Introduction . . . . .	5
2.2 Relativistic Impulse Approximation . . . . .	5
2.3 Quantum Hadrodynamics . . . . .	7
2.4 Associated KY Production on Free Nucleons . . . . .	14
<b>3 Theory of the Quasifree <math>A(\nu, \ell KY)B</math> Process</b>	<b>25</b>
3.1 Theoretical Formalism . . . . .	25
3.2 Nuclear Transition Matrix Element . . . . .	31
3.3 RPWIA Model for Quasifree $A(\nu, \ell KY)B$ Reaction . . . . .	33
<b>4 Final State Interactions in the <math>A(\nu, \ell KY)B</math> Processes</b>	<b>36</b>
4.1 Introduction . . . . .	36
4.2 Hyperon-nucleus Interaction . . . . .	37
4.3 Kaon-Nucleus Interaction . . . . .	38
4.4 The Kaon Optical Potential . . . . .	39
4.5 Equation of Motion for the Kaon . . . . .	42
4.6 Evaluation of the Radial KG-Equation . . . . .	43
4.7 Numerical Analysis of Kaon Distortion . . . . .	48
<b>5 RDWIA Model for the Quasifree <math>A(\nu, \ell KY)B</math> Process</b>	<b>61</b>
5.1 Introduction . . . . .	61
5.2 Relativistic Kinematics of the RDWIA Model . . . . .	61
5.3 The Differential Cross Section of the Quasifree $A(\nu, \ell KY)B$ reactions . . . . .	63
5.4 Evaluation of Matrix Element within RDWIA Model . . . . .	64

<b>6 Numerical Analysis of the RDWIA Model</b>	<b>69</b>
6.1 Introduction . . . . .	69
6.2 Relativistic Kinematics in the c.m. Frame . . . . .	69
6.3 Computation of the Matrix Element . . . . .	70
<b>7 Results and Discussion</b>	<b>80</b>
7.1 RPWIA Analysis Results of the $K^+ \Lambda$ Production . . . . .	80
7.2 RDWIA Analysis Results of the $K^+ \Lambda$ Production . . . . .	86
7.3 Comparison between RPWIA and RDWIA-I Results . . . . .	92
<b>8 Summary and Conclusion</b>	<b>97</b>
<b>Appendices</b>	<b>100</b>
<b>A Computing the Kinematics</b>	<b>101</b>
A.1 Flow Diagram for Quasifree Kinematics . . . . .	101
A.2 Flow Diagram for Open Kinematics . . . . .	101
<b>B Block-matrix Form of <math>\hat{J}^\mu(q)</math></b>	<b>104</b>
<b>C Numerical Methods</b>	<b>109</b>
C.1 Gaussian Quadrature . . . . .	109
C.2 Fourth-order Runge-Kutta Method . . . . .	110
<b>D Conversion of Multidimensional Summation</b>	<b>112</b>
D.1 Independent Summation Indices . . . . .	112
D.2 Dependent Summation Indices . . . . .	114
<b>Bibliography</b>	<b>116</b>



# List of Figures

2.1	The radial wave functions $g_{E\kappa}(r)$ and $f_{E\kappa}(r)$ of bound state neutron occupying the RSM orbitals of ${}^4\text{He}$ , ${}^{12}\text{C}$ , ${}^{16}\text{O}$ , and ${}^{40}\text{Ca}$ . These radial components of the Dirac spinor determined from the nonlinear Walecka model with the NL3 parametrization.	10
2.2	The radial wave functions $g_{E\kappa}(r)$ and $f_{E\kappa}(r)$ in coordinate space for the neutron orbitals of ${}^{208}\text{Pb}$ . They are computed using the nonlinear QHD model with the NL3 parameter set.	11
2.3	The scalar density $\rho_S(r)$ (left panel) and the vector density $\rho_V(r)$ (right panel) of ${}^{40}\text{Ca}$ as calculated via the relativistic mean field approximation to the original Walecka model (QHD-I) and its extensions: QHD-II, NL2, and FSUGold.	12
2.4	The scalar density $\rho_S(r)$ and the vector density $\rho_V(r)$ in ${}^{12}\text{C}$ , ${}^{16}\text{O}$ , ${}^{40}\text{Ca}$ , and ${}^{208}\text{Pb}$ . They are determined from the radial wave functions $g_{E\kappa}(r)$ and $f_{E\kappa}(r)$ obtained from the RMF approximation to the nonlinear Walecka model with NL3 parameter set.	13
2.5	Lowest order Feynman diagram of neutrino-induced strange particle production from a free nucleon.	14
2.6	Schematic diagram of a free nucleon going, upon interacting with a weak gauge boson, into an exclusive channel which contains a kaon and hyperon in the final state.	15
2.7	Tree-level Born diagrams of the weak hadronic vertex for the neutrino-induced associated production process: $\nu n \rightarrow \ell K^+ \Lambda$ .	17
2.8	The SU(3) octet representations of (a) pseudoscalar-mesons ( $J^\pi = 0^-$ ) and (b) baryons ( $J^\pi = \frac{1}{2}^+$ ) along with their corresponding masses in MeV and quark compositions. Note that the quark compositions of $\pi^0$ and $\eta$ are $(u\bar{u} + d\bar{d})/\sqrt{2}$ and $(u\bar{u} + d\bar{d} - 2s\bar{s})/\sqrt{6}$ , respectively.	18
3.1	The lowest-order Feynman diagram for the neutrino-induced associated production of strange particles on nuclei. This is the Born approximation which states that in the limit of low four-momentum transfer the dominant contribution to the differential cross section comes from a single-boson-exchange reaction mechanism, and thus validating the first consequence of the RIA scheme.	25
3.2	The vertex approximation invoked within the RIA model. This is in agreement with the second consequence of the RIA scheme which states that the vector gauge boson interacts with a single bound nucleon inside the target nucleus, and subsequently a kaon is produced in conjunction with a hyperon. The rest of the bound nucleons behave as spectators.	26
3.3	The kinematics of the quasifree reaction $A(\nu, \ell KY)B$ in the laboratory frame. The geometry of the reaction process is depicted using three planes: scattering, kaon production, and hyperon production planes. Note that, the recoil of the residual nucleus is left out of this geometric representation of the kinematics only for convenience sake.	27
3.4	Momentum space radial wave functions of the bound nucleon. The top(bottom) panels contain the curves for proton (neutron) bound to the $1s^{1/2}$ and $1p^{3/2}$ orbitals of ${}^{12}\text{C}$ . The solid (dashed), dotted(dash-dotted), dash-dot-dotted (short-dashed), and short-dotted (short-dash-dotted) curves of $g_{E\kappa}(f_{E\kappa})$ correspond to QHD-I, QHD-II, NL3, and FSUGold parameterizations, respectively, to the Walecka model.	34

4.1	Diagrammatic illustration of the RDWIA-II treatment of the $A(\nu, \ell KY)B$ process. The elliptic shaded blob represents the optical model interaction of the final state hyperon with the residual nucleus, whereas the kaon FSI is turned off. . . . .	37
4.2	Diagrammatic illustration of the $A(\nu, \ell KY)B$ process treated within RDWIA-I framework, whereby the kaon FSI, represented by the elliptic shaded blob, is considered. In the RDWIA-I treatment we turn off the hyperon FSI. . . . .	38
4.3	The optical potential parameters $b_0$ (left panel) and $b_1$ (right panel) as a function of the two-body kaon lab momentum. Both are determined, in the unit of $\text{fm}^3$ , from Martin's phase shift analysis of the $K^+N$ scattering amplitudes. . . . .	41
4.4	$b'_0$ as a function of the two-body kaon lab momentum. . . . .	42
4.5	Complex functions $g(r)$ and $f(r)$ , appearing in the second-order differential equation, Eq. (4.6.3). They are plotted as a function of the distance of kaon with respect to the $^{16}\text{O}$ target at $k_{\text{lab}} = 0.65 \text{ GeV}$ . The real (imaginary) parts of the two radial functions are displayed in the left (right) panels. The optical potential parameters are determined from the phase shifts of Martin and use is made of the nuclear matter density obtained from the NL3 parametrized QHD model. . . . .	44
4.6	Flow diagram for the subroutine ROPFLIJ which is written in Fortran 95 in order to calculate the dimensionless partial wave amplitudes $F_{L,I,2J}(\kappa)$ defined in Eq. (4.4.2). . . . .	50
4.7	Flow diagram of a Fortran 95 subroutine, ROPLAMP, which is designed to calculate the spin-isospin averaged $K^+N$ scattering amplitudes $(f_{AV}^L)_{\text{c.m.}}$ based on Eq. (4.7.9). . . . .	51
4.8	Flow diagram for a subroutine ROPPAR, as written in Fortran 95, for calculating the kaon optical potential $b_L$ ( $L = 0, 1$ ). . . . .	52
4.9	Flow diagram for a Fortran 95 subroutine ROPFUNC, which determines the two functions $g(r)$ and $f(r)$ through which the optical potential is introduced into the radial KG-equation. . . . .	53
4.10	Flow diagram for ROPSOLV subroutine in order to numerically solve, by using the RK4 integration method, for the radial partial-waves of the final state kaon interacting with the residual nucleus before exiting with asymptotic momentum $\mathbf{k}$ . . . . .	54
4.11	Dependence of the generalized phase shift $\gamma_l(k)$ on the matching radius $R$ . This illustrates the behavior of $\gamma_l(k)$ calculated for three partial waves ( $l = 0, 1, 2$ ) of kaon, and for $R$ in the range of $0 < R < 14 \text{ fm}$ . The K-B c.m. frame momentum of kaon is fixed at $k = 0.65 \text{ GeV}$ . . . . .	55
4.12	Illustration of how $\delta_l(k)$ and $\eta_l(k)$ behave for wider choice of the matching radius $R$ , for $l = 2$ partial wave of kaon, and for fixed K-B c.m. momentum of kaon at $k = 0.65, 0.85, \text{ and } 1.25 \text{ GeV}$ . . . . .	55
4.13	Radial dependence of partial waves of kaon in the final state of $A(\nu, \ell KY)B$ process. The FSI of kaon is considered to be with the residual nucleus of $^{16}\text{O}$ target. Relative momentum of kaon is fixed at $k = 0.65 \text{ GeV}$ . These radial waves are normalized using outgoing boundary conditions. . . . .	56
4.14	Partial waves of kaon, in the final state of $A(\nu, \ell KY)B$ process, plotted as a function of radial distance. These radial wave functions are normalized using outgoing boundary conditions. Here the FSI of kaon is considered to be with the residual nucleus of $^{16}\text{O}$ target. Relative momentum of kaon is fixed at $k = 0.65 \text{ GeV}$ . . . . .	57
4.15	Comparison of the numerically generated radial parts $R_{l_{\text{KB}}, k}^+(r)$ of kaon distorted wave (DW) with the corresponding spherical Bessel function $j_{l_{\text{KB}}}(kr)$ of expanded plane wave (PW) of kaon in terms of partial waves. Notice that the radial parts of DW are complex-valued solutions to account for kaon absorption in the optical potential formalism, whereas the spherical Bessel functions are real. The plots are generated for $k = 0.25 \text{ GeV}$ , and for $l_{\text{KB}} = 0, 1, 2, \text{ and } 3$ partial waves of K-B system, where B is the residual nucleus for the $^{16}\text{O}$ target. . . . .	58

4.16	Comparison of radial partial waves of kaon distorted wave (DW) with the corresponding spherical Bessel function the plane wave (PW) of a free kaon. The plots are generated for $k = 0.65$ GeV, and $l_{KB} = 0, 1, 2,$ and $3$ partial waves of K-B system, where B is the residual nucleus for the $^{16}\text{O}$ target in the $A(\nu, \ell\text{KY})\text{B}$ process. . . . .	59
4.17	Nuclear phase shifts (left panel) and absorption coefficients (right panel), for the first seven partial waves, as a function of the relative momentum of kaon. They are obtained by comparing the numerical solutions of the radial KG-equation determined in the interior region of residual nucleus with the asymptotic waves at the matching radius, beyond which the kaon optical potential is considered to have a vanishing contribution and we have fixed that radius at $R = 10$ fm. . . . .	60
6.1	Schematic comparison of execution times of sequential and parallel processes of the same computational problem. . . . .	72
6.2	Memory architectures of parallel computers: (a) shared-memory system whereby multiple processors share a common global address, and (b) distributed-memory system in which processors with their own private memory are interconnected by communication network. . . . .	73
6.3	Flow diagram of what a serial execution of the weak nuclear transition currents $\mathcal{H}_1^\mu$ and $\mathcal{H}_2^\mu$ on a single processor looks like. Here we only intend to illustrate the parallelizable parts without bothered by the detail of the actual calculation. Since the summation is performed over very large number of terms on a single processor, such computations using the standard personal computer have been proven to be time consuming. . . . .	76
6.4	Flow diagram providing a rough illustration as to how the parallel computations of the nuclear transition currents $\mathcal{H}_1^\mu$ and $\mathcal{H}_2^\mu$ on a computer cluster are carried out. Note that this illustration does not show the detailed calculations, instead it emphasizes on the parallelization mechanism based on distributed-memory architecture. Here very large number of terms are partially summed over by individual processors of the cluster, simultaneously; hence resolving the problem of long execution time of the corresponding serial program. . . . .	77
6.5	Execution time as a function of number of processors for three data sets. Here we only considered special cases for the sake of examining the improvement of the MPI program in terms of computational speed. These plots are generated after adding together the execution times and data sizes of MPI routines of $\mathcal{H}_1^\mu$ and $\mathcal{H}_2^\mu$ . For each data set the list of execution times is scaled down by a factor of the inverse of the execution time on a single processor. . . . .	79
7.1	Missing momentum distribution of the RPWIA differential cross section for the neutrino-induced $\text{K}^+\Lambda$ production on $^{12}\text{C}$ . The short-dashed (short-dash-dotted) line is the contribution from the neutrons in $1s^{1/2}(1p^{3/2})$ orbital, and the solid line is their total sum. The quasifree kinematic inputs are fixed at $\omega = 1.46$ GeV, $Q^2 = 0.05$ GeV <sup>2</sup> , and $\theta_{p'_1} = 10$ deg. . . . .	81
7.2	Angular distribution of the RPWIA differential cross section with respect to the kaon angle for the exclusive reaction $A(\nu, \mu^-\text{K}^+\Lambda)\text{B}$ on $^{12}\text{C}$ . The quasifree kinematic inputs are fixed at $\omega = 1.46$ GeV, $Q^2 = 0.05$ GeV <sup>2</sup> , and $p_m = 0.12$ GeV. The short-dashed (short-dash-dotted) line is the contribution from the neutrons in $1s^{1/2}(1p^{3/2})$ orbital, and the solid line is their total contribution. . . . .	82
7.3	Angular distribution of the RPWIA differential cross section with respect to the kaon angle for neutrino-induced $\text{K}^+\Lambda$ production on $^{12}\text{C}$ in energy range $1.5 \leq E_k \leq 3$ GeV calculated under open kinematics. The curves correspond to the individual contributions of the orbitals and their sum at $\omega = 1.32$ GeV, $Q^2 = 0.12$ GeV <sup>2</sup> , $T_K = 300$ MeV, and $\theta_{p'_2} = 0.5$ deg. . . . .	83

7.4	Angular distribution of the RPWIA differential cross section with respect to the $\Lambda$ -hyperon angle for neutrino-induced $K^+ \Lambda$ production on neutron orbital of $^{12}\text{C}$ target under open kinematics at $\theta_{p'_1} = 5$ deg and $T_K = 300$ MeV. . . . .	84
7.5	Energy distribution of the RPWIA differential cross section with respect to the kaon kinetic energy for the process $^{12}\text{C}(\nu, \mu^- K^+ \Lambda)$ under open kinematic setting at $\omega = 1.32$ GeV, $Q^2 = 0.12$ GeV <sup>2</sup> , $\theta_{p'_1} = 10$ deg, and $\theta_{p'_2} = 2.5$ deg. . . . .	85
7.6	Missing momentum distribution of the RDWIA differential cross section for the neutrino-induced CC $K^+ \Lambda$ production on $^4\text{He}$ (top-left panel), $^{12}\text{C}$ (top-right panel), $^{16}\text{O}$ (bottom-left panel), $^{40}\text{Ca}$ (bottom-right panel) nuclei in the c.m. frame under quasifree kinematics. Under this setting, the neutrino incident energy, energy transfer, and norm-square of four-momentum transfer, angle of outgoing kaon are fixed in laboratory frame at $E_k = 2.5$ GeV, $\omega = 1.4$ GeV, $Q^2 = 0.12$ GeV <sup>2</sup> , and $\theta_{p'_1} = 15$ deg, respectively. . . . .	86
7.7	Kaon angle dependence of the RDWIA differential cross section for the exclusive reaction $A(\nu, \mu^- K^+ \Lambda)B$ on $^4\text{He}$ (top-left panel), $^{12}\text{C}$ (top-right panel), $^{16}\text{O}$ (bottom-left panel), $^{40}\text{Ca}$ (bottom-right panel) nuclei in the c.m. frame under quasifree kinematics. Under this setting, the neutrino incident energy, missing momentum, energy transfer, and norm-square of four-momentum transfer are fixed at $E_k = 2.5$ GeV, $p_m = 0.12$ GeV, $\omega = 1.4$ GeV, and $Q^2 = 0.12$ GeV <sup>2</sup> , respectively, in laboratory frame. . . . .	87
7.8	Kaon angle dependence of the RDWIA differential cross section, which is calculated via the open kinematics in the c.m. frame, for the neutrino-induced CC $K^+ \Lambda$ production on neutron orbitals of $^{208}\text{Pb}$ . Under this kinematic setting, the laboratory frame kinematic inputs are fixed at $E_k = 2.5$ GeV, $\omega = 2.0$ GeV, $Q^2 = 0.12$ GeV <sup>2</sup> , $T_K = 350$ MeV, and $\theta_{p'_2} = 15$ deg. . . . .	88
7.9	Kaon kinetic energy dependence of the RDWIA differential cross section, which is calculated via the open kinematics in the c.m. frame, for the neutrino-induced CC $K^+ \Lambda$ production on neutron orbitals of $^{12}\text{C}$ (left panel) and $^{40}\text{Ca}$ (right panel). Under this kinematic setting, the laboratory frame kinematic inputs are fixed at $E_k = 2.5$ GeV, $\omega = 1.4$ GeV, $Q^2 = 0.12$ GeV <sup>2</sup> , and $\theta_{p'_1} = \theta_{p'_2} = 5$ deg. . . . .	89
7.10	Comparison between the kaon angle dependence of the RPWIA(solid blue line) and RDWIA (dashed red line) differential cross sections, which are calculated via the quasifree kinematics in the c.m. frame, of the neutrino-induced CC $K^+ \Lambda$ production on $^4\text{He}$ . The laboratory frame kinematic inputs are fixed at $E_k = 2.5$ GeV, $p_m = 0.12$ GeV, $\omega = 1.4$ GeV, and $Q^2 = 0.12$ GeV <sup>2</sup> . . . . .	90
7.11	Comparison between the kaon angle dependence of the RPWIA(solid blue line) and RDWIA (dashed red line) differential cross sections, which are calculated via the quasifree kinematics in the c.m. frame, of the neutrino-induced CC $K^+ \Lambda$ production on $^{12}\text{C}$ . The laboratory frame kinematic inputs are fixed at $E_k = 2.5$ GeV, $p_m = 0.12$ GeV, $\omega = 1.4$ GeV, and $Q^2 = 0.12$ GeV <sup>2</sup> . . . . .	91
7.12	Comparison between the kaon angle dependence of the RPWIA(solid blue line) and RDWIA (dashed red line) differential cross sections, which are calculated via the quasifree kinematics in the c.m. frame, of the neutrino-induced CC $K^+ \Lambda$ production on $1s^{1/2}$ (top panel), $1p^{3/2}$ (bottom-left panel), and $1p^{1/2}$ (bottom-right panel) orbitals of $^{40}\text{Ca}$ . The laboratory frame kinematic inputs are fixed at $E_k = 2.5$ GeV, $p_m = 0.12$ GeV, $\omega = 1.4$ GeV, and $Q^2 = 0.12$ GeV <sup>2</sup> . . . . .	92
7.13	Comparison between the kaon angle dependence of the RPWIA(solid blue line) and RDWIA (dashed red line) differential cross sections, which are calculated via the quasifree kinematics in the c.m. frame, of the neutrino-induced CC $K^+ \Lambda$ production on $1d^{5/2}$ (top panel), $2s^{1/2}$ (bottom-left panel), and $1d^{3/2}$ (bottom-right panel) orbitals of $^{40}\text{Ca}$ . The laboratory frame kinematic inputs are fixed at $E_k = 2.5$ GeV, $p_m = 0.12$ GeV, $\omega = 1.4$ GeV, and $Q^2 = 0.12$ GeV <sup>2</sup> . . . . .	93

7.14	Angular distributions of the differential cross section with respect to the kaon angle for the exclusive reaction $A(\nu, \mu^- K^+ \Lambda)B$ on bound neutrons in $1s^{1/2}$ , $1p^{3/2}$ , $1p^{1/2}$ , $1d^{5/2}$ , $2s^{1/2}$ , $1d^{3/2}$ , $1f^{7/2}$ , $2p^{3/2}$ , and $1f^{5/2}$ orbitals of $^{208}\text{Pb}$ calculated in the RPWIA (solid blue line) and RDWIA (dashed red line) frameworks. . . . .	94
7.15	Angular distributions of the differential cross section with respect to the kaon angle for the exclusive reaction $A(\nu, \mu^- K^+ \Lambda)B$ on bound neutrons in $2p^{1/2}$ , $1g^{9/2}$ , $1g^{7/2}$ , $2d^{5/2}$ , $2d^{3/2}$ , $3s^{1/2}$ , $1h^{11/2}$ , $1h^{9/2}$ , and $2f^{7/2}$ orbitals of $^{208}\text{Pb}$ calculated in the RPWIA (solid blue line) and RDWIA (dashed red line) frameworks. . . . .	95
7.16	Angular distributions of the differential cross section with respect to the kaon angle for the exclusive reaction $A(\nu, \mu^- K^+ \Lambda)B$ on bound neutrons in $2f^{5/2}$ , $3p^{3/2}$ , $3p^{1/2}$ , and $1i^{13/2}$ orbitals of $^{208}\text{Pb}$ calculated in the RPWIA (solid blue line) and RDWIA (dashed red line) frameworks. . . . .	96
A.1	Flow diagram illustrates how the quasifree kinematics part of KINLAB1 subroutine calculates the laboratory frame four-momenta. The four-momenta at the production vertex are determined in two steps as this setting requires that the energies of the outgoing kaon and hyperon to be the same as their two-body values and the use of a finite value for the missing momentum can be set to only shift the hyperon angle from its free space value. . . . .	102
A.2	Flow diagram illustrates how the open kinematics part of KINLAB1 subroutine calculates the laboratory frame four-momenta. This setting calculates all unknown quantities in straightforward manner by assigning nine kinematic inputs at the start and letting $p_m$ vary over the entire range of the momentum distribution of the bound nucleon. . . . .	103

# List of Tables

1.1	Some of observed neutrino-induced exclusive strange particle production channels from the bubble chamber experiments at ANL, BNL and CERN. . . . .	3
2.1	Standard form factors for CC weak transition between baryons belonging to octet representation of SU(3). . . . .	21
2.2	SU(3) predicted values of the strong coupling constants, which are also related via the isospin symmetry. . . . .	22
4.1	Three different scenarios that can be explored within the RDWIA formalism of the $A(\nu, \ell KY)B$ process. . . . .	37
4.2	The inelastic threshold momentum $\kappa_{in}$ and maximum momentum $\kappa_{max}$ in the $K^+N$ c.m. system, are fixed in the phase shift analysis by Martin. . . . .	40
4.3	The upper limits of summation over the parameters from Martin's phase shift analysis.	40
7.1	Relativistic shell structure of $^{12}C$ as calculated from the QHD model with the NL3 parameter set. . . . .	80
7.2	Relativistic shell structure of $^{16}O$ , including the binding energies of both proton and neutron orbitals, as calculated from the Walecka model with the NL3 parameter sets.	81
D.1	Lists of integer values of indices: (i) when sequential summation is performed upon a function using two indices: $i_1$ and $i_2$ ; and (ii) when the same operation is carried out using a single index $s$ . Here $N_1$ and $N_2$ are set to 2. This table illustrates how simply one can deduce the two indices from their single-index representation $s$ . The upper limit for the indices are fixed at the beginning and hence their determination becomes Dependant on $s$ , $N_1$ and $N_2$ . Note that the dependence on both $s$ and $N_2$ visibly notable but one may ask the what is the importance of $i_1^{max}$ . The answer is simple. The maximum value of $s$ depends on both upper limits. . . . .	113
D.2	List of successive values of indices: angular momentum and its projection, when summing over a function that is specified by both. This list gives a guidance as to how we can express the two original indices as a function of the new index $s$ such that the two-dimensional summation is converted to one-dimensional summation. The upper limit of $s$ can be determined from $l_{max}$ . . . . .	115



# Chapter 1

## Introduction

The study of neutrino interactions has played a key role in testing various models of the electroweak theory. The neutrino-nucleus interaction, in particular, has become one of the major theoretical and experimental topics in the fields of astrophysics, cosmology, particle and nuclear physics. For example, neutrino-induced weak nuclear reactions in the energy range from 0.5 to 3 GeV have attracted much attention due to the key role they play as major mechanisms through which the analysis of neutrino-oscillation experiments is carried out[1, 2]. At the fundamental level, the detailed investigations of various exclusive channels of the neutrino-nucleus interactions provide important insight into the structure of hadrons - the bound states of Quantum Chromodynamics (QCD), and weak hadronic currents. On top of that, evidence of the oscillation signal and nonzero mass of atmospheric neutrinos have been reported in Refs. [3, 4]. As a result, a thorough understanding of neutrino interactions complements our knowledge of particle and nuclear physics from theoretical, experimental and observational studies that have been mainly established based on electromagnetic interactions.

With regard to the structure of hadrons and weak hadronic currents, it has been experimentally discovered that up and down quarks and antiquarks cannot fully describe the spin structure of a nucleon within the Standard Model[5]. Along this line, studies at Brookhaven National Laboratory (BNL) also indicated the role of other quark flavors after reporting a non-vanishing contribution of the strange-quark axial current of the nucleon to the neutrino-nucleon cross section[6]. The theoretical and experimental studies of neutrino scattering are considered to be the optimal tools for extracting information about the contribution of strange quarks to the nucleon spin. Since the neutrino scattering experiments are carried out using not just nucleons but also nuclear targets, the nuclear structure effects must be taken into account. The FINeSE Collaboration[7] has proposed to measure the strange-quark contribution to the spin of the nucleon by using neutral-current (NC) elastic scattering; and in response to the proposal the detailed theoretical studies of quasielastic neutrino-nucleus scattering have been performed by the authors of Refs. [8, 9, 10]. Thus if the strange-quark contribution to the nucleon spin is found to be significant, it may trigger the need to modify or move beyond the standard model.

### 1.1 Background Information

In the energy region from 1 to 3 GeV, the weak nucleon and nuclear reactions induced by neutrinos involve exclusive channels of associated strangeness production even if they are not the dominating processes. The study of neutrino-induced strangeness associated production provides an improved understanding of basic symmetries of the standard model, strange-quark content of the nucleon, structure of the weak hadronic form factors, strong coupling constants, and medium modification of the elementary process amplitudes. Therefore, associated production of strange particles via the weak neutrino-nucleus interaction is worthy of further theoretical investigation due to the above reasons and also it serves as the best platform whereby we can readily study how our understanding of both particle and nuclear physics overlap.

Precision neutrino physics requires good theoretical knowledge of neutrino-induced weak nuclear interactions owing to the presence of such processes as backgrounds in the detection of the neutrino-oscillation signal. Along these lines, using several nuclear targets like Carbon, Oxygen and Lead, MiniBooNE[2], MINER $\nu$ A[11], and K2K[12] experiments have reportedly been gathering high statistics data on neutrino-oscillation signals along with backgrounds such as exclusive cross sections for associated production channels. The dominant backgrounds, however, are the quasielastic[8, 9, 10, 13] and pion production[14, 15, 16, 17] processes and subsequently they have been extensively studied because not only of their larger experimental cross sections but also relative simplicity to establish theoretical descriptions. Thus, the theoretical cross sections of these background processes need to be made available to fully describe the neutrino-nucleus interactions in the analysis of the neutrino-oscillation data in the incident energy region from 0.5 to 3 GeV[18].

Beyond the standard model the supersymmetric grand unification theories (SUSY GUTs) clearly emphasize the significance of a thorough understanding of neutrino-induced strangeness associated production backgrounds due to the fact that their subsequent decay processes, when initiated by atmospheric neutrino fluxes, mimic the nucleon decay signal[19, 20]. Currently, there is an ongoing proton decay search being carried out by using the world's largest nucleon decay detector Super-KamioKande[21], and future proposed plans such as LAGUNA[22] and also other next generation experiments involving underground Megaton detectors such as Hyper-KamioKande[23] and UNO[24]. The success of these experiments depends on how they will be able to separate the backgrounds from the decay signal despite the effort to minimize their impact.

Early experimental observations of the neutrino-induced exclusive processes, in which a kaon belonging to a pseudoscalar meson octet is produced in conjunction with a hyperon belonging to a baryon octet, were first reported at ANL[25], CERN[26, 27, 28], and BNL[29]. The data from those experiments, however, are known to have low statistics and large systematic errors. From a theoretical perspective, previous rough theoretical estimations for associated strangeness production processes done by Shrock[30], Mecklenburg[31], Amer[32], and Dewan[33] were based on the assumption that those reactions took place on a free nucleon. Nevertheless, in most experiments the actual targets are nuclei or nucleons bound inside the nuclei; and hence it necessitates the fact that we must take into account the nuclear structure and final state interaction effects[33]. Because of the above uncertainties incurred on both sides, no proper comparison between theoretical and experimental analyses of the associated production processes has been performed.

Neutrino-nucleus interactions may involve exclusive channels containing either one or two strange particles in the energy region of interest. For convenience, these semi-leptonic strange particle production processes can be classified in three categories based on whether the elementary hadronic current operator of the reaction preserves or changes electric charge and strangeness quantum numbers: (i) the CC and strangeness conserving,  $\Delta S = 0$ , associated production processes in which an  $S = 1$  pseudoscalar meson ( $K^+$  or  $K^0$ ) is produced in conjunction with an  $S = -1$  hyperon ( $\Lambda$  or  $\Sigma^{\pm,0}$ ); (ii) CC and  $\Delta S = 1$  processes, whereby the  $\Delta S = \Delta Q$  selection rule only permits the production of a single strange particle:  $K^+$  or  $K^0$  meson; and (iii) neutrino-induced exclusive associated production processes involving the NC and  $\Delta S = 0$  form the third category. Table 1.1 lists some of the experimentally observed exclusive channels from the three categories[25, 27, 29]. Note that NC and  $\Delta S = 1$  is absent in the above classification scheme of exclusive production channels owing to the fact that these processes have never been observed.

Hopefully, high statistics data will be available from the ongoing and planned experiments such as MINER $\nu$ A. Therefore, a renewed effort is required to develop theoretical models for the neutrino-induced associated production on nuclei by incorporating the nuclear structure and/or final state interaction (FSI) effects. These models will allow the comprehensive analysis of experimental data for these exclusive channels in the energy region of our interest. Motivated



by the ever-growing experimental interests, in our recent work[34, 35] we have revived a long-forgotten theoretical study of neutrino-induced associated production on a free nucleon with particular interest in CC and  $\Delta S = 0$  exclusive channels. The paper introduced a new technique of extracting weak hadronic elementary amplitudes from a model-dependent evaluation of the hadronic vertex in the framework of electroweak theory and fundamental symmetries of the standard model. In addition, the most general nature of our formulation for elementary processes makes it very convenient to be extended to studying the CC  $\Delta S = 1$  and NC  $\Delta S = 0$  exclusive channels, without having to make significant alterations. On the other hand, Rafi Alam *et al.*[36] have recently investigated the CC and  $\Delta S = 1$  processes, in which a single strange particle ( $S = 1$ ) is produced, by employing the effective Lagrangian formulation in the chiral symmetry framework.

**Table 1.1:** Some of observed neutrino-induced exclusive strange particle production channels from the bubble chamber experiments at ANL, BNL and CERN.

Reaction Category	Exclusive Process
CC, $\Delta S = 0$	$\nu_\mu + p \rightarrow \mu^- + K^+ + \Sigma^+$
	$\nu_\mu + n \rightarrow \mu^- + K^0 + \Sigma^+$
	$\nu_\mu + n \rightarrow \mu^- + K^+ + \Sigma^0$
	$\nu_\mu + n \rightarrow \mu^- + K^+ + \Lambda$
CC, $\Delta S = 1$	$\nu_\mu + p \rightarrow \mu^- + K^+ + p$
	$\nu_\mu + n \rightarrow \mu^- + K^0 + p$
NC, $\Delta S = 0$	$\nu_\mu + p \rightarrow \nu + K^0 + \Sigma^+$
	$\nu_\mu + p \rightarrow \nu + K^+ + \Sigma^0$
	$\nu_\mu + p \rightarrow \nu + K^+ + \Lambda$
	$\nu_\mu + n \rightarrow \nu + K^+ + \Sigma^-$
	$\nu_\mu + n \rightarrow \nu + K^0 + \Sigma^0$
	$\nu_\mu + n \rightarrow \nu + K^0 + \Lambda$

In this work, a fully relativistic description for the associated production of strange particles on nuclei via the weak interaction is presented. The main aim of this work is to offer theoretical predictions in terms of the angular, missing momentum, and energy distributions of the differential cross section of the reaction in the energy region between 1 GeV and 3 GeV. We develop relativistic models, which will make use of the elementary weak amplitudes, based on the relativistic impulse approximation (RIA) prescription. Therefore, these theoretical models will be constructed by using our previous work as one of the basic ingredients, and also aimed at accounting for nuclear structure and FSI effects. The nuclear structure effects such as Fermi motion, Pauli blocking, and binding energy correction are incorporated through the bound state wave function of a nucleon inside a nucleus; and this wave function is calculated from the relativistic mean field (RMF) approximation to the Walecka model with the NL3 parameter set. On the other hand, the elementary weak hadronic amplitudes are extracted from the Born term approximation, in which we assume that the SU(3) symmetry estimates of the strong coupling constants and the Cabibbo V-A theory which makes use of the conserved vector current (CVC) hypothesis are valid in the description of the elementary process. As a consequence, a meaningful interpretation of data and an improved understanding of hadronic and nuclear weak interactions, with particular interest in testing the Cabibbo V-A theory, SU(3) symmetry, and nuclear effects will hopefully be possible in the near future.

## 1.2 Outline of Dissertation

This dissertation is organized as follows: Chapter 2 is devoted to providing theoretical preliminaries. That is, we give an overview of the RIA scheme, Walecka model, and elementary production process on the free nucleon, which are basic ingredients crucial to constructing the theoretical description for the exclusive associated production of strange particles on nuclei. First, we present key assumptions that immediately follow the invocation of the impulse approximation and based on these assumptions of the RIA scheme we introduce two different frameworks: RPWIA and RDWIA, which will independently be used to model the exclusive reactions of great interest. Second, we review the Walecka model developed to describe the dynamics of nuclear many-body system using hadronic degrees of freedom in a fully relativistic approach which addresses the issue of nuclear structure effects via the bound state wave function since the reaction occurs inside a nucleus. Finally, we deal with the theoretical description of the underlying elementary processes on a free nucleon with particular interest in the weak hadronic weak current. In chapter 3, we develop the theoretical formalism of our models in terms of the differential cross section that will be followed by the kinematic description and the derivation of the nuclear transition matrix element of the exclusive reaction. Lastly, we construct the RPWIA model that will give us the first theoretical predictions of the neutrino-induced associated production on nuclei.

In chapter 4, we deal with the final state interactions in terms of the relativistic optical potential. After giving a brief overview of the Coulomb distortion of the final lepton and hyperon-nucleus interaction, we will go on to perform a rigorous formulation of kaon-nucleus interaction leading up to the calculation of the kaon distorted wave function by numerically solving the approximate Klein-Gordon equation containing the Kisslinger form optical potential. Then, in chapter 5 we present the theoretical description of the neutrino-induced strangeness associated production on nuclei using the RDWIA model. Although the formalism is general in nature, in this study we focus on a situation that allows the investigation of the kaon FSI effects by turning the hyperon FSI off. The numerical aspects of the theoretical description developed in chapter 5 are dealt with in chapter 6 whereby high performance computing techniques are introduced to address the computational complexity imposed by the invariant matrix element. Eventually, the numerical results for the RPWIA and RDWIA calculations for the exclusive CC and  $\Delta S = 0$   $K^+ \Lambda$  production on  ${}^4\text{He}$ ,  ${}^{12}\text{C}$ ,  ${}^{16}\text{O}$ ,  ${}^{40}\text{Ca}$ , and  ${}^{208}\text{Pb}$  nuclei under two kinematic settings are presented, compared and discussed in chapter 7. Finally, we give a summary and conclusion in chapter 8.

## Chapter 2

# Preliminaries for Neutrino-induced Kaon-Hyperon Production on Nuclei.

### 2.1 Introduction

Neutrino-induced associated production of strange particles on nuclei is one of the most challenging research areas of particle and nuclear physics which has not yet been fully explored, particularly, from the theoretical stand point. By contrast, there are a number of theoretical works done with regard to the underlying elementary processes on a free nucleon by the authors of Refs. [30, 31, 32, 33, 35]. In this chapter, we introduce a widely accepted theoretical prescription with which a reliable study of exclusive neutrino-nucleus reaction processes is possible. The main focus of this chapter is to set up a groundwork for the subsequent chapters in our endeavor to construct a theoretical framework that leads to the relativistic description of the exclusive reaction mechanism. In what follows, therefore, we give a brief overview of basic ingredients that will help establish such a framework within which the neutrino-induced associated production of strange particles on nuclei can be described reasonably well.

### 2.2 Relativistic Impulse Approximation

In most theoretical studies of lepton and hadron induced nuclear reactions involving the production of exclusive channels, it is common practice to implement several reasonable approximations. So far the impulse approximation has been the most plausible scheme in modelling the scattering of an energetic particle from an atomic nucleus. The compelling argument that validates the application of this scheme is that the momentum transfer to the target nucleus is relatively small as compared to the momenta transfer to the ejected particles. Further, the binding energy of the nucleons inside the nucleus is expected to be very small as compared to the incident energy of the projectile for this scheme to hold. Consequently, for a few GeV lepton or hadron interacting with a nucleus the impulse approximation can be considered as an acceptable approach. Thus, within the framework of impulse approximation only a single nucleon inside a nucleus that interacts with the incident particle, while the remaining bound nucleons act as spectators.

The impulse approximation scheme was, traditionally, applied in the nonrelativistic calculations of nuclear collisions, whereby the states of the incident particle and the bound nucleons are fully described by the Schrödinger equations[37, 38]. Then, an alternative relativistic approach was pioneered by Clark *et al.*[39, 40] in the study of nucleon-nucleus scatterings based on a formalism that describes the initial and final states of the reactions in terms of the Dirac equations; and it was further elaborated by authors of Refs. [41, 42, 43, 44]. As a matter of fact, this scheme has proven itself as a powerful rival to the nonrelativistic impulse approximation, and is commonly referred as the relativistic impulse approximation (RIA). One of the attractive features of the RIA scheme is that it can be formulated in the covariant form making it applicable in the plausible modelling of nuclear reactions over a wide kinematic range as well as under

extreme conditions.

The five major consequences of applying the RIA scheme in the study of nuclear reactions are: (i) the incident particle interacts with the target nucleus via a single-boson-exchange mechanism (i.e., the Born approximation); (ii) the vector gauge boson is absorbed only by a single bound nucleon inside the nucleus while other nucleons are being treated as spectators; (iii) the in-medium many-body current operator describing the transition between final and initial nuclear states is replaced by a sum of a free space current operators of individual nucleons; (iv) the nuclear structure effects are incorporated via the bound state wave function, of the nucleon inside the nucleus; and (v) the FSI effects on the ejected particles can be accounted for by using their corresponding distorted waves.

The first consequence is similar to the Born approximation which states that the interaction between the energetic particle and target nucleus can best be described by the lowest-order Feynman diagram. The second consequence of the RIA scheme circumvents a complication incurred by multiple rescattering problem in the evaluation of the weak nuclear matrix element. The third consequence allows us to perform theoretical calculations without being obscured by the details of nuclear transition densities. The fourth consequence, which directly results from the second consequence, is the realization of the significance of the in-medium modification effects such as Fermi motion, Pauli blocking, and nuclear binding that should be included in a fully relativistic manner. Finally, the fifth consequence can be dealt with by constructing the relativistic optical potentials that model the FSI effects and make their inclusion relatively easy.

Following its success in the description of the nucleon-nucleus reaction, the RIA scheme has also been invoked in other nuclear reaction studies such as quasifree photoproduction of mesons[45, 46, 47], quasifree electroproduction of mesons[48, 49], and quasielastic neutrino-nucleus scattering[9, 10, 50, 51]. More importantly the theoretical predictions of these studies have been able to provide good descriptions of the corresponding experimental data. Motivated by these plausible theoretical studies, we also base our work on the RIA scheme with the aim of developing the theoretical description of neutrino-induced associated production of strange particles on nuclei.

In general, the RIA scheme allows the study of lepton-induced nuclear reactions within two frameworks: (i) the RPWIA framework, whereby all of the projectile and ejectiles of the nuclear reaction are described by the relativistic plane waves, (ii) the RDWIA framework, which takes into account the FSI effects via the distorted wave functions of the ejected particles. Theoretical models developed for lepton-induced nuclear reactions within the RPWIA framework play an important role to study problems such as the strange quark content of the nucleon[9] and polarization observables in lepton-nucleus scatterings[46], which are barely sensitive to distortion effects. On top of that, the RPWIA offers a starting ground upon which other sophisticated but feasible models such as those which are aimed at taking the FSI effects into consideration. In other words, the RDWIA framework is an extension of the plane-wave limit calculations, and it is an attempt to offer a complete theoretical description of the lepton-induced nuclear scatterings. Thus, once the calculations of the differential cross sections and/or other observables are performed, we will be able compare the distorted wave analysis results with their plane wave counterparts to observe how the FSIs influence those quantities.

In the subsequent sections we give a detailed review of two important ingredients, of which the first one is presented in the next section, that is, the relativistic nuclear structure model that generates the bound state wave function of the constituent nucleon such that the nuclear medium effects can be accounted for; and in the last section we recapitulate our previous work[35], which was devoted to calculating the differential cross sections for the underlying elementary processes of neutrino-induced associated production on a free nucleon.

### 2.3 Quantum Hadrodynamics

In the investigation of neutrino-induced associated production of strange particles on nuclei, the RIA scheme is commonly invoked in order to provide a reasonable relativistic description of the neutrino-nucleus many-body problem. As such, the theoretical formulation of the reaction process starts with the assumption that the incident neutrino interacts with an individual nucleon inside the nucleus. In order to establish such a theory for the exclusive channel of the neutrino-nucleus scattering, we need an approach that ensures the incorporation of the nuclear structure effects in a fully relativistic way via the bound state wave function of the nucleon. As a result, we resort to the Quantum Hadrodynamics (QHD) model, which was introduced by Walecka[52]. In the QHD model the nuclear many-body system, which is assumed to consist of strongly interacting baryons via the exchange of mesons, is studied using the hadronic degrees of freedom as opposed to the underlying theory of strong interactions, QCD. It is worth noting that QHD is the effective field theory of the nuclear dynamics which is constrained by QCD symmetries: Lorentz invariance, parity invariance, gauge invariance, isospin symmetry and spontaneously broken chiral symmetry.

The QHD model within the RMF approximation has enjoyed considerable success in providing a quantitative description of the bulk and the single-particle properties of nuclei. With a very limited number of phenomenological parameters, the effective Lagrangian prescription is able to reproduce the ground-state properties of spherical and deformed nuclei[53, 54, 55]. The nuclear shell structure, spin-orbit splitting, nuclear saturation, and density dependence of the interaction are the natural consequence of the relativistic treatment of nuclear dynamics as opposed to the nonrelativistic approach that incorporates these relativistic effects via an *ad hoc* adjustment to the potentials[56]. The small binding energies of the bound nucleons inside the nucleus have offered strong motivation to the long-held argument that the nonrelativistic description of nuclear dynamics should be adequate. However, the RMF theory strongly challenges such an argument by stating that the relatively small binding energies are the direct consequences of the cancellation between a large attraction Lorentz-scalar potential and a large repulsion Lorentz-vector potential.

The original QHD model of Walecka consists of the Lagrangian density that considers nuclear matter as a many-body system of baryons interacting with one another via the exchange of the neutral scalar  $\sigma$  and neutral vector  $\omega$  mesons. It is the simplest version of QHD, and there are other models developed as a straightforward extension of the Walecka model with the aim of addressing some of its inaccuracies. Moreover, this model of Walecka is often referred as QHD-I in order to make it distinguishable from its extensions. The first of such extensions is referred as QHD-II and was developed by Serot[57]. In addition to the  $\sigma$  and  $\omega$  mesons, the QHD-II effective Lagrangian formalism incorporates: (i) isovector vector  $\rho$  meson, which accounts for mass splitting of nucleons in isospin asymmetric nuclear matter; (ii) electromagnetic field  $A^\mu$  to account for the in-medium Coulomb repulsion between the protons; and (iii) pseudoscalar pion fields, which, however, vanish at the mean field level due to their violation of parity invariance. This extension was successful in allowing the quantitative comparison of theory with experiment.

Though the parameters of the original Walecka model are fitted to reproduce the bulk properties of the saturation nuclear matter, the incompressibility coefficient is found to be too large ( $K = 560$  MeV) as compared with the value,  $K = 210 \pm 30$  MeV, obtained from breathing mode energy experiments[58]. In response to such a discrepancy, Boguta and Bodmer[59] proposed the inclusion of scalar meson self-interaction to the Lagrangian density in a nonlinear fashion. As a consequence, the RMF approach is able to prove a quantitative description of the ground state properties of not only stable nuclei, but also of those ones which are far from the valley of beta-stability[60, 61, 62].

The ansatz of QHD models starts with the usual Lagrangian formalism, whereby a set of equations of motion are derived from a Lagrangian density representing the dynamics of nuclei. Now we start with writing down the Lagrangian density for the nonlinear Walecka model as

follows:

$$\begin{aligned}
 \mathcal{L} &= \bar{\psi} \left[ i\gamma^\mu \left( \partial_\mu - g_\omega \omega_\mu - g_\rho \boldsymbol{\tau} \cdot \boldsymbol{\rho}_\mu - \frac{e}{2}(1 + \tau_3)A_\mu \right) \right. \\
 &\quad \left. - (M - g_\sigma \sigma) \right] \psi + \frac{1}{2} \partial^\mu \sigma \partial_\mu \sigma - U(\sigma) \\
 &\quad - \frac{1}{4} \Omega^{\mu\nu} \Omega_{\mu\nu} + \frac{1}{2} m_\omega^2 \omega^\mu \omega_\mu - \frac{1}{4} \mathbf{R}^{\mu\nu} \cdot \mathbf{R}_{\mu\nu} \\
 &\quad + \frac{1}{2} m_\rho^2 \boldsymbol{\rho}^\mu \cdot \boldsymbol{\rho}_\mu - \frac{1}{4} F^{\mu\nu} F_{\mu\nu}.
 \end{aligned} \tag{2.3.1}$$

Here  $\psi$  denotes the spinor field of isospin doublet nucleon;  $m_\sigma(g_\sigma)$ ,  $m_\omega(g_\omega)$ , and  $m_\rho(g_\rho)$  are the masses(coupling constants) of the  $\sigma$ ,  $\omega$ , and  $\rho$  mesons, respectively.  $M$  is the nucleon mass; and the nonlinear self-interaction of the  $\sigma$  meson is incorporated via

$$U(\sigma) = \frac{1}{2} m_\sigma \sigma^2 + \frac{1}{3} g_2 \sigma^3 + \frac{1}{4} g_3 \sigma^4. \tag{2.3.2}$$

The field tensors for the vector mesons and electromagnetic field are

$$\Omega^{\mu\nu} = \partial^\mu \omega^\nu - \partial^\nu \omega^\mu, \tag{2.3.3}$$

$$\mathbf{R}^{\mu\nu} = \partial^\mu \boldsymbol{\rho}^\nu - \partial^\nu \boldsymbol{\rho}^\mu - g_\rho (\boldsymbol{\rho}^\mu \times \boldsymbol{\rho}^\nu), \tag{2.3.4}$$

$$F^{\mu\nu} = \partial^\mu A^\nu - \partial^\nu A^\mu. \tag{2.3.5}$$

The set of equations of motion can now be derived from Eq. (2.3.1) through the application of the Euler-Lagrangian equation:

$$\frac{\partial \mathcal{L}}{\partial \phi(x)} - \partial_\mu \left( \frac{\partial \mathcal{L}}{\partial (\partial_\mu \phi)} \right) = 0. \tag{2.3.6}$$

Thus, the equations of motion for the baryons is the usual Dirac equation:

$$\left[ \gamma^\mu (i\partial_\mu - V_\mu) - (M - S) \right] \psi = 0, \tag{2.3.7}$$

where

$$V_\mu = g_\omega \omega_\mu + g_\rho \boldsymbol{\tau} \cdot \boldsymbol{\rho}_\mu + \frac{e}{2}(1 + \tau_3)A_\mu, \tag{2.3.8}$$

$$S = g_\sigma \sigma, \tag{2.3.9}$$

and the field equations of mesons and photon are Klein-Gordon equations:

$$(\partial^\mu \partial_\mu + m_\sigma^2) \sigma = -g_\sigma \bar{\psi} \psi - g_2 \sigma^2 - g_3 \sigma^3, \tag{2.3.10}$$

$$\partial_\nu \Omega^{\mu\nu} + m_\omega^2 \omega^\mu = g_\omega \bar{\psi} \gamma^\mu \psi, \tag{2.3.11}$$

$$\partial_\nu \mathbf{R}^{\mu\nu} + m_\rho^2 \boldsymbol{\rho}^\mu = g_\rho \bar{\psi} \gamma^\mu \boldsymbol{\tau} \psi + g_\rho (\boldsymbol{\rho}_\nu \times \mathbf{R}^{\mu\nu}), \tag{2.3.12}$$

$$\partial_\nu F^{\mu\nu} = e \bar{\psi} \gamma^\mu \frac{1 + \tau_3}{2} \psi. \tag{2.3.13}$$

### 2.3.1 Relativistic Mean Field Theory

The Dirac equation, Eq. (2.3.7), and the Klein-Gordon equations, Eqs. (2.3.10)-(2.3.13), form a system of coupled, nonlinear differential equation, and solving them exactly becomes a formidable task. The most widely accepted prescription to circumvent such a complication is to resort to the effective Lagrangian formalism, which is based on the relativistic Hartree approximation. In this approximation the meson field operators are replaced by their expectation values, which are the classical fields[63, 64]. Now considering a uniform nuclear matter we have

$$\sigma(x) \rightarrow \langle \sigma(x) \rangle = \sigma_0(\mathbf{x}), \tag{2.3.14}$$

$$\omega^\mu(x) \rightarrow \langle \omega^\mu(x) \rangle = g^{\mu 0} \omega_0(\mathbf{x}), \tag{2.3.15}$$

$$\boldsymbol{\rho}_i^\mu(x) \rightarrow \langle \boldsymbol{\rho}_i^\mu(x) \rangle = g^{\mu 0} \delta_{i3} \rho_0(\mathbf{x}), \tag{2.3.16}$$

$$A^\mu(x) \rightarrow \langle A^\mu(x) \rangle = g^{\mu 0} A_0(\mathbf{x}). \tag{2.3.17}$$



In a static, spherically symmetric nucleus, the spatial components of  $\omega^\mu$ ,  $\rho^\mu$ , and  $A^\mu$  have a vanishing contribution because of the current conservation. As a result, one only has to deal with the time-like component of the vector fields:  $\omega_0$ ,  $\rho^0$ , and  $A^0$ . Further, the charge conservation ensures that only the third-component ( $\rho_{0,3}$ ) of the isovector  $\rho^0$  contributes to the interaction. Similarly, the baryon source term in the Klein-Gordon equations are replaced by their ground state expectation values[65]:

$$\bar{\psi}(x)\psi(x) \rightarrow \langle \bar{\psi}(x)\psi(x) \rangle = \rho_s(\mathbf{x}), \quad (2.3.18)$$

$$\bar{\psi}(x)\gamma^\mu\psi(x) \rightarrow \langle \bar{\psi}(x)\gamma^\mu\psi(x) \rangle = g^{\mu 0}\rho_v(\mathbf{x}), \quad (2.3.19)$$

$$\bar{\psi}(x)\gamma^\mu\tau_i\psi(x) \rightarrow \langle \bar{\psi}(x)\gamma^\mu\tau_i\psi(x) \rangle = g^{\mu 0}\delta_{i3}\rho_3(\mathbf{x}), \quad (2.3.20)$$

$$\bar{\psi}(x)\gamma^\mu\tau_p\psi(x) \rightarrow \langle \bar{\psi}(x)\gamma^\mu\tau_p\psi(x) \rangle = g^{\mu 0}\rho_p(\mathbf{x}). \quad (2.3.21)$$

Here  $\tau_p$  denotes the proton projection operator:  $\tau_p = (1 + \tau_3)/2$ ;  $\rho_s(\mathbf{x})$  is the Lorentz-scalar density,  $\rho_v(\mathbf{x})$  is the vector or baryon density,  $\rho_3(\mathbf{x})$  is the isovector density, which is the difference between neutron  $\rho_n$  and proton  $\rho_p$  densities. Therefore, the mean field approximation of meson and photon fields, and also baryon source terms gives rise to the set of relativistic Hartree equations of which the Dirac equation is given by

$$\left[ -i\boldsymbol{\alpha} \cdot \boldsymbol{\nabla} + V_0(\mathbf{x}) + \beta(M - S_0(\mathbf{x})) \right] \psi(\mathbf{x}) = E\psi(\mathbf{x}), \quad (2.3.22)$$

where

$$V_0(\mathbf{x}) = g_\omega\omega_0(\mathbf{x}) + g_\rho\tau_3\rho_{0,3}(\mathbf{x}) + e\tau_p A_0(\mathbf{x}), \quad (2.3.23)$$

$$S_0(\mathbf{x}) = g_\sigma\sigma_0(\mathbf{x}), \quad (2.3.24)$$

and  $E$  is a single-particle energy of nucleon. Similarly, the Klein-Gordon equations also take the form

$$-\nabla^2\phi_0 + U'(\phi_0) = \pm g_\phi\rho_\phi, \quad (2.3.25)$$

where  $\phi_0$  denotes  $\sigma_0(\mathbf{x})$ ,  $\omega_0(\mathbf{x})$ ,  $\rho_{0,3}(\mathbf{x})$ , and  $A_0(\mathbf{x})$  classical fields;  $g_\phi$  and  $\rho_\phi$  refer to the corresponding coupling constants and the baryon source terms, respectively, and  $U'(\phi_0)$  is the first-derivative of  $U(\phi_0)$ , which is defined for individual boson fields as

$$U(\sigma_0) = \frac{1}{2}m_\sigma^2\sigma_0^2 + \frac{1}{3}g_2\sigma_0^3 + \frac{1}{4}g_3\sigma_0^4, \quad (2.3.26)$$

$$U(\omega_0) = \frac{1}{2}m_\omega^2\omega_0^2, \quad (2.3.27)$$

$$U(\rho_{0,3}) = \frac{1}{2}m_\rho^2\rho_{0,3}^2, \quad (2.3.28)$$

$$U(A_0) = 0. \quad (2.3.29)$$

Note also that the right-hand side of Eq. (2.3.25) takes the plus(minus) sign for vector(scalar) fields. Therefore, Eqs. (2.3.22) and (2.3.25) form a system of coupled differential equations also known as the relativistic Hartree equation. An iterative procedure is implemented to self-consistently solve the Dirac equation, Eq. (2.3.22), with scalar and vector potentials obtained from the solutions of the Klein-Gordon equations of the form give in Eq. (2.3.25). In so doing, the nucleon spinor and meson fields are expanded in the basis of the spherical harmonics.

The nonlinear Walecka model with an accurately calibrated NL3 parameter set has so far been remarkably successful in describing the ground state properties of spherical and deformed nuclei[55]. It has also been extrapolated to examine the astrophysical observables. however, the mean field model with NL3 parametrization gives rise to an equation of state (EoS) for a neutron star that is stiffer, both for symmetric nuclear matter as well as for the symmetry energy. As a consequence, the model predicts a considerably large radius and limiting mass for neutron star. In response to such poor astrophysical predictions by NL3 model, Todd-Rutel

and Piekarewicz[66] proposed a new set of parameters, dubbed as FSUGold. This model only modifies the meson self-interaction potential  $U(\sigma)$  of Eq. (2.3.1) in order to accommodate, in addition to the scalar meson self-interaction, the vector meson self-interaction and mixed isoscalar-isovector coupling. That is,

$$U(\sigma) \rightarrow U(\sigma, \omega^\mu, \rho^\mu) = \frac{\kappa}{3!} (g_\sigma \sigma)^2 + \frac{\lambda}{4!} (g_\sigma \sigma)^4 - \frac{\zeta}{4!} (g_\omega^2 \omega_\mu \omega^\mu)^2 - \Lambda_v (g_\rho^2 \rho_\mu \cdot \rho^\mu) (g_\omega^2 \omega_\mu \omega^\mu). \quad (2.3.30)$$

Here  $\kappa$ ,  $\lambda$ , and  $\zeta$  are the coupling constants of isoscalar meson self-interactions, which are responsible in the softening of the EoS for symmetric nuclear matter[67], whereas isoscalar-isovector coupling constant  $\Lambda_v$  improves the density dependence of the symmetry energy and neutron skin thickness for heavy nuclei[66]. The FSUGold parameter set is constrained by not only QCD symmetries and experimental data, which is the case for other QHD models, but also by observational data on neutron star. Therefore, since this model gives rise to the softening of EoS and the symmetry energy, it is able to predict a considerably small radius and mass limit of the neutron star[66].

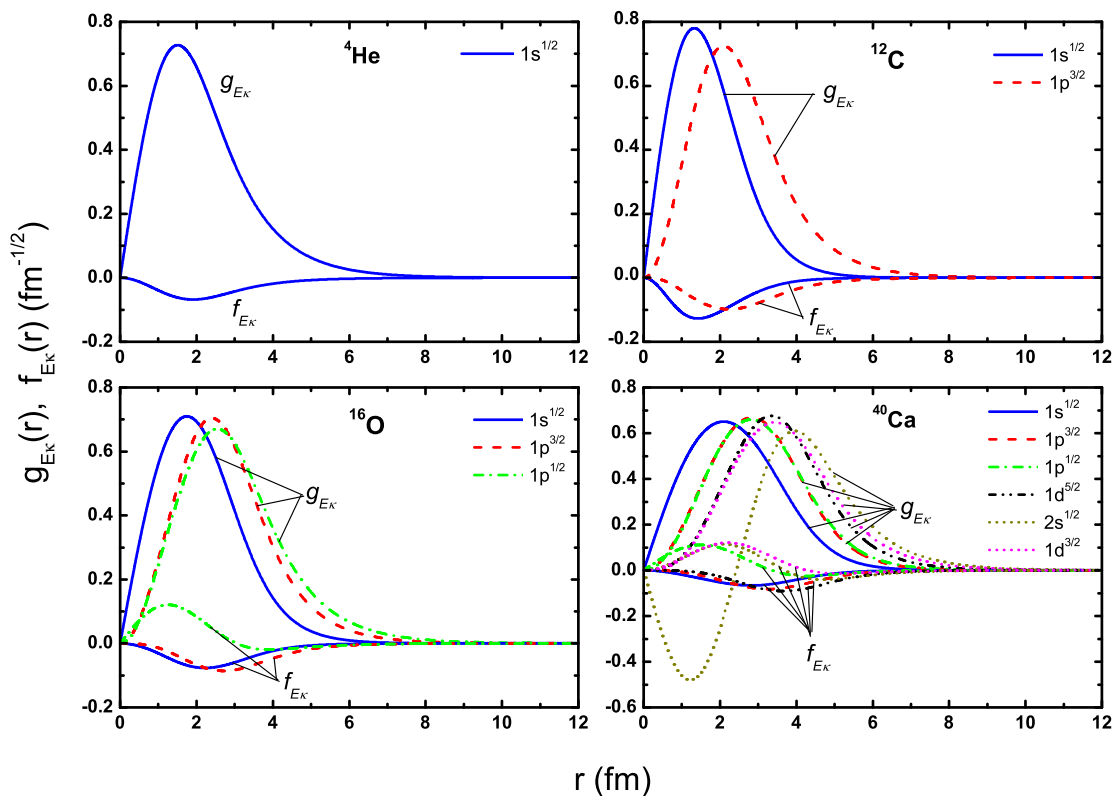


**Figure 2.1:** The radial wave functions  $g_{E\kappa}(r)$  and  $f_{E\kappa}(r)$  of bound state neutron occupying the RSM orbitals of  ${}^4\text{He}$ ,  ${}^{12}\text{C}$ ,  ${}^{16}\text{O}$ , and  ${}^{40}\text{Ca}$ . These radial components of the Dirac spinor determined from the nonlinear Walecka model with the NL3 parametrization.

### 2.3.2 Relativistic Shell Model

In this theoretical investigation of neutrino-induced associated production of strange particles on nuclei, the nuclear structure information is incorporated through the wave functions of bound state nucleons calculated withing the framework of the relativistic shell model (RSM). In order to do so, we must find physical and self-consistent solutions to the single-particle Dirac equation



as defined in Eq. (2.3.22), which is derived from the effective Lagrangian formalism of the nonlinear Walecka model. For spherical nuclei, the positive energy Dirac spinors or orbitals will therefore be written as

$$U_{E\kappa m}(\mathbf{x}) = \frac{1}{x} \begin{pmatrix} g_{E\kappa}(x)\mathcal{Y}_{\kappa m}(\hat{\mathbf{x}}) \\ if_{E\kappa}(x)\mathcal{Y}_{-\kappa m}(\hat{\mathbf{x}}) \end{pmatrix}, \quad (2.3.31)$$

where  $\kappa$  is the generalized relativistic angular momentum which uniquely specifies both the orbital  $l$  and total  $j$  angular momenta:

$$j = |\kappa| - \frac{1}{2}, \quad l = \begin{cases} \kappa, & \text{for } \kappa > 0, \\ 1 - \kappa, & \text{for } \kappa < 0, \end{cases} \quad (2.3.32)$$

and  $m$  is the projection of  $j$ ;  $\mathcal{Y}_{\kappa m}(\hat{\mathbf{x}})$  is the spin-angular wave function, which couples the Pauli

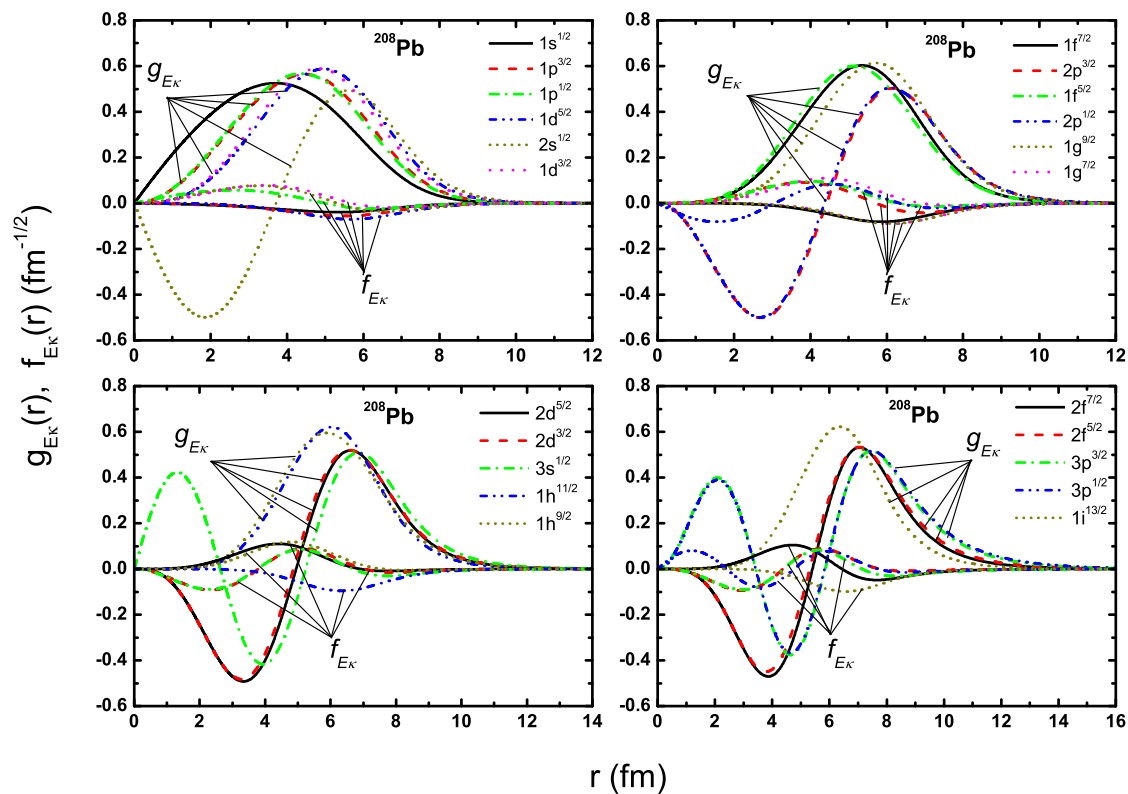


**Figure 2.2:** The radial wave functions  $g_{E\kappa}(r)$  and  $f_{E\kappa}(r)$  in coordinate space for the neutron orbitals of  $^{208}\text{Pb}$ . They are computed using the nonlinear QHD model with the NL3 parameter set.

spinor  $\chi_{s_{z'}}$  with the spherical harmonics  $Y_{l,m_l}$  of order  $l$ , and by setting  $m_l = m - s_{z'}$  we may write:

$$\mathcal{Y}_{\kappa m} = \sum_{s_{z'} = \pm \frac{1}{2}} \left\langle l, \frac{1}{2}, m - s_{z'}, s_{z'} \middle| j, m \right\rangle Y_{l, m - s_{z'}}(\hat{\mathbf{x}}) \chi_{s_{z'}}. \quad (2.3.33)$$

Here the expansion constants of Eq. (2.3.33) are the usual Clebsch-Gordon coefficients. Note that  $-\kappa$  in the lower component of the Dirac spinor in Eq. (2.3.31) corresponds to the orbital angular momentum  $l' = 2j - l$ . The upper and lower radial components of the Dirac orbital are denoted by  $g_{E\kappa}(x)$  and  $f_{E\kappa}(x)$ , respectively. Therefore, by substituting Eq. (2.3.31) into Eq. (2.3.22) we obtain two coupled differential equations of the bound nucleon radial wave functions.

That is,

$$\frac{d}{dx}g_{E\kappa}(x) + \frac{\kappa}{x}g_{E\kappa}(x) - [E - V_0 + M - S_0]f_{E\kappa}(x) = 0, \quad (2.3.34)$$

$$\frac{d}{dx}f_{E\kappa}(x) - \frac{\kappa}{x}f_{E\kappa}(x) + [E - V_0 - M + S_0]g_{E\kappa}(x) = 0, \quad (2.3.35)$$

with the following normalization condition

$$\int_0^\infty dr \left[ g_{E\kappa}^2(x) + f_{E\kappa}^2(x) \right] = 1. \quad (2.3.36)$$

Thus Eqs. (2.3.34) and (2.3.35) are the coupled differential equations which provide a relativistic description of the ground states of the spherical nuclei. The solutions must be self-consistent in such a way that the meson and electromagnetic fields used to generate the Dirac mean field potentials must satisfy the Klein-Gordon equations, Eq. (2.3.25) with baryon sources terms or nuclear densities calculated from the solutions of these two coupled radial differential equations. Fig. 2.1 depicts the numerical solutions of Eqs. (2.3.34) and (2.3.35), namely, the

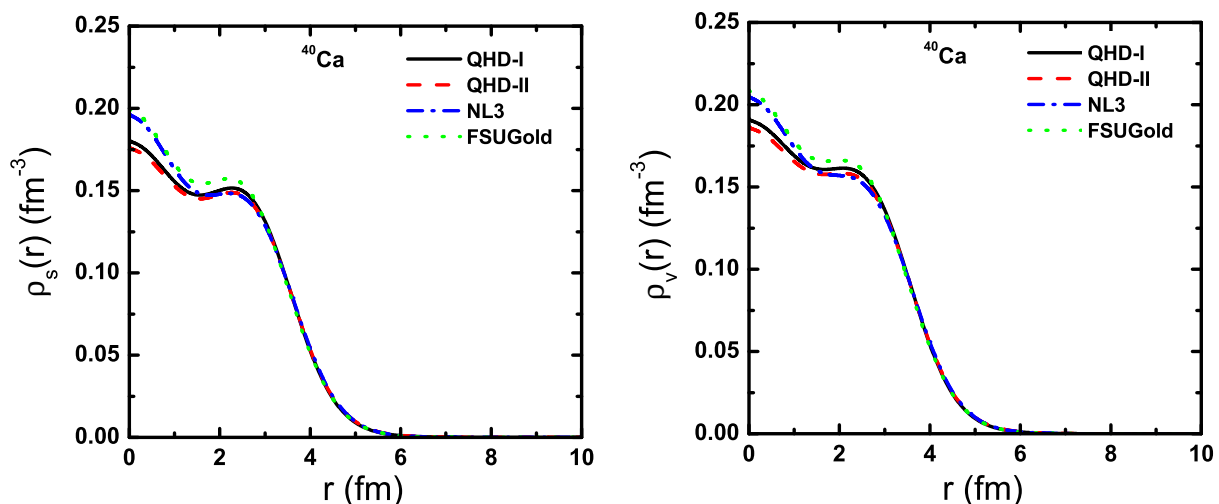


**Figure 2.3:** The scalar density  $\rho_s(r)$  (left panel) and the vector density  $\rho_v(r)$  (right panel) of  $^{40}\text{Ca}$  as calculated via the relativistic mean field approximation to the original Walecka model (QHD-I) and its extensions: QHD-II, NL2, and FSUGold.

radial wave functions  $g_{E\kappa}(r)$  and  $f_{E\kappa}(r)$  of the RSM neutron orbitals for  $^4\text{He}$ ,  $^{12}\text{C}$ ,  $^{16}\text{O}$ , and  $^{40}\text{Ca}$ . Similarly, Fig. 2.2 shows the coordinate space dependence of  $g_{E\kappa}(r)$  and  $f_{E\kappa}(r)$  for the bound state neutrons of  $^{208}\text{Pb}$ . These radial components of the Dirac spinor determined from the RMF approximation of the nonlinear Walecka model with the NL3 parameter set. We also notice that Eqs. (2.3.18) - (2.3.21) are a clear indications that the relativistic treatment of the nuclear structure offers five types of nuclear densities: scalar, vector, axial-vector, tensor, and pseudoscalar nuclear densities in a quite natural way as opposed to the nonrelativistic formalism which essentially offers only one of them, namely, the matter (vector) density. This is very crucial evidence on how rich the RMF treatment of the nuclear many-body problem is as compared to the nonrelativistic approach. The nuclear densities Eqs. (2.3.18) - (2.3.21) can be rewritten,

with  $r = |\mathbf{x}|$ , as

$$\rho_s(r) = \sum_{\alpha} \bar{U}_{\alpha}(\mathbf{x}) U_{\alpha}(\mathbf{x}), \quad (2.3.37)$$

$$\rho_v(r) = \sum_{\alpha} \bar{U}_{\alpha}(\mathbf{x}) \gamma^0 U_{\alpha}(\mathbf{x}), \quad (2.3.38)$$

$$\rho_3(r) = \sum_{\alpha} U_{\alpha}^{\dagger}(\mathbf{x}) \tau_3 U_{\alpha}(\mathbf{x}), \quad (2.3.39)$$

$$\rho_p(r) = \sum_{\alpha} U_{\alpha}^{\dagger}(\mathbf{x}) \frac{1 + \tau_3}{2} U_{\alpha}(\mathbf{x}), \quad (2.3.40)$$

where  $U_{\alpha}$  are a single-particle Dirac spinors, and  $\alpha = \{nljm\}$  is the quantum number required to specify a particular state in the relativistic shell structure of a given nucleus. Note that the summations are carried out over all occupied single-particle states. Fig. 2.3 displays the

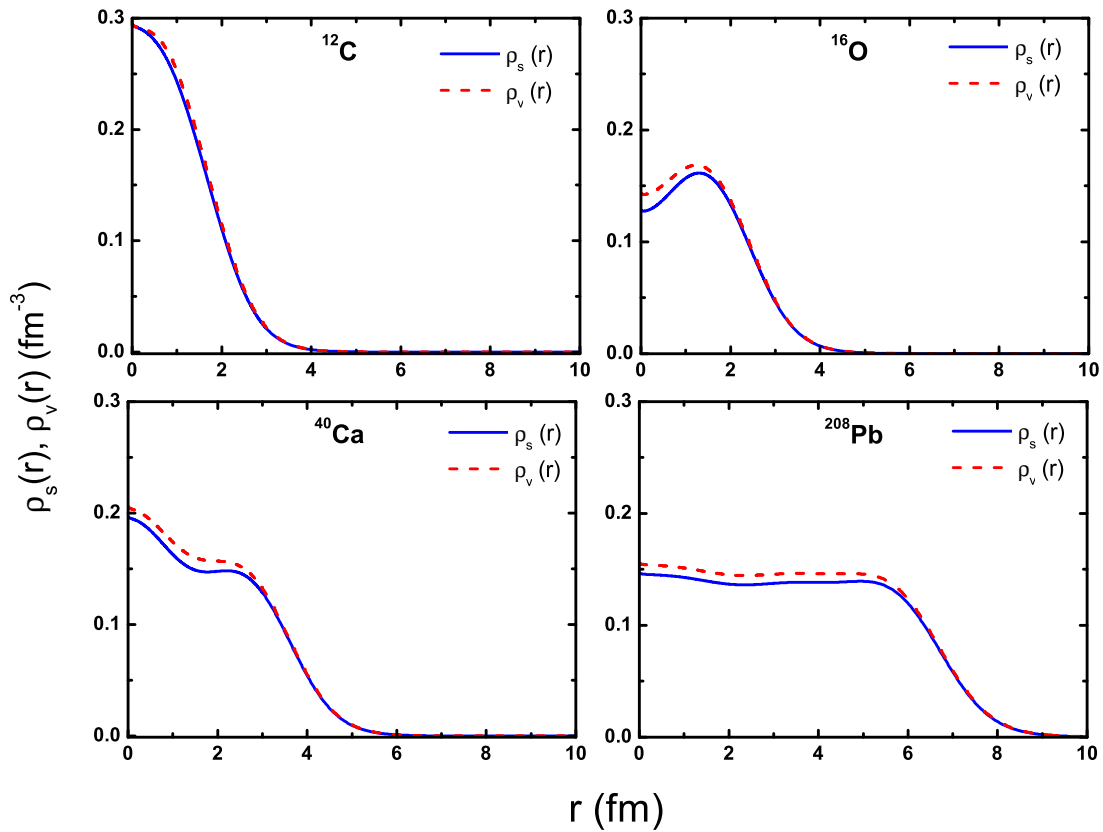


**Figure 2.4:** The scalar density  $\rho_s(r)$  and the vector density  $\rho_v(r)$  in  $^{12}\text{C}$ ,  $^{16}\text{O}$ ,  $^{40}\text{Ca}$ , and  $^{208}\text{Pb}$ . They are determined from the radial wave functions  $g_{E\kappa}(r)$  and  $f_{E\kappa}(r)$  obtained from the RMF approximation to the nonlinear Walecka model with NL3 parameter set.

scalar density  $\rho_s(r)$  (left panel) and the vector density  $\rho_v(r)$  (right panel) of  $^{40}\text{Ca}$  as calculated within the RMF approximation to the Walecka model with QHD-I, QHD-II, NL2, and FSUGold parameterizations, whereas Fig. 2.4 illustrates the behavior  $\rho_s(r)$  and  $\rho_v(r)$  for  $^{12}\text{C}$ ,  $^{16}\text{O}$ ,  $^{40}\text{Ca}$ , and  $^{208}\text{Pb}$ , as calculated from from the RMF approximation to the nonlinear Walecka model with NL3 parameter set.

## 2.4 Associated KY Production on Free Nucleons

As has been the case for numerous semi-leptonic problems, the study of neutrino-nucleus scattering depends on a good understanding of the underlying elementary process. It is therefore worthwhile to give a brief overview on the neutrino-induced strangeness production on a free nucleon, which is one of the basic ingredients when one invokes the RIA treatment of the nuclear reaction. Several of such elementary production processes were reported from bubble chamber experiments at ANL[25], CERN[26], and BNL[29]. Rough theoretical estimations of associated production cross sections from neutrino-nucleon scattering were performed in the mid seventies and early eighties by Shrock[30], Mecklenburg[31], and Dewan[33] using hadronic degree of freedom, where as Amer[32] approached the same problem using the quark model.

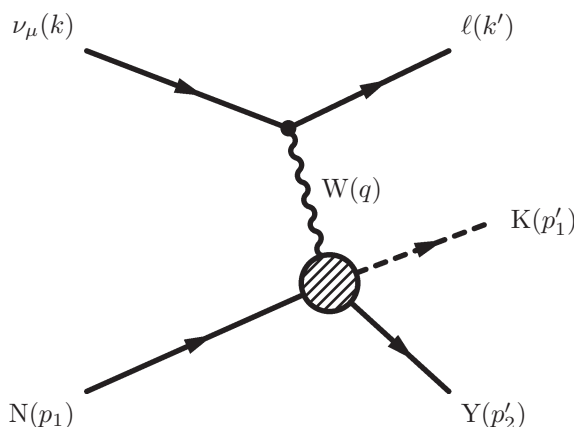


**Figure 2.5:** Lowest order Feynman diagram of neutrino-induced strange particle production from a free nucleon.

In this section, however, we focus on the most recent work that has been developed in Ref. [34] and published in Ref. [35], in which a theoretical study of the underlying exclusive production channels has been revived with particular interest in the CC and  $\Delta S = 0$  processes. The ultimate goal of this section is, therefore, to provide a proper introduction to the model-independent weak hadronic current operator in its general representation form. Subsequently, we will illustrate how the elementary current operator with eighteen unknown form factors can be determined using a model-dependent approach to weak hadronic transitions.

The neutrino-induced associated production of strange particles from a free nucleon as illustrated in Fig. 2.5 is of the form

$$\nu(k) + N(p) \longrightarrow \ell(k') + K(p'_1) + Y(p'_2), \quad (2.4.1)$$

where  $\nu$  and  $\ell$  denote the incident neutrino and outgoing lepton, respectively; whereas N, K, and Y represent the target nucleon, outgoing kaon, and outgoing hyperon, respectively. The corresponding four-momenta of the participating particles are labeled by the variables given in the parenthesis. Based on the standard procedure the Lorentz invariant matrix element of the elementary reaction can be constructed from the Feynman diagram shown in Fig. 2.5 such that

$$|\mathcal{M}_{fi}|_{\text{free}}^2 = \frac{G_F^2}{2} \eta_c^2 L_{\mu\nu} W^{\mu\nu}, \quad (2.4.2)$$

where  $G_F = 1.166 \times 10^{-5} \text{ GeV}^{-2}$  is the Fermi constant, and

$$\eta_c = \begin{cases} \cos \theta_C, & \text{for CC \& } \Delta S = 0 \\ \sin \theta_C, & \text{for CC \& } \Delta S = 1 \\ \frac{1}{2}, & \text{for NC \& } \Delta S = 0. \end{cases} \quad (2.4.3)$$

Here  $\theta_C$  denotes the phenomenological constant known as the Cabibbo angle ( $\cos \theta_C \approx 0.97$ ), which is introduced in order to account for the asymmetry reported in the experimental detection of the  $\Delta S = 0$  and  $\Delta S = 1$  CC exclusive processes. The leptonic tensor  $L_{\mu\nu}$  is completely specified on the basis of the electroweak theory of Glashow, Salam, and Weinberg. Thus for the CC process it can be written as

$$L_{\mu\nu} = \frac{2}{k^0 k'^0} \left[ k_\mu K_\nu + k_\nu K_\mu - k \cdot K g_{\mu\nu} + i \varepsilon_{\mu\nu\alpha\beta} k^\alpha K^\beta \right], \quad (2.4.4)$$

where  $\varepsilon_{\mu\nu\alpha\beta}$  is the four-dimensional antisymmetric Levi-Civita tensor with convention  $\varepsilon^{0123} = -\varepsilon_{0123} = 1$ , and

$$K^\mu = \frac{1}{2} (k'^\mu - h' m_l s'^\mu) \quad (2.4.5)$$

with  $h'$  being the helicity state corresponding to the spin polarization four-vector  $s'^\mu$  of the final lepton defined as

$$s'^\mu = \frac{1}{m_l} \left( |\mathbf{k}'|, E_{k'} \hat{\mathbf{k}}' \right). \quad (2.4.6)$$

Note that Eq. (2.4.4) is calculated by considering a non-covariant normalization for the helicity representation of the spinor fields of neutrino and final lepton, and for neutral current (NC) processes we have  $K^\mu \rightarrow k'^\mu$ . The hadronic tensor  $W^{\mu\nu}$ , on the other hand, is given as

$$W_{\mu\nu} = H_\mu H_\nu^\dagger, \quad (2.4.7)$$

where

$$H^\mu = \bar{U}_Y(\mathbf{p}'_2, s'_2) \hat{J}^\mu(q) U_N(\mathbf{p}, s) \quad (2.4.8)$$

and  $\hat{J}^\mu(q)$  is the weak hadronic current operator, which is a very complicated object. As a result, we resort to expressing  $\hat{J}^\mu(q)$  using a model-independent decomposition that leads up to the representation of the hadronic vertex in terms of eighteen parameters, which are calculated via a model-dependent analysis of the hadronic vertex.

### 2.4.1 Decomposition of Hadronic Current

Here we give a brief illustration of how the general form of the weak hadronic current operator, which represents the blob or production vertex in Fig. 2.6, has been constructed in Ref [34]. In that thesis, we have addressed this particular problem by decomposing  $\hat{J}^\mu$  in terms of invariant amplitudes which can fully parameterize the weak hadronic transition vertex.

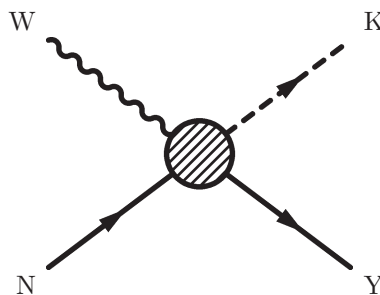


**Figure 2.6:** Schematic diagram of a free nucleon going, upon interacting with a weak gauge boson, into an exclusive channel which contains a kaon and hyperon in the final state.

The decomposition procedure starts with the consideration of the global structure of  $\hat{J}^\mu(q)$ , that is, it is a Lorentz four-vector, and a  $4 \times 4$  square matrix in the Dirac spinor space. With that in mind, the most general form of  $\hat{J}^\mu(q)$  was derived, for the first time, to represent the (N, KY) weak transition[34], shown in Fig. 2.6, by extending the basic principles employed to construct a nucleon electromagnetic current in terms of two form factors[68, 69]. Having sandwiched  $\hat{J}^\mu(q)$

between two Dirac spinors of on-shell particles, we can perform the first linear decomposition of the current operator in terms of the bilinear covariant basis[70]:  $I$ ,  $\gamma_5$ ,  $\gamma^\mu$ ,  $\gamma_5\gamma^\mu$ , and  $\sigma^{\mu\nu}$ . That is

$$\bar{U}_Y(\mathbf{p}'_2)\hat{J}^\mu(q)U_N(\mathbf{p}_1) = \bar{U}_Y(\mathbf{p}'_2) \left[ \tilde{A}^\mu I + \tilde{B}^\mu \gamma_5 + \tilde{C}^{\mu\nu} \gamma_\nu + \tilde{D}^{\mu\nu} \gamma_5 \gamma_\nu + \tilde{E}^{\mu\nu\alpha} \sigma_{\nu\alpha} \right] U(\mathbf{p}_1), \quad (2.4.9)$$

where  $\tilde{A}^\mu$ ,  $\tilde{B}^\mu$ ,  $\tilde{C}^{\mu\nu}$ ,  $\tilde{D}^{\mu\nu}$ ,  $\tilde{E}^{\mu\nu\alpha}$  are unknown tensors that need further decomposition by making use of three independent four-momenta:  $q^\mu$ ,  $p^\mu$ , and  $p_2'^\mu$ ; the metric tensor:  $g^{\mu\nu}$ ; the antisymmetric Levi-Civita tensor  $\varepsilon^{\mu\nu\alpha\beta}$  that we have at our disposal. In this study we are more interested in the final expression of  $\hat{J}^\mu(q)$  as the detailed derivation can be found in Ref. [34]. Therefore, the Dirac algebra and Gordon-like identities are applied repeatedly on the gamma matrices, four-momenta, and their combinations to finally come up with the most general representation of the weak hadronic current operator:

$$\begin{aligned} \bar{U}_Y(\mathbf{p}'_2)\hat{J}^\mu(q)U_N &= \bar{U}_Y(\mathbf{p}'_2) \left[ \tilde{A}^\mu I + \tilde{B}^\mu \gamma_5 + \tilde{C}_1 \gamma^\mu + \tilde{C}^\mu \not{q} + \tilde{D}_1 \gamma_5 \gamma^\mu \right. \\ &\quad \left. + \tilde{D}^\mu \gamma_5 \not{q} + \tilde{D}_5 \not{q} \gamma^\mu + \tilde{D}_6 \gamma_5 \not{q} \gamma^\mu \right] U_N(\mathbf{p}_1), \end{aligned} \quad (2.4.10)$$

where

$$\begin{aligned} \tilde{A}^\mu &= \tilde{A}_1 q^\mu + \tilde{A}_2 p_1^\mu + \tilde{A}_3 p_2'^\mu + \tilde{A}_4 \varepsilon^{\mu\nu\alpha\beta} q_\nu p_{1\alpha} p_{2\beta}', \\ \tilde{B}^\mu &= \tilde{B}_1 q^\mu + \tilde{B}_2 p_1^\mu + \tilde{B}_3 p_2'^\mu + \tilde{B}_4 \varepsilon^{\mu\nu\alpha\beta} q_\nu p_{1\alpha} p_{2\beta}', \\ \tilde{C}^\mu &= \tilde{C}_2 q^\mu + \tilde{C}_3 p_1^\mu + \tilde{C}_4 p_2'^\mu, \\ \tilde{D}^\mu &= \tilde{D}_2 q^\mu + \tilde{D}_3 p_1^\mu + \tilde{D}_4 p_2'^\mu, \end{aligned} \quad (2.4.11)$$

and use is made of the Dirac slash notation  $\not{a} = a_\mu \gamma^\mu$  for any arbitrary four-vector  $a^\mu$ . Thus in such a general representation of the weak hadronic current operator, there are eighteen Lorentz invariant form factors with which the hadronic vertex of Fig. 2.6 can be parameterized. Note that throughout this study we adopt the Bjorken-Drell[68] conventions for the Dirac matrices.

As mentioned earlier, a similar procedure has already been used to establish two such form factors to represent a single proton electromagnetic transition vertex. That is,

$$\langle p' | j_{\text{em}}^\mu | p \rangle = \bar{U}_p(\mathbf{p}') \left[ F_1(q^2) \gamma^\mu + \frac{iF_2(q^2)}{2M} \sigma^{\mu\nu} q_\nu \right] U_p(\mathbf{p}), \quad (2.4.12)$$

with  $q^\mu = p^\mu - p'^\mu$ ; and by using these two parameters the nucleon structure has successfully been studied via the electron scattering which has led to a reasonable interpretation of experimental data. Moreover, it is important to point out the fact that this model-independent derivation of the most general form of  $\hat{J}^\mu(q)$  is somewhat similar in spirit with the CGLN[71] mechanism, which was developed for the study of photo- and electro-production of mesons on nucleons and nuclei. It is also worthy noting that as opposed to the electromagnetic current operator, there is no need to impose current conservation and other symmetries such as parity, time-reversal, and charge conjugation on the weak hadronic current operator as it is known to violate all of these. For this reason that the model-independent expansion of  $\hat{J}^\mu(q)$  contains as many as eighteen parameterization amplitudes for the (N, KY) weak transition vertex.

## 2.4.2 The Born-term Model

As shown in subsection 2.4.1, the most general form of  $\hat{J}^\mu(q)$ , which represents the weak transition of a nucleon to a pair of strange particles, namely, a kaon and hyperon, consists of yet to be determined eighteen Lorentz invariant form factors. Unlike the case for the two form factors of the electromagnetic current, the phenomenological determination of the eighteen form factors becomes a formidable task. As a result, we resort to a model-dependent evaluation of these weak hadronic current amplitudes. In doing so, the Born-term model was introduced such that the hadronic vertex in Fig. 2.6 is approximated by the tree-level Born diagrams shown in Fig. 2.7

for the  $\nu n \rightarrow \ell K^+ \Lambda$  weak production channel. In this model we are strictly taking into account the background (nonresonant) contributions: a nucleon-, hyperon-, and kaon-exchange currents of the  $s$ -,  $u$ -, and  $t$ -channels, which are directly related to the three Lorentz invariant kinematic variables:  $s = (q+p_1)^2$ ,  $u = (q-p'_2)^2$ , and  $t = (q-p'_1)^2$ , respectively. This approximation is valid near threshold where strong resonances are considered to be absent except for the lowest-lying ones, which in fact decay mainly into  $N\pi$  and  $N\pi\pi$ [30].

At this stage, it is very important to point out the fact that the tree-level Born diagrams introduce three type of transition vertices: (i) a baryon weak coupling vertex via the  $s$ - and  $u$ -channels; (ii) a pseudoscalar strong coupling vertex via all Born-channels; (iii) a meson weak coupling vertex via the  $t$ -channel. Therefore, the corresponding current amplitudes of these channels cannot be determined unless relevant models are invoked to specify these three vertex types.

### 2.4.2.1 Quark Model of Hadrons

Heisenberg was the first to postulate that the strong interaction does not distinguish between a proton and neutron. He proposed, using the  $SU(2)$  symmetry formulation, that the proton and neutron are to be regarded as two isospin states of a single particle, the nucleon. In other words, the two particles form the nucleon isospin doublet. Similarly, the  $K^+$  and  $K^0$  mesons also correspond to a kaon isospin doublet. In addition,  $(\Sigma^+, \Sigma^0, \Sigma^-)$  and  $(\pi^+, \pi^0, \pi^-)$  form the  $\Sigma$

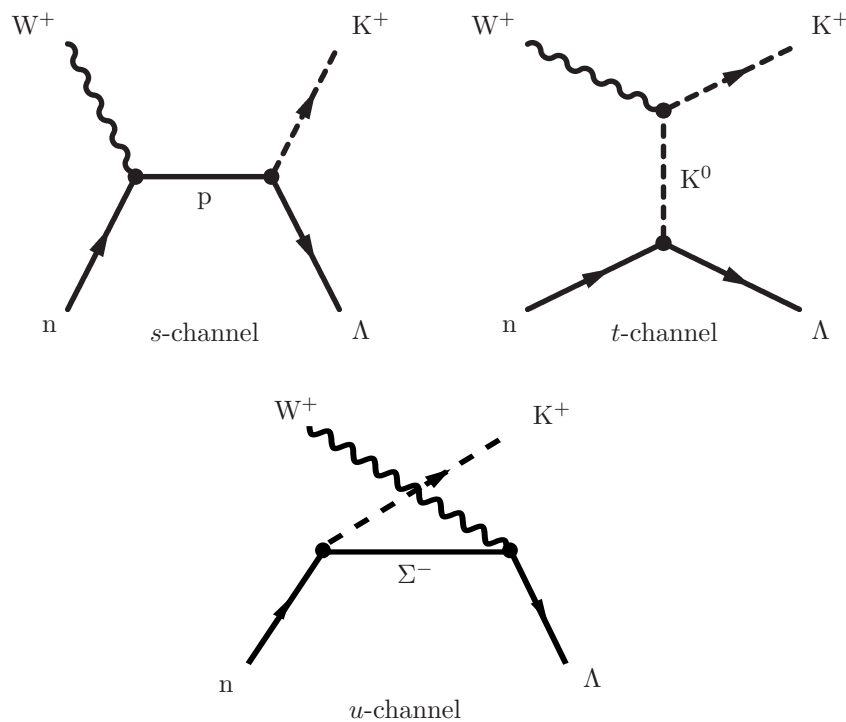


**Figure 2.7:** Tree-level Born diagrams of the weak hadronic vertex for the neutrino-induced associated production process:  $\nu n \rightarrow \ell K^+ \Lambda$ .

hyperon and pion isospin triplets, respectively, whereas  $\Xi^0$  and  $\Xi^-$  hyperons belong to  $\Xi$  isospin doublet, and the same applies to  $K^-$  and  $\bar{K}^0$  mesons. We also notice that the  $\Lambda$  hyperon and  $\eta$  meson are regarded as isospin singlets.

In the sixties, Gellmann[72] and Zweig[73] independently proposed the classification of hadrons using  $SU(3)$  flavor symmetry, which is in fact the generalization of its subgroup, the  $SU(2)$  isospin symmetry. Their scheme is based on three quark flavors: up-, down-, and strange-quarks. The



strange-quark introduces additional quantum number called strangeness  $S$ , which is a conserved quantity in the strong and electromagnetic interactions; and this quantum number is related to electric charge  $\mathcal{Q}$ :

$$\mathcal{Q} = I_3 + \frac{1}{2}Y, \quad (2.4.13)$$

where  $I_3$  is the third component of isospin and the weak hypercharge  $Y$  is introduced and defined as  $Y = B + S$ , with  $B$  denoting the baryon quantum number.

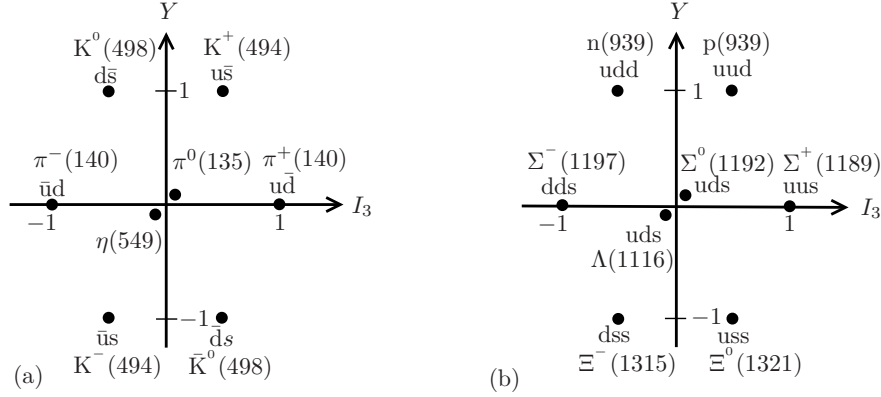


**Figure 2.8:** The SU(3) octet representations of (a) pseudoscalar-mesons ( $J^\pi = 0^-$ ) and (b) baryons ( $J^\pi = \frac{1}{2}^+$ ) along with their corresponding masses in MeV and quark compositions. Note that the quark compositions of  $\pi^0$  and  $\eta$  are  $(u\bar{u} + d\bar{d})/\sqrt{2}$  and  $(u\bar{u} + d\bar{d} - 2s\bar{s})/\sqrt{6}$ , respectively.

The three light quarks and the corresponding antiquarks belong to the fundamental representations  $3$  and  $\bar{3}$  of the SU(3) group. In the context of group theory, these representations have been combined in specific patterns to construct many-quark systems, which have successfully reproduced the same quantum numbers of the well-known light hadrons. To be more specific, the SU(3) octet representations of mesons ( $B = 0$  and  $J^\pi = 0^-$ ) and baryons ( $B = 1$  and  $J^\pi = \frac{1}{2}^+$ ) can be constructed by taking the Kronecker products  $3 \otimes \bar{3}$  and  $3 \otimes 3 \otimes 3$ , respectively, of the fundamental representations. The weight diagrams of (a) pseudoscalar meson and (b) baryon octets are depicted in Fig. 2.8 along with their respective quark compositions and masses.

Suppose  $q(x)$  is the three-component quark field which is constructed from the up-, down- and strange-quark base states. If the mass differences of the three quarks are ignored, the Lagrangian density of the quark field is defined as

$$\mathcal{L} = \bar{q}(x) (i \not{\partial} + m_q) q(x), \quad (2.4.14)$$

where  $m_q$  is the quark mass. In the language of group theory, all three-dimensional unitary unimodular matrices, whose action on the quark field leave the Lagrangian density invariant, form the SU(3) group. If one assumes  $U$  as the member of SU(3) group, then it can be written as

$$U = e^{i \sum_{j=1}^8 \theta_j \frac{\lambda_j}{2}}. \quad (2.4.15)$$

Here  $\theta_j$  are real parameters, and  $\lambda_j$  denote eight independent  $3 \times 3$  traceless matrices, which are the generators of SU(3) group. The standard choices for  $\lambda_j$  were given by Gellmann[74]; and the algebra is closed under the commutation relation:

$$\left[ \frac{\lambda_i}{2}, \frac{\lambda_j}{2} \right] = i f_{ijk} \frac{\lambda_k}{2}, \quad (2.4.16)$$

where  $f_{ijk}$  are the antisymmetric structure constants of SU(3). These generators also satisfy the anti-commutation relation of the form:

$$\left\{ \frac{\lambda_i}{2}, \frac{\lambda_j}{2} \right\} = \frac{1}{3} \delta_{ij} + d_{ijk} \frac{\lambda_k}{2}, \quad (2.4.17)$$



where  $d_{ijk}$  are the symmetric structure constants of SU(3).

### 2.4.2.2 Weak Baryon Transition

As a starting step in the evaluation of the Born diagrams, we first take a look at the Cabibbo V-A theory with which we describe a single-particle CC weak transition between octet baryons. At the quark level, we can introduce the vector  $V_i^\mu$  and the axial-vector  $A_i^\mu$  currents:

$$V_i^\mu = \bar{q}\gamma^\mu \frac{\lambda_i}{2} q, \quad A_i^\mu = \bar{q}\gamma^\mu \gamma_5 \frac{\lambda_i}{2} q, \quad (2.4.18)$$

which form their own SU(3) current octets. Furthermore, we can use these octet currents to construct flavor changing vector and axial-vector currents:

$$J_{d \rightleftharpoons u}^\mu = V_1^\mu \pm iV_2^\mu, \quad J_{d \rightleftharpoons u}^{5\mu} = A_1^\mu \pm iA_2^\mu, \quad \text{for CC \& } \Delta S = 0, \quad (2.4.19)$$

$$J_{s \rightleftharpoons u}^\mu = V_4^\mu \pm iV_5^\mu, \quad J_{s \rightleftharpoons u}^{5\mu} = A_4^\mu \pm iA_5^\mu, \quad \text{for CC \& } \Delta S = \mp 1, \quad (2.4.20)$$

$$J_{s \rightleftharpoons d}^\mu = V_6^\mu \pm iV_7^\mu, \quad J_{s \rightleftharpoons d}^{5\mu} = A_6^\mu \pm iA_7^\mu, \quad \text{for NC \& } \Delta S = \mp 1. \quad (2.4.21)$$

Reports from decay experiments of mesons have indicated that the CC and strangeness conserving processes are favored in comparison to the CC and strangeness changing ones. As a consequence, the Cabibbo angle  $\theta_c$  was introduced to explain such asymmetry of quark level weak interactions. On the other hand, the quark electromagnetic current is obtained by using the definition of electric charge  $\mathcal{Q}$  in Eq. (2.4.13), and now with  $I_3 = (1/2)\lambda_3$  and  $Y = (1/\sqrt{3})\lambda_8$ , we have

$$J_{\text{em}}^\mu = \bar{q}\gamma^\mu \mathcal{Q} q = V_3^\mu + \frac{1}{\sqrt{3}}V_8^\mu \quad (2.4.22)$$

Within the SU(2) isospin treatment, the nucleon electromagnetic current in Eq. (2.4.14) can be rewritten as

$$\begin{aligned} \langle N' | j_{\text{em}}^\mu | N \rangle &= \bar{U}_{N'} \left[ F_1^{\text{IS}}(q^2) \gamma^\mu + \frac{iF_2^{\text{IS}}(q^2)}{2M} \sigma^{\mu\nu} q_\nu \right] \frac{I}{2} U_N \\ &+ \bar{U}_{N'} \left[ F_1^{\text{IV}}(q^2) \gamma^\mu + \frac{iF_2^{\text{IV}}(q^2)}{2M} \sigma^{\mu\nu} q_\nu \right] \frac{\tau_3}{2} U_N, \end{aligned} \quad (2.4.23)$$

where  $U_N$  is the two component nucleon spinor field and  $F_i^{\text{IS}}$  and  $F_i^{\text{IV}}$  are isoscalar and isovector components of the nucleon form factors, respectively; and they are determined from the proton  $f_i^p(Q^2)$  and neutron  $f_i^n(Q^2)$  form factors:

$$F_i^{\text{IS}} = f_i^p(Q^2) + f_i^n(Q^2), \quad i = 1, 2 \quad (2.4.24)$$

$$F_i^{\text{IV}} = f_i^p(Q^2) - f_i^n(Q^2). \quad (2.4.25)$$

In the Cabibbo theory[75], it has been suggested that single-particle weak currents of baryons transform according to the octet representation of SU(3). In addition, the conserved vector current (CVC) hypothesis states that the vector part of the baryon weak current is in the same octet as the electromagnetic current. Thus with the assumption of exact SU(3) symmetry, the matrix element of an octet current  $\mathcal{O}_j$  between the baryon octet states  $B_k$  and  $B_i$  can be written in terms of two reduced matrix elements[76]:

$$\langle B_i | \mathcal{O}_j | B_k \rangle = if_{ijk} F + d_{ijk} D, \quad (2.4.26)$$

where  $F$  and  $D$  correspond to antisymmetric and symmetric couplings of the two octet baryons. Thus the electromagnetic current between two baryon octet states becomes:

$$\langle B_i | j_{\text{em}}^\mu | B_k \rangle = i \left[ f_{i3k} + \frac{1}{\sqrt{3}} f_{i8k} \right] F_V^\mu + \left[ d_{i3k} + \frac{1}{\sqrt{3}} d_{i8k} \right] D_V^\mu. \quad (2.4.27)$$

Here the subscript  $V$  is assigned to emphasize that the electromagnetic current belongs to the vector current octet. If one expresses the proton and neutron in terms of baryon octet states:

$$p = \frac{1}{\sqrt{2}}(B_4 + iB_5), \quad n = \frac{1}{\sqrt{2}}(B_6 + iB_7), \quad (2.4.28)$$

then the vector parts of  $D^\mu$  and  $F^\mu$  can be determined from the nucleon electromagnetic form factors. That is,

$$F_i^D = -\frac{3}{2}f_i^n(Q^2), \quad i = 1, 2, \quad (2.4.29)$$

$$F_i^F = f_i^p(Q^2) + \frac{1}{2}f_i^n(Q^2). \quad (2.4.30)$$

The weak transition between  $B$  and  $B'$  baryon octet states is often expressed in the standard V-A form:

$$\langle B' | J^\mu(q) | B \rangle = \bar{U}_{B'} \left[ F_1(Q^2) \gamma^\mu + \frac{iF_2(Q^2)}{2M} \sigma^{\mu\nu} q_\nu - G_A(Q^2) \gamma^\mu \gamma_5 \right] U_B, \quad (2.4.31)$$

where  $F_1$ ,  $F_2$ , and  $G_A$  are the Dirac, Pauli, and axial-vector form factors, respectively. This is a clear indication that  $D^\mu$  and  $F^\mu$  also contain the corresponding axial-vector parts:  $G_A^D$  and  $G_A^F$ . Note that the nucleon form factors  $f_i^p(Q^2)$  and  $f_i^n(Q^2)$  are determined from electron scattering experiments[77]:

$$f_1^p(Q^2) = \left( \frac{1 + \tau(1 + \lambda_p)}{1 + \tau} \right) G_D^V(Q^2), \quad (2.4.32)$$

$$f_2^p(Q^2) = \left( \frac{\lambda_p}{1 + \tau} \right) G_D^V(Q^2), \quad (2.4.33)$$

$$f_1^n(Q^2) = \left( \frac{\lambda_n \tau(1 - \eta)}{1 + \tau} \right) G_D^V(Q^2), \quad (2.4.34)$$

$$f_2^n(Q^2) = \left( \frac{\lambda_n(1 + \tau\eta)}{1 + \tau} \right) G_D^V(Q^2), \quad (2.4.35)$$

where  $\lambda_p = 1.79$ ,  $\lambda_n = -1.91$ , and a dipole form factor  $G_D^V(Q^2)$  is given by

$$G_D^V(Q^2) = (1 + Q^2/M_V^2)^{-2} = (1 + 4.97\tau)^{-2}, \quad (2.4.36)$$

with

$$\eta = (1 + 5.6\tau)^{-1}, \quad \tau = Q^2/(4M^2). \quad (2.4.37)$$

Therefore, the octet baryon weak transition form factors  $F_1(Q^2)$  and  $F_2(Q^2)$  can be determined in terms of the nucleon electromagnetic form factors, directly, via the CVC hypothesis. In a similarly fashion, the axial-vector contributions are obtained from the nucleon axial-vector form factor  $g_A(Q^2)$ , that is,

$$F_A^D = \frac{D}{F + D} g_A(Q^2), \quad (2.4.38)$$

$$F_A^F = \frac{F}{F + D} g_A(Q^2), \quad (2.4.39)$$

where  $D = 0.78 \pm 0.02$ ,  $F = 0.45 \pm 0.022$ , and

$$g_A(Q^2) = (F + D) G_D^A(Q^2). \quad (2.4.40)$$

Here  $G_D^A(Q^2)$  also takes the dipole form:

$$G_D^A(Q^2) = (1 + Q^2/M_A^2)^{-2} = (1 + 3.31\tau)^{-2}. \quad (2.4.41)$$

Therefore, we can calculate the standard form factors shown in Eq. (2.4.31) from the nucleon electromagnetic form factors  $f_i^{p,n}$  and axial-vector form factor  $g_A$ , and some of them are listed in Table 2.1.

### 2.4.2.3 Strong Coupling Constants

All channels in the Born term model contain the strong coupling vertex. The model-dependent evaluation of the weak hadronic current amplitudes relies on the proper specification of the corresponding strong coupling constants  $g_{\text{KYN}}$  of such vertices. However, to our knowledge these

**Table 2.1:** Standard form factors for CC weak transition between baryons belonging to octet representation of SU(3).

Weal Transition	$F_i$	$G_A$
$n \rightarrow p$	$f_i^p(Q^2) - f_i^n(Q^2)$	$\frac{g_A(Q^2)}{3F + D}$
$p \rightarrow \Lambda$	$-\sqrt{\frac{3}{2}} f_i^p(Q^2)$	$-\sqrt{\frac{1}{6}} \frac{3F + D}{F + D} g_A(Q^2)$
$\Sigma^\pm \rightarrow \Lambda$	$-\sqrt{\frac{3}{2}} f_i^n(Q^2)$	$\sqrt{\frac{2}{3}} \frac{D}{F + D} g_A(Q^2)$

coupling constants have not been measured precisely. As a result, we resort to the SU(3) prediction of such constants. The strong coupling constants  $g_{\text{KYN}}$  are related to the experimentally well-known coupling constant  $g_{\pi\text{NN}}$  via the SU(3) symmetry[78]:

$$g_{\text{K}^+\Lambda\text{p}} = -\frac{1}{\sqrt{3}}(3 - 2\alpha^D)g_{\pi\text{NN}}, \quad (2.4.42)$$

$$g_{\text{K}^+\Sigma^0\text{p}} = (2\alpha^D - 1)g_{\pi\text{NN}}, \quad (2.4.43)$$

where the experimental value of  $g_{\pi\text{NN}}$  is fixed at[79]:

$$\frac{g_{\pi\text{NN}}^2}{4\pi} = 14.3 \pm 0.2, \quad (2.4.44)$$

and  $\alpha^D$  is a fraction of D-type coupling[80]:

$$\alpha^D = \frac{D}{F + D} = 0.644 \pm 0.006. \quad (2.4.45)$$

The 20% broken SU(3) symmetry predicts the rough bounds on the  $g_{\text{K}^+\Lambda\text{p}}$  and  $g_{\text{K}^+\Sigma^0\text{p}}$  values:

$$-4.4 \leq \frac{g_{\text{K}^+\Lambda\text{p}}}{\sqrt{4\pi}} \leq -3.0, \quad (2.4.46)$$

$$+0.9 \leq \frac{g_{\text{K}^+\Sigma^0\text{p}}}{\sqrt{4\pi}} \leq +1.3. \quad (2.4.47)$$

$$(2.4.48)$$

For this study, however, we fix their values at

$$\frac{g_{\text{K}^+\Lambda\text{p}}}{\sqrt{4\pi}} = -3.8, \quad \frac{g_{\text{K}^+\Sigma^0\text{p}}}{\sqrt{4\pi}} = +1.2. \quad (2.4.49)$$

Finally, we apply the isospin symmetry in order to relate the rest of the coupling constants:  $g_{\text{K}^+\Lambda\text{n}}$ ,  $g_{\text{K}^0\Sigma^0\text{n}}$ ,  $g_{\text{K}^0\Sigma^+\text{p}}$ , and  $g_{\text{K}^+\Sigma^0\text{n}}$  [47]. Table 2.2 summarizes the SU(3) predicted values used in this calculation.

### 2.4.2.4 Meson Weak Transition

As can be seen in Fig. 2.7, the  $t$ -channel of the Born-term model contains the weak transition vertex of the pseudoscalar meson. Therefore, we must specify such a current matrix element in advance in order to be able to evaluate the Born diagrams. Shrock[30] indicated that only the vector current contribute to the weak transition of the pseudoscalar meson belonging to the octet representation of SU(3). As a result, we adopt the meson current formulation presented in Ref. [31]. That is

$$\langle K^{\lambda'} | \hat{J}^\mu(q) | K^\lambda \rangle = \begin{cases} (2p_1^\mu - q^\mu) F_{K^\lambda}(q^2), & \lambda = \lambda', \\ (2p_1^\mu - q^\mu) F_{K^{\lambda',\lambda}}(q^2), & \lambda \neq \lambda', \end{cases} \quad (2.4.50)$$

where  $\lambda, \lambda' \in \{0, +\}$ . For the NC cases the form factors  $F_{K^0}(q^2)$  and  $F_{K^+}(q^2)$  are identified

**Table 2.2:** SU(3) predicted values of the strong coupling constants, which are also related via the isospin symmetry.

$\frac{g_{K^+\Lambda p}}{\sqrt{4\pi}}$	$\frac{g_{K^+\Sigma^0 p}}{\sqrt{4\pi}}$	$\frac{g_{K^0\Lambda n}}{\sqrt{4\pi}}$	$\frac{g_{K^0\Sigma^0 n}}{\sqrt{4\pi}}$	$\frac{g_{K^0\Sigma^0 p}}{\sqrt{4\pi}}$	$\frac{g_{K^+\Sigma^- n}}{\sqrt{4\pi}}$
-3.8	1.2	-3.8	-1.2	1.7	1.7

with the isovector electromagnetic form factors:

$$F_{K^0} = +F_{K,\rho} + F_{K,\omega} + F_{K,\phi}, \quad (2.4.51)$$

$$F_{K^+} = -F_{K,\rho} + F_{K,\omega} + F_{K,\phi}, \quad (2.4.52)$$

$$(2.4.53)$$

where  $F_{K,\kappa}$  ( $\kappa = \rho, \omega, \phi$ ) are the vector meson form factors defined as

$$F_{K,\rho}(q^2) = \frac{F_{K,\rho}(0)}{1 - q^2/m_\rho^2}, \quad F_{K,\rho}(0) = 0.33 \pm 0.04, \quad m_\rho = 0.770 \text{ MeV}, \quad (2.4.54)$$

$$F_{K,\omega}(q^2) = \frac{F_{K,\omega}(0)}{1 - q^2/m_\omega^2}, \quad F_{K,\omega}(0) = 0.17 \pm 0.04, \quad m_\omega = 0.783 \text{ MeV}, \quad (2.4.55)$$

$$F_{K,\phi}(q^2) = \frac{F_{K,\phi}(0)}{1 - q^2/m_\phi^2}, \quad F_{K,\phi}(0) = 0.50, \quad m_\phi = 1.020 \text{ MeV}. \quad (2.4.56)$$

On the other hand, for the CC case, the two form factors  $F_{K^+,0}$  and  $F_{K^0,+}$  are obtained from the NC form factors  $F_{K^0}$  and  $F_{K^+}$ :

$$F_{K^+,0} = -F_{K^0,+} = F_{K^+} - F_{K^0} = 2F_{K,\rho}. \quad (2.4.57)$$

### 2.4.2.5 Evaluation of Invariant Amplitudes

In this section we determine the eighteen unknown form factors which parametrize the hadronic vertex of neutrino-induced associated production of strange particles from free nucleons. In doing so, we must evaluate the individual channels of the tree-level Born diagrams shown in Fig. 2.7. Here we pay particular attention to the CC and  $\Delta S = 0$  process:  $\nu n \rightarrow \mu^- K^+ \Lambda$ .

To begin with, we first take a look at the  $s$ -channel with two vertices: (i) the CC weak transition vertex of nucleon, which is parametrized by the standard vector and axial-vector form factors as

$$\langle p | \hat{J}_{W^+}^\mu(q) | n \rangle = \bar{U}_p \left[ F_1^N(Q^2) \gamma^\mu + \frac{iF_2^N(Q^2)}{2M} \sigma^{\mu\nu} q_\nu - G_A^N(Q^2) \gamma^\mu \gamma_5 \right] U_n, \quad (2.4.58)$$

where  $F_1^N(Q^2)$ ,  $F_2^N(Q^2)$ , and  $G_A^N$  are given in Table 2.1; and (ii) the pseudoscalar strong coupling vertex defined as

$$\langle K^+ \Lambda | p \rangle = g_{K^+ \Lambda p} \bar{U}_\Lambda \gamma_5 U_p, \quad (2.4.59)$$

where the strong coupling constant  $g_{K^+ \Lambda p}$  is given in Table 2.2. Thus the contribution of the  $s$ -channel have the following form

$$\langle \Lambda | \hat{J}_{s, CC}^\mu | n \rangle = \bar{U}_\Lambda \left[ \left( g_{K^+ \Lambda p} \gamma_5 \right) g_s \left( \hat{J}_{W^+}^\mu (n \rightarrow p) \right) \right] U_n, \quad (2.4.60)$$

where  $g_s$  is the propagation of the  $s$ -channel:

$$g_s = \frac{\not{q} + \not{p} + M_N}{s - M_N^2}, \quad (2.4.61)$$

and  $\hat{J}_{W^+}^\mu (B \rightarrow B') = \langle B' | \hat{J}_{W^+}^\mu | B \rangle$ . Therefore, by exhaustively applying the Dirac algebra and the momentum space Dirac equation of the on-shell particles we rewrite Eq. (2.4.60) in terms of the basis elements of the most general weak hadronic current operator. Then we apply the method of identification to re-express the invariant amplitudes of  $\hat{J}^\mu(q)$  using the non-vanishing  $s$ -channel contributions:

$$\tilde{A}_2 = -G_s G_A^N, \quad (2.4.62)$$

$$\tilde{B}_1 = -G_s (M_N/M) F_2^N, \quad (2.4.63)$$

$$\tilde{B}_2 = +2G_s F_1^N, \quad (2.4.64)$$

$$\tilde{C}_1 = +2M_N G_s G_A^N, \quad (2.4.65)$$

$$\tilde{D}_1 = +G_s (F_2^N/M)(q^2/2 + p \cdot q), \quad (2.4.66)$$

$$\tilde{D}_2 = -G_s F_2^N/M, \quad (2.4.67)$$

$$\tilde{D}_3 = -G_s F_2^N/M, \quad (2.4.68)$$

$$\tilde{D}_5 = -G_s G_A^N, \quad (2.4.69)$$

$$\tilde{D}_6 = +G_s [F_1^N + (M_N/M)F_2^N], \quad (2.4.70)$$

where

$$G_s = g_{K^+ \Lambda p} \frac{1}{s - M_N^2} \quad (2.4.71)$$

and

$$F_i^N = f_i^p(Q^2) - f_i^n(Q^2), \quad G_A^N = g_A(Q^2). \quad (2.4.72)$$

Secondly, we have the  $u$ -channel contribution of the Born term approximation. This channel also contains two vertices that need to be specified. (i) The CC weak transition of  $\Sigma^-$  hyperon to  $\Lambda$  hyperon, for which we can write the standard transition current as

$$\langle \Lambda | \hat{J}_{W^+}^\mu(q) | \Sigma^- \rangle = \bar{U}_\Lambda \left[ F_1^Y(Q^2) \gamma^\mu + \frac{iF_2^Y(Q^2)}{2M} \sigma^{\mu\nu} q_\nu - G_A^Y(Q^2) \gamma^\mu \gamma_5 \right] U_{\Sigma^-}, \quad (2.4.73)$$

and (ii) the strong interaction vertex:

$$\langle K^+ \Sigma^- | n \rangle = g_{K^+ \Sigma^- n} \bar{U}_{\Sigma^-} \gamma_5 U_n, \quad (2.4.74)$$

Thus the  $u$ -channel current contribution can be written as

$$\langle \Lambda | \hat{J}_{u, CC}^\mu | n \rangle = \bar{U}_\Lambda \left[ \left( \hat{J}_{W^+}^\mu (\Sigma^- \rightarrow \Lambda) \right) g_u \left( g_{K^+ \Sigma^- n} \gamma_5 \right) \right] U_n, \quad (2.4.75)$$

where the  $u$ -channel propagator  $g_u$  is defined as

$$g_u = \frac{\not{q} - \not{p}'_2 + M_{\Sigma^-}}{u - M_{\Sigma^-}^2}. \quad (2.4.76)$$

Similarly, the Dirac algebra is used repeatedly to expand Eq. (2.4.75) to eventually come up with the following non-vanishing contributions:

$$\tilde{A}_1 = +2G_u G_A^Y, \quad (2.4.77)$$

$$\tilde{A}_3 = -2G_u G_A^Y, \quad (2.4.78)$$

$$\tilde{B}_1 = +G_u [2F_1^Y + F_2^Y(M_\Lambda - M_{\Sigma^-})/2M], \quad (2.4.79)$$

$$\tilde{B}_3 = -2G_u F_1^Y, \quad (2.4.80)$$

$$\tilde{C}_1 = +G_u G_A^Y (M_\Lambda - M_{\Sigma^-}) \quad (2.4.81)$$

$$\tilde{D}_1 = -G_u [(M_\Lambda + M_{\Sigma^-})F_1^Y + F_2^Y(q \cdot p'_2 - q^2/2)/M], \quad (2.4.82)$$

$$\tilde{D}_2 = -G_u F_2^Y/2M, \quad (2.4.83)$$

$$\tilde{D}_4 = +G_u F_2^Y/M \quad (2.4.84)$$

$$\tilde{D}_5 = -G_u G_A^Y \quad (2.4.85)$$

$$\tilde{D}_6 = -G_u [F_1^N + F_2^Y(M_\Lambda - M_{\Sigma^-}/2M)], \quad (2.4.86)$$

where

$$G_u = g_{K^+\Sigma^-n} \frac{1}{u - M_{\Sigma^-}^2}, \quad (2.4.87)$$

and

$$F_i^Y = -\sqrt{\frac{3}{2}} f_i^n(Q^2), \quad G_A^Y = \sqrt{\frac{2}{3}} \frac{D}{F+D} g_A(Q^2). \quad (2.4.88)$$

Finally, we are left with the derivation of the  $t$ -channel contribution in our model-dependent analysis. One of this channel's vertices belongs to that of the CC weak transition of the pseudoscalar meson:  $K^0 \rightarrow K^+$ , which is defined as

$$\langle K^+ | \hat{J}_{W^+}^\mu(q) | K^0 \rangle = (2p_1'^\mu - q^\mu) F_{K^+,0}(q^2), \quad (2.4.89)$$

and the other vertex is that of the familiar pseudoscalar strong coupling:

$$\langle K^0 | \Lambda | n \rangle = g_{K^0 \Lambda n} \bar{U}_\Lambda \gamma_5 U_n. \quad (2.4.90)$$

Now the  $t$ -channel current takes a form:

$$\langle \Lambda | \hat{J}_{t,CC}^\mu | n \rangle = \bar{U}_\Lambda \left[ \left( g_{K^0 \Lambda n} \gamma_5 \right) g_t \left( \hat{J}_{W^+}^\mu(K^0 \rightarrow K^+) \right) \right] U_n, \quad (2.4.91)$$

where the  $t$ -channel propagator is defined as

$$G_t = \frac{1}{t - M_{K^0}^2}. \quad (2.4.92)$$

Thus, the  $t$ -channel contribution is taken into account through the following invariant form factors of the most general weak hadronic current operator:

$$\tilde{B}_1 = +G_t F_{K^+,0}(q^2), \quad (2.4.93)$$

$$\tilde{B}_2 = +2G_t F_{K^+,0}(q^2), \quad (2.4.94)$$

$$\tilde{B}_3 = -2G_t F_{K^+,0}(q^2). \quad (2.4.95)$$

Note, therefore, that from the tree-level Born diagrams for the  $\nu N \rightarrow \ell K^+ \Lambda$  process, there are no contributions coming through five amplitudes:  $\tilde{A}_4$ ,  $\tilde{B}_4$ ,  $\tilde{C}_2$ ,  $\tilde{C}_3$ , and  $\tilde{C}_4$ , of the general representation of the weak hadronic current operator. In addition, the  $s$ -,  $u$ -, and  $t$ -channel currents, respectively, are left with only nine, ten, and three non-vanishing invariant amplitudes of  $\hat{J}^\mu(q)$ , Eq. (2.4.10), through which they contribute to the cross sections of the elementary reaction process. Eventually, the overall model-dependent weak hadronic current operator can be obtained by adding the contribution of individual channels of the Born-term model.

## Chapter 3

# Theory of the Quasifree $A(\nu, \ell KY)B$ Process

### 3.1 Theoretical Formalism

In this chapter, we develop a fully relativistic formalism for associated strange particle production via the neutrino-nucleus scattering. We base our model on the following important assumptions of the RIA scheme: (i) the interaction proceeds via a single-boson-exchange mechanism, (ii) only a single bound nucleon inside a nucleus involves in the interaction, (iii) the in-medium current operator is replaced by a free weak hadronic current operator, and (iv) the RMF approximation to the Walecka model is used to account for the nuclear structure effects through the bound state wave function of the nucleon. In chapter 2, we gave a brief overview of these basic ingredients that we use to develop a plausible theoretical description for the reaction of great interest. With these points in mind, we are now in a position to embark on the study of the neutrino-induced associated strangeness production on nuclei near the threshold energy of the underlying elementary process. The exclusive reactions under consideration are of the form:

$$\nu(k^\mu) + A(P^\mu) \longrightarrow \ell(k'^\mu) + K(p_1'^\mu) + Y(p_2'^\mu) + B(P'^\mu). \quad (3.1.1)$$

In this model we assume that an incoming neutrino,  $\nu$ , with four momentum  $k^\mu = (E_k, \mathbf{k})$  scatters off an  $A$ -body target nucleus,  $A$ , with four-momentum  $P^\mu = (E, \mathbf{P})$ , via a single-boson-exchange, into the final lepton,  $\ell$ , with  $k'^\mu = (E_{k'}, \mathbf{k}')$ . In the exclusive associated production channel, the final state is expected to produce a pseudoscalar meson,  $K$ , with  $p_1'^\mu = (E_{p_1'}, \mathbf{p}_1')$

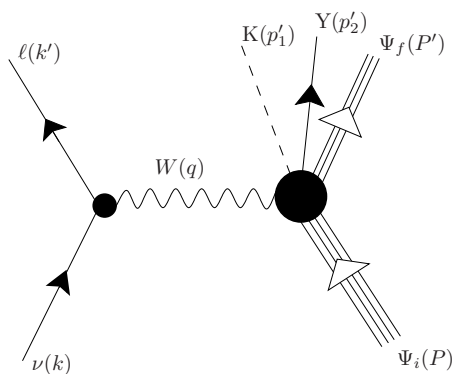


**Figure 3.1:** The lowest-order Feynman diagram for the neutrino-induced associated production of strange particles on nuclei. This is the Born approximation which states that in the limit of low four-momentum transfer the dominant contribution to the differential cross section comes from a single-boson-exchange reaction mechanism, and thus validating the first consequence of the RIA scheme.

in conjunction with a hyperon,  $Y$ , with  $p_2'^\mu = (E_{p_2'}, \mathbf{p}_2')$ , and both exit the reaction vicinity, leaving behind a recoiling  $A - 1$ -body residual nucleus,  $B$ , whose four momentum is labeled as  $P'^\mu = (E', \mathbf{P}')$ . We denote the masses of the incident neutrino, final lepton, target nucleus, kaon, hyperon, and residual nucleus as  $m_\nu$ ,  $m_\ell$ ,  $M_A$ ,  $M_K$ ,  $M_Y$ , and  $M_B$ , respectively. It is also worth

noting that in this study neutrinos are considered massless ( $m_\nu = 0$ ); and in such a reaction the exchange particle is the weak gauge boson,  $W = W^\pm$  or  $Z^0$ , that carries the four-momentum transfer  $q^\mu = (\omega, \mathbf{q})$  of the reaction. Fig. 3.1 shows the diagrammatic scheme of a single-boson-exchange reaction mechanism for the  $A(\nu, \ell KY)B$  process, which is the lowest-order Feynman diagram invoked under the Born approximation.

### 3.1.1 Differential Cross Section for the Quasifree Process

The derivation of the differential cross section for  $A(\nu, \ell KY)B$  is performed by adopting the standard procedure by Bjorken and Drell[68]. Thus, the general form of the differential cross section for the quasifree reaction represented in Fig. 3.1 can be written in the laboratory frame, whereby the four-momentum of the target nucleus becomes  $P^\mu = (M_A, \mathbf{0})$ , as

$$\begin{aligned} d\sigma &= \frac{1}{|\mathbf{v}_1 - \mathbf{v}_2|} (2\pi)^4 \delta^4(k + P - k' - p'_1 - p'_2 - P') \\ &\times |\mathcal{M}_{fi}|^2 \frac{1}{2E_{p'_1}} \frac{d^3\mathbf{k}'}{(2\pi)^3} \frac{d^3\mathbf{p}'_1}{(2\pi)^3} \frac{d^3\mathbf{p}'_2}{(2\pi)^3} \frac{d^3\mathbf{P}'}{(2\pi)^3}, \end{aligned} \quad (3.1.2)$$

where  $|\mathbf{v}_1 - \mathbf{v}_2|$  is the relative velocity of the incident neutrino with respect to the target nucleus:

$$|\mathbf{v}_1 - \mathbf{v}_2| = \frac{4[(k \cdot P)^2 - m_\nu^2 M_A^2]^{1/2}}{2E_k 2E} \rightarrow 1, \quad (3.1.3)$$

partly owing to the fact that the neutrino is treated as massless particle. The overall energy-momentum conservation is enforced by the four-dimensional delta function and we will address this aspect of the reaction in the kinematic section.  $\mathcal{M}_{fi}$  is the invariant matrix element that contains the dynamical information of the quasifree reaction of our interest.

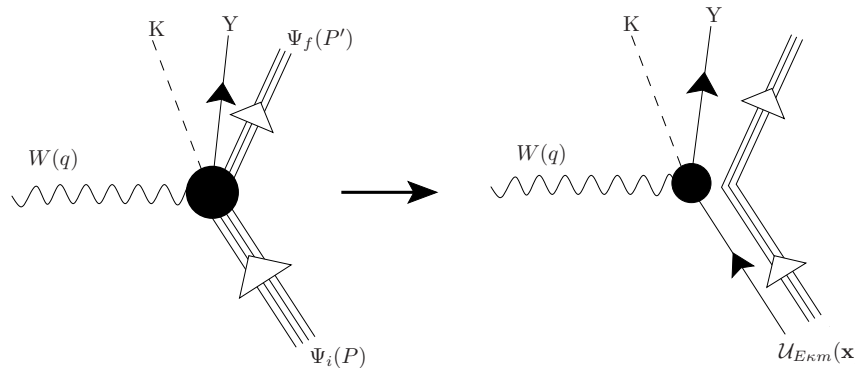


**Figure 3.2:** The vertex approximation invoked within the RIA model. This is in agreement with the second consequence of the RIA scheme which states that the vector gauge boson interacts with a single bound nucleon inside the target nucleus, and subsequently a kaon is produced in conjunction with a hyperon. The rest of the bound nucleons behave as spectators.

This study is aimed at evaluating the quasifree reaction cross section for the associated production of strange particles within the RIA scheme. We have already invoked one of the RIA assumptions that the production process proceeds via a single-boson-exchange. Now we impose the second approximation that states the electroweak gauge boson interacts with a single bound nucleon inside the nucleus rather than the target nucleus as a whole and hence the term “quasifree” is introduced in attempt to convey this meaning. In Fig. 3.2 we have illustrated this consequence of the RIA scheme in a form of vertex approximation imposed on the lowest-order Feynman diagram, Fig. 3.1, of the exclusive reaction  $A(\nu, \ell KY)B$ . In the kinematic section we will show that this approximation gives rise to the second energy-momentum conservation that may further impose constraint on the degrees of freedom of the reaction.



### 3.1.2 Kinematic Description of $A(\nu, \ell KY)B$ Process

In this subsection, we aim at evaluating the differential cross section by imposing kinematic conditions on the exclusive neutrino-nucleus reactions with particular interest in the associated production of strange particles. In order to provide the quantitative predictions of this theoretical study a proper evaluation of the reaction cross section given in Eq. (3.1.2) is necessary. As is customary, in the relativistic description of a semi-leptonic weak interactions, the differential cross section can be separated into kinematic and dynamic factors. This feature, in turn, gives us the luxury of treating these parts individually without loss of generality. In what follows, therefore, we study all available degrees of freedom of the quasifree process and kinematic constraints that must be invoked in order to determine them.

The geometric representation of the reaction process is depicted in Fig. 3.3 whereby the participating particles are constrained to three different planes - an indication that the quasifree process is inherited with kinematic flexibility in comparison to the free process. The figure also fixes the coordinate axes by which we define the directions of three-momenta of the particles. The  $z$ -axis is set along the direction of the three-momentum transfer:

$$\hat{\mathbf{z}} = \hat{\mathbf{q}}. \quad (3.1.4)$$

The lepton scattering plane can be used to specify the other two coordinate axes:

$$\hat{\mathbf{y}} = \frac{\hat{\mathbf{k}} \times \hat{\mathbf{k}'}}{\sin \theta_\ell}, \quad \hat{\mathbf{x}} = \hat{\mathbf{z}} \times \hat{\mathbf{y}}, \quad (3.1.5)$$

where  $\theta_\ell$  is the lepton scattering angle. Noting that we are working in the rest frame of the target nucleus, our choice of coordinates gives rise to the vanishing  $y$ -components of any three-momenta constrained in the scattering plane.

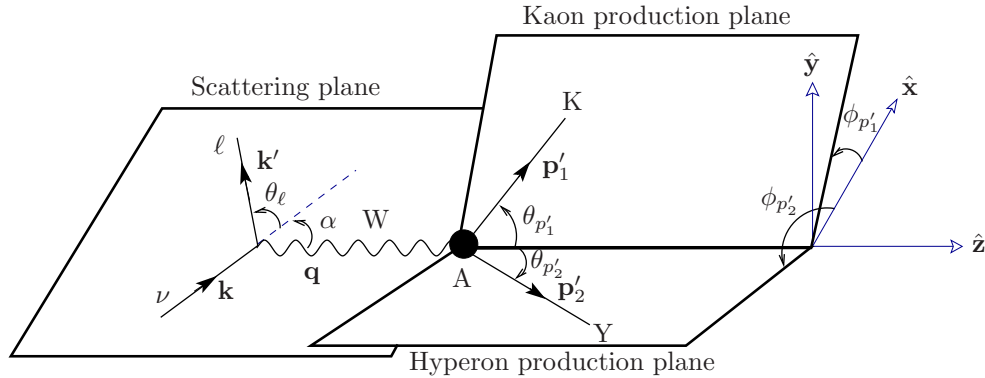


**Figure 3.3:** The kinematics of the quasifree reaction  $A(\nu, \ell KY)B$  in the laboratory frame. The geometry of the reaction process is depicted using three planes: scattering, kaon production, and hyperon production planes. Note that, the recoil of the residual nucleus is left out of this geometric representation of the kinematics only for convenience sake.

The evaluation of the leptonic weak transition requires the determination the four-momenta  $k^\mu$ ,  $k'^\mu$ , and  $q^\mu$  given that the kinematic variables  $E_k$ ,  $\omega$ , and  $Q^2$  are fixed, where  $Q^2 = |\mathbf{q}|^2 - \omega^2$ . Thus one needs to impose energy-momentum conservation at the leptonic vertex:

$$\omega = E_k - E_{k'}, \quad \mathbf{q} = \mathbf{k} - \mathbf{k}', \quad (3.1.6)$$

and the explicit form of the three-momentum conservation can be written as

$$|\mathbf{k}| \sin \alpha - |\mathbf{k}'| \sin(\alpha + \theta_\ell) = 0, \quad (3.1.7)$$

$$|\mathbf{k}| \cos \alpha - |\mathbf{k}'| \cos(\alpha + \theta_\ell) = |\mathbf{q}|. \quad (3.1.8)$$

To be more precise, given the three kinematic inputs:  $E_k$ ,  $\omega$ , and  $Q^2$ , the quantities that we should be calculating are  $E_{k'}$ ,  $\theta_\ell$ ,  $\alpha$ ,  $|\mathbf{k}|$ , and  $|\mathbf{k}'|$ . Thus, using energy conservation in Eq. (3.1.6) we can quickly fix  $E_{k'}$ ; and then the on-shell relations for the incident neutrino and final state lepton fix  $|\mathbf{k}|$  and  $|\mathbf{k}'|$ :

$$E_k^2 = |\mathbf{k}|^2, \quad E_{k'}^2 = |\mathbf{k}'|^2 + m_\ell^2. \quad (3.1.9)$$

Now the three-momenta of  $\nu$  and  $\ell$  can be written component-wise as

$$\begin{aligned} k_x &= |\mathbf{k}| \sin \alpha, & k'_x &= |\mathbf{k}'| \sin(\alpha + \theta_\ell), \\ k_y &= 0, & k'_y &= 0, \\ k_z &= |\mathbf{k}| \cos \alpha, & k'_z &= |\mathbf{k}'| \cos(\alpha + \theta_\ell), \end{aligned} \quad (3.1.10)$$

where

$$\sin \alpha = \frac{|\mathbf{k}'|}{|\mathbf{q}|} \sin \theta_\ell, \quad \cos \alpha = \frac{1}{|\mathbf{q}|} [|\mathbf{k}| - |\mathbf{k}'| \cos \theta_\ell], \quad (3.1.11)$$

and

$$\cos \theta_\ell = \frac{2E_k(E_k - \omega) - Q^2 - m_\ell^2}{2E_k \sqrt{(E_k - \omega)^2 - m_\ell^2}}. \quad (3.1.12)$$

Note that in the Feynman diagrammatic formulation of the quasifree process, the weak gauge boson is identified as an internal line or a virtual particle, as a result it violates the on-shell condition (i.e.,  $q^2 \neq M_W^2$ ).

We now focus on the production vertex of Fig. 3.1 whereby the electroweak gauge boson is coupled with the target nucleus as a whole resulting in a final channel consists of not only two strange particles (kaon and hyperon) but also a residual nucleus. Thus, the energy-momentum conservation must be imposed at this vertex as well such that our theory remains consistent with the fundamental principle of relativistic quantum mechanics. As a result, we obtain the following relations in the laboratory frame:

$$\omega + M_A = E_{p'_1} + E_{p'_2} + E', \quad (3.1.13)$$

$$\mathbf{P}' = \mathbf{q} - \mathbf{p}'_1 - \mathbf{p}'_2, \quad (3.1.14)$$

where  $E' = M_B + T'$  under the assumption that the recoil three-momentum of the residual nucleus is negligibly small, and hence the recoil kinetic energy  $T'$  can be defined as  $T' = |\mathbf{P}'|^2/2M_B$ , and the recoil three-momentum is also often referred as the missing momentum  $\mathbf{p}_m$ :

$$\mathbf{p}_m = \mathbf{P}'. \quad (3.1.15)$$

The masses of the target nucleus and residual nucleus are calculated as

$$M_A = AM_N, \quad M_B = M_A - (M_N - E_b), \quad (3.1.16)$$

where  $A$  is the nucleon number in the target nucleus,  $M_N$  is a free state nucleon mass, and  $E_b$  is the binding energy of the nucleon orbital which is obtained from the relativistic shell model of nuclei. In this study, therefore, we make use of the  $E_b$  values from the RMF approximation of the nonlinear Walecka model with the NL3 parameter set.

The differential cross section defined in Eq. (3.1.2) must be evaluated such that its angular and energy distributions can be investigated as a means to quantitatively illustrate the theoretical predictions of this work. In order to do so, we should integrate over the four-dimensional delta function in the standard expression of the differential cross section by using experimental facts as a guide. Now we consider the CC quasifree processes which have bigger cross sections measured from bubble chamber experiments as compared to the NC neutrino-induced associated production processes[25, 81]; and hence this study is also inclined towards reaction processes of

the former type. Thus, in the CC neutrino-induced processes the outgoing lepton would be a negatively charged muon, whose path can be tracked by modern particle detectors. The same can be said for the final state kaon. As for the final state hyperon, it is only the direction of  $\mathbf{p}'_2$  which is needed to be observed by detectors regardless of its magnitude. In contrast, the recoiling residual nucleus goes undetected. Consequently, we must integrate over the recoil three-momentum of the residual nucleus,  $\mathbf{P}'$ , to find that

$$d\sigma = \frac{1}{2(2\pi)^8} \frac{1}{E_{p'_1}} \delta(E + \omega - E_{p'_1} - E_{p'_2} - E') |\mathcal{M}_{fi}|^2 d^3\mathbf{k}' d^3\mathbf{p}'_1 d^3\mathbf{p}'_2, \quad (3.1.17)$$

by enforcing the overall three-momentum conservation, Eq. (3.1.14), at the production vertex of Fig. 3.1. It becomes obvious that Eq. (3.1.17) is not calculable until the remaining one dimensional delta function is eliminated which is meant to ensure the energy conservation at the vertex where the vector gauge boson interacts with the target nucleus. Therefore, we must integrate over the hyperon energy,  $E_{p'_2}$ , and subsequently the five-fold differential cross section can be obtained in the laboratory frame:

$$\frac{d^5\sigma}{dE_{k'} d(\cos\theta_\ell) dE_{p'_1} d\Omega_{p'_1} d\Omega_{p'_2}} = \frac{1}{2(2\pi)^7} \frac{E_{k'} E_{p'_2} |\mathbf{k}'| |\mathbf{p}'_1| |\mathbf{p}'_2|}{\left| 1 + \frac{E_{p'_2}}{E'} \left[ 1 - \frac{(\mathbf{q} - \mathbf{p}'_1) \cdot \mathbf{p}'_2}{|\mathbf{p}'_2|^2} \right] \right|} \overline{\sum} |\mathcal{M}_{fi}|^2, \quad (3.1.18)$$

where  $\overline{\sum}$  denotes the sum over final spins and the average over initial spins; and the integration over the delta function of Eq. (3.1.17) helps us maintain the overall energy conservation, Eq. (3.1.13), in our relativistic description of the quasifree reaction  $A(\nu, \ell KY)B$ .

On the other hand, when the impulse approximation of Fig. 3.2 is imposed on the weak nuclear transition vertex, the weak boson,  $W(q)$ , is supposedly absorbed by a single bound nucleon with four-momentum  $p_i^\mu = (E_i, \mathbf{p}_i)$  and the quasifree production of the kaon in conjunction with the hyperon becomes one of its few exclusive channels. In this reaction picture the rest of the nucleons are assumed to behave as spectators. As the direct consequence of this RIA assumption, we end up with the second version of energy-momentum conservation, which can be written in the laboratory frame as

$$E_i = E_{p'_1} + E_{p'_2} - \omega, \quad (3.1.19)$$

$$\mathbf{p}_i = \mathbf{p}'_1 + \mathbf{p}'_2 - \mathbf{q}. \quad (3.1.20)$$

Note that  $\mathbf{p}_i = -\mathbf{p}_m$  and the bound nucleon is off its mass shell as long as  $\mathbf{P}'$  remains nonzero, whereas, based on the Feynman interpretation of the production vertex of the reaction, the target nucleus, residual nucleus, outgoing hadrons: kaon and hyperon, are on their respective mass shell.

Within the impulse approximation imposed at the interaction vertex of  $A(\nu, \ell KY)B$ , the kinematic setting for the quasifree process can be specified based on our knowledge of the corresponding free process:  $\nu N \rightarrow \ell KY$ . Free process: (i) sixteen degrees of freedom, (ii) eight constraints from the on shell conditions and energy-momentum conservation, and hence (iii) demands the fixing of eight kinematic quantities as inputs. Quasifree process: (a) sixteen degrees of freedom, (b) seven constraints as the bound nucleon does not satisfy the on shell condition, and subsequently (c) at most nine quantities must be fixed as kinematic inputs to fully calculate the four-momenta of the reaction. Note that there are kinematic quantities that we fix based on the geometric layout we establish for the reaction process. First, we merge the kaon and hyperon production planes of Fig. 3.3 into a single production plane by imposing the following conditions:  $\phi_{p'_1} = \phi_{p'_2} - 180^\circ = \phi$ . Further, we limit ourselves to the coplanar geometric setup, whereby the production plane containing both strange particles coincides with the lepton scattering plane (i.e.  $\phi = 0$ ). Moreover, the direction  $\hat{\mathbf{q}}$  of the three-momentum transfer has already been specified in Eq. 3.1.4. The quasifree process:  $A(\nu, \ell KY)B$ , provides

a great deal of kinematic flexibility as compared to the underlying free process:  $\nu\text{N} \rightarrow \ell\text{KY}$ . The reason being in the former process the bound nucleon is known to have a distributions of momentum states as opposed to the one in the latter process.

Because of such very rich kinematic features, the quasifree process can be studied using more than one kinematic settings[47, 48, 82]; and in this study we have implemented only two of these kinematic settings. (i) The kinematic setting that involves the fixing of the magnitude of the missing momentum  $p_m = |\mathbf{p}_m|$  at a finite value; and this setting is often referred as ‘‘quasifree kinematics’’ owing to its close resemblance to the kinematics at the hadronic vertex of the underlying free process. This kinematic arrangement gives rise to varying energies of the outgoing kaon and hyperon over the whole range of the kaon angle  $\theta_{p'_1}$ ; and hence it is suitable for the investigation of the final state interaction effects. (ii) The other kinematic setting is more of a natural geometric arrangement that makes the entire momentum distribution of the bound nucleon accessible for the study of the quasifree reaction, and hence it is referred as ‘‘open kinematics’’. Note that in both kinematic settings four quantities:  $\hat{\mathbf{q}}$ ,  $\phi_{p'_1}$ , and  $\phi_{p'_2}$  are fixed beforehand. Further, since the recoil kinetic energy of the residual nucleus is negligibly small, we make the following approximation in both settings:

$$E' \approx M_A - (M_N - E_b), \quad (3.1.21)$$

and now the overall energy conservation defined in Eq. (3.1.13) becomes

$$E_{p'_2} \approx \omega + M_N - E_{p'_1} - E_b. \quad (3.1.22)$$

In the quasifree kinematics, the quantities that we must fix at the production vertex are  $\omega$ ,  $Q^2$ ,  $\theta_{p'_1}$ , and  $p_m$ ; and then calculate  $E_{p'_1}$ ,  $E_{p'_2}$ , and  $\theta_{p'_2}$ , among other unknown kinematics. Note that under this setting we have a total of eight kinematic quantities fixed at the start which seems to be in violation of the required nine as mentioned earlier. This is, in fact, what makes such a kinematic setting unique since it requires only eight quantities to be fixed as is the case for the free process to determine the unknown nine quantities. Therefore, in this setting the calculation of the four-momenta:  $p_1^\mu$ ,  $p_2^\mu$ , and  $p_i^\mu$  is performed in two steps. In the first step, the missing momentum is set to zero, and the  $E_{p'_1}$  and  $E_{p'_2}$  are calculated for the elementary process embedded inside the nucleus. Note that this kinematic is somewhat similar to the free process except for the binding energy that it must take into account. First, the physical value of kaon total energy  $z = E_{p'_1}$  should be obtained for a fixed value of  $\theta_{p'_1}$  by solving a quadratic equation derived from Eqs. (3.1.20) and (3.1.22) with  $|\mathbf{p}_i| = 0$ . That is,

$$\lambda_0 - \lambda_1 z + \lambda_2 z^2 = 0, \quad (3.1.23)$$

with

$$\lambda_0 = (\kappa_1^2 + \kappa_3)^2 + \kappa_2 M_K, \quad \lambda_1 = 4\kappa_1(\kappa_1^2 + \kappa_3), \quad \lambda_2 = 4\kappa_1^2 - \kappa_2^2, \quad (3.1.24)$$

where

$$\kappa_1 = \omega + M_N - E_b, \quad \kappa_2 = 2|\mathbf{q}| \cos \theta_{p'_2}, \quad \kappa_3 = M_K^2 - M_Y^2 - |\mathbf{q}|^2. \quad (3.1.25)$$

Once  $E_{p'_1}$  is determined, then we can use Eq. (3.1.20) to calculate  $E_{p'_2}$ . Note that, as long as  $p_m$  remains zero Eq. (3.1.20) is an exact expression instead of being an approximation. In the second step, we assign a finite value to  $p_m$  and then calculate the angle of the outgoing hyperon by making use of the values of  $E_{p'_1}$  and  $E_{p'_2}$  obtained in the first step. Therefore, in the quasifree kinematics the energies remain at their two-body values even when the missing momentum becomes nonzero; and this comes at the cost of the shifting of  $\theta_{p'_2}$  from its free space value. Now we should calculate the new value of  $\theta_{p'_2}$  for nonzero  $p_m$  given  $\omega$ ,  $Q^2$ ,  $\theta_{p'_1}$ ,  $E_{p'_1}$ , and  $E_{p'_2}$ . Starting from Eq. (3.1.8) we end up with the following trigonometric equation:

$$A_0 \cos \theta_{p'_2} - A_1 \sin \theta_{p'_2} = A_2, \quad (3.1.26)$$

where

$$A_0 = 2|\mathbf{p}'_2| \left( |\mathbf{p}'_1| \cos \theta_{p'_1} - |\mathbf{q}| \right), \quad (3.1.27)$$

$$A_1 = 2|\mathbf{p}'_2||\mathbf{p}'_1| \sin \theta_{p'_1}, \quad (3.1.28)$$

$$A_2 = p_m^2 - |\mathbf{q}|^2 - |\mathbf{p}'_1|^2 - |\mathbf{p}'_2|^2 + 2\mathbf{q} \cdot \mathbf{p}'_1. \quad (3.1.29)$$

We now solve Eq. (3.1.26) by introducing two parameters:  $\beta$  and  $B_0$ :

$$\tan \beta = \frac{A_1}{A_0}, \quad B_0^2 = A_0^2 + A_1^2, \quad (3.1.30)$$

such that we have

$$A_0 = B_0 \cos \beta, \quad A_1 = B_0 \sin \beta. \quad (3.1.31)$$

Thus, Eq. (3.1.26) now becomes

$$B_0 \cos(\beta + \theta_{p'_2}) = A_2, \quad (3.1.32)$$

which can be rearranged to calculate  $\theta_{p'_2}$  as

$$\theta_{p'_2} = \left| \cos^{-1} \left( \frac{A_2}{B_0} \right) - \tan^{-1} \left( \frac{A_1}{A_0} \right) \right|. \quad (3.1.33)$$

Note that, use has been made of the on-shell relations for both kaon and hyperon throughout. In Appendix A, Fig. A.1 depicts the flow diagram on how to calculate the laboratory frame four-momenta in the quasifree kinematic setting using a Fortran 95 program.

In the open kinematic setting, one needs to fix the values of  $\omega$ ,  $Q^2$ ,  $E_{p'_2}$ ,  $\theta_{p'_1}$ , and  $\theta_{p'_2}$ ; and then calculate  $E_{p'_1}$  and  $p_m$ , among other quantities. In this kinematic setting, we have nine quantities fixed in advance and also there are eight constraints imposed by energy-momentum conservation and on-shell conditions; and hence we are left with seven unknown kinematic quantities. Unlike the quasifree kinematic, the calculation of four-momenta of the reaction is straightforward. The step-by-step calculations under this setting is shown in Appendix A, Fig. A.2. We start with calculating the masses of the target and residual nuclei; the magnitude of the three-momentum transfer; and the hyperon total energy  $E_{p'_2}$  using Eq. (3.1.21). After a check on the quantities of being in the energetically acceptable region, we calculate  $E_i$ ,  $|\mathbf{p}'_1|$ , and  $|\mathbf{p}'_2|$ . That should then be followed by the determination of all four-momenta needed to specify the kinematic and dynamic factors of the reaction cross section. Fortran 95 subroutine, KINLAB1, has been developed to calculate these four-momenta for both settings: quasifree and open kinematics, based on the flow diagrams shown in Figs. A.1 and A.2 of Appendix A.

## 3.2 Nuclear Transition Matrix Element

Although there are certain theoretical models[30, 35] to describe the interaction vertices of the underlying elementary process on free nucleons, to our knowledge, there are hardly any attempts to extend those models to study the neutrino-induced associated production on nuclei. Therefore, this manuscript offers the first of such theoretical descriptions of the exclusive reaction  $A(\nu, \ell\text{KY})B$ . Motivated by the fact that the weak and electromagnetic interactions are connected, our model for the weak nuclear transition of the neutrino-induced associated production is developed based on theoretical work done on the production of mesons in conjunction with baryons via electron-nucleus scattering[48]. At this point, we invoke the third consequence of the RIA scheme (see section 2.2 of chapter 2), in order to take the vertex approximation, Fig. 3.2, a step further. The third RIA assumption ensures that the on-shell detail of the weak hadronic current for associated production on a free nucleon remains unchanged when being embedded inside the nucleus. Thus, the weak nuclear current simply becomes the sum of individual contributions from the nucleons in the nucleus, whereby the in-medium nucleon current is replaced

by the free space one. The nuclear structure effects such as Fermi motion, Pauli blocking, and nuclear binding are taken into account through the bound state wave function of the nucleon which is calculated from the RMF approximation to the Walecka model (see chapter 2 section 2.3).

Based on Fig. 3.2 and the above argument, the general expression for the weak nuclear transition matrix element can now be constructed for the exclusive reaction  $A(\nu, \ell\text{KY})B$ . That is,

$$\mathcal{M}_{fi} = \eta \mathcal{L}_\mu \frac{g^{\mu\nu}}{M_W^2} \mathcal{H}_\nu. \quad (3.2.1)$$

The electroweak theory gives the exact expression for the leptonic current  $\mathcal{L}_\mu$ . That is,

$$\mathcal{L}_\mu = \bar{U}_\ell(\mathbf{k}', h') \gamma_\mu (I - \gamma_5) \nu(\mathbf{k}, h), \quad (3.2.2)$$

where the helicity representations  $\nu(\mathbf{k}, h)$  and  $U_\ell(\mathbf{k}', h')$  of the Dirac spinors for the incident neutrino and final state lepton, respectively, can be written as

$$\nu(\mathbf{k}, h) = C_\nu \begin{pmatrix} \phi^h(\hat{\mathbf{k}}) \\ \frac{h|\mathbf{k}|}{E_k + m_\nu} \phi^h(\hat{\mathbf{k}}) \end{pmatrix}, \quad U_\ell(\mathbf{k}', h') = C_\ell \begin{pmatrix} \phi^{h'}(\hat{\mathbf{k}}') \\ \frac{h'|\mathbf{k}'|}{E_{k'} + m_\ell} \phi^{h'}(\hat{\mathbf{k}}') \end{pmatrix}. \quad (3.2.3)$$

Here  $h$  and  $h'$  denote helicity eigenvalues of the neutrino and final state lepton, respectively, whose spins are longitudinally polarized. Note that the treatment of a neutrino as a massless particle has a significant consequence in that the neutrino can only appear as a left-handed particle, that is, a fermion with negative helicity state:  $h = -1$ . As a matter of fact, this is the reason behind neutrinos being coupled to other particles only via the weak interaction which is experimentally observed to violate parity. By the same token, for a CC process the helicity eigenvalue  $h'$  of the final lepton can be either positive or negative:  $h' = \pm 1$ , owing to the fact that the final state lepton is a negatively-charged muon with nonzero mass. A Pauli spinor  $\phi^\lambda(\hat{\mathbf{p}})$  should now become an eigenstate of the helicity operator  $\boldsymbol{\sigma} \cdot \mathbf{p}/|\mathbf{p}|$  with spin polarization in the direction of the three-momentum:  $\hat{\mathbf{p}} \equiv \hat{\mathbf{p}}(\theta, \phi)$ , and hence it can take either of these helicity eigenvalues:  $\lambda = \pm 1$  for spin projection parallel or antiparallel to the direction of motion. Thus,  $\phi^{\lambda=\pm 1}(\hat{\mathbf{p}})$  can take the form

$$\phi^{\lambda=+1}(\hat{\mathbf{p}}) = \begin{pmatrix} \cos(\theta/2) \\ \sin(\theta/2)e^{i\phi} \end{pmatrix}, \quad \phi^{\lambda=-1}(\hat{\mathbf{p}}) = \begin{pmatrix} -\sin(\theta/2)e^{-i\phi} \\ \cos(\theta/2) \end{pmatrix}. \quad (3.2.4)$$

The Dirac spinors are normalized non-covariantly, as a result we have

$$C_\nu = \sqrt{\frac{1}{2}}, \quad C_\ell = \sqrt{\frac{E_{k'} + m_\ell}{2E_{k'}}}. \quad (3.2.5)$$

In the framework of the relativistic impulse approximation, the weak nuclear current  $\mathcal{H}^\mu$  is written as the sum of currents from the individual nucleons inside the nucleus[51, 83]:

$$\mathcal{H}^\mu = \int d^3\mathbf{x} e^{i\mathbf{q}\cdot\mathbf{x}} \bar{\Psi}_{\hat{i}_2, s'_2}^{(-)}(\mathbf{x}, \mathbf{p}'_2) [\Phi^{(-)}(\mathbf{x}, \mathbf{p}'_1)]^* \hat{J}^\mu(q) \mathcal{U}_{E\kappa m}(\mathbf{x}), \quad (3.2.6)$$

where  $J^\mu(q)$ , which replaces the in-medium nucleon current, is the weak hadronic current operator for the neutrino-induced strange particle production on a free nucleon that has been derived in Ref. [35] and reviewed in chapter 2 section 2.4 of this manuscript;  $\mathcal{U}_{E\kappa m}(\mathbf{x})$  is the bound state wave function of the in-medium nucleon whose expression is given in chapter 2, Eq. (2.3.31), with radial components calculated from the relativistic shell model;  $\Phi^{(-)}(\mathbf{x}, \mathbf{p}'_1)$



and  $\Psi_{\hat{i}_2, s'_2}^{(-)}(\mathbf{x}, \mathbf{p}'_2)$  are the wave functions of the final state kaon and hyperon, respectively, both having the incoming boundary conditions as indicated by the minus superscript. For now, both of these wave functions are kept general. The weak coupling factor  $\eta$ , may take either of the following values depending on the production channel being studied:

$$\frac{\eta}{M_W^2} = \frac{G_F}{\sqrt{2}} \eta_c, \quad (3.2.7)$$

where  $\eta_c$  is defined in chapter 2, Eq. (2.4.3). This formulation is valid in the limit  $Q^2 \ll M_W^2$ . Note also that  $\hat{i}'_2$  is an arbitrary spin quantization axis specified in the rest frame of the hyperon and  $s'_2$  is the spin projection of the hyperon about this polarization axis. Now we can determine the norm-squared nuclear matrix element as

$$\overline{\sum} |\mathcal{M}_{fi}|^2 = \frac{G_F^2}{2} \eta_c^2 \sum_{h', m, s'_2} [\mathcal{L}_\mu \mathcal{L}_\nu^\dagger] [\mathcal{H}^\mu \mathcal{H}^{\nu\dagger}]. \quad (3.2.8)$$

### 3.3 RPWIA Model for Quasifree $A(\nu, \ell KY)B$ Reaction

The study of semi-leptonic scattering processes off nuclei is always challenging owing to the complications that arise when taking into account the nuclear structure and FSI effects in order to establish a reasonable theoretical description. In the framework of the relativistic impulse approximation we assume that such effects are accounted for through the wave functions when the underlying elementary  $\nu N \rightarrow \ell KY$  process is embedded inside the nuclear medium. We incorporate the nuclear structure effects via the bound state wave function of the nucleon inside the nucleus, whereas the FSIs, such as the strong and/or Coulomb interactions between final state particles and the residual nucleus, are other important effects in the study of the neutrino-induced quasifree processes that come into play via the distorted wave functions of outgoing kaon and hyperon.

In the RPWIA model, however, we assume that these FSI effects are negligible and hence the outgoing kaon and hyperon are described by plane wave functions. In the study of the quasifree KY photo-production processes[46, 47], the RPWIA formalism is implemented to calculate the hyperon recoil polarization as it is found to be insensitive to the FSI effects. In addition, the RPWIA model was used by authors of Refs. [9, 10] in their successful investigation of the sensitivity of the quasi-elastic neutrino-nucleus current to strange quark content of the axial form-factor of the nucleon.

In this section, we present a fully relativistic formalism within the RPWIA framework. This should be done for a number of reasons. First, it serves as a starting point and baseline theory for the study of the exclusive reaction using a more complicated RDWIA model as well as in the analysis of high statistics data when available in the near future. Second, the inclusion of distorted wave functions represents a considerable numerical challenge as is evident in somewhat similar work done on proton-induced exclusive reactions[43, 44]. It might therefore be very difficult to disentangle effects related to nuclear structure, the description of the bound state wave function, the elementary process and distortions of the outgoing particles all in one go. Finally, despite their significance role in the present and future data analysis in the neutrino-oscillation experiments and the proton decay searches, the scarcity of theoretical work on the neutrino-induced strangeness associated production on nuclei,  $A(\nu, \ell KY)B$ , is also what has motivated us to establish such a baseline formalism.

Now we evaluate the invariant matrix element in the RPWIA framework. In the plane-wave limit, the outgoing kaon and hyperon, respectively, are described by the wave functions of the forms:

$$[\Phi^{(-)}(\mathbf{x}, \mathbf{p}'_1)]^* = e^{-i\mathbf{p}'_1 \cdot \mathbf{x}}, \quad \overline{\Psi}_{\hat{i}'_2, s'_2}^{(-)}(\mathbf{x}, \mathbf{p}'_2) = e^{-i\mathbf{p}'_2 \cdot \mathbf{x}} \overline{U}_Y(\mathbf{p}'_2, \hat{i}'_2, s'_2), \quad (3.3.1)$$



where the Dirac spinor field of hyperon is defined as

$$U_Y(\mathbf{p}'_2, \hat{\mathbf{i}}'_2, s'_2) = C_Y \begin{pmatrix} \phi^{s'_2}(\hat{\mathbf{i}}'_2) \\ \frac{\boldsymbol{\sigma} \cdot \mathbf{p}'_2}{E_{p'_2} + M_Y} \phi^{s'_2}(\hat{\mathbf{i}}'_2) \end{pmatrix}. \quad (3.3.2)$$

Here the generalized Pauli spinor with respect to an arbitrary spin quantization axis,  $\hat{\mathbf{i}} \equiv \hat{\mathbf{i}}(\alpha, \beta)$ ,

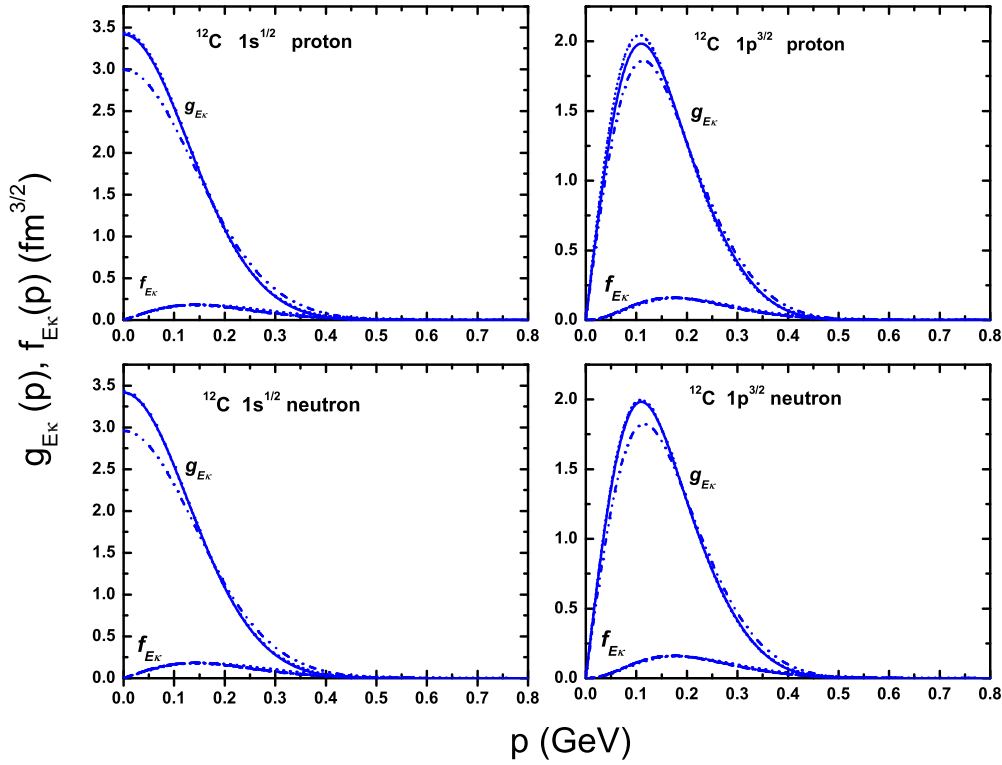


**Figure 3.4:** Momentum space radial wave functions of the bound nucleon. The top(bottom) panels contain the curves for proton (neutron) bound to the  $1s^{1/2}$  and  $1p^{3/2}$  orbitals of  $^{12}\text{C}$ . The solid (dashed), dotted(dash-dotted), dash-dot-dotted (short-dashed), and short-dotted (short-dash-dotted) curves of  $g_{E_\kappa}$  ( $f_{E_\kappa}$ ) correspond to QHD-I, QHD-II, NL3, and FSUGold parameterizations, respectively, to the Walecka model.

is defined in terms of the Wigner D-function as

$$\phi^s(\alpha, \beta) = \sum_{s'=\pm\frac{1}{2}} \mathcal{D}_{ss'}^{\frac{1}{2}}(\alpha, \beta, 0) \chi_{s'}, \quad (3.3.3)$$

and non-covariant normalization Eq. (3.3.2) gives:

$$C_Y = \sqrt{\frac{E_{p'_2} + M_Y}{2E_{p'_2}}}. \quad (3.3.4)$$

Upon plugging the plane wave functions of the outgoing kaon and hyperon given in Eq. (3.3.1) into Eq. (5.4.36), the weak nuclear current becomes

$$\mathcal{H}^\mu = \int d^3\mathbf{x} e^{-i(\mathbf{p}'_1 + \mathbf{p}'_2 - \mathbf{q}) \cdot \mathbf{x}} \bar{U}_Y(\mathbf{p}'_2, \hat{\mathbf{i}}'_2, s'_2) \hat{J}^\mu(q) \mathcal{U}_{E_{K\kappa m}}(\mathbf{x}). \quad (3.3.5)$$

Note, however, that from Eq. (3.1.20) we know that  $\mathbf{p}'_1 + \mathbf{p}'_2 - \mathbf{q}$  is, in fact, the three-momentum  $\mathbf{p}_i$  of the bound nucleon; and also the Dirac spinor field of hyperon and the weak hadronic current operator are independent of  $\mathbf{x}$ . Therefore, the weak nuclear transition current becomes

$$\mathcal{H}^\mu = \bar{U}_Y(\mathbf{p}'_2, \hat{i}'_2, s'_2) \hat{J}^\mu(q) \mathcal{U}_{E\kappa m}(\mathbf{p}_i), \quad (3.3.6)$$

where  $\mathcal{U}_{E\kappa m}(\mathbf{p}_i)$  is the Fourier transform of the coordinate space wave function of the bound nucleon:

$$\mathcal{U}_{E\kappa m}(\mathbf{p}_i) = \int d^3\mathbf{x} e^{-i\mathbf{p}_i \cdot \mathbf{x}} \mathcal{U}_{E\kappa m}(\mathbf{x}). \quad (3.3.7)$$

This means that within the RPWIA model the weak nuclear transition is proportional to the Fourier transform of the bound state wave function of the struck nucleon. In order to express the momentum space wave function of the bound nucleon in the explicit form we use Eq. (2.3.31) given in section 2.3 of chapter 2 and the partial wave expansion of  $e^{-i\mathbf{p}_i \cdot \mathbf{x}}$ . That is,

$$e^{-i\mathbf{p}_i \cdot \mathbf{x}} = 4\pi \sum_{l,m} (-1)^l i^l j_l(p_i x) Y_{lm}(\hat{\mathbf{p}}_i) Y_{lm}^*(\hat{\mathbf{x}}), \quad (3.3.8)$$

where  $j_l(p_i x)$  is the spherical Bessel function of order  $l$ . Note that  $p_i$  stands for  $|\mathbf{p}_i|$ . Therefore, the momentum space bound state wave function can now be written as

$$\mathcal{U}_{E\kappa m}(\mathbf{p}_i) = 4\pi (-i)^l \begin{pmatrix} g_{E\kappa}(p_i) \mathcal{Y}_{\kappa m}(\hat{\mathbf{p}}_i) \\ f_{E\kappa}(p_i) \boldsymbol{\sigma} \cdot \hat{\mathbf{p}}_i \mathcal{Y}_{\kappa m}(\hat{\mathbf{p}}_i) \end{pmatrix}, \quad (3.3.9)$$

where the momentum space upper and lower component radial wave functions are defined as

$$g_{E\kappa}(p_i) = \int dx x g_{E\kappa}(x) j_l(p_i x), \quad (3.3.10)$$

$$f_{E\kappa}(p_i) = \text{sgn}(\kappa) \int dx x f_{E\kappa}(x) j_l(p_i x). \quad (3.3.11)$$

Fig. 3.4 shows the  $p_i$  dependence of the momentum space radial wave functions for the bound nucleons in the  $1s^{1/2}$  and  $1p^{3/2}$  orbitals of  $^{12}\text{C}$ . These wave functions are obtained by using four parameter sets in the RMF approximation to Walecka model. The plots indicate that, under proper kinematic settings, one can explore the missing momentum distribution of the cross section and subsequently investigate how the nuclear medium effects influence the reaction process. In short, the characteristic curves of the radial components wave functions suggest that significantly larger cross sections may be obtained by carefully tuning the magnitude of the missing momentum within a proper range. The angular, missing momentum and energy distributions of the RPWIA differential cross section for the quasifree  $A(\nu, \ell KY)B$  reaction are presented and discussed in chapter 7 using both kinematical settings.

## Chapter 4

# Final State Interactions in the $A(\nu, \ell KY)B$ Processes

### 4.1 Introduction

In the previous chapter, we have successfully established the RPWIA formalism whereby any possible effects of the final state interactions of the outgoing particles with the residual nucleus are turned off. Nevertheless, the plane-wave limit calculations usually take into account the nuclear structure effects such as Fermi motion, Pauli blocking, and binding energy corrections via the bound state wave functions of nucleons inside a nucleus. As a result, the RPWIA framework offers elegant and baseline calculations of the reaction process. From experimental stand point, however, the differential cross sections describing the exclusive reaction  $A(\nu, \ell KY)B$  are highly likely to be influenced by the final state interactions of the ejectiles with the recoiling residual nucleus.

#### 4.1.1 Coulomb Distortion of Lepton

In a charged current processes, the final lepton, which is a negatively charged muon, interacts with the Coulomb field generated by the residual nucleus. In theory, the Coulomb distortion of the final lepton is accounted for by replacing its plane wave with the distorted wave obtained by solving the Dirac equation containing the Coulomb potential of the nucleus[84]:

$$[-i\boldsymbol{\alpha} \cdot \boldsymbol{\nabla} + m_\ell\beta + V_c(\mathbf{x})]\psi_\ell(\mathbf{x}) = E_\ell\psi_\ell(\mathbf{x}) \quad (4.1.1)$$

where  $m_\ell$  and  $E_\ell$  are mass and energy of the final lepton, respectively. The Coulomb potential  $V_c(\mathbf{x})$  is constructed by considering a uniform, spherical nucleus of effective charge, radius  $R$  and  $Z$  number of protons, with  $r = |\mathbf{x}|$ :

$$V_c(r) = \begin{cases} Z\alpha \frac{r^2 - 3R^2}{2R^3}, & r < R \\ \frac{Z\alpha}{r}, & r > R. \end{cases} \quad (4.1.2)$$

For low energy quasi-elastic neutrino-nucleus scattering, the Coulomb distortion on the wave function of the final lepton is found to significantly influence the scattering cross sections[85]. However, authors of Ref.[86] has pointed out that in the energy region from 1 to 3 GeV, of the incident neutrino, such a distortion effect is relatively small. Therefore, since our study is focused on scattering process in the same energy range, the Coulomb distortion effects are neglected in our calculations.

#### 4.1.2 Final State Interaction of Hadrons

It is important to stress that in this work the RDWIA treatment strictly refers to the consideration of either kaon distortion (K-FSI), hyperon distortion (Y-FSI), or both (KY-FSI) in

the description of the neutrino-induced strangeness production on nuclei. As Table 4.1 summarizes, the influence of the three different cases can separately be explored within the RDWIA description of the  $A(\nu, \ell KY)B$  processes. For the first case, which we label as RDWIA-I, we take into account the kaon distortion by turning off the hyperon FSI. Within the RDWIA-II treatment, however, we do the exact opposite of the first case, that is, we only deal with hyperon distortion. The third scenario (RDWIA-III) is where both FSIs are turned on and their effects studied simultaneously. Thus the RDWIA-III treatment leads to the investigation as to how the kaon and hyperon distortions interfere with each other and how that affects the exclusive cross sections of the associated production of strange particles.

**Table 4.1:** Three different scenarios that can be explored within the RDWIA formalism of the  $A(\nu, \ell KY)B$  process.

RDWIA	I	II	III
K-FSI	On	Off	On
Y-FSI	Off	On	On

## 4.2 Hyperon-nucleus Interaction

Within the RDWIA framework, the final state hyperon, in the neutrino-induced associated production process, interacts with the residual nucleus before exiting the reaction vicinity. In order to examine to what extent the production cross sections are affected by hyperon FSI, one should have a better understanding of the dynamics behind hyperon-nucleus interaction. Fig. 4.1 displays the lowest-order Feynman diagram for the  $A(\nu, \ell KY)B$  process with the addition of an elliptic shaded blob representing the optical potential approximation to the final state interaction of hyperon with the residual nucleus. To our knowledge, however, there are only very few theoretical works devoted to offering a detailed study of such a reaction, and this is mainly because of the scarcity of experimental data on hyperon scattering off nuclei.

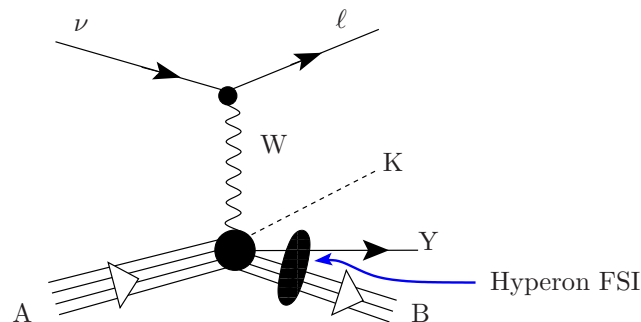


**Figure 4.1:** Diagrammatic illustration of the RDWIA-II treatment of the  $A(\nu, \ell KY)B$  process. The elliptic shaded blob represents the optical model interaction of the final state hyperon with the residual nucleus, whereas the kaon FSI is turned off.

On the other hand, one has excellent theoretical and experimental developments with regard to nucleon-nucleus interactions. For example, the Dirac phenomenology[87] was used to construct a global optical model in order to describe the nucleon-nucleus interactions. This optical model has been proven to provide a successful description of the nucleon-nucleus scattering data over a wide range of energy and nuclei.

Among very few attempts, Cooper *et al.*[88, 89] have constructed a hyperon-nucleus optical potential based on the global nucleon-nucleus Dirac optical potential and the constituent quark model. Their prescription starts off with the parameters of the nucleon optical potential obtained

from the fitting procedure of Ref. [87] and then, it makes use of the scaling procedure that the constituent quark model imposes on strong coupling constants to relate the parameters of the hyperon-nucleus optical potential to that of the nucleon-nucleus optical potential. The underlying constituent quark model can further be used in order to include the Lorentz tensor potential to account for the small spin-orbit splitting. A quantitative description using such an optical potential is possible only when the parameters of the hyperon optical potential are fairly adjusted to fit the data on hypernuclear binding.

Thus once the hyperon-nucleus optical potential is constructed from the global nucleon-nucleus optical potential via the constituent quark model, the hyperon distorted wave function can be obtained by solving the Dirac equation of a from:

$$\left[ -i\boldsymbol{\alpha} \cdot \boldsymbol{\nabla} + V_0(r) + \beta[M_Y + S(r)] - i\frac{(f/g)}{2M_Y}\beta\boldsymbol{\alpha} \cdot \boldsymbol{\nabla}V_0(r) + V_c(r) \right] \psi_Y(\mathbf{x}) = E_Y\psi_Y(\mathbf{x}) \quad (4.2.1)$$

where  $S(r)$  is the scalar potential and  $V_0(r)$  time-like component of the vector potential. The fourth and fifth terms on the left hand side of the Dirac equation are there to account for the contributions of the tensor and Coulomb couplings, respectively. The hyperon distorted wave function can also be generated by using a Schrödinger equation with an equivalent nonrelativistic optical potential  $U(r) = U_{\text{cen}}(r) + U_{\text{so}}(r)\mathbf{s} \cdot \mathbf{l}$ [47].

Note, however, that this study is aimed at addressing the first case of the RDWIA treatment, in which the hyperon FSI is turned off, allowing the pure examination of distortion effects of kaon FSI on the exclusive production cross sections. Moreover, RDWIA-I offers a baseline formalism upon which the theoretical description of  $A(\nu, \ell KY)B$  process can be constructed when one decides to implement either of RDWIA-II or RDWIA-III treatment.

### 4.3 Kaon-Nucleus Interaction

When the elementary process  $\nu N \rightarrow \ell KY$  takes place inside the nuclear medium, the final state hadrons inevitably interact with the residual nucleus. We start with Fig. 4.2 that shows the schematic diagram of the  $A(\nu, \ell KY)B$  process with kaon FSI, which is represented by the elliptic shaded blob, originating from the strong and/or electromagnetic interactions of produced kaon with the residual nucleus. The consideration of the kaon FSI in the analysis of the in-medium neutrino-induced strangeness production presents an enormous challenge. The kaon-nucleus

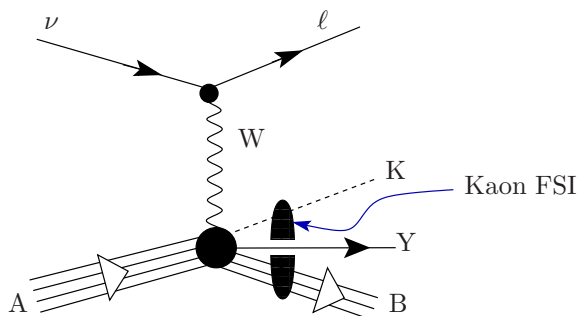


**Figure 4.2:** Diagrammatic illustration of the  $A(\nu, \ell KY)B$  process treated within RDWIA-I framework, whereby the kaon FSI, represented by the elliptic shaded blob, is considered. In the RDWIA-I treatment we turn off the hyperon FSI.

system is known to be one of the most complicated many-body problems and only approximate theories have so far been suggested to describe its dynamics. Subsequently, one also faces difficulty while attempting to find and implement a reliable prescription for the inclusion of the kaon FSI effects into the theoretical analysis of the reaction process.

In the low and intermediate energy region,  $k_{\text{lab}} \leq 1$  GeV, the  $K^+$  is weakly absorbed in the nuclear medium with a mean free path of roughly 5 – 7 fm; and hence it is capable of

penetrating the nuclear interior[90]. In this energy region, the  $K^+$ -nucleon ( $K^+N$ ) system exhibits no resonances or bound states, and inelastic scattering is not allowed. As opposed to the pion-nucleus system, the large medium effects due to the annihilation process ( $\pi NN \rightarrow NN$ ), and delta resonance and propagation are completely absent from the  $K^+$ -nucleus interaction[91]. In the energy range  $k_{\text{lab}} \leq 1$  GeV, the  $K^+N$  interaction can almost entirely be described as a simple background (nonresonant) scattering process.

Note, however, that the above arguments for the  $K^+$ -nucleus interaction may not be generalized to the  $K^-$ -nucleus system because of the fact that not only do  $K^+$  and  $K^-$  have different strangeness quantum numbers but also they do not belong to the same isospin multiplets. As a result, a crossing symmetry which is supposedly able to relate two such interactions is absent[92]. In fact, the  $K^-$ -nucleus interaction is rather strongly absorptive, giving rise to the formation of many narrow resonance and bound states. Thus, like  $\pi^\pm$ , the  $K^-$ -nucleus interaction is confined to the nuclear periphery.

#### 4.4 The Kaon Optical Potential

In this section we develop the standard description of the kaon-nucleus interaction on the basis of the underlying two-body kaon-nucleon interaction. A widely accepted prescription for constructing the kaon-nucleus theory starts off with the lowest-order approximation to the Kerman-McManus-Thaler (KMT) multiple scattering theory[93]. Thus we introduce the relativistic optical potential (ROP) formalism as it is known to reduce the kaon-nucleus many-body problem to an equivalent potential scattering problem. The main reasons behind the popularity of the optical model potential are: (i) the simplicity of the formalism, (ii) the absence of other feasible alternatives, and more importantly, (iii) its success in reproducing experimental data on the elastic kaon-nucleus scatterings[90]. Following the standard prescription, the kaon-nucleus optical potential is constructed from the factorized, first-order KMT multiple scattering formulation, whereby it takes the product form of the two-body kaon-nucleon  $t$ -matrix and the nuclear matter density[94]. This approach is often referred as the  $t\rho$ -approximation. This approximation assumes that the nucleon inside the nucleus are frozen, and hence neglects the Fermi motion of individual nucleons.

In the energy region  $k_{\text{lab}} \leq 1$  GeV,  $K^+N$  scattering is dominated by elastic channels. Further, the charge exchange ( $K^+, K^0$ ) channel is identified with elastic scattering, and can be included in the first-order optical model potential[90]. A successful interpretation of the  $K^+$ -nucleus interaction strongly relies on an accurate analysis of the elementary  $K^+N$  scattering amplitudes. Very few approaches have been developed along this line, but a phase shift analysis of the  $K^+N$  amplitudes has been proven to be more reliable. The most commonly used phase shift analyses, for the study kaon-nucleus system, are those of Martin[95] and BGRT[96, 97]. However, the phase shifts of Martin have been known to offer the best complete analysis, which is successfully able to reproduce  $K^+$ -nucleus elastic scattering data better than BGRT and other parameterizations[98].

In the literature, various authors have introduced several forms for the meson-nucleus optical potential. But the Kisslinger form[99] and the Laplacian form[100, 101] are the most widely used ones, whereas the other forms are mostly their modified versions[102, 103]. Now we define a rather general form of the meson optical potential with adjustable coefficients to take any of the above forms:

$$-2EV(r) = A_1(r) + \nabla^2 A_2(r) + \nabla \cdot A_3(r) \nabla + \nabla^4 A_4(r), \quad (4.4.1)$$

where  $A_i(r)$  are unknown functions which are yet to be determined from the microscopic analysis of kaon-nucleus scattering. These functions are defined in such a way that they can effectively transfer two important aspects of the kaon-nucleus system: (i) the underlying  $K^+N$  elementary scattering; and (ii) the nuclear structure information, into the RDWIA description of in-medium scattering process that involves a kaon in either initial channel, final channel, or both channels.

When considering the isospin treatment of the meson-baryon systems, the two-body  $K^+N$  processes are described using scattering amplitudes which are characterized by a smooth energy-dependence. As is customary, these  $K^+N$  amplitudes are expanded in terms of dimensionless partial-wave amplitudes  $F_{l_{\pm}}^I$ , which are defined in the  $K^+N$  center-of-mass system as follows:

$$F_{l_{\pm}}^I(\kappa) = \left[ \frac{1}{C_l(\kappa)} \sum_{n=0}^{N_l-1} \left( a_{l_{\pm}}^I \right)_n \left( \frac{\kappa}{\kappa_{\max}} \right)^n - i \left[ 1 + \Theta(\kappa - \kappa_{\text{in}}) \left( R_{l_{\pm}}^I \right)^2 \right] \right]^{-1}, \quad (4.4.2)$$

where

$$C_l(\kappa) = \frac{\kappa^{2l+1}}{1 + (\kappa/\kappa_{\text{in}})^{2l+1}}, \quad (4.4.3)$$

$$R_{l_{\pm}}^I(\kappa) = \sum_{m=1}^{M_l} \left( b_{l_{\pm}}^I \right)_m \left( \frac{\kappa - \kappa_{\text{in}}}{\kappa_{\max} - \kappa_{\text{in}}} \right)^m. \quad (4.4.4)$$

Here  $I$  and  $l_{\pm} = l \pm \frac{1}{2}$  denote total isospin and spin-orbit states of  $K^+N$  system, respectively and parameters  $a_{l_{\pm}}^I$  and  $b_{l_{\pm}}^I$  are determined from the phase shift analysis of the  $K^+N$  scattering data.  $\kappa_{\text{in}}$  and  $\kappa_{\max}$ , respectively, are inelastic threshold and maximum momenta of the analysis in the  $K^+N$  c.m. system and are fixed in Table 4.2. The upper summation limits  $N_l$  and  $M_l$  for individual KN partial waves are summarized in Table 4.3.

**Table 4.2:** The inelastic threshold momentum  $\kappa_{\text{in}}$  and maximum momentum  $\kappa_{\max}$  in the  $K^+N$  c.m. system, are fixed in the phase shift analysis by Martin.

	GeV	fm <sup>-1</sup>
$\kappa_{\text{in}}$	0.31	1.57
$\kappa_{\max}$	0.73	3.70

The phase shift analysis of the  $K^+N$  scattering data clearly indicates that the dominant contribution to the elastic and total cross sections comes from the  $s$ - and  $p$ -waves at the energy region  $k_{\text{lab}} < 1$  GeV. As a result, the kaon optical potential can best be manipulated to take the Kisslinger form:

$$-2EV(r) = Ak^2b_0\rho(r) - Ab_1\nabla \cdot \rho(r)\nabla \quad (4.4.5)$$

where  $k$  is the kaon momentum in the kaon-nucleus c.m. system,  $A$  the nucleon number,  $\rho(r)$  the nuclear matter density normalized to unity:

$$\int d^3\mathbf{r} \rho(r) = 1. \quad (4.4.6)$$

We can see that Eq. (4.4.5) is the reduced version of Eq. (4.4.1) if one performs the following identifications:  $A_1(r) = Ak^2b_0\rho(r)$ ,  $A_3(r) = -Ab_1\rho(r)$ , and  $A_2(r) = A_4(r) = 0$ . The optical

**Table 4.3:** The upper limits of summation over the parameters from Martin's phase shift analysis.

$l$	0	1	2	3
$N_l$	5	5	4	3
$M_l$	3	3	2	2

potential parameters  $b_l$  are related to the spin-averaged  $K^+N$  c.m. amplitudes  $(f_{AV}^l)_{\text{c.m.}}$  [98]:

$$b_l = \frac{4\pi}{k_{\text{lab}} \kappa^2} \left( f_{AV}^l \right)_{\text{c.m.}}, \quad (4.4.7)$$



where  $k_{\text{lab}}$  and  $\kappa$  are the kaon momenta in KN lab and c.m. frames, respectively. As stated earlier, the spin-isospin averaged  $K^+N$  amplitudes  $(f_{AV}^l)_{\text{c.m.}}$  are expanded in terms of the partial-wave amplitudes given in Eq. (4.4.2) as follows:

$$(f_{AV}^l)_{\text{c.m.}} = \frac{Z}{2A}\Sigma_1 + \frac{N-Z}{2A}\Sigma_2, \quad (4.4.8)$$

where

$$\Sigma_1 = \sum_{I=0,1} (2I+1) \left[ (l+1)F_{l_+}^I + lF_{l_-}^I \right], \quad (4.4.9)$$

$$\Sigma_2 = \sum_{I=0,1} \left[ (l+1)F_{l_+}^I + lF_{l_-}^I \right]. \quad (4.4.10)$$

With a few algebraic steps the optical potential parameters become:

$$b_l = \frac{4\pi}{k_{\text{lab}} \kappa^2} \sum_{I=0,1} \mathcal{W}_I \left[ (l+1)F_{l_+}^I + lF_{l_-}^I \right], \quad (4.4.11)$$

where  $\mathcal{W}_I$  are the isospin weighing coefficients:

$$\mathcal{W}_0 = \frac{A-Z}{2A}, \quad \mathcal{W}_1 = \frac{A+Z}{2A}. \quad (4.4.12)$$

Thus  $b_0$  and  $b_1$  are complex parameters through which the  $K^+N$  scattering information is extrapolated to the  $K^+$ -nucleus system; and the Kisslinger model is known to be the best vehicle to carry out such a translation using these parameters. In addition, the possible absorption of an  $s$ - and  $p$ -wave kaon in the nuclear medium is accounted for via the imaginary parts of

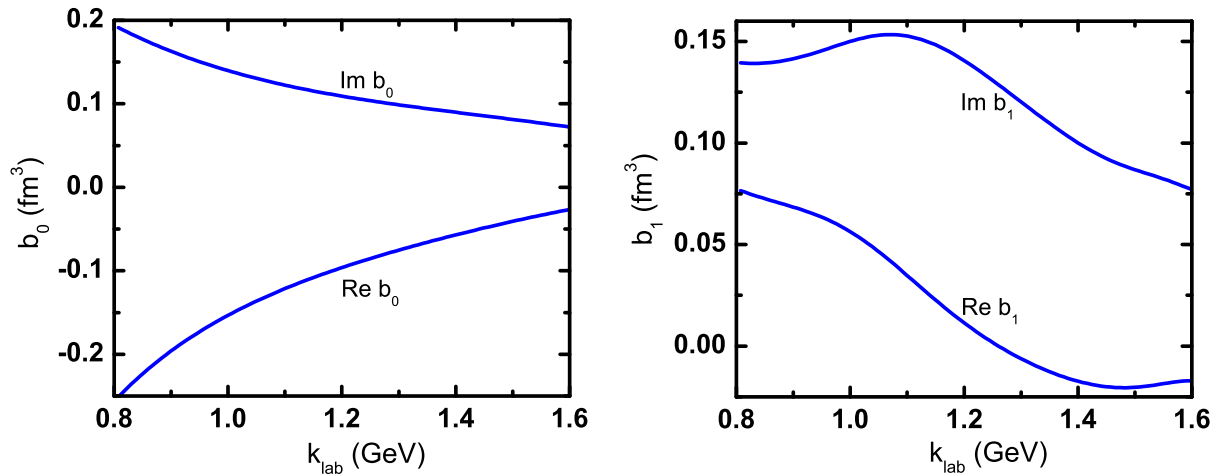


**Figure 4.3:** The optical potential parameters  $b_0$  (left panel) and  $b_1$  (right panel) as a function of the two-body kaon lab momentum. Both are determined, in the unit of  $\text{fm}^3$ , from Martin's phase shift analysis of the  $K^+N$  scattering amplitudes.

the optical potential parameters. The charge exchange term, which is proportional to  $\rho_n - \rho_p$ , has been dropped since it has a negligible contribution in the Kisslinger potential[104]. Fig. 4.3 displays the energy-dependent kaon optical potential parameters  $b_0$  and  $b_1$ , as a function of the two-body kaon lab momentum, calculated from a phase shift analysis of  $K^+N$  scattering amplitudes by Martin[95]. In some cases  $b_0$  is set to absorb  $k^2$  in the first term of the Kisslinger form optical potential given in Eq. (4.4.5), and Fig. 4.4 shows how this particular parameter ( $b'_0 = \kappa^2 b_0$ ) behaves with respect to kaon c.m. momentum.

## 4.5 Equation of Motion for the Kaon

In the last section, a rather approximate model for the kaon-nucleus interaction was constructed via the optical potential formalism. Subsequently, in this section we focus on developing a mechanism through which the kaon FSI effects, in the form of the optical potential, are incorporated into the distorted wave analysis of the neutrino-induced strangeness production from nuclei. In order to do so, we follow a widely accepted relativistic prescription. That is, we distort the kaon wave function by carefully constructing its equation of motion such that its interaction with the residual nucleus is taken into account through an equivalent optical potential.

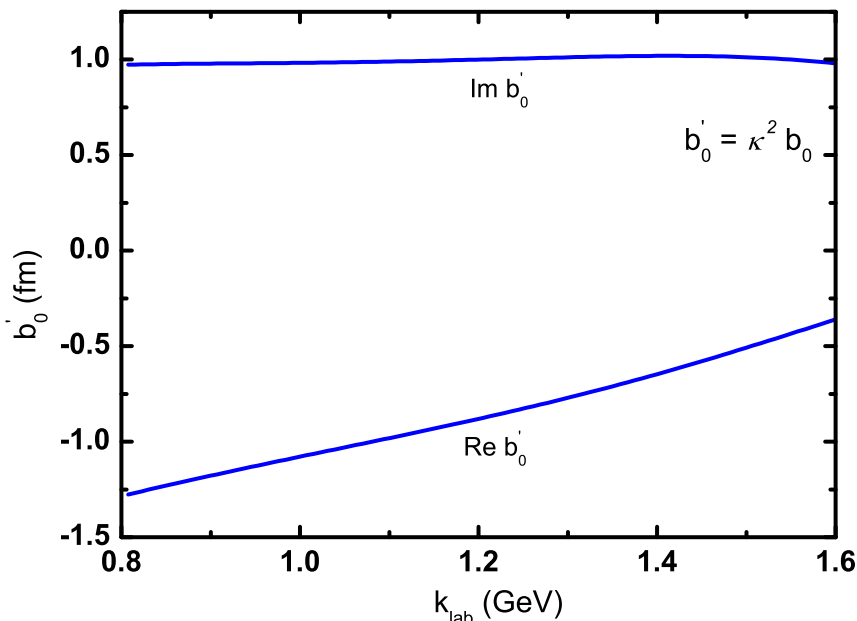


Figure 4.4:  $b'_0$  as a function of the two-body kaon lab momentum.

In the absence of an external scattering potential, a relativistic kaon can be described by the standard Klein-Gordon equation (KG-equation):

$$(\partial^\mu \partial_\mu + m_K^2) \phi = 0, \quad (4.5.1)$$

which is satisfied by a solution of plane wave form

$$\phi(x, k) = e^{-i(E_k t - \mathbf{x} \cdot \mathbf{k})}. \quad (4.5.2)$$

Nevertheless, when such a particle comes under the influence of external field emitted by some scattering center, it may no longer be described by the usual plane wave. As is familiar for a spin-0 meson interaction with an electromagnetic field, the Lorentz transformation properties of the field and the minimal substitution principle of quantum mechanics determine how the KG-equation should be modified to produce a distorted wave of the meson[105].

The distorted wave of the final state kaon is therefore obtained by solving the approximate KG-equation into which the nonlocal and energy-dependent optical potential of the Kisslinger form is introduced in an *ad hoc* fashion. Since the kaon-nucleus interaction has not been fully understood, the Lorentz transformation property of the kaon optical potential cannot be established. Thus following the most common assumption in the literature, we treat the optical potential  $V$ , like the Coulomb potential  $V_c$ , as the time-like component of an arbitrary four-vector[106]. Thus the KG-equation takes the following approximate form:

$$[-\nabla^2 + \mathbf{k}^2 + (2E_k - V_c)V_c] \phi^{(+)}(\mathbf{r}, \mathbf{k}) = -2E_k V \phi^{(+)}(\mathbf{r}, \mathbf{k}). \quad (4.5.3)$$

Here we followed the tradition of dropping terms such as  $V_c V$  and  $V^2$ , and this guarantees that the inclusion of the optical potential is in a linear fashion [105]. The asymptotic momentum  $\mathbf{k}$  and total energy  $E_k$  of kaon in the kaon-nucleus c.m. system obey the on-shell relation:  $E_k^2 = m_K^2 + \mathbf{k}^2$ .  $\phi^{(+)}(\mathbf{r}, \mathbf{k})$  denotes the kaon distorted wave with outgoing boundary condition.

In order to obtain the numerical solution of the above approximate KG-equation, the kaon distorted wave should be expanded in terms of partial waves. That is,

$$\phi^{(+)}(\mathbf{r}, \mathbf{k}) = 4\pi \sum_{l,m} i^l R_{l,k}^{(+)}(r) Y_{lm}(\hat{\mathbf{r}}) Y_{lm}^*(\hat{\mathbf{k}}) \quad (4.5.4)$$

where  $R_{l,k}^{(+)}(r)$  is the radial part of the wave function and  $Y_{lm}(\theta, \varphi)$  the usual spherical harmonics. The angular momentum  $l$  and its projection  $m$  specify the partial waves of the kaon-nucleus system. Since the kaon optical potential is treated on the same footing as the Coulomb potential emitted from a uniform and spherically symmetric charge distribution, we expect that the distortion information of the kaon to come through the radial part of the wave function. In other words, the optical potential is independent of the angular coordinates; and hence we can apply the ‘‘separation of variables’’ in order to independently solve the radial KG-equation:

$$\left[ \frac{d^2}{dr^2} - \mathbf{k}^2 - \frac{l(l+1)}{r^2} + (V_c - 2E_k)V_c \right] U_{l,k}^{(+)}(r) = -r \left[ -2E_k V \frac{U_{l,k}^{(+)}(r)}{r} \right], \quad (4.5.5)$$

where  $U_{l,k}^{(+)}(r) = r R_{l,k}^{(+)}(r)$ ; and use is made of the explicit form of the gradient operator squared:

$$\nabla^2 = \frac{d^2}{dr^2} + \frac{2}{r} \frac{d}{dr} - \frac{\hat{L}^2}{r^2}, \quad (4.5.6)$$

where  $\hat{L}^2$  is the square of the angular momentum operator of the kaon-nucleus system with the corresponding eigenvalue of  $l(l+1)$ . The Coulomb potential is usually taken into account in a nonrelativistic manner; in this study, however, we have decided to ignore its contribution to the kaon distortion as we intend to offer a fully relativistic description.

## 4.6 Evaluation of the Radial KG-Equation

In section 4.5, the approximate form of the KG-equation was derived and then reduced to a radial-dependent, second-order ordinary differential equation (ODE) containing the optical potential as shown in Eq. (4.5.5). In what follows we take a few steps further to simplify the radial KG-equation upon introducing the explicit form of the kaon optical potential. In so doing, Eq. (4.5.5) will be manipulated to take a convenient form such that one can employ an iterative method to perform a numerical integration of the differential equation.

Now we reconsider the Kisslinger form of optical potential given in Eq. (4.4.5), which is the first-order approximation with respect to the nuclear density. Noting that Eq. (4.5.5) is purely radial dependent, we can show, after a few steps of algebra, that Eq. (4.4.5) becomes

$$-2EV(r) = Ak^2 b_0 \rho(r) - Ab_1 \left( \rho'(r) + \frac{2}{r} \rho(r) \right) \frac{d}{dr} - Ab_1 \rho(r) \left[ \frac{d}{dr} - \frac{l(l+1)}{r^2} \right], \quad (4.6.1)$$

where  $\rho'(r)$  is the first-derivative of the nuclear matter density. After a few more algebraic steps the radial KG-equation takes an explicit form:

$$\left[ \frac{d^2}{dr^2} - \frac{l(l+1)}{r^2} + \mathbf{k}^2 \right] U_{l,k}^{(+)}(r) = \left[ -Ak^2 b_0 \rho(r) - Ab_1 \frac{\rho'(r)}{r} + Ab_1 \rho'(r) \frac{d}{dr} + Ab_1 \rho(r) \left( \frac{d^2}{dr^2} - \frac{l(l+1)}{r^2} \right) \right] U_{l,k}^{(+)}(r). \quad (4.6.2)$$

For the sake of computational convenience, however, we prefer to write Eq. (4.5.5) in a more compact form as

$$U_{l,k}^{(+)}(r) - g(r)U_{l,k}^{\prime(+)}(r) + \left[ f(r) - \frac{l(l+1)}{r^2} \right] U_{l,k}^{(+)}(r) = 0, \quad (4.6.3)$$

where  $U_{l,k}^{(+)} = dU_{l,k}^{(+)} / dr$ , and

$$g(r) = \frac{Ab_1\rho'(r)}{1 - Ab_1\rho(r)}, \quad (4.6.4)$$

$$f(r) = \frac{Ab_0\rho'(r)}{1 - Ab_1\rho(r)}k^2 + \frac{1}{r} \frac{Ab_1\rho'(r)}{1 - Ab_1\rho(r)}. \quad (4.6.5)$$

Note that  $g(r)$  and  $f(r)$  are independent of angular momentum, and thus remain the same for all partial waves. In Fig. 4.5 we depict the behavior of the two complex functions with respect to the radial coordinate in the c.m. frame of the kaon and residual nucleus, for a reaction process that takes place on  $^{16}\text{O}$  target, at  $k_{\text{lab}} = 0.65$  GeV. As a consequence, solutions of a linear second-order differential equation are expected to be complex wave functions.

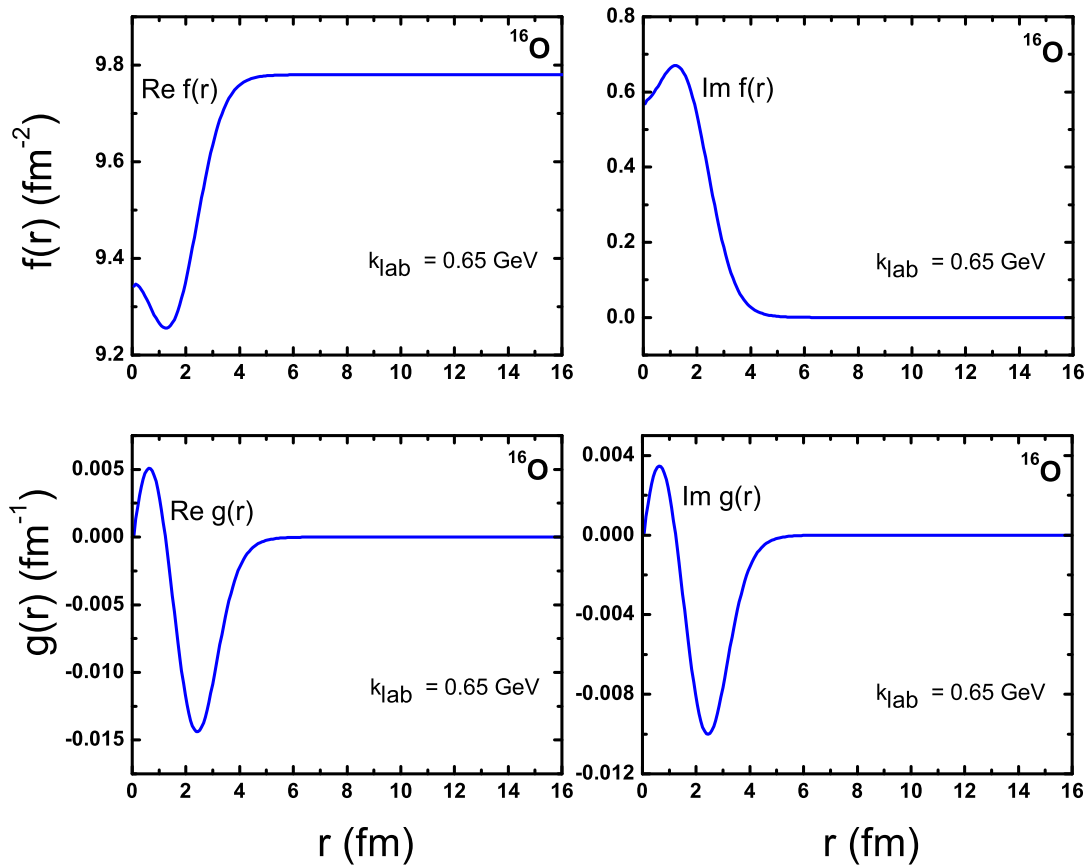


**Figure 4.5:** Complex functions  $g(r)$  and  $f(r)$ , appearing in the second-order differential equation, Eq. (4.6.3). They are plotted as a function of the distance of kaon with respect to the  $^{16}\text{O}$  target at  $k_{\text{lab}} = 0.65$  GeV. The real (imaginary) parts of the two radial functions are displayed in the left (right) panels. The optical potential parameters are determined from the phase shifts of Martin and use is made of the nuclear matter density obtained from the NL3 parametrized QHD model.

Traditionally, the nuclear density  $\rho(r)$ , as it appears in the kaon optical potential of the Kisslinger type, is given a form of either Gaussian, Fermi, or Wood-Saxon distribution which

is determined using macroscopic models within nonrelativistic limit, and its parameters are fixed using electron scattering data. Note, however, that these distributions cannot guarantee a detailed incorporation of the nuclear structure information into the optical potential. For this very reason, in this work, we exploit the richness of a relativistic treatment of nuclear matter. Thus, in order to ensure a fully relativistic distorted wave analysis of the exclusive reaction  $A(\nu, \ell KY)B$ , we make use of the nuclear matter(vector) density obtained from the RMF approximation of the Walecka model with NL3 parameter set[55]. Note that a similar attempt was made to include the nuclear matter density, which is obtained from QHD-II model, to calculate a relativistic optical potential for the study of photoproduction of mesons on nuclei[82]. The nuclear vector density,  $\rho_V(r)$ , is defined in chapter 2, Eq. (2.3.38), and further simplification allows us to write  $\rho_V(r)$  in terms of the upper and lower radial components of the bound state wave functions as

$$\rho_V(r) = \sum_{\alpha}^{\text{occ}} \bar{u}_{\alpha}(\mathbf{r}) \gamma^0 u_{\alpha}(\mathbf{r}) = \sum_{\alpha}^{\text{occ}} \left( \frac{2j_{\alpha} + 1}{4\pi r^2} \right) [g_{\alpha}^2(r) + f_{\alpha}^2(r)]. \quad (4.6.6)$$

#### 4.6.1 Boundary Conditions

The radial KG-equation, which is a second-order ODE, can have infinitely many solutions depending on our choice of boundary conditions. When dealing with initial-value problems such as Eq. (4.6.3), which do not have a unique solution, the choice of more appropriate boundary conditions play a key role in generating a physically sound solutions. In this context, by boundary condition we mean the asymptotic behavior of the wave function that must be taken into account before starting the numerical integration. Thus the radial KG-equation should be integrated in a finite volume, within which the optical potential has a non-vanishing contribution, after being initialized at or near the origin and then the generated solution is normalized to an asymptotic wave at larger distance where the optical potential drops to zero. Under such considerations the radial functions  $g(r)$  and  $f(r)$  can be approximated as

$$\lim_{r \rightarrow \infty} [\text{Re } g(r), \text{Im } g(r)] \approx [0, 0], \quad \lim_{r \rightarrow \infty} [\text{Re } f(r), \text{Im } f(r)] \approx [k^2, 0], \quad (4.6.7)$$

and such a large distance behavior of the two functions is well reflected in Fig. 4.5. Now one can treat  $g(r)$  and  $f(r)$ , with no loss of generality, as real functions in the region where the optical potential vanishes. As a result, Eq. (4.6.3) can be reduced to a common differential equation:

$$\mathcal{V}_{l,k}^{\prime(+)}(r) + \left[ k^2 - \frac{l(l+1)}{r^2} \right] \mathcal{V}_{l,k}^{(+)}(r) = 0, \quad (4.6.8)$$

for which a solution can be constructed analytically using the spherical Bessel  $j_l(kr)$  and Neumann  $n_l(kr)$  functions. The most general solution however is built using their linear combinations[107]:

$$h_l^{\pm}(kr) = j_l(kr) \pm in_l(kr), \quad (4.6.9)$$

where  $h_l^{\pm}(kr)$  are known as the spherical Hankel functions. Thus, based on Ref. [108] one can write the solution of for Eq. (4.6.9) as

$$\mathcal{R}_{l,k}^{(+)}(r) = \alpha_+ h_l^+(kr) + \alpha_- h_l^-(kr), \quad (4.6.10)$$

where  $\mathcal{V}_{l,k}^{(+)}(r) = r \mathcal{R}_{l,k}^{(+)}(r)$ . The coefficients  $\alpha_+$  and  $\alpha_-$  are determined by examining the asymptotic behavior of Eq. (4.6.10) as  $r \rightarrow \infty$ . From the phase shift analysis of scattering amplitudes of two-body problem in Ref. [108], we have the asymptotic form of  $\mathcal{R}_{l,k}^{(+)}(r)$ :

$$\lim_{r \rightarrow \infty} \mathcal{R}_{l,k}^{(+)}(r) = \frac{e^{i\gamma_l}}{kr} \sin(kr - l\pi/2 + \gamma_l), \quad (4.6.11)$$

where we have used the generalized phase shift  $\gamma_l$  which is a complex function of kaon energy and with a real part being related to the nuclear phase shift  $\delta_l$ , while the inelasticity coefficient  $\eta_l$  is determined from the imaginary part. That is,

$$\delta_l = \text{Re } \gamma_l, \quad \eta_l = e^{-2\text{Im } \gamma_l}. \quad (4.6.12)$$

These relations can also be put together and become

$$\gamma_l = \delta_l - \frac{i}{2} \ln \eta_l. \quad (4.6.13)$$

Now by using the asymptotic behaviors of  $h_l^\pm(kr)$ , that is

$$\lim_{r \rightarrow \infty} h_l^\pm(kr) = \pm \frac{1}{ikr} e^{\pm i(kr - l\pi/2)}, \quad (4.6.14)$$

we can manipulate Eq. (4.6.10) and then compare it to Eq. (4.6.11) to obtain

$$\alpha_+ = \frac{1}{2} e^{2i\gamma_l}, \quad \alpha_- = \frac{1}{2}. \quad (4.6.15)$$

Thus Eq. (4.6.10) now becomes

$$\mathcal{R}_{l,k}^{(+)}(r) = \frac{1}{2} [S_l(k) h_l^+(kr) + h_l^-(kr)], \quad (4.6.16)$$

in the range whereby the optical potential has a vanishing contribution and  $S_l(k)$  is scattering matrix element defined as:

$$S_l(k) = e^{2i\gamma_l} = \eta_l e^{2i\delta_l}. \quad (4.6.17)$$

Note again, that the Coulomb potential in the range  $r > R$  has as well been ignored, as this study is of a more exploratory nature.

The boundary condition at  $r = 0$  must also be specified so as to start the numerical integration of the initial-value problem of Eq. (4.6.3). As is evident from  $U_{l,k}^{(+)}(r) = r R_{l,k}^{(+)}(r)$ , Eq. (4.6.3) is subject to the boundary condition

$$\left( \text{Re } U_{l,k}^{(+)}, \text{Im } U_{l,k}^{(+)} \right) \Big|_{r=0} = (0, 0). \quad (4.6.18)$$

We assume that in the immediate neighborhood of  $r = 0$  the optical potential has a relatively small contribution and the radial KG-equation is satisfied by analytical solutions constructed from the linear combinations of the spherical Bessel functions  $j_l(kr)$  and  $n_l(kr)$ . However, the boundary condition given in Eq. (4.6.18) helps us identify those solutions which are physically acceptable. In so doing, we first examine the asymptotic behavior of  $j_l(kr)$  and  $n_l(kr)$  as  $r \rightarrow 0$ :

$$\lim_{r \rightarrow 0} j_l(kr) = \frac{(kr)^l}{(2l+1)!!}, \quad \lim_{r \rightarrow 0} n_l(kr) = -\frac{(2l-1)!!}{(kr)^{l+1}}, \quad (4.6.19)$$

where  $(2l+1)!! = (2l+1)(2l-1) \cdots 5 \cdot 3 \cdot 1$ . Since we are interested in physical solutions in the nuclear interior which includes the origin, we must drop any term from the general solution as long as it poses a risk of singularity at and near  $r = 0$ . Along these lines, we learn from Eq. (4.6.19) that  $n_l(rk)$  suffers from an irregularity at  $r = 0$ . Therefore, we approximate the radial wave function to take a form:

$$\lim_{r \rightarrow 0} \left( \text{Re } U_{l,k}^{(+)}, \text{Im } U_{l,k}^{(+)} \right) \approx \left( \frac{r(kr)^l}{(2l+1)!!}, 0 \right). \quad (4.6.20)$$

Eq. (4.6.20) is consistent with the fact that in free space the complex radial wave function  $U_{l,k}^{(+)}(r)/r$  must coincide with the real spherical Bessel function  $j_l(kr)$ . Note that, for safety sake, we set the imaginary part of  $U_{l,k}^{(+)}(r)$  to zero in the neighborhood of  $r = 0$ , as we are not

well aware of how it behaves within that region. Therefore, such appropriate specification of the boundary conditions as  $r \rightarrow 0$  and  $r \rightarrow \infty$  guarantees to give rise to a physically sound numerical solutions by solving the radial KG-equation using the fourth-order Runge-Kutta algorithm.

It is important to stress the fact that a kaon in the final channel of  $A(\nu, \ell KY)B$  process is described by a wave function  $\phi^{(-)}(\mathbf{r}, \mathbf{k})$ , where the minus superscript refers to the fact that the wave function is constrained by an incoming boundary condition. However, the radial KG-equation, containing the Kisslinger type optical potential, was carefully designed to solve for the distorted kaon wave function  $\phi^{(+)}(\mathbf{r}, \mathbf{k})$  with outgoing boundary condition. Thus it is necessary to establish a proper relation between the two wave functions with opposite boundary conditions. Goldberger and Watson[108] have used the time reversal operator  $\mathcal{T}_0$  to relate the two scalar functions as:

$$\phi^{(-)}(\mathbf{r}, \mathbf{k}) = \mathcal{T}_0 \phi^{(+)}(\mathbf{r}, -\mathbf{k}). \quad (4.6.21)$$

Based on this definition, it has been shown in Ref. [108] that the radial parts of the individual partial waves of incident and ejected kaons can be related as follows:

$$R_{l,k}^{(-)}(r) = (-1)^l \mathcal{T}_0 \left[ R_{l,k}^{(+)}(r) \right] = (-1)^l \left[ R_{l,k}^{(+)}(r) \right]^*, \quad (4.6.22)$$

which can be proved by using the following property of spherical harmonics with a dummy index  $m$ :

$$\sum_{m=-l}^l \left[ Y_{lm}(\hat{\mathbf{r}}) Y_{lm}^*(-\hat{\mathbf{k}}) \right]^* = \sum_{m=l}^{-l} Y_{lm}(\hat{\mathbf{r}}) Y_{lm}^*(-\hat{\mathbf{k}}), \quad (4.6.23)$$

and subsequently the wave function of the final state kaon with the incoming boundary condition becomes:

$$\phi^{(-)}(\mathbf{r}, \mathbf{k}) = 4\pi \sum_{l,m} i^l (-1)^l \left[ R_{l,k}^{(+)}(r) \right]^* Y_{lm}(\hat{\mathbf{r}}) Y_{lm}^*(-\hat{\mathbf{k}}). \quad (4.6.24)$$

Therefore, one can always solve the radial KG-equation for incident waves and then transform them, using the time reversal operator, into ejected waves, and vice-versa.

#### 4.6.2 Normalization of the Kaon Radial Wave Function

Upon initiating the numerical integration of Eq. (4.6.3) based on the information we have from the boundary condition at  $r = 0$ , one must stop the iteration at the matching radius  $R$  (which will be fixed in the next section) and compare the interior numerical solutions with the corresponding asymptotic solutions given in Eq. (4.6.16) at that point. Such a comparison is what leads to the determination of the nuclear phase shifts  $\delta_l$  and absorption coefficients  $\eta_l$  for individual partial waves. Once energy-dependent quantities  $\delta_l$  and  $\eta_l$  are determined, the next step would be to compute the normalization factors for the numerical solutions generated in the finite volume  $r \leq R$ . In order to do so, we rewrite Eq. (4.6.16) as

$$\mathcal{R}_{l,k}^{(+)}(r) = e^{i\gamma_l} \left[ \cos \gamma_l j_l(kr) - \sin \gamma_l n_l(kr) \right], \quad (4.6.25)$$

and then we perform the matching in terms of the complex logarithmic derivatives  $\beta_l$  as follows:

$$\beta_l = \left( \frac{r}{R_{l,k}^{(+)}} \frac{dR_{l,k}^{(+)}}{dr} \right)_{r=R} = kR \frac{[j_l'(kr) \cos \gamma_l - n_l'(kr) \sin \gamma_l]}{j_l(kr) \cos \gamma_l - n_l(kr) \sin \gamma_l}, \quad (4.6.26)$$

where  $j_l'(n_l')$  denotes the first-derivative of  $j_l(n_l)$  with respect to  $kr$ . For convenience sake we rewrite  $\beta_l$  for  $r \leq R$  in terms of  $U_{l,k}^{(+)}$  instead of  $R_{l,k}^{(+)}$ :

$$\beta_l = \frac{r}{R_{l,k}^{(+)}} \frac{dR_{l,k}^{(+)}}{dr} = \frac{r}{U_{l,k}^{(+)}} \frac{dU_{l,k}^{(+)}}{dr} - 1, \quad (4.6.27)$$



and now, at the matching point, the generalized nuclear phase shift  $\gamma_l$  can be determined using

$$\tan \gamma_l = \frac{kR j_l'(kR) - \beta_l j_l(kR)}{kR n_l'(kR) - \beta_l n_l(kR)}. \quad (4.6.28)$$

Notice that  $\tan \gamma_l$  is simply a complex number generated numerically. Thus we can determine the nuclear phase shift  $\delta_l$  and absorption coefficient  $\eta_l$  using Eq. (4.6.12) given

$$\gamma_l = \frac{-i}{2} \ln \left( \frac{1 + i \tan \gamma_l}{1 - i \tan \gamma_l} \right), \quad (4.6.29)$$

where  $\ln$  is a function defined over the complex ( $\mathbb{C}$ ) domain such that  $\ln : \mathbb{C} \rightarrow \mathbb{C}$ , which is the extension of the elementary real function known as the natural logarithm. Once  $\delta_l$  and  $\eta_l$  are numerically fixed, we use the identity

$$e^{2i\gamma_l} = \frac{1 + i \tan \gamma_l}{1 - i \tan \gamma_l}, \quad (4.6.30)$$

in order to determine the normalization coefficients  $\mathcal{N}_{l,k}(R)$  which are defined, at the matching radius  $r = R$ , as the ratio between the asymptotic waves  $\mathcal{R}_{l,k}^{(+)}(r)$  given in Eq. (4.6.25) and the interior numerical solutions  $R_{l,k}^{(+)}$  of Eq. (4.6.3). That is,

$$\mathcal{N}_{l,k}(R) = \left( \frac{\mathcal{R}_{l,k}^{(+)}(r)}{R_{l,k}^{(+)}(r)} \right) \Big|_{r=R} = \frac{j_l(kR) - \tan \gamma_l n_l(kR)}{1 - i \tan \gamma_l} \left( \frac{1}{R_{l,k}^{(+)}(r)} \right) \Big|_{r=R}, \quad (4.6.31)$$

and these coefficients ensure the continuity of the radial kaon wave functions from the interior to exterior regions of the finite volume of range  $r \leq R$ . The next step is very important in that it gives rise to a more physical radial wave. The original numerical solution set of  $U_{l,k}^{(+)}(r)$  generated from Eq. (4.6.3) must be appropriated using this normalization factor determine by imposing outgoing boundary condition. That is,

$$\left( R_{l,k}^{(+)}(r) \right) \Big|_{r \leq R} \longrightarrow \mathcal{N}_{l,k}(R) \left( R_{l,k}^{(+)}(r) \right) \Big|_{r \leq R}. \quad (4.6.32)$$

Therefore, the overall radial wave function of kaon in the range  $0 \leq r \leq \infty$  can be written as

$$\left[ R_{l,k}^{(+)}(r) \right]_{r=0}^{\infty} = \Theta(R - r) \mathcal{N}_{l,k} R_{l,k}^{(+)}(r) + \Theta(r - R) \mathcal{R}_{l,k}^{(+)}(r), \quad (4.6.33)$$

where  $\Theta$  is the unit step function defined as:

$$\Theta(x) = \begin{cases} 1 & \text{for } x > 0 \\ 1/2 & \text{for } x = 0 \\ 0 & \text{for } x < 0. \end{cases} \quad (4.6.34)$$

However, since we are more interested in the radial wave in the interior region, where the optical potential has a non-vanishing contribution, the kaon FSI we need for our RDWIA calculations can sufficiently be represented by  $\mathcal{N}_{l,k} R_{l,k}^{(+)}(r)$ . Thus inside the finite volume the full kaon distort wave function with outgoing boundary condition can be rewritten as

$$\left[ \phi^{(+)}(\mathbf{r}, \mathbf{k}) \right]_{r < R} = 4\pi \sum_{l,m} i^l \mathcal{N}_{l,k} R_{l,k}^{(+)}(r) Y_{lm}(\hat{\mathbf{r}}) Y_{lm}^*(\hat{\mathbf{k}}) \quad (4.6.35)$$

## 4.7 Numerical Analysis of Kaon Distortion

In this section we focus on the numerical implementation of the problems we laid out in the previous sections. We have used Fortran 95 to code the kaon FSI problem, as Fortran is the

most widely used programming language in the nuclear scattering studies. The main goal of this section is to generate the numerical solutions of the radial KG-equation given in Eq. (4.6.3) based on the detailed information we have previously outlined. In order to achieve our goal, we implement the extended version of the fourth-order Runge-Kutta algorithm to solve the complex second-order differential equation. In so doing, we break down the main problem into manageable pieces, for which we design the corresponding Fortran codes. Once each piece of code is tested independently, we put them together in order to be able to solve the main problem.

#### 4.7.1 Kinematics

To begin with, we first specify the kinematics of the kaon FSI calculation as the analysis of the dynamics part depends on it. As is customary, the kaon-nucleus interaction is studied in the c.m. frame, whereby both participants have equal but opposite momenta. In this study we do not distinguish between the center-of-mass and center-of-momentum frames of a given system. Note however, that in the distorted wave analysis of neutrino-induced associated production of strange particles from nuclei, the kinematic quantities are determined in the rest frame of the target nucleus A. That being said, we now label the rest frame of A and B nuclei as Lab1 and Lab2, respectively, such that they can easily be distinguished. The kaon distorted waves, that we are hoping to generate, are going to be used in the RDWIA treatment of the reaction process  $A(\nu, \ell KY)B$ . Thus the four-momentum  $k_1'^{\mu} = (E_{k_1}', \mathbf{k}_1')$  of kaon in the K-B c.m. frame must be determined from Lab1 kinematics of K and B:  $p_1'^{\mu} = (E_{p_1}', \mathbf{p}_1')$  and  $P_1'^{\mu} = (E', \mathbf{P}')$ , using Lorentz transformation. That is,

$$E_{k_1}' = \gamma_1' (E_{p_1}' - \beta_1' \cdot \mathbf{p}_1'), \quad (4.7.1)$$

$$\mathbf{k}_1' = \gamma_1' (\mathbf{p}_{1\parallel}' - E_{p_1}' \beta_1') + \mathbf{p}_{1\perp}', \quad (4.7.2)$$

where

$$\beta_1' = \frac{\mathbf{p}_1' + \mathbf{P}'}{E_{p_1}' + E'}, \quad \gamma_1' = \frac{1}{\sqrt{1 - \beta_1'^2}}, \quad (4.7.3)$$

and

$$\mathbf{p}_{1\parallel}' = \frac{\beta_1' \cdot \mathbf{p}_1'}{\beta_1'^2} \beta_1', \quad \mathbf{p}_{1\perp}' = \mathbf{p}_1' - \mathbf{p}_{1\parallel}'. \quad (4.7.4)$$

Thus in the K-B c.m. frame the three-momentum and energy of the residual nucleus B are  $-\mathbf{k}_1'$  and  $(\mathbf{k}_1'^2 + M_B^2)^{1/2}$ , respectively, where  $M_B$  is its rest mass. In the previous sections it has been argued that the dynamical information for the kaon-nucleus interaction comes from the underlying KN scattering amplitudes analyzed in the KN c.m. system. As a result, the Lorentz transformation of the relative momentum  $\mathbf{k}_1'$  is required from the K-B c.m. frame to the KN c.m. frame. But such a transformation becomes a formidable task unless one resorts to some sort of approximation owing to the fact the nucleons in the nuclear medium are bound states. In so doing, we invoke the ‘‘frozen’’ nucleon approximation such that each nucleon, in the moving nucleus B and with its Fermi motion being neglected, has a momentum  $\mathbf{p}_i = -\mathbf{k}_1'/A_B$ , where  $A_B = A - 1$  is the nucleon number of the residual nucleus. The energy can also be determined via the on-shell relation:  $E_i^2 = \mathbf{p}_i^2 + M_N^2$ , where  $M_N$  is the nucleon rest mass. Now we can determine the relative momentum of the kaon in the KN c.m. frame by introducing the Lorentz invariant variable:

$$s = (k_1'^{\mu} + p_i^{\mu})^2 = (E_{k_1}' + E_i)^2 - \left( \frac{A_B - 1}{A_B} \right)^2 k_1'^2, \quad (4.7.5)$$

where  $k_1' = |\mathbf{k}_1'|$ . Now we denote the four-vector of kaon in the KN c.m. frame by  $\kappa_1'^{\mu} = (E_{\kappa_1}', \boldsymbol{\kappa}_1')$ , we can show that

$$\kappa_1' = \frac{1}{2\sqrt{s}} \sqrt{\lambda(s, M_K^2, M_N^2)}, \quad E_{\kappa_1}' = \frac{1}{2\sqrt{s}} (s + M_K^2 - M_N^2), \quad (4.7.6)$$

where  $\kappa'_1 = |\mathbf{\kappa}'_1|$  and use is made of the triangle function  $\lambda$  defined as:

$$\lambda(x, y, z) = (x - y - z)^2 - 4yz. \quad (4.7.7)$$

Using the same approximation, we can also perform another transformation from K-B c.m. frame to the rest frame of the nucleon, which is labeled as Lab3:

$$(k'_1)_{\text{lab3}} = \frac{1}{2M_N} \sqrt{\lambda(s, M_K^2, M_N^2)}, \quad (E_{k'_1})_{\text{lab3}} = \frac{1}{2M_N} (s - M_K^2 - M_N^2), \quad (4.7.8)$$

where  $(k'_1)_{\text{lab3}} = |(k'_1)_{\text{lab3}}|$  and  $(E_{k'_1})_{\text{lab3}}$  are such that  $(k'_1{}^\mu)_{\text{lab3}} = ((E_{k'_1})_{\text{lab3}}, (k'_1)_{\text{lab3}})$ . Thus by using these kinematic quantities one can determine the optical potential parameters. A Fortran subroutine, ROPLOTT, has been designed to take the Lab1 four momenta  $p_1{}^\mu = (E_{p_1}, \mathbf{p}'_1)$  and  $P_1{}^\mu = (E', \mathbf{P}')$  of the final state kaon and the residual nucleus, respectively, as input

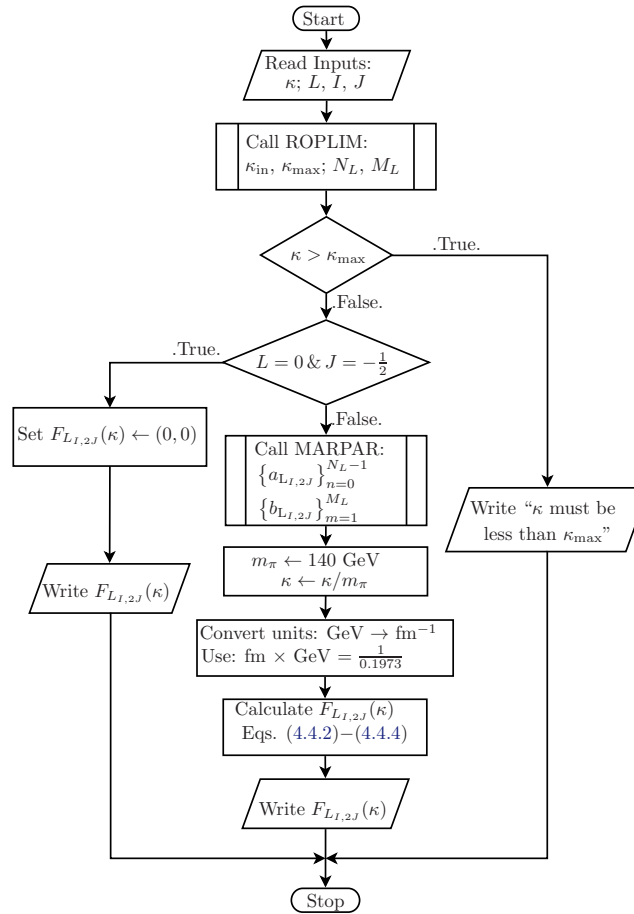


**Figure 4.6:** Flow diagram for the subroutine ROPFLIJ which is written in Fortran 95 in order to calculate the dimensionless partial wave amplitudes  $F_{L,I,2,J}(\kappa)$  defined in Eq. (4.4.2).

variables, perform Lorentz transformation using Eqs. (4.7.1) - (4.7.4), and then return the four-momentum of kaon  $k_1{}^\mu = (E_{k_1}, \mathbf{k}'_1)$  in the K-B c.m. frame. The second subroutine of the kinematic part is named as ROPKIN, which takes  $k'_1$ ,  $m_K$ ,  $M_N$ , and  $A_B$  as inputs, and then returns the kaon momenta  $\kappa'_1$  and  $(k'_1)_{\text{lab3}}$  in KN c.m. and Lab3 frames, respectively, by coding Eqs. (4.7.5) - (4.7.8) into the subroutine.

## 4.7.2 ROP Parameters

Here we focus on the coding of the dynamic part of the kaon FSI, whose input comes from the phase shift analysis of the underlying elementary KN scattering experiment by Martin.

The first subroutine, MARPAR, for this particular problem is to make Martin's sets of parameters, given in Table 4 of Ref. [95], accessible for computation. Thus the subroutine is written in such a way that for individual KN eigen-channels specified by  $\{L, I, J\}$  it returns the corresponding sets of parameters:  $\{a_{L,I,2J}\}_{n=0}^{N_L-1}$  and  $\{b_{L,I,2J}\}_{m=1}^{M_L}$ , in array format, where  $L_{I,2J} \in \{S_{01}, S_{11}, P_{01}, P_{03}, \dots\}$ . The second subroutine, ROPLIM, is thus created to be able to access constant limits used in Martin's analysis such as kinematic limits (Table 4.2):  $\kappa'_{1in}$  and  $\kappa'_{1max}$ ; and summation limits (Table 4.3):  $N_L$  and  $M_L$ , with which we specify the dimensions of the arrays for the above parameter sets.

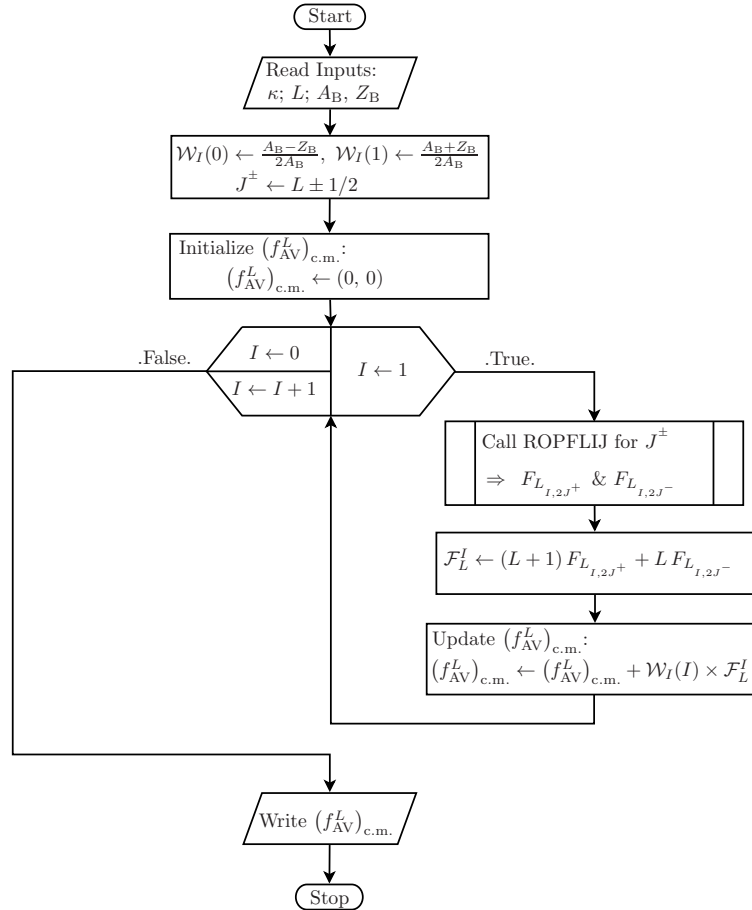


**Figure 4.7:** Flow diagram of a Fortran 95 subroutine, ROPLAMP, which is designed to calculate the spin-isospin averaged  $K^+N$  scattering amplitudes  $(f_{AV}^L)_{c.m.}$  based on Eq. (4.7.9).

The next step would be to write a code which performs the iterative summation over Martin's parameters so as to determine the dimensionless partial wave amplitudes  $F_{L,I,2J}(\kappa'_1)$ , defined in Eq. (4.4.2). This particular problem is being taken care of by the third subroutine, ROPFLIJ, with inputs:  $L, I, J$ , and  $\kappa'_1$  and output:  $F_{L,I,2J}(\kappa'_1)$ . It is important to note, therefore, that the first two subroutines: MARPAR and ROPLIM, are going to be called inside ROPFLIJ subroutine. For the sake of convenience and also to be consistent with the previous sections, from now on we use  $k, \kappa$ , and  $k_{lab}$  in place of  $k'_1, \kappa'_1$ , and  $(k'_1)_{lab3}$  to represent the same kinematic quantities. Care must be taken whether the same unit is being used consistently throughout each chapter, and hence in the ROPFLIJ subroutine we convert quantities given in  $\text{GeV}^b$  into their equivalent value in  $\text{fm}^{-b}$ , using the definition:  $\text{fm} \times \text{GeV} = 1/0.1973$ . In addition, since Martin's parameters are determined in units of  $m_\pi = 1$ , every term or factor  $a$  in units  $\text{GeV}^b$ , for any arbitrary integer  $b$ , is going to be rewritten as  $a/m_\pi^b$ , with  $m_\pi = 140 \text{ GeV}$ . This ensures that

$F_{L_{I,2J}}(\kappa)$  remains dimensionless. In Fig. 4.6 we show the flow diagram on how the ROPFLIJ subroutine, written in Fortran 95, can be progressively executed to calculate  $F_{L_{I,2J}}(\kappa'_1)$ .

The fourth subroutine, ROPLAMP, computes the spin-isospin averaged KN scattering amplitude for each  $L$  as discussed in section 4.4:

$$(f_{AV}^L)_{c.m.} = \sum_{I=0,1} \mathcal{W}_I \left[ (L+1)F_{L+1/2}^I + LF_{L-1/2}^I \right], \quad (4.7.9)$$

and the inputs of this subroutine are:  $k$ ,  $L$ ,  $A_B$ , and  $Z_B$ , and the output is going to be  $(f_{AV}^L)_{c.m.}$ . Here  $Z_B$  denotes the proton number of the residual nucleus B, and  $A_B$  and  $Z_B$  are included because of the isospin weighing coefficients  $\mathcal{W}_I$  defined in Eq. (4.4.12). As is evident from Eq. (4.7.9), we need to call ROPFLIJ inside the ROPLAMP subroutine in order to be able to compute  $F_{L_{I,2J}^\pm} \equiv F_{L\pm 1/2}^I(\kappa)$ . This has to do with the fact the ROP must be incorporated into the radial KG-equation in units which are consistent with the expression and its solutions. Fig. 4.7 illustrates execution flow of ROPLAMP subroutine to determine the elementary amplitudes

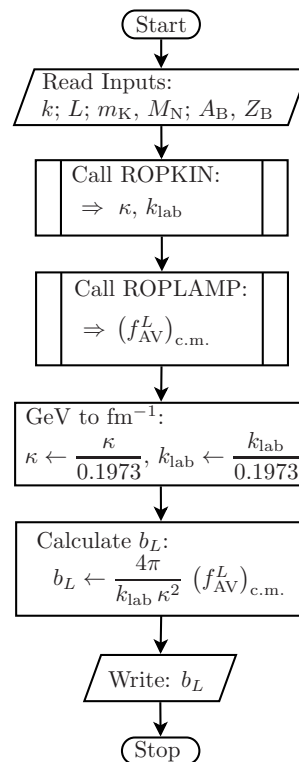


**Figure 4.8:** Flow diagram for a subroutine ROPPAR, as written in Fortran 95, for calculating the kaon optical potential  $b_L$  ( $L = 0, 1$ ).

$(f_{AV}^L)_{c.m.}$ . Finally, we must be able to compute the optical potential parameters  $b_L$ , defined in Eq. (4.4.7), using a subroutine named ROPPAR that makes use of the ROPKIN and ROPLAMP subroutines; and the flowchart for ROPPAR is shown in Fig. 4.8. The plots in Figs. 4.3 and 4.4, showing the energy dependence of the ROP parameters, are generated using this subroutine.

### 4.7.3 Numerical Integration

The attempt to find an analytical solution of the radial KG-equation along with the optical potential has been proven to be formidable. As a consequence, we resort to introducing the numerical integration methods to deal with the second-order differential equation. Although there are a number of numerical methods such as Euler, Heun, and Noumerov iteration methods, we rather employ a “self-starting” fourth-order Runge-Kutta (RK4) integration method to solve

the complex, linear, second-order differential equation given in Eq. (4.6.3). This choice is motivated by the fact that the RK4 method (i) is best suited for initial value problems (IVP's), (ii) shows good convergence and stability relative to the other methods such as Euler and midpoint integration techniques, and (iii) provides the solution along with its first-derivative. Note however, that RK4 is traditionally designed to deal with first-order ODE, whereas our

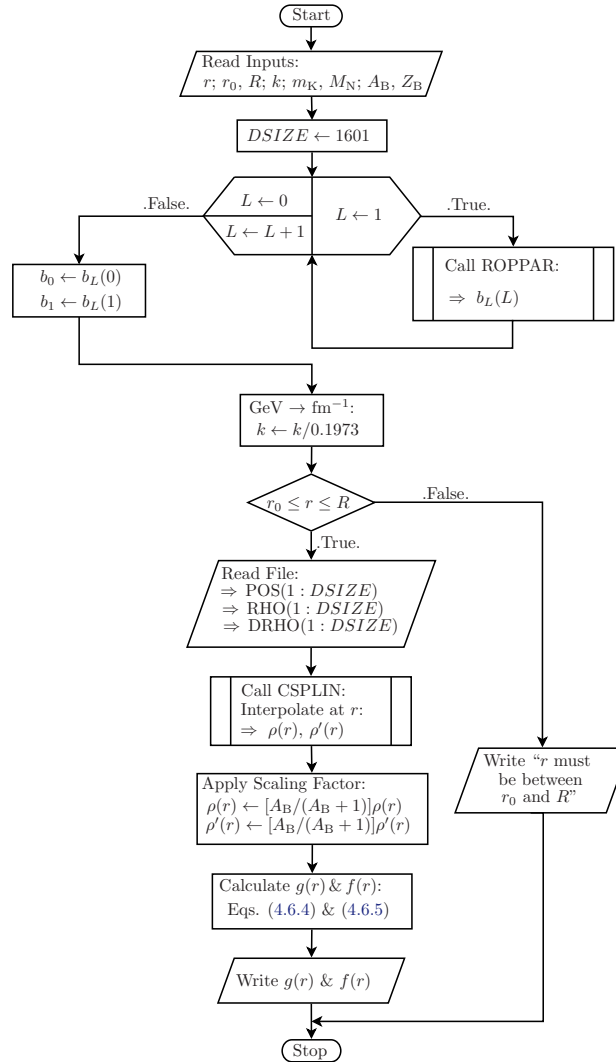


**Figure 4.9:** Flow diagram for a Fortran 95 subroutine ROPFUNC, which determines the two functions  $g(r)$  and  $f(r)$  through which the optical potential is introduced into the radial KG-equation.

problem is a complex, second-order ODE. The RK4 method for the coupled system of equation is a slightly different from its standard definition as discussed in Appendix C section C.2.

Thus, we begin with converting Eq. (4.6.3) into a system of coupled equations. For the sake of convenience we now introduce two unknown complex wave functions  $\xi(r)$  and  $\zeta(r)$  such that:

$$\xi(r) = U_{l,k}^{(+)}(r) \quad (4.7.10)$$

$$\zeta(r) = U_{l,k}'^{(+)}(r) \quad (4.7.11)$$

and hence their first-derivatives become:

$$\frac{d\xi(r)}{dr} = F_1(r, \xi(r), \zeta(r)), \quad (4.7.12)$$

$$\frac{d\zeta(r)}{dr} = F_2(r, \xi(r), \zeta(r)), \quad (4.7.13)$$

where

$$F_1(r, \xi(r), \zeta(r)) = \zeta(r), \quad (4.7.14)$$

$$F_2(r, \xi(r), \zeta(r)) = g(r)\zeta(r) - \left[ f(r) - \frac{l(l+1)}{r^2} \right] \xi(r). \quad (4.7.15)$$

Thus Eqs. (4.7.12) and (4.7.13) form a system of coupled, complex, linear, first-order differential equations, which is equivalent to the radial KG-equation in Eq. (4.6.3). Note that this way of

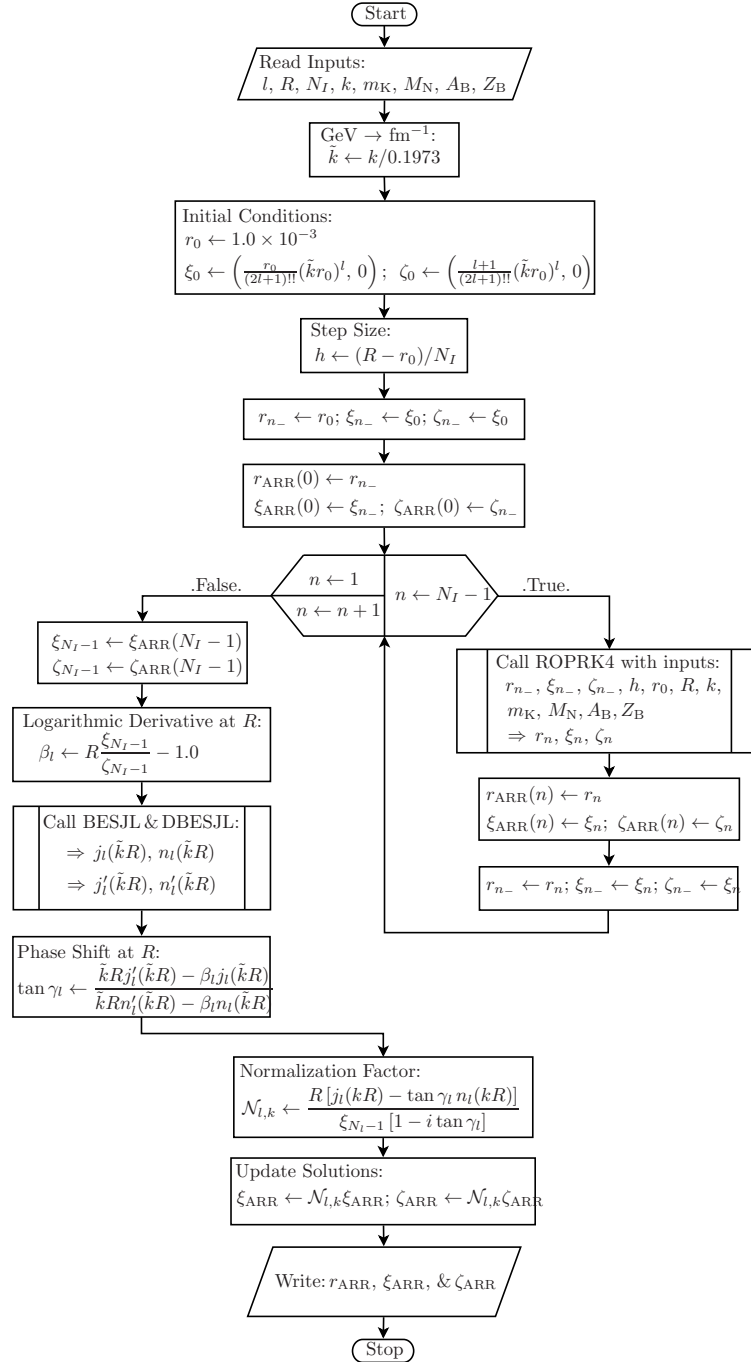


**Figure 4.10:** Flow diagram for ROPSOLV subroutine in order to numerically solve, by using the RK4 integration method, for the radial partial-waves of the final state kaon interacting with the residual nucleus before exiting with asymptotic momentum  $\mathbf{k}$ .

writing the two coupled differential equations is to make use of the RK4 iteration equations defined in Eqs. (C.2.13) - (C.2.15) of Appendix C.



It is worth noting, once again, that the RK4 method solves for both  $U_{l,k}^{(+)}$  and  $U_{l,k}'^{(+)}$ , simultaneously. This feature of the RK4 iteration method becomes a crucial advantage particularly when we intend to apply the continuity of the logarithmic derivatives at the matching radius

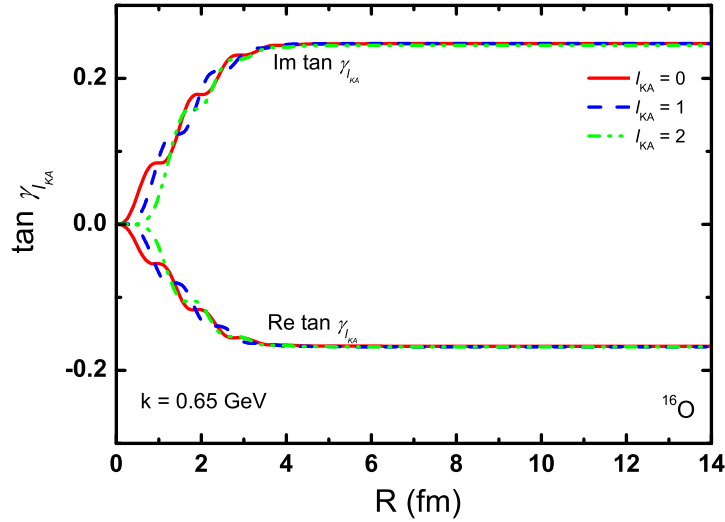


**Figure 4.11:** Dependence of the generalized phase shift  $\gamma_l(k)$  on the matching radius  $R$ . This illustrates the behavior of  $\gamma_l(k)$  calculated for three partial waves ( $l = 0, 1, 2$ ) of kaon, and for  $R$  in the range of  $0 < R < 14$  fm. The K-B c.m. frame momentum of kaon is fixed at  $k = 0.65$  GeV.

$r = R$ ; and hence the step size is fixed, by definition, using  $h = (R - r_0)/N_I$ , where  $N_I$  be the number of iterations we intend to execute with good convergence and stability. In order

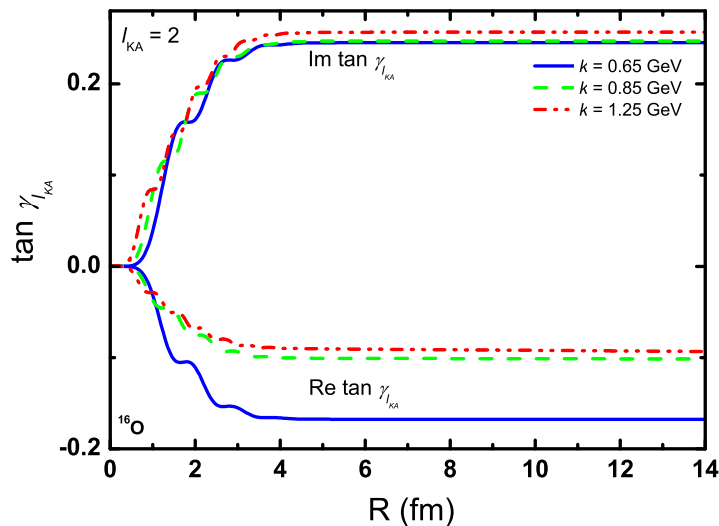


**Figure 4.12:** Illustration of how  $\delta_l(k)$  and  $\eta_l(k)$  behave for wider choice of the matching radius  $R$ , for  $l = 2$  partial wave of kaon, and for fixed K-B c.m. momentum of kaon at  $k = 0.65, 0.85,$  and  $1.25$  GeV.

to proceed further with this analysis we must write a subroutine that returns the two radial functions  $g(r)$  and  $f(r)$  through which the kaon FSI is incorporated to the radial KG-equation. Here however, we must make certain assumptions with regard to the nuclear matter density of the residual nucleus. In this work, the RMF description of the nuclear structure is carried out for target nuclei such as  ${}^4\text{He}$ ,  ${}^{12}\text{C}$ ,  ${}^{16}\text{O}$ ,  ${}^{40}\text{Ca}$  and  ${}^{208}\text{Pb}$ , and now we consider the residual nucleus to be the target itself with a single hole. Thus we assume that the nuclear matter densities we have determined for the target nuclei can be extrapolated to their respective final state nuclei. In so doing, we also make a small correction on their normalizations in that the new densities

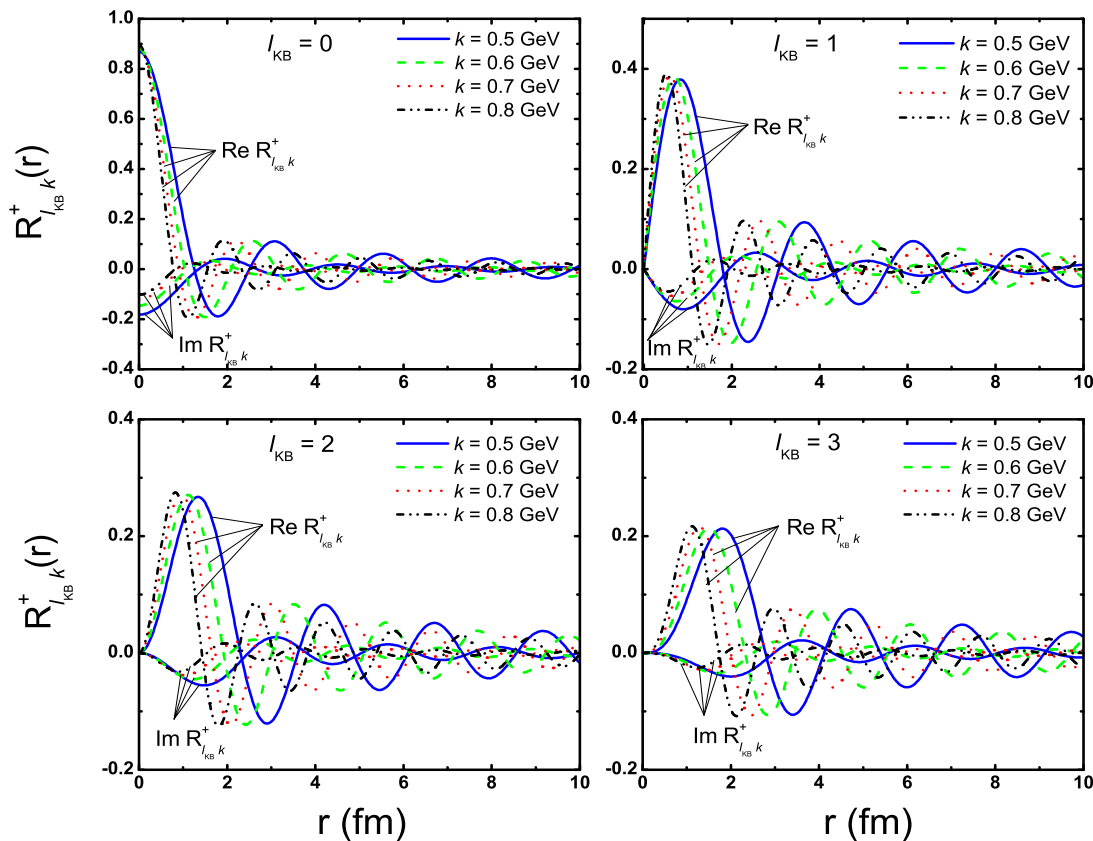


**Figure 4.13:** Radial dependence of partial waves of kaon in the final state of  $A(\nu, \ell KY)B$  process. The FSI of kaon is considered to be with the residual nucleus of  ${}^{16}\text{O}$  target. Relative momentum of kaon is fixed at  $k = 0.65$  GeV. These radial waves are normalized using outgoing boundary conditions.

must account for  $A - 1$  nuclear states, where  $A$  is the nucleon number for the target nucleus. That is,

$$\rho_{V,B}(r) = \frac{A-1}{A} \rho_{V,A}(r). \quad (4.7.16)$$

Note that this assumption is based on the normalization of the nuclear vector density  $\rho_{V,A}$  to  $A$  instead of unity, in which case we must automatically drop the factor  $A$  from the Kisslinger form optical potential given in Eq. (4.4.5). A subroutine called ROPFUNC is designed to perform such calculations. It takes  $r$ ,  $r_0$ ,  $R$ ,  $k$ ,  $m_K$ ,  $M_N$ ,  $A_B$  and  $Z_B$  as input variables, where  $r_0$  denotes the radial distance we usually fix at the close proximity of the origin and  $R$  is the maximum radial distance or matching radius of the numerical integration; subsequently it calculates the two output functions, at radial distance  $r$ , by using Eqs. (4.6.4) and (4.6.5). The three important ingredients of this subroutine are: (i) the use of the ROPPAR subroutine to compute  $b_L$  values; (ii) file reading to access discrete values of the RMF nuclear vector density and its first-derivative given at equidistant radial positions. Here the three columns of the file

are read into three arrays: POS, RHO, and DRHO; (iii) calling a subroutine that allows us interpolate  $\rho$  and  $\rho'$  at any given radial distance  $r$  within a range of  $r_0 \leq r \leq R$ . Thus for this problem we introduce the cubic spline subroutine: CSPLIN<sup>1</sup>, which is accompanied by the function subprogram CSEVAL to evaluate the spline at any arbitrary point. This choice has to do with the fact that the cubic spline is known to offer the best interpolation with minimum error in comparison to other methods. In Fig. 4.9 the structure of the ROPFUNC subroutine that emphasizes on the execution flow of the code to generate the radial functions  $g(r)$  and  $f(r)$  at any given distance  $r$ ; and this same subroutine is used to plot the functions in Fig. 4.5.

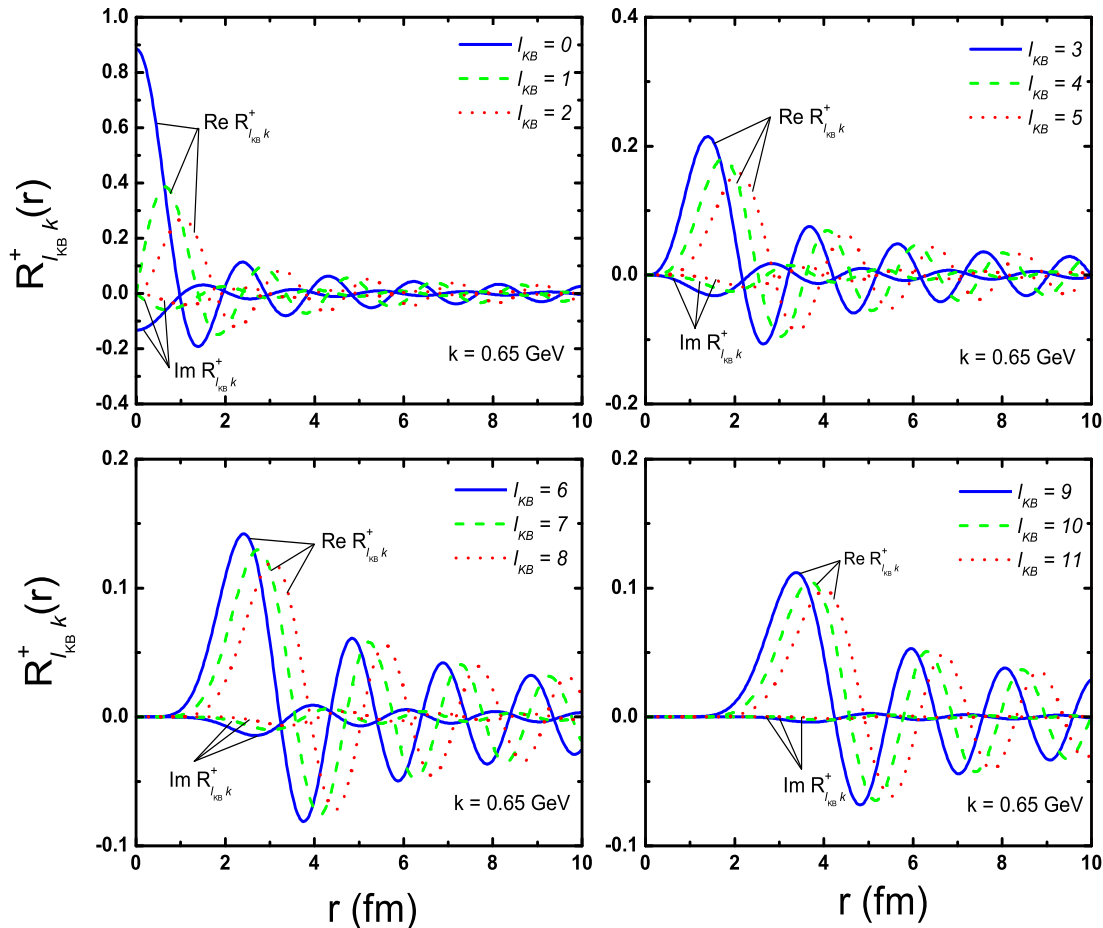


**Figure 4.14:** Partial waves of kaon, in the final state of  $A(\nu, \ell KY)B$  process, plotted as a function of radial distance. These radial wave functions are normalized using outgoing boundary conditions. Here the FSI of kaon is considered to be with the residual nucleus of  $^{16}\text{O}$  target. Relative momentum of kaon is fixed at  $k = 0.65$  GeV.

Once complex functions  $g(r)$  and  $f(r)$  are coded, the numerical implementation of the RK4 integration method to solve the radial KG-equation, which is rewritten as the system of coupled first-order differential equations, becomes somewhat easier. In order to do so, we write function subprograms for  $F_1(r, \xi, \zeta)$  and  $F_2(r, \xi, \zeta)$  which are complex functions and defined in Eqs. (4.7.12) and (4.7.13), in a manner that they can suitably be used in the RK4 iteration code. Note that in this context we consider  $r, \xi$ , and  $\zeta$  as independent variables.  $F_1$  can be coded in straightforward manner as it only depends on  $\zeta$ , whereas  $F_2$  depends not only on the three variables but also on additional arguments with which we need to specify the radial functions

<sup>1</sup>This code was designed by G. E. Forsythe, M. A. Malcolm & C. B. Moler[109], & modified by W. M. Coughran, 1976.

$g(r)$  and  $f(r)$  by calling the ROPFUNC subroutine in the subprogram. Thus the two Fortran 95 functions are coded as  $F1(r, \xi, \zeta)$  and  $F2(r, \xi, \zeta; \text{args})$ , where “args” represents the additional arguments  $r_0, R, k, m_K, M_N, A_B$  and  $Z_B$ . Next, a single iteration RK4 form is coded as ROPRK4 subroutine based on Eqs. (C.2.13) - (C.2.15) defined in Appendix C. Thus the ROPRK4 subroutine takes  $r_n, \xi_n$ , and  $\zeta_n$  as inputs along with other arguments:  $h, r_0, R, k, m_K, M_N, A_B$ , and  $Z_B$ , and then returns  $r_{n+1}, \xi_{n+1}$ , and  $\zeta_{n+1}$  as outputs. It is important to mention that in this Fortran 95 subroutine  $\xi_n, \zeta_n, \xi_{n+1}, \zeta_{n+1}, \{k_i\}_{i=1}^4$ , and  $\{m_j\}_{j=1}^4$  are declared as double complex data type.

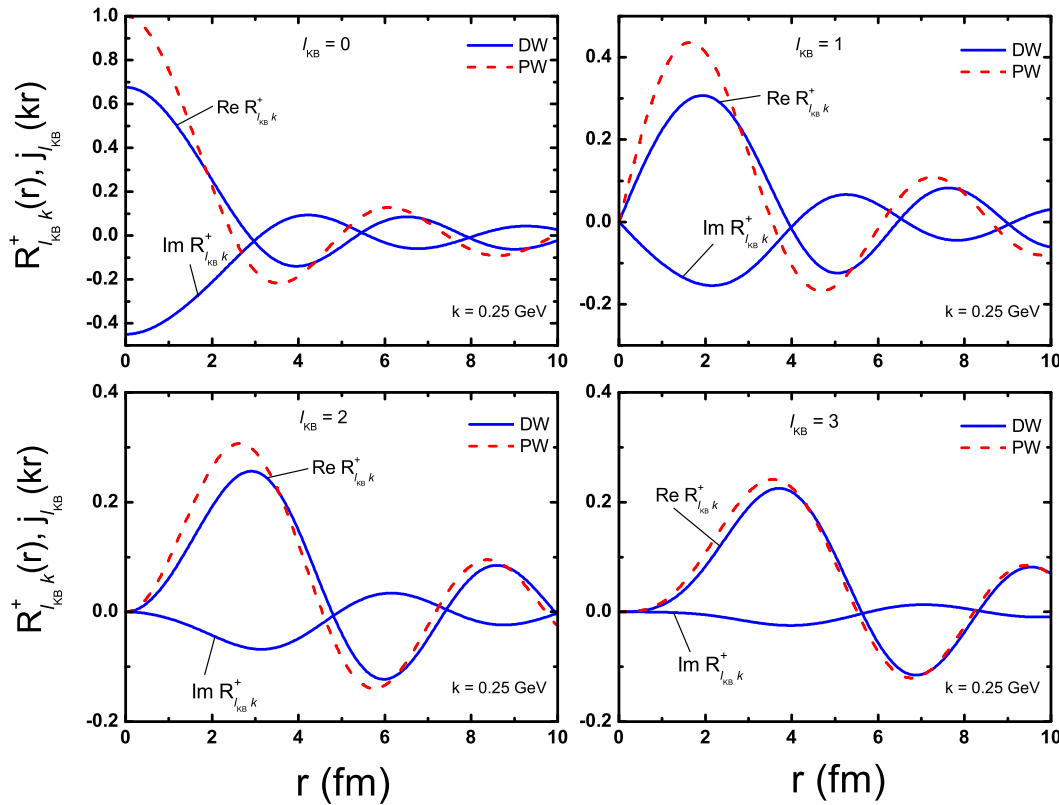


**Figure 4.15:** Comparison of the numerically generated radial parts  $R_{l_{KB},k}^+(r)$  of kaon distorted wave (DW) with the corresponding spherical Bessel function  $j_{l_{KB}}(kr)$  of expanded plane wave (PW) of kaon in terms of partial waves. Notice that the radial parts of DW are complex-valued solutions to account for kaon absorption in the optical potential formalism, whereas the spherical Bessel functions are real. The plots are generated for  $k = 0.25$  GeV, and for  $l_{KB} = 0, 1, 2$ , and  $3$  partial waves of K-B system, where B is the residual nucleus for the  $^{16}\text{O}$  target.

Since we are dealing with the initial value problem, for which the RK4 method is found to be very suitable, we can only start the iteration procedure by imposing the initial conditions  $\xi_0$  and  $\zeta_0$  at  $r_0$ . At this point, we draw our attention back to what we have discussed in subsection 4.6.1 on the boundary condition at  $r = 0$ . Thus by ensuring  $r_0$  to be small, we can fix  $\xi_0$  and  $\zeta_0$  at:

$$\xi_0 = \lim_{r \rightarrow r_0} \left( \text{Re } U_{l,k}^{(+)}, \text{Im } U_{l,k}^{(+)} \right) \approx \left( \frac{r_0 (kr_0)^l}{(2l+1)!!}, 0 \right), \quad (4.7.17)$$

$$\zeta_0 = \lim_{r \rightarrow r_0} \left( \text{Re } U_{l,k}'^{(+)}, \text{Im } U_{l,k}'^{(+)} \right) \approx \left( \frac{l+1}{(2l+1)!!} (kr_0)^l, 0 \right). \quad (4.7.18)$$

We focus on the final piece of the puzzle, which is the design of a subroutine that can perform the RK4 integrations on the radial KG-equation to solve for the distorted partial-waves of the ejected kaon in the  $A(\nu, \ell KY)B$  process. We are interested in a subroutine that returns three arrays

of dimension  $N_I$ ; one for the integration variable  $r$ :  $r_{ARR}$ , and the other two for the solutions of the integration  $\xi(r)$  and  $\zeta(r)$ :  $\xi_{ARR}$  and  $\zeta_{ARR}$ . We name this subroutine as ROPSOLV and is developed in such a way that it only takes  $l$ ,  $R$ ,  $N_I$ ,  $k$ ,  $m_K$ ,  $M_N$ ,  $A_B$ , and  $Z_B$  as input variables to be able to numerically solve the radial KG-equation in the range of  $r_0 \leq r \leq R$  at each interval of  $r_n = r_0 + nh$ , where  $n = 1, 2, 3, \dots, N_I - 1$ . This is done by iteratively

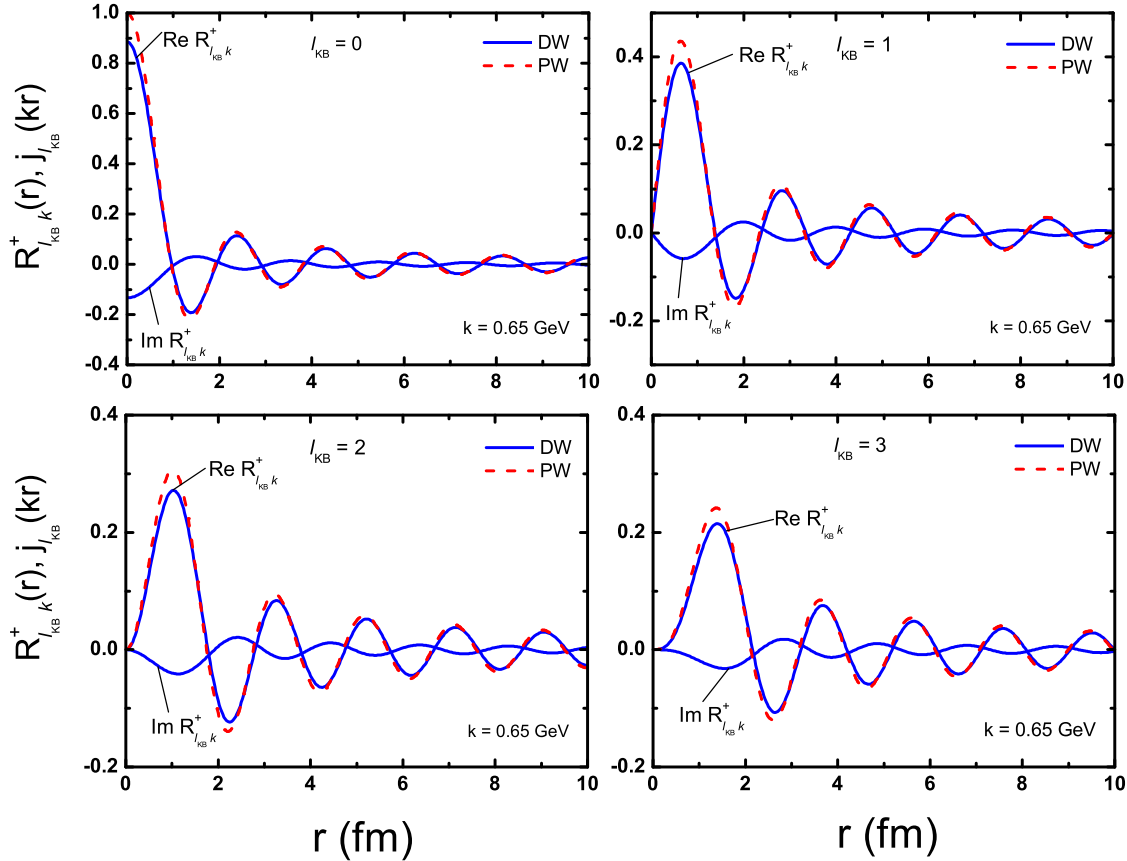


**Figure 4.16:** Comparison of radial partial waves of kaon distorted wave (DW) with the corresponding spherical Bessel function the plane wave (PW) of a free kaon. The plots are generated for  $k = 0.65$  GeV, and  $l_{KB} = 0, 1, 2$ , and 3 partial waves of K-B system, where B is the residual nucleus for the  $^{16}\text{O}$  target in the  $A(\nu, \ell KY)B$  process.

calling the ROPRK4 subroutine inside ROPSOLV. In a later stage of execution after  $\xi_{N_I-1}$  and  $\zeta_{N_I-1}$  are successfully solved, the subroutine must determine the asymptotic solution which is defined in Eq. (4.6.16) such that the generalized phase shift  $\gamma_l$  (Eq. (4.6.28)), and henceforth the normalization factor  $\mathcal{N}_{l,k}$  (Eq. (4.6.31)) can be obtained at the matching radius  $r = R$ . In so doing, we call external subroutines: BESJK<sup>2</sup> and DBESJL<sup>3</sup>, to determine  $j_l(kr)$ ,  $n_l(kr)$ ,  $j'_l(kr)$ , and  $n'_l(kr)$  at the matching point. Finally, before ROPSOLV returns the solutions it must multiply the old arrays  $\xi_{ARR}$  and  $\zeta_{ARR}$  by the normalization factor  $\mathcal{N}_{l,k}$  in order to ensure the generated solutions are physically acceptable. Fig. 4.10 displays the flow diagram for the ROPSOLV subroutine to generate the radial partial-wave of kaon by numerically integrating, with the RK4 method, the radial KG-equation containing the kaon FSI effects that comes into the picture via the complex functions  $g(r)$  and  $f(r)$  of Eqs. (4.6.4) and (4.6.5).

<sup>2</sup>This subroutine is our modified version of the original function subprogram SPHBES published in Ref. [110]. It generates the spherical Bessel  $j_l(kr)$  and Neuman  $n_l(kr)$  functions based on the formulae given in Ref. [111].

<sup>3</sup>In this subroutine we call BESJL to calculate the first-derivatives  $j'_l(kr)$  and  $n'_l(kr)$  by using the central-difference formula.

In Figs. 4.11 and 4.12 we illustrate the behavior of the generalized phase shift  $\gamma_l$  as a function of the matching radius  $R$  for the case of  $^{16}\text{O}$  target. The first figure displays curves for  $l = 0, 1, 2$  partial waves by fixing the relative momentum of kaon; whereas the second figure contains curves of  $\tan \gamma_l$  for  $l = 2$  partial wave but three different values of the kaon momentum. Each of  $\tan \gamma_l$  has the real part, which is related the nuclear phase shift  $\delta_l$ , as well as the imaginary part, which is related the absorption factor  $\eta_l$ . The purpose of these plots is to examine the region where we can safely fix the matching radius and such proper selection is based on the fact that  $\gamma_l$  depends only on the relative momentum  $k$  of the kaon but not the matching radius. In the region  $R < 6$  fm both figures clearly show the dependence of  $\tan \gamma_l$  on  $R$ , whereas in the region  $R > 6$  fm it becomes constant. Noting that  $r = 6$  fm is a typical nuclear size, any choice of the matching radius in the exterior region which is not too far from  $r = 6$  fm would be more appropriate and for this particular problem we fix  $R$  at 10 fm.

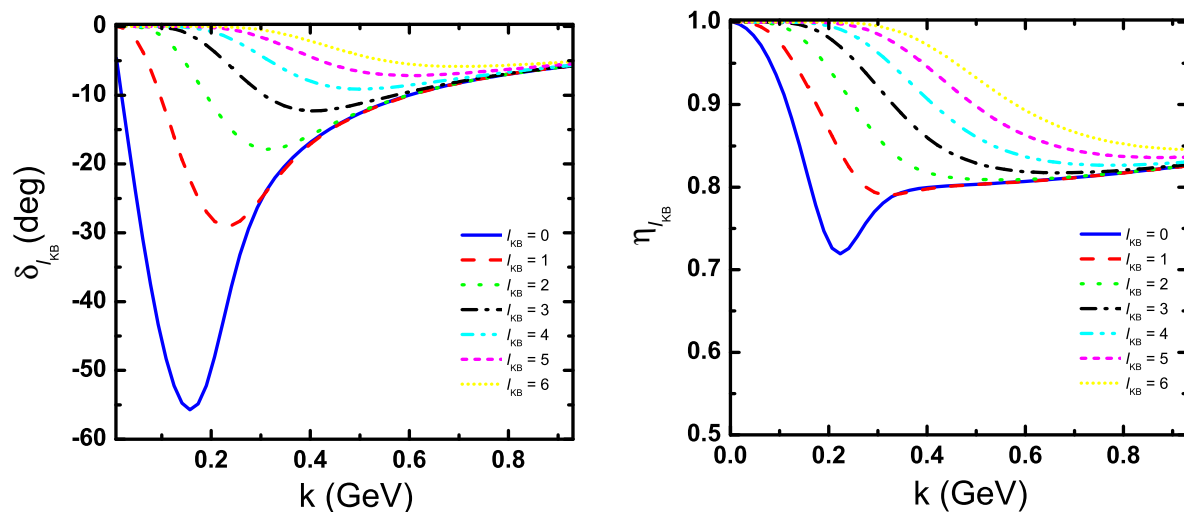


**Figure 4.17:** Nuclear phase shifts (left panel) and absorption coefficients (right panel), for the first seven partial waves, as a function of the relative momentum of kaon. They are obtained by comparing the numerical solutions of the radial KG-equation determined in the interior region of residual nucleus with the asymptotic waves at the matching radius, beyond which the kaon optical potential is considered to have a vanishing contribution and we have fixed that radius at  $R = 10$  fm.

Distorted partial waves of the kaon as functions of the radial coordinate, at the relative momentum  $k = 0.65$  GeV of kaon, are shown in Fig. 4.14. Here we are considering the FSI of kaon with the residual nucleus which resulted from the exclusive  $A(\nu, \ell KY)B$  reaction on  $^{16}\text{O}$  target. These radial waves are normalized using outgoing boundary conditions. In addition, Fig. 4.13 illustrates the radial parts of the distorted kaon wave functions with outgoing boundary conditions. The first four partial waves are plotted for various relative momenta of the final state kaon to help us examine their energy-dependent behavior. Again here  $^{16}\text{O}$  is what we consider as a target for the  $A(\nu, \ell KY)B$  process. On the other hand, in Figs. 4.15 and 4.16 we compare the partial waves from our calculation with the corresponding spherical Bessel functions, which are the radial parts in the partial wave expansion of the kaon plane wave. The real part  $\text{Re } R_{l,k}^{(+)}(r)$  is what we compare with  $j_l(kr)$ , since the imaginary part characterizes only the distorted radial wave. Clearly the effect of the kaon FSI is more visible at low energy. Finally, Fig. 4.17 shows the kaon relative momentum dependence of the nuclear phase shifts  $\delta_l$  and the absorption factors  $\eta_l$  computed at the matching radius.

## Chapter 5

# RDWIA Model for the Quasifree $A(\nu, \ell KY)B$ Process

### 5.1 Introduction

In this chapter we present the relativistic formulation of the quasifree  $A(\nu, \ell KY)B$  reaction processes in the RDWIA framework. In chapter 3, we developed the RPWIA formalism within which the underlying production process  $\nu N \rightarrow \ell KY$  has successfully been embedded in the nuclear medium. The RPWIA model of the  $A(\nu, \ell KY)B$  reactions is constructed in order to avoid the numerical complexity of a full RDWIA treatment, and yet focus on essentials such as a free space weak hadronic current operator and bound state wave function of a nucleon. The RDWIA model can be considered as the extension of the RPWIA model by replacing the plane waves of hadrons in the final channel of the exclusive nuclear reaction with the distorted waves that account for the FSI effects.

In chapter 4, the details of the FSIs have been presented in a manner that would make possible the incorporation of their effects in the calculation of the reaction cross sections. As it has been clearly stated, we have chosen the RDWIA-I model, whereby one assumes that the kaon(hyperon) FSI is turned on(off). Thus, in this particular case the kaon distortion was accounted for via the relativistic optical potential of the kaon-nucleus interaction. Consequently, the kaon optical potential is determined from the phase shift analysis of the underlying  $K^+N$  scattering process. The nuclear structure information is accounted for by using the nuclear density obtained from the relativistic shell model.

The other important ingredients of the RDWIA formalism are those essentials introduced in the RPWIA treatment of the reaction: (i) the wave function of the bound state nucleon through which we take into account the nuclear structure effects and (ii) the hadronic weak current of the neutrino-induced associated production on free nucleon. Following the relativistic description given in section 2.3 of chapter 2, the RMF approximation to the nonlinear Walecka model[55] has been used to generate the bound state wave functions. Finally, in section 2.4 we gave a brief overview on the theoretical description of the elementary process based on our previous work[35].

This chapter is organized as follows: In section 5.2 we discuss the relativistic kinematics relevant for the distorted wave analysis of the quasifree  $A(\nu, \ell KY)B$  processes. Section 5.3 consists of a fully relativistic formalism the reaction process within the RDWIA framework. In section 5.4 we evaluate the exclusive reaction matrix element within the distorted wave analysis.

### 5.2 Relativistic Kinematics of the RDWIA Model

In chapter 3, the laboratory frame kinematic description of the RPWIA model was given in detail but for the RDWIA model we cannot apply those kinematics directly. Instead we proceed from what is known in the previous calculation. The reason being that the distorted waves, through which the FSI effects are incorporated, are usually calculated in the center-of-mass frames. For



example, this is the case in the study of exclusive  $(p, 2p)$  reactions[112, 113], whereby an incident proton knocks out another bound proton from a specific orbital of a target nucleus resulting in two protons and residual nucleus in the final state. In this study we also use a similar prescription, that is, the kinematic quantities in the center-of-mass systems can be obtained from the Lorentz transformations of the corresponding laboratory frame kinematic quantities calculated in chapter 3. This allows us to calculate a physically sound differential cross sections of the quasifree  $A(\nu, \ell\text{KY})B$  processes.

To begin with, if we look at the incident neutrino, its four-momentum  $k_A^\mu = (E_{k_A}, \mathbf{k}_A)$  in the  $\nu$ -A center-of-mass system is obtained from the corresponding laboratory frame four-momentum  $k^\mu = (E_k, \mathbf{k})$ . That is

$$\begin{pmatrix} E_{k_A} \\ \mathbf{k}_A \end{pmatrix} = \begin{pmatrix} \gamma_{\nu A}(E_k - \boldsymbol{\beta}_{\nu A} \cdot \mathbf{k}) \\ \gamma_{\nu A}(\mathbf{k}_\parallel - E_k \boldsymbol{\beta}_{\nu A}) + \mathbf{k}_\perp \end{pmatrix}, \quad (5.2.1)$$

where

$$\boldsymbol{\beta}_{\nu A} = \frac{\mathbf{k}}{E_k + M_A}, \quad \gamma_{\nu A} = \frac{1}{\sqrt{1 - \beta_{\nu A}^2}}, \quad (5.2.2)$$

and

$$\mathbf{k}_\parallel = \frac{\boldsymbol{\beta}_{\nu A} \cdot \mathbf{k}}{\beta_{\nu A}^2} \boldsymbol{\beta}_{\nu A}, \quad \mathbf{k}_\perp = \mathbf{k} - \mathbf{k}_\parallel. \quad (5.2.3)$$

The RDWIA model is constructed in the center-of-momentum (c.m.) frame, where the total three-momentum of the collision is fixed at zero. Thus, except for the wave functions of the participating particles, the rest of the kinematic and dynamic information of the reaction are specified using the c.m. frame four-momenta. These quantities can now be calculated via the Lorentz transformation of their respective quantities in the rest frame of the target nucleus using Eq. (5.2.2). Thus, the four-momenta in the c.m. frame are labeled as  $k_A^\mu = (E_{k_A}, \mathbf{k}_A)$  for the neutrino,  $k_A'^\mu = (E_{k_A'}, \mathbf{k}_A')$  for the final lepton,  $P_A^\mu = (E_A, \mathbf{P}_A)$  for the target nucleus,  $p_{1,A}'^\mu = (E_{p_{1,A}'}, \mathbf{p}_{1,A}')$  for the final state kaon,  $p_{2,A}'^\mu = (E_{p_{2,A}'}, \mathbf{p}_{2,A}')$  for the final state hyperon, and  $P_A'^\mu = (E_A', \mathbf{P}_A')$  for the residual nucleus. The same way the c.m. frame four-momentum of the incident neutrino is calculated in Eq. (5.2.1) the rest of these quantities also can be determined.

Now we proceed to calculate the relative three-momenta of the final lepton. This can be done by using the Lorentz transformation of the laboratory frame four-momentum  $k'^\mu = (E_{k'}, \mathbf{k}')$  of the final lepton to the corresponding four-momentum  $k_B'^\mu = (E_{k_B'}, \mathbf{k}_B')$  in the  $\ell$ -B center-of-mass system:

$$\begin{pmatrix} E_{k_B'} \\ \mathbf{k}_B' \end{pmatrix} = \begin{pmatrix} \gamma_{\ell B}(E_{k'} - \boldsymbol{\beta}_{\ell B} \cdot \mathbf{k}') \\ \gamma_{\ell B}(\mathbf{k}'_\parallel - E_{k'} \boldsymbol{\beta}_{\ell B}) + \mathbf{k}'_\perp \end{pmatrix}, \quad (5.2.4)$$

where

$$\boldsymbol{\beta}_{\ell B} = \frac{\mathbf{k}' + \mathbf{P}'}{E_{k'} + E'}, \quad \gamma_{\ell B} = \frac{1}{\sqrt{1 - \beta_{\ell B}^2}}, \quad (5.2.5)$$

and

$$\mathbf{k}'_\parallel = \frac{\boldsymbol{\beta}_{\ell B} \cdot \mathbf{k}'}{\beta_{\ell B}^2} \boldsymbol{\beta}_{\ell B}, \quad \mathbf{k}'_\perp = \mathbf{k}' - \mathbf{k}'_\parallel. \quad (5.2.6)$$

Similarly, we must be able to calculate the relative three-momenta  $\mathbf{p}'_{1,B}$  and  $\mathbf{p}'_{2,B}$  of the final state kaon and hyperon in their respective K-B and Y-B center-of-mass systems. This can be attained by employing the Lorentz transformations of the laboratory frame four-momentum  $p_1'^\mu = (E_{p_1'}, \mathbf{p}_1')$  [ $p_2'^\mu = (E_{p_2'}, \mathbf{p}_2')$ ] of kaon [hyperon] to the corresponding K-B [Y-B] center-of-mass frame four-momentum  $p_{1,B}'^\mu = (E_{p_{1,B}'}, \mathbf{p}_{1,B}')$  [ $p_{2,B}'^\mu = (E_{p_{2,B}'}, \mathbf{p}_{2,B}')$ ]:

$$\begin{pmatrix} E_{p'_{1,B}} \\ \mathbf{p}'_{1,B} \end{pmatrix} = \begin{pmatrix} \gamma_{\text{KB}} \left( E_{p'_1} - \boldsymbol{\beta}_{\text{KB}} \cdot \mathbf{p}'_1 \right) \\ \gamma_{\text{KB}} \left( (\mathbf{p}'_1)_{\parallel} - E_{p'_1} \boldsymbol{\beta}_{\text{KB}} \right) + (\mathbf{p}'_1)_{\perp} \end{pmatrix}, \quad (5.2.7)$$

$$\begin{pmatrix} E_{p'_{2,B}} \\ \mathbf{p}'_{2,B} \end{pmatrix} = \begin{pmatrix} \gamma_{\text{YB}} \left( E_{p'_2} - \boldsymbol{\beta}_{\text{YB}} \cdot \mathbf{p}'_2 \right) \\ \gamma_{\text{YB}} \left( (\mathbf{p}'_2)_{\parallel} - E_{p'_2} \boldsymbol{\beta}_{\text{YB}} \right) + (\mathbf{p}'_2)_{\perp} \end{pmatrix}, \quad (5.2.8)$$

where

$$\boldsymbol{\beta}_{\text{KB}} = \frac{\mathbf{p}'_1 + \mathbf{P}'}{E_{p'_1} + E'}, \quad \gamma_{\text{KB}} = \frac{1}{\sqrt{1 - \beta_{\text{KB}}^2}}, \quad (5.2.9)$$

$$\boldsymbol{\beta}_{\text{YB}} = \frac{\mathbf{p}'_2 + \mathbf{P}'}{E_{p'_2} + E'}, \quad \gamma_{\text{YB}} = \frac{1}{\sqrt{1 - \beta_{\text{YB}}^2}}, \quad (5.2.10)$$

and

$$(\mathbf{p}'_1)_{\parallel} = \frac{\boldsymbol{\beta}_{\text{KB}} \cdot \mathbf{p}'_1}{\beta_{\text{KB}}^2} \boldsymbol{\beta}_{\text{KB}}, \quad (\mathbf{p}'_1)_{\perp} = \mathbf{p}'_1 - (\mathbf{p}'_1)_{\parallel}, \quad (5.2.11)$$

$$(\mathbf{p}'_2)_{\parallel} = \frac{\boldsymbol{\beta}_{\text{YB}} \cdot \mathbf{p}'_2}{\beta_{\text{YB}}^2} \boldsymbol{\beta}_{\text{YB}}, \quad (\mathbf{p}'_2)_{\perp} = \mathbf{p}'_2 - (\mathbf{p}'_2)_{\parallel}. \quad (5.2.12)$$

Note that these calculations of relative three-momenta after collision take into account the recoil of the residual nucleus.

### 5.3 The Differential Cross Section of the Quasifree $A(\nu, \ell\text{KY})B$ reactions

As it was the case for the RPWIA model, in this formalism we follow the prescription of Bjorken and Drell[68] to construct the differential cross section of the reaction process. The exclusive associated production process consists of an incident neutrino and nucleus target in the initial state; and outgoing lepton, kaon, hyperon, and recoiling residual nucleus in the final state. As a result, the standard form of the differential cross section must be suited for this particular problem and it can be written in the c.m. frame as

$$\begin{aligned} d\sigma_{\text{c.m.}} &= \frac{1}{|\mathbf{v}_{1,A} - \mathbf{v}_{2,A}|} (2\pi)^4 \delta^4 \left( k_A + P_A - k'_A - p'_{1,A} - p'_{2,A} - P'_A \right) \\ &\times |\mathcal{M}_{fi}|^2 \frac{1}{2E_{p'_{1,A}}} \frac{d^3\mathbf{k}'_A}{(2\pi)^3} \frac{d^3\mathbf{p}'_{1,A}}{(2\pi)^3} \frac{d^3\mathbf{p}'_{2,A}}{(2\pi)^3} \frac{d^3\mathbf{P}'_A}{(2\pi)^3}, \end{aligned} \quad (5.3.1)$$

where the c.m. frame relative velocity of the neutrino can be written in the invariant form:

$$\begin{aligned} |\mathbf{v}_{1,A} - \mathbf{v}_{2,A}| &= \frac{4 \left[ (k_A \cdot P_A)^2 - m_\nu^2 M_A^2 \right]^{1/2}}{2E_{k_A} 2E_A} \\ &= \frac{\sqrt{s}}{E_A}, \end{aligned} \quad (5.3.2)$$

which is the case as long as the incident neutrino is considered massless. The total c.m. energy is denoted by  $\sqrt{s} = E_A + E_{k_A}$ . Thus Eq. (5.3.1) now becomes

$$\begin{aligned} d\sigma_{\text{c.m.}} &= \frac{1}{2(2\pi)^8} \frac{E_A}{E_{p'_{1,A}} \sqrt{s}} \delta^4 \left( k_A + P_A - k'_A - p'_{1,A} - p'_{2,A} - P'_A \right) \\ &\times |\mathcal{M}_{fi}|^2 d^3\mathbf{k}'_A d^3\mathbf{p}'_{1,A} d^3\mathbf{p}'_{2,A} d^3\mathbf{P}'_A. \end{aligned} \quad (5.3.3)$$

Experimentally, the recoiling residual nucleus usually goes undetected as stated before and hence we must integrate over its three-momentum  $\mathbf{P}'_A$ . This in turn ensures the conservation of three-momentum of the reaction. Thus, we now have

$$\begin{aligned} d\sigma_{\text{c.m.}} &= \frac{1}{2(2\pi)^8} \frac{E_A}{E_{p'_{1,A}} \sqrt{s}} \delta(E_A + \omega_A - E_{p'_{1,A}} - E_{p'_{2,A}} - E'_A) \\ &\times |\mathcal{M}_{fi}|^2 d^3\mathbf{k}'_A d^3\mathbf{p}'_{1,A} d^3\mathbf{p}'_{2,A}, \end{aligned} \quad (5.3.4)$$

with

$$\mathbf{P}'_A = \mathbf{P}_A + \mathbf{q}_A - \mathbf{p}'_{1,A} - \mathbf{p}'_{2,A}, \quad (5.3.5)$$

where the c.m. energy and momentum transfers:  $\omega_A$  and  $\mathbf{q}_A$ , respectively, are defined as

$$\omega_A = E_{k_A} - E_{k'_A}, \quad \mathbf{q}_A = \mathbf{k}_A - \mathbf{k}'_A. \quad (5.3.6)$$

It is worth noting that in the c.m. frame the three-momenta must also obey the condition  $\mathbf{k}_A + \mathbf{P}_A = \mathbf{k}'_A + \mathbf{p}'_{1,A} + \mathbf{p}'_{2,A} + \mathbf{P}'_A = 0$ . In order to be able to numerically demonstrate the predictions of this theoretical model the differential cross section for the neutrino-induced exclusive associated production must be expressed in terms of the energies and solid angles in the c.m. frame. In doing so, we write the momentum-space volume elements using their spherical coordinates:

$$d^3\mathbf{k}'_A = (2\pi) |\mathbf{k}'_A| E_{k'_A} dE_{k'_A} d(\cos \theta_{\ell,A}), \quad (5.3.7)$$

$$d^3\mathbf{p}'_{1,A} = |\mathbf{p}'_{1,A}| E_{p'_{1,A}} dE_{p'_{1,A}} d\Omega_{p'_{1,A}}, \quad (5.3.8)$$

$$d^3\mathbf{p}'_{2,A} = |\mathbf{p}'_{2,A}| E_{p'_{2,A}} dE_{p'_{2,A}} d\Omega_{p'_{2,A}}. \quad (5.3.9)$$

Notice that, use has been made of the on-shell relations. Upon substituting Eqs. (5.3.7) - (5.3.9) into Eq. (5.3.4), we invoke the conservation of total energy of the reaction at production vertex by integrating over the undetected hyperon energy  $E_{p'_{2,A}}$ . Therefore, the five-fold unpolarized differential cross section in the c.m. frame can now be written as

$$\frac{d^5\sigma_{\text{c.m.}}}{dE_{k'_A} d(\cos \theta_{\ell,A}) dE_{p'_{1,A}} d\Omega_{p'_{1,A}} d\Omega_{p'_{2,A}}} = \frac{1}{2(2\pi)^7} \frac{E_A}{\sqrt{s}} \frac{E_{k'_A} E_{p'_{2,A}} |\mathbf{k}'_A| |\mathbf{p}'_{1,A}| |\mathbf{p}'_{2,A}|}{\left| 1 + \frac{E_{p'_{2,A}}}{E'_A} \left[ 1 - \frac{(\mathbf{p}'_{2,A} + \mathbf{P}'_A) \cdot \mathbf{p}'_{2,A}}{|\mathbf{p}'_{2,A}|^2} \right] \right|} \overline{\sum} |\mathcal{M}_{fi}|^2. \quad (5.3.10)$$

## 5.4 Evaluation of Matrix Element within RDWIA Model

The nuclear transition matrix element, which carries the dynamics the exclusive  $A(\nu, \ell\text{KY})B$  reaction, must now be evaluated within the RDWIA framework such that the FSI effects can be taken into account in a convenient manner. We start from the most general expression we gave in chapter 3, Eq. (3.2.1), but here it is specified using the c.m. frame kinematic quantities. The wave functions of the initial and final state particles are calculated as functions of their relative three-momenta. That is,

$$\text{Neutrino :} \quad \nu \longrightarrow \nu(\mathbf{k}_A, h), \quad (5.4.1)$$

$$\text{Final Lepton :} \quad \bar{U}_\ell \longrightarrow \bar{U}_\ell(\mathbf{k}'_B, h'), \quad (5.4.2)$$

$$\text{Bound Nucleon :} \quad \mathcal{U}_{E\kappa m} \longrightarrow \mathcal{U}_{E\kappa m}(\mathbf{x}), \quad (5.4.3)$$

$$\text{Kaon :} \quad [\Phi^{(-)}]^* \longrightarrow [\Phi^{(-)}(\mathbf{x}, \mathbf{p}'_{1,B})]^*, \quad (5.4.4)$$

$$\text{Hyperon :} \quad \bar{\Psi}_{i'_2, s'_2}^{(-)} \longrightarrow \bar{\Psi}_{i'_2, s'_2}^{(-)}(\mathbf{x}, \mathbf{p}'_{2,B}). \quad (5.4.5)$$

The leptonic current can now be defined as

$$\mathcal{L}_\mu = \bar{U}_\ell(\mathbf{k}'_B, h') \gamma_\mu (1 - \gamma_5) \nu(\mathbf{k}_A, h). \quad (5.4.6)$$

When one intends to consider the effect of the Coulomb interaction between the final lepton and the residual nucleus, the usual plane wave form of  $\bar{U}_\ell(\mathbf{k}'_B, h')$  becomes the distorted spinor field. Nevertheless, as we clearly stated in chapter 4, in the incident energy range of interest the final lepton can be described by plane wave reasonably well.

The single-particle weak nuclear transition current  $\mathcal{H}^\mu$  is also defined as

$$\mathcal{H}^\mu = \int d^3\mathbf{x} e^{i\mathbf{q}_A \cdot \mathbf{x}} \bar{\Psi}_{\hat{\mathbf{i}}'_2, s'_2}^{(-)}(\mathbf{x}, \mathbf{p}'_{2,B}) [\Phi^{(-)}(\mathbf{x}, \mathbf{p}'_{1,B})]^* J^\mu(q_A) \mathcal{U}_{E\kappa m}(\mathbf{x}). \quad (5.4.7)$$

Since we restrict this study to the RDWIA-I case, we now expand the weak nuclear transition current in such a way that the kaon FSI effects can be incorporated quite conveniently. In doing so, we resort to decomposing the kaon wave function in terms of partial waves:

$$\Phi^{(-)}(\mathbf{x}, \mathbf{p}'_{1,A}) = 4\pi \sum_{l_3 m_3} i^{l_3} (-1)^{l_3} R_{l_3, p'_{1,B}}^{(-)}(x) Y_{l_3 m_3}(\hat{\mathbf{x}}) Y_{l_3 m_3}^*(\hat{\mathbf{p}}'_{1,B}), \quad (5.4.8)$$

with  $R_{l_3, p'_{1,B}}^{(-)}(x) = (-1)^{l_3} [R_{l_3, p'_{1,B}}^{(+)}(x)]^*$ . On the other hand,  $\bar{\Psi}_{\hat{\mathbf{i}}'_2, s'_2}^{(-)}(\mathbf{x}, \mathbf{p}'_{2,B})$  is replaced by the standard plane wave function for free state hyperon.

$$\bar{\Psi}_{\hat{\mathbf{i}}'_2, s'_2}^{(-)}(\mathbf{x}, \mathbf{p}'_{2,B}) = e^{-i\mathbf{p}'_{2,B} \cdot \mathbf{x}} \bar{U}_Y(\mathbf{p}'_{2,B}, \hat{\mathbf{i}}'_2, s'_2), \quad (5.4.9)$$

with the Dirac spinor field defined as

$$U_Y(\mathbf{p}'_{2,B}, \hat{\mathbf{i}}'_2, s'_2) = C_Y \begin{pmatrix} \phi^{s'_2}(\hat{\mathbf{i}}'_2) \\ \frac{\boldsymbol{\sigma} \cdot \mathbf{p}'_{2,B}}{E_{p'_{2,B}} + M_Y} \phi^{s'_2}(\hat{\mathbf{i}}'_2) \end{pmatrix}, \quad (5.4.10)$$

which is normalized non-covariantly:

$$C_Y = \sqrt{\frac{E_{p'_{2,B}} + M_Y}{2E_{p'_{2,B}}}}. \quad (5.4.11)$$

Thus, the explicit expression of  $\mathcal{H}^\mu$  is given as

$$\begin{aligned} \mathcal{H}^\mu &= \int d^3\mathbf{x} \left[ 4\pi \sum_{l_1 m_1} i^{l_1} j_{l_1}(p'_A x) Y_{l_1 m_1}(\hat{\mathbf{x}}) Y_{l_1 m_1}^*(\hat{\mathbf{p}}'_A) \right] \\ &\times \left[ 4\pi \sum_{l_3 m_3} i^{l_3} (-1)^{l_3} R_{l_3, p'_{1,B}}^{(+)}(x) Y_{l_3 m_3}(\hat{\mathbf{x}}) Y_{l_3 m_3}^*(\hat{\mathbf{p}}'_{1,B}) \right] \mathcal{N}^\mu, \end{aligned} \quad (5.4.12)$$

where

$$\mathcal{N}^\mu = \bar{U}_Y(\mathbf{p}'_{2,B}, \hat{\mathbf{i}}'_2, s'_2) \hat{J}^\mu(q_A) \mathcal{U}_{E\kappa m}(\mathbf{x}), \quad (5.4.13)$$

and the expression in the first square bracket is the partial wave expansion of the plane wave  $\exp(i\mathbf{p}'_A \cdot \mathbf{x})$  with  $\mathbf{p}'_A = \mathbf{q}_A - \mathbf{p}'_{2,B}$ .

The overview of the general representation of the hadronic weak current operator  $J^\mu(q_A)$  was given in chapter 2 and its most general representation is written in Eq. (2.4.10). In this distorted wave formalism, however, it must be rewritten in a block matrix representation, that is,

$$\hat{J}^\nu = \begin{pmatrix} \hat{J}_{11}^\nu & \hat{J}_{12}^\nu \\ \hat{J}_{21}^\nu & \hat{J}_{22}^\nu \end{pmatrix}, \quad (5.4.14)$$

where  $\hat{J}_{ij}^\mu$ ,  $i, j = 1, 2$  are  $2 \times 2$  block matrices. In Appendix B, we have given, by making use of the block matrix representation of the bilinear covariant basis elements, the thorough derivation of individual block matrices starting from the original expression of the weak hadronic current operator in chapter 2, Eq. (2.4.10). Thus, we take the final expressions of the block matrices written in compact form as:

$$\hat{J}_{11}^\mu(q) = \tilde{A}_{11}^\mu I_2 + \tilde{B}_{11}^\mu q^i \sigma^i + \tilde{C}_{11} \delta_i^\mu \sigma^i + \tilde{D}_{11} \delta_i^\mu \epsilon_{ijk} q^j \sigma^k, \quad (5.4.15)$$

where

$$\tilde{A}_{11}^\mu = \tilde{A}^\mu + \tilde{C}_1 \delta_0^\mu + \tilde{C}^\mu q_0 + \tilde{D}_5 q^\mu, \quad (5.4.16)$$

$$\tilde{B}_{11}^\mu = \tilde{D}^\mu + \tilde{D}_6 \delta_0^\mu, \quad (5.4.17)$$

$$\tilde{C}_{11} = -\tilde{D}_1 + \tilde{D}_6 q_0, \quad (5.4.18)$$

$$\tilde{D}_{11} = -i\tilde{D}_5. \quad (5.4.19)$$

$$\hat{J}_{12}^\mu(q) = \tilde{A}_{12}^\mu I_2 + \tilde{B}_{12}^\mu q^i \sigma^i + \tilde{C}_{12} \delta_i^\mu \sigma^i + \tilde{D}_{12} \delta_i^\mu \epsilon_{ijk} q^j \sigma^k, \quad (5.4.20)$$

where

$$\tilde{A}_{12}^\mu = \tilde{B}^\mu - \tilde{D}_1 \delta_0^\mu - \tilde{D}^\mu q_0 + \tilde{D}_6 q^\mu, \quad (5.4.21)$$

$$\tilde{B}_{12}^\mu = -\tilde{C}^\mu + \tilde{D}_5 \delta_0^\mu, \quad (5.4.22)$$

$$\tilde{C}_{12} = \tilde{C}_1 + \tilde{D}_5 q_0, \quad (5.4.23)$$

$$\tilde{D}_{12} = -i\tilde{D}_6. \quad (5.4.24)$$

$$\hat{J}_{21}^\mu(q) = \tilde{A}_{21}^\mu I_2 + \tilde{B}_{21}^\mu q^i \sigma^i + \tilde{C}_{21} \delta_i^\mu \sigma^i + \tilde{D}_{21} \delta_i^\mu \epsilon_{ijk} q^j \sigma^k, \quad (5.4.25)$$

where

$$\tilde{A}_{21}^\mu = \tilde{B}^\mu + \tilde{D}_1 \delta_0^\mu + \tilde{D}^\mu q_0 + \tilde{D}_6 q^\mu, \quad (5.4.26)$$

$$\tilde{B}_{21}^\mu = \tilde{C}^\mu + \tilde{D}_5 \delta_0^\mu, \quad (5.4.27)$$

$$\tilde{C}_{21} = -\tilde{C}_1 + \tilde{D}_5 q_0, \quad (5.4.28)$$

$$\tilde{D}_{21} = -i\tilde{D}_6. \quad (5.4.29)$$

$$\hat{J}_{22}^\mu(q) = \tilde{A}_{22}^\mu I_2 + \tilde{B}_{22}^\mu q^i \sigma^i + \tilde{C}_{22} \delta_i^\mu \sigma^i + \tilde{D}_{22} \delta_i^\mu \epsilon_{ijk} q^j \sigma^k, \quad (5.4.30)$$

where

$$\tilde{A}_{22}^\mu = \tilde{A}^\mu - \tilde{C}_1 \delta_0^\mu - \tilde{C}^\mu q_0 + \tilde{D}_5 q^\mu, \quad (5.4.31)$$

$$\tilde{B}_{22}^\mu = -\tilde{D}^\mu + \tilde{D}_6 \delta_0^\mu, \quad (5.4.32)$$

$$\tilde{C}_{22} = \tilde{D}_1 + \tilde{D}_6 q_0, \quad (5.4.33)$$

$$\tilde{D}_{22} = -i\tilde{D}_5. \quad (5.4.34)$$

Here the common basis are  $I_2$ ,  $\mathbf{q} \cdot \boldsymbol{\sigma}$ ,  $\delta_i^\mu \sigma^i$ , and  $\delta_i^\mu [\mathbf{q} \times \boldsymbol{\sigma}]_i$ . The Dirac spinor  $\bar{U}_Y$  for the outgoing hyperon must be written as

$$\bar{U}_Y = C_Y \left( \begin{array}{cc} \phi_{s'_2}^\dagger(\hat{\mathbf{i}}'_2) & -\phi_{s'_2}^\dagger(\hat{\mathbf{i}}'_2) \frac{\boldsymbol{\sigma} \cdot \mathbf{p}'_{2,B}}{E_{p'_{2,B}} + M_Y} \end{array} \right). \quad (5.4.35)$$

On the other hand, the bound state wave function of the in-medium nucleon is explicitly defined in chapter 2, Eq. (2.3.31). That is,

$$\mathcal{U}_{E\kappa m}(\mathbf{x}) = \frac{1}{x} \left( \begin{array}{c} g_{E\kappa} \mathcal{Y}_{\kappa m}(\hat{\mathbf{x}}) \\ if_{E\kappa} \mathcal{Y}_{-\kappa m}(\hat{\mathbf{x}}) \end{array} \right), \quad (5.4.36)$$

where  $\mathcal{Y}_{\kappa m}(\hat{\mathbf{x}})$  is the usual spin-angular wave function defined as

$$\mathcal{Y}_{\kappa m}(\hat{\mathbf{x}}) = \sum_{s_z = \pm \frac{1}{2}} \left\langle l_2, \frac{1}{2}, m_2, s_z \left| j, m \right. \right\rangle Y_{l_2, m_2}(\hat{\mathbf{x}}) \chi_{s_z}. \quad (5.4.37)$$

with  $m_2 = m - s_z$ ,  $\langle l, \frac{1}{2}, m - s_z, s_z | j, m \rangle$  are the Clebsch-Gordon coefficients, and  $\chi_{s_z}$  is the usual Pauli spinor. Hence Eq. (5.4.13) becomes

$$\mathcal{N}^\mu = C_Y \begin{pmatrix} \phi_{s'_2}^\dagger(\hat{\mathbf{i}}'_2) & -\phi_{s'_2}^\dagger(\hat{\mathbf{i}}'_2) \frac{\boldsymbol{\sigma} \cdot \mathbf{p}'_{2,B}}{E_{p'_{2,B}} + M_Y} \end{pmatrix} \begin{pmatrix} \hat{J}_{11}^\mu & \hat{J}_{12}^\mu \\ \hat{J}_{21}^\mu & \hat{J}_{22}^\mu \end{pmatrix} \begin{pmatrix} \frac{g_{E\kappa}}{x} \mathcal{Y}_{\kappa m}(\hat{\mathbf{x}}) \\ i \frac{f_{E\kappa}}{x} \mathcal{Y}_{-\kappa m}(\hat{\mathbf{x}}) \end{pmatrix}, \quad (5.4.38)$$

$$= \mathcal{N}_1^\mu + \mathcal{N}_2^\mu + \mathcal{N}_3^\mu + \mathcal{N}_4^\mu, \quad (5.4.39)$$

where

$$\mathcal{N}_1^\mu = C_Y \phi_{s'_2}^\dagger(\hat{\mathbf{i}}'_2) \hat{J}_{11}^\mu(q_A) \frac{g_{E\kappa}(x)}{x} \mathcal{Y}_{\kappa m}(\hat{\mathbf{x}}), \quad (5.4.40)$$

$$\mathcal{N}_2^\mu = i C_Y \phi_{s'_2}^\dagger(\hat{\mathbf{i}}'_2) \hat{J}_{12}^\mu(q_A) \frac{f_{E\kappa}(x)}{x} \mathcal{Y}_{-\kappa m}(\hat{\mathbf{x}}), \quad (5.4.41)$$

$$\mathcal{N}_3^\mu = -C_Y \phi_{s'_2}^\dagger(\hat{\mathbf{i}}'_2) \frac{\boldsymbol{\sigma} \cdot \mathbf{p}'_{2,B}}{E_{p'_{2,B}} + M_Y} \hat{J}_{21}^\mu(q_A) \frac{g_{E\kappa}(x)}{x} \mathcal{Y}_{\kappa m}(\hat{\mathbf{x}}), \quad (5.4.42)$$

$$\mathcal{N}_4^\mu = -i C_Y \phi_{s'_2}^\dagger(\hat{\mathbf{i}}'_2) \frac{\boldsymbol{\sigma} \cdot \mathbf{p}'_{2,B}}{E_{p'_{2,B}} + M_Y} \hat{J}_{22}^\mu(q_A) \frac{f_{E\kappa}(x)}{x} \mathcal{Y}_{-\kappa m}(\hat{\mathbf{x}}). \quad (5.4.43)$$

We now substitute these explicit forms of the four terms  $\mathcal{N}^\mu$  into Eq. (5.4.12) and express the weak nuclear current  $\mathcal{H}^\mu$  as

$$\mathcal{H}^\mu = \mathcal{H}_1^\mu + \mathcal{H}_2^\mu, \quad (5.4.44)$$

where

$$\begin{aligned} \mathcal{H}_1^\mu &= C_Y (4\pi)^2 \sum_{l_1 m_1} \sum_{l_3 m_3} (-1)^{l_3} i^{l_1 + l_3} Y_{l_1 m_1}^*(\hat{\mathbf{p}}'_A) Y_{l_3 m_3}(\hat{\mathbf{p}}'_{1,B}) \sum_{s_z = \pm \frac{1}{2}} \left\langle l_2, \frac{1}{2}, m_2, s_z \left| j, m \right. \right\rangle \\ &\times (-1)^{m_3} Y_{m_1 - m_3}^{l_1 \ l_3 \ l_2} \mathcal{G}_E^{\kappa \ l_1 \ l_3} \left[ \phi_{s'_2}^\dagger(\hat{\mathbf{i}}'_2) \left\{ \hat{J}_{11}^\mu - \frac{\boldsymbol{\sigma} \cdot \mathbf{p}'_{2,B}}{E_{p'_{2,B}} + M_Y} \hat{J}_{21}^\mu \right\} \chi_{s_z} \right], \end{aligned} \quad (5.4.45)$$

$$\begin{aligned} \mathcal{H}_2^\mu &= i C_Y (4\pi)^2 \sum_{l_1 m_1} \sum_{l_3 m_3} (-1)^{l_3} i^{l_1 + l_3} Y_{l_1 m_1}^*(\hat{\mathbf{p}}'_A) Y_{l_3 m_3}(\hat{\mathbf{p}}'_{1,B}) \sum_{s_z = \pm \frac{1}{2}} \left\langle l'_2, \frac{1}{2}, m_2, s_z \left| j, m \right. \right\rangle \\ &\times (-1)^{m_3} Y_{m_1 - m_3}^{l_1 \ l_3 \ l'_2} \mathcal{F}_E^{\kappa \ l_1 \ l_3} \left[ \phi_{s'_2}^\dagger(\hat{\mathbf{i}}'_2) \left\{ \hat{J}_{12}^\mu - \frac{\boldsymbol{\sigma} \cdot \mathbf{p}'_{2,B}}{E_{p'_{2,B}} + M_Y} \hat{J}_{22}^\mu \right\} \chi_{s_z} \right]. \end{aligned} \quad (5.4.46)$$

Here the terms  $\mathcal{G}_E^{\kappa \ l_1 \ l_3}$  and  $\mathcal{F}_E^{\kappa \ l_1 \ l_3}$  denote the integrated radial parts:

$$\mathcal{G}_E^{\kappa \ l_1 \ l_3} = \int dx x j_{l_1}(p'_A x) R_{l_3, p'_{1,B}}^{(+)}(x) g_{E\kappa}(x), \quad (5.4.47)$$

$$\mathcal{F}_E^{\kappa \ l_1 \ l_3} = \int dx x j_{l_1}(p'_A x) R_{l_3, p'_{1,B}}^{(+)}(x) f_{E\kappa}(x), \quad (5.4.48)$$

whereas integration of three spherical harmonics over a solid angle in coordinate space are labeled as  $Y_{m_1 - m_3}^{l_1 \ l_3 \ l_2}$  and  $Y_{m_1 - m_3}^{l_1 \ l_3 \ l'_2}$ :

$$Y_{m_1 - m_3}^{l_1 \ l_3 \ l_2} = (-1)^{m_3} \int d\Omega Y_{l_1 m_1}(\hat{\mathbf{x}}) Y_{l_3 m_3}^*(\hat{\mathbf{x}}) Y_{l_2 m_2}(\hat{\mathbf{x}}), \quad (5.4.49)$$

$$Y_{m_1 - m_3}^{l_1} Y_{m_2}^{l_3} Y_{m_2}^{l_2} = (-1)^{m_3} \int d\Omega Y_{l_1 m_1}(\hat{\mathbf{x}}) Y_{l_3 m_3}^*(\hat{\mathbf{x}}) Y_{l_2 m_2}(\hat{\mathbf{x}}). \quad (5.4.50)$$

Note that  $l_2' = 2j - l_2$  is the so called the ‘‘other’’ angular momentum. The last two angular integrations, Eqs. (5.4.49) and (5.4.50), are none other than the Gaunt coefficients which are strongly constrained by a number of symmetric conditions[114]. Use is made of one of the properties of the spherical harmonics:

$$\sum_{l_3 m_3} Y_{l_3 m_3}(\hat{\mathbf{x}}) Y_{l_3 m_3}^*(\hat{\mathbf{p}}'_{2,B}) = \sum_{l_3 m_3} Y_{l_3 m_3}^*(\hat{\mathbf{x}}) Y_{l_3 m_3}(\hat{\mathbf{p}}'_{2,B}). \quad (5.4.51)$$

It is also worth noting that the distorted wave formalism of the weak nuclear transition current can be used in the plane wave limit calculations after performing the following substitution in Eqs. (5.4.47) and (5.4.48):

$$R_{l_3, p'_{1,B}}^{(+)}(x) \longrightarrow j_{l_3}(xp'_{1,B}), \quad (5.4.52)$$

where  $j_{l_3}(xp'_{1,B})$  is the spherical Bessel function which can be calculated analytically, and  $R_{l_3, p'_{1,B}}^{(+)}(x)$  is the complex function as opposed to  $j_{l_3}(xp'_{1,B})$ .



## Chapter 6

# Numerical Analysis of the RDWIA Model

### 6.1 Introduction

This chapter introduces important computation techniques that we intend to employ in order to carry out the numerical studies of the neutrino-induced associated production of strange particles on nuclei. One of the main goals of this theoretical undertaking is to generate the quantitative predictions for the quasifree  $A(\nu, \ell KY)B$  reactions within the RDWIA framework. As opposed to the plane-wave limit treatment, the distorted wave analysis of such reaction processes presents unprecedented numerical challenges. The primary reason being the complexity introduced when re-deriving the expression of weak nuclear current  $\mathcal{H}^\mu$  such that it can further accommodate the FSI effects. To this end, we implement high level numerical methods that make possible cost-effective and time-saving computation of the differential cross sections describing the exclusive neutrino-nucleus weak interaction.

### 6.2 Relativistic Kinematics in the c.m. Frame

The kinematic factor of the five-fold differential cross section in Eq. (5.3.10) requires that all four-momenta be specified in the c.m. frame. Note, however, that the kinematics of the quasifree  $A(\nu, \ell KY)B$  processes has been calculated in the laboratory frame (Lab1) whereby the target nucleus is considered at rest. The Fortran 95 subroutine KINLAB1 is developed to compute all Lab1 four-momenta for two different kinematic arrangements. Subsequently, we must be able to transform those Lab1 kinematic quantities to the c.m. frame. In so doing, the Fortran 95 subroutine: KINCOM, has been designed in order to perform the Lorentz transformation of four-momenta from Lab1 frame to c.m. frame using the following boost parameters:  $\beta_{\nu A}$  and  $\gamma_{\nu A}$  (see Eq. (5.2.2)). Hence KINCOM takes the Lab1 four-momenta:  $k^\mu, k'^\mu, P^\mu, q^\mu, p_1'^\mu, p_2'^\mu$ , and  $P'^\mu$  as inputs, and then returns their respective c.m. frame four-momenta:  $k_A^\mu, k'_A{}^\mu, P_A^\mu, q_A^\mu, p_{1,A}'^\mu, p_{2,A}'^\mu$  and  $P_A'^\mu$  as outputs.

In the RDWIA model, the invariant matrix element is treated on a slightly deferent footing with regard to the various kinematic quantities needed to specify its components. For example, the elementary hadronic current  $\hat{J}^\mu$ , which we have embedded inside the nuclear medium, is fully specified by the c.m. frame kinematics. On the other hand, the wave functions are calculated using the corresponding relative three-momenta with respect to (i) the target for particles in the initial channel, and (ii) residual nucleus for particles in the final channel of the quasifree reaction. Since our study is restricted to the RDWIA-I case, the only distortion effect we are taking into account is that of the final state kaon. As a result, all participating particles except for the kaon are described as the plane waves, which are also defined as functions of the respective relative three-momenta:  $\mathbf{k}_A, \mathbf{k}'_B, \mathbf{p}'_{1,B}$ , and  $\mathbf{p}'_{2,B}$ , instead of the three-momenta in the c.m. frame. Subsequently, another Fortran 95 subroutine, dubbed as KINREL, is developed to compute the relative momenta from the corresponding Lab1 quantities by using Eqs. (5.2.2), (5.2.5), (5.2.9) and (5.2.10).

### 6.3 Computation of the Matrix Element

The computational complexity of this study arises mainly from the dynamic part of the RDWIA cross section. In Eq. (5.3.10), the leptonic current  $\mathcal{L}^\mu$  can be programmed in straightforward manner using our knowledge of helicity representation of Dirac spinors and gamma matrices as clearly shown in chapter 3. On the other hand, the in-medium hadronic weak current  $\mathcal{H}^\mu$  as explicitly expressed in Eq. (5.4.44) is a clear indication as to how its numerical implementation would not be an easy task if one relied on the traditional computational methods. In other words, an attempt to approach such a problem using a serial program becomes notoriously time consuming. Therefore, we should make use of advanced but easily accessible computational techniques, which are cost-effective as well as time-saving at the same time.

#### 6.3.1 High Performance Computing: $\mathcal{H}^\mu$ Calculation

Here we present the numerical implementation of the weak nuclear transition current  $\mathcal{H}^\mu$ . The method we develop here is one of the main contributions of this study. The ultimate challenge we encounter in this particular problem are: (i) the incorporation of the distorted wave function of kaon, (ii) the integration of the radial parts of  $\mathcal{H}^\mu$ , (iii) the inclusion of the Gaunt coefficients without violating their symmetric properties, and most of all, (iv) the programming of multi-index summation arising from partial wave expansions.

The kaon FSI has been studied in a great detail in chapter 4, and it has been shown that the radial Klein-Gordon equation containing the optical model potential can be solved numerically using the fourth-order Runge-Kutta iteration method to generate distorted wave functions of the kaon. In the numerical analysis of the RDWIA model, the distorted partial waves of the outgoing kaon are calculated beforehand for  $l_3$  in the range  $0 \leq l_3 \leq l_3^{\max}$  and then stored in a datafile for later retrieval<sup>1</sup>. It should also be pointed out that the calculation of the kaon distorted wave function does not demand the use high performance computing.

The integration of the radial parts, which are given in Eqs. (5.4.47) and (5.4.48), of the weak nuclear transition current also presents a challenge in the distortion wave formulation of the reaction process. It is easy to understand that any attempt to perform analytical integration of these expressions becomes a formidable task; and the main reason is that the distorted partial waves of the outgoing kaon can only be made available as an array of inputs. Consequently, we resort to a numerical integration method known as the Gaussian quadrature which has been tried-and-tested to produce very accurate results for various cases of integral problems. A brief overview of the Gaussian quadrature is given in Appendix C section C.1. Thus, it is convenient to rewrite the radial parts of  $\mathcal{H}_1^\mu$  and  $\mathcal{H}_2^\mu$  as

$$\mathcal{G}_{E \ p'_A \ p'_{1,B}}^{\kappa \ l_1 \ l_3} = \int dx \mathcal{G}_{E\kappa, l_1, l_3, p'_A, p'_{1,B}}^{(+)}(x), \quad (6.3.1)$$

$$\mathcal{F}_{E \ p'_A \ p'_{1,B}}^{\kappa \ l_1 \ l_3} = \int dx \mathcal{F}_{E\kappa, l_1, l_3, p'_A, p'_{1,B}}^{(+)}(x), \quad (6.3.2)$$

where

$$\mathcal{G}_{E\kappa, l_1, l_3, p'_A, p'_{1,B}}^{(+)}(x) = x j_{l_1}(p'_A x) R_{l_3, p'_{1,B}}^{(+)}(x) g_{E\kappa}(x), \quad (6.3.3)$$

$$\mathcal{F}_{E\kappa, l_1, l_3, p'_A, p'_{1,B}}^{(+)}(x) = x j_{l_1}(p'_A x) R_{l_3, p'_{1,B}}^{(+)}(x) f_{E\kappa}(x). \quad (6.3.4)$$

Based on the visual inspection of these two integrals, we have found that the region very far from the typical nuclear size has a vanishing contribution for both cases. As a result, we can compute the integrals by replacing the infinite limit with finite values

$$\int_0^\infty \longrightarrow \int_{x_{\min}}^{x_{\max}} \quad (6.3.5)$$

---

<sup>1</sup>Note that the notations  $l_{KB}$  in chapter 4 and  $l_3$  in this chapter refer to the same quantity - the angular momentum of the kaon in the K-B system.

without loss of generality. Thus, in order to apply the Gaussian quadrature, Eqs. (6.3.1) and (6.3.2) should be written in the form of Eq. (C.1.2) of Appendix C. That is,

$$\mathcal{G}_{E p'_A p'_{1,B}}^{\kappa l_1 l_3} = (x_{\max} - x_{\min}) \sum_{k=1}^N \mathcal{G}_{E\kappa, l_1, l_3, p'_A, p'_{1,B}}^{(+)} ((x_{\max} - x_{\min})x_k + x_{\min})\omega_k, \quad (6.3.6)$$

$$\mathcal{F}_{E p'_A p'_{1,B}}^{\kappa l_1 l_3} = (x_{\max} - x_{\min}) \sum_{k=1}^N \mathcal{F}_{E\kappa, l_1, l_3, p'_A, p'_{1,B}}^{(+)} ((x_{\max} - x_{\min})x_k + x_{\min})\omega_k. \quad (6.3.7)$$

Therefore, use is made of the most common Fortran subroutine called GAULEG[115] in order to generate the roots  $x_k$  of the Legendre polynomials and the corresponding weighing coefficients  $\omega_k$  of the Gaussian quadrature. In this case, GAULEG takes the integral limits:  $r_{\min} = 0$  and  $r_{\max} = 1$ ; the number of integration points:  $N$ , and its outputs are one-dimensional arrays of length  $N$  in which the values of  $x_k$  and  $\omega_k$  are stored. Subsequently, these outputs of roots and weights of the quadrature are used to calculate the radial parts of  $\mathcal{H}_1^\mu$  and  $\mathcal{H}_2^\mu$  according to Eqs. (6.3.6) and (6.3.6).

We now turn our attention to the angular parts of  $\mathcal{H}^\mu$  whereby we have integrals over three spherical harmonics. In what follows we carefully lay out the numerical implementation of these Gaunt coefficients as defined in Eqs. (5.4.49) and (5.4.50). Unlike the integral of the radial parts, the Gaunt coefficients have a pivotal role to play when we apply the HPC method to compute the weak nuclear transition current. Thus, it is necessary to highlight some of their important features that are relevant to our relativistic distorted wave analysis of the quasifree reaction processes.

The major computational challenges in generating the Gaunt coefficients are accuracy and speed specially when large values of the angular momenta are assigned as inputs of the subroutine. The issue of accuracy in calculating the Gaunt coefficients arises from their analytical expression containing very large factorials which are enormously difficult to evaluate on a standard personal computer. Though there are a number of successful schemes[116, 117] that guarantee the calculation of the Gaunt coefficient with high accuracy, they are far from being perfect owing to the fact that they are characterized by very slow computing times. Consequently, other schemes have emerged with the aim of addressing such problem with computation speed. Rasch and Yu[118], for example, introduced a very efficient storage scheme which can pre-calculate and store nonzero Gaunt coefficients along with suitable indices that will be used for later retrieval.

As a matter of fact, the development of the most accurate and fastest schemes solely depends on the symmetric properties of the Gaunt coefficients:

$$|l_1 - l_2| \leq l_3 \leq (l_1 + l_2), \quad (6.3.8)$$

$$l_1 + l_2 + l_3 = 0 \pmod{2}, \quad (6.3.9)$$

$$m_1 = m_3 - m_2, \quad (6.3.10)$$

which are sufficient conditions for the corresponding Gaunt coefficient to be nonzero. In addition, the Gaunt coefficients  $Y_{m_1 m_2 m_3}^{l_1 l_2 l_3}$  satisfy symmetric conditions such as invariance under any permutation of the columns, and parity transformation, respectively, shown as

$$Y_{m_1 m_2 m_3}^{l_1 l_2 l_3} = Y_{m_{\sigma(1)} m_{\sigma(2)} m_{\sigma(3)}}^{l_{\sigma(1)} l_{\sigma(2)} l_{\sigma(3)}}, \quad (6.3.11)$$

$$Y_{m_1 m_2 m_3}^{l_1 l_2 l_3} = Y_{-m_1 -m_2 -m_3}^{l_1 l_2 l_3}, \quad (6.3.12)$$

where  $\sigma$  is the permutation of a set  $\{1, 2, 3\}$ .

In this study, however, we use the Fortran subroutine written by Weniger and Steinborn [119] to recursively compute the Gaunt coefficients in terms of the Wigner 3jm symbols[120]. The program was developed by taking into account the above symmetric properties, and hence the calculations of zero Gaunt coefficients can be avoided, as a result, saving larger storage space.

In addition, due to the constraints imposed by these symmetric conditions, GAUNT subroutine takes only four inputs:  $l_2$ ,  $m_2$ ,  $l_3$ , and  $m_3$ , whereas  $l_1$  and  $m_1$  are computed by the program along the way, for nonzero Gaunt coefficients, as

$$m_1 = m_3 - m_2, \quad (6.3.13)$$

$$l_1 = l_1^{\min}, l_1^{\min} + 2, l_1^{\min} + 4, \dots, l_1^{\max} - 2, l_1^{\max}, \quad (6.3.14)$$

with

$$l_1^{\max} = l_2 + l_3, \quad (6.3.15)$$

$$l_1^{\min} = \begin{cases} \tilde{l}_1, & \text{if } \tilde{l}_1 + l_1^{\max} \text{ is even,} \\ \tilde{l}_1 + 1, & \text{if } \tilde{l}_1 + l_1^{\max} \text{ is odd,} \end{cases} \quad (6.3.16)$$

where

$$\tilde{l}_1 = \max \{|l_2 - l_3|, |m_1|\}. \quad (6.3.17)$$

Once the Gaunt coefficients are calculated in double precision format, they are stored in one-dimensional array  $ARGNT$  of length  $NGAUNT = (l_1^{\max} - l_1^{\min})/2 + 1$ . Hence the outputs of GAUNT are:  $l_1^{\min}$ ,  $l_1^{\max}$ ,  $m_1$ ,  $NGAUNT$ , and  $ARGNT$ .

### 6.3.2 Overview of Parallel Computing

Parallelization is a technique with which one optimizes a sequential data structure or algorithm such that the execution time is almost certainly be minimized as can be illustrated in Fig. 6.1. In the simplest sense, parallel computing can be understood as a simultaneous implementation

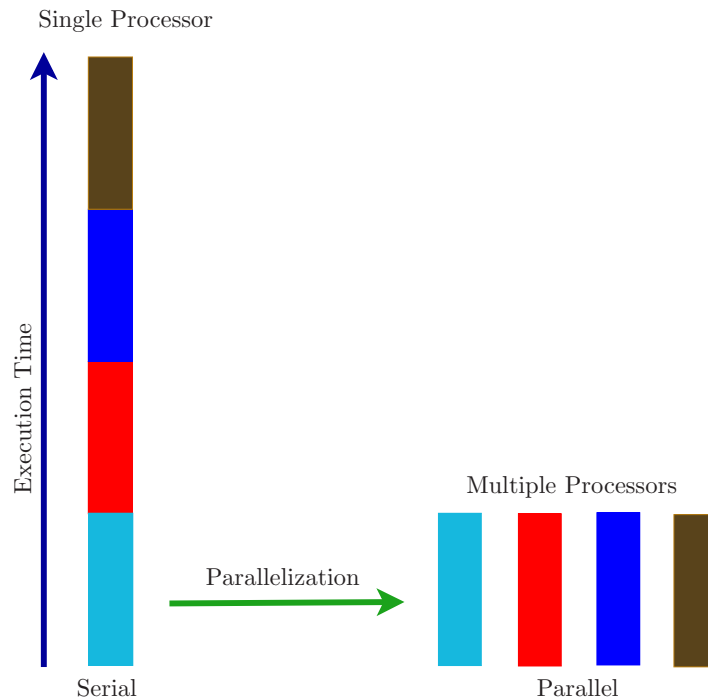


**Figure 6.1:** Schematic comparison of execution times of sequential and parallel processes of the same computational problem.

of multiple processors to be able to solve a bigger problem which is broken into smaller parts. In this work, we carry out parallel computing by using a set of interconnected computers that work together as a single unit which is often referred as a computer cluster. The availability of low-cost computers, high-speed networks, and open-source software for HPC computing are responsible for the emergence of computer clusters as the popular optimization tools.

Parallel computers can roughly be classified into two memory architectures: shared-memory and distributed-memory parallel computers as depicted in Fig. 6.2. In the shared-memory system processors share access to a global address space. This memory architecture provides a user-friendly programming environment and is also well-known for fast and uniform inter-processor data sharing. Lack of cpu-to-memory scalability, as well as design and production challenges are some of the drawbacks of the shared-memory architecture[121]. In the distributed-memory systems, on the other hand, individual processors have their own local memories which are

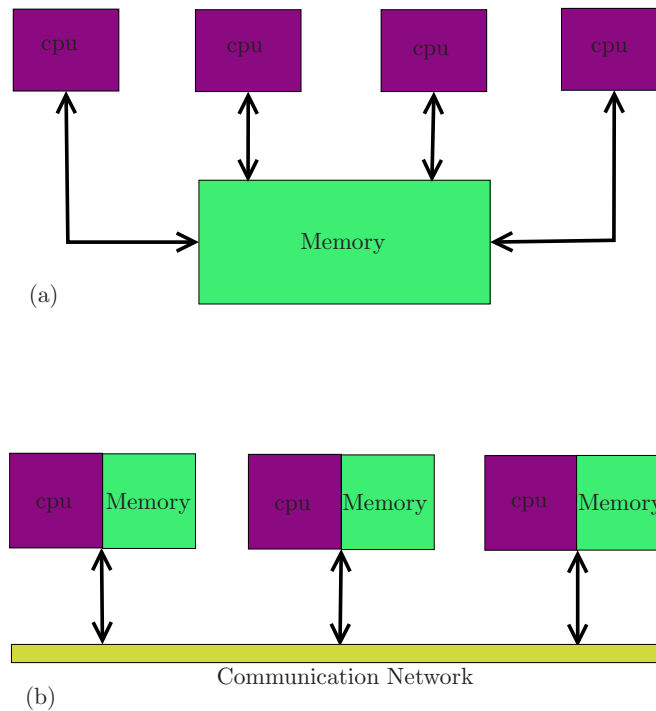


**Figure 6.2:** Memory architectures of parallel computers: (a) shared-memory system whereby multiple processors share a common global address, and (b) distributed-memory system in which processors with their own private memory are interconnected by communication network.

interconnected via a communication network. It has the following advantages: (i) scalability of memory as the number of processors increases, (ii) each processor on the system operates independently, and (iii) the system can be built in a cost-effective way. It also has some disadvantages: non-uniform memory access times, and the fact that the programmer takes more responsibility for ensuring the inter-processor communication and synchronization. In recent years, however, the largest and fastest computers, namely, supercomputers of the world are emerging as a hybrid distributed-shared memory architecture.

Computer clusters are the most popular distributed-memory systems for parallel computing. There are a number of parallel programming models that has been introduced; but message passing interface or MPI is the most widely used Application Programming Interface (API) for developing parallel programs running on distributed-memory systems[122]; and it has become the *de facto* standard for inter-processor communication. MPI, by itself, is more of specification for programmers with regard to what message passing libraries, compilers and runtime environment should be used to launch an MPI program. MPI declares its own data type and supports C, C++ and Fortran programming languages. In Fortran case, for example, all MPI programs must have a line at the beginning that includes header file: “`mpif.h`”. Although there are various implementations of MPI, the most popular one is known as MPICH which is free and open-source software.

### 6.3.3 $\mathcal{H}^\mu$ Parallelization

The first step one often takes to design the parallel program is to break down the problem into smaller pieces to be partially computed among processors. The two partitioning approaches are task-parallelism and data-parallelism. In task-parallelism the programmer wants each processor to perform a portion of the instruction set of the problem. In data-parallelism, one partitions the data needed as input to solve the problem among the processors. The calculation of the weak nuclear transition current  $\mathcal{H}^\mu$  involving multidimensional summation of very large number of terms, each of which is a complex algebraic object that requires elegant multi-step calculations, gives rise to very long execution times. Consequently, we employ the concept of data-parallelism in order to design the parallel optimization algorithm. In Appendix D, we have presented the technique we developed to convert a multidimensional summation to an equivalent one-dimensional summation by only working with summation indices without being hindered by the details of the actual problem. In fact, this technique goes hand-in-hand with the implementation of data-parallelism.

Now we turn our attention to the weak nuclear transition current  $\mathcal{H}^\mu$  as explicitly expressed in Eq. (5.4.44). For brevity, we only focus on  $\mathcal{H}_1^\mu$  as the techniques we develop here can easily be extended to  $\mathcal{H}_2^\mu$ ; and for convenience we first rewrite the expression (see Eq. 5.4.45) of  $\mathcal{H}_1^\mu$  in the following manner:

$$\mathcal{H}_1^\mu = \sum_{l_1=0}^{l_1^{\max}} \sum_{m_1=-l_1}^{l_1} \sum_{l_3=0}^{l_3^{\max}} \sum_{m_3=-l_3}^{l_3} \sum_{s_z=\pm\frac{1}{2}} H_{1,l_2,m_2}^\mu(l_1, m_1, l_3, m_3, s_z). \quad (6.3.18)$$

Note that  $l_2$  and  $m_2$  are fixed at the start and hence there is no need to perform summation over both indices. As it stands,  $\mathcal{H}_1^\mu$  is considered as a five-dimensional summation which we intend to convert to one-dimensional summation. For the sake of convenience, we may transform  $m_1$ ,  $m_3$ , and  $s_z$  such that

$$\mathcal{H}_1^\mu = \sum_{l_1=0}^{l_1^{\max}} \sum_{\tilde{m}_1=0}^{2l_1} \sum_{l_3=0}^{l_3^{\max}} \sum_{\tilde{m}_3=0}^{2l_3} \sum_{\tilde{s}_z=0}^1 H_{1,l_2,m_2}^\mu(l_1, \tilde{m}_1 - l_1, l_3, \tilde{m}_3 - l_3, \tilde{s}_z - 1/2), \quad (6.3.19)$$

where  $\tilde{m}_1 = m_1 + l_1$ ,  $\tilde{m}_3 = m_3 + l_3$ , and  $\tilde{s}_z = s_z + 1/2$ . At this point, we invoke the symmetric conditions, Eqs. (6.3.13) and (6.3.14), of the Gaunt coefficients as imposed by GAUNT subroutine. Consequently, large chunks of zero terms are avoided as we drop the summation over  $m_1$ , and therefore Eq. (6.3.18) reduces to a four-dimensional summation with a new and minimized range of summation over  $l_1$ :

$$\mathcal{H}_1^\mu = \sum_{\tilde{l}_1=0}^{\tilde{l}_1^{\max}} \sum_{l_3=0}^{l_3^{\max}} \sum_{\tilde{m}_3=0}^{2l_3} \sum_{\tilde{s}_z=0}^1 H_{1,l_2,m_2}^\mu(\tilde{l}_1^{\min} + 2\tilde{l}_1, \tilde{m}_3 - l_3 - m_2, l_3, \tilde{m}_3 - l_3, \tilde{s}_z - 1/2), \quad (6.3.20)$$

where

$$\tilde{l}_1^{\max} = \frac{\tilde{l}_1^{\max} - \tilde{l}_1^{\min}}{2}. \quad (6.3.21)$$

Note that  $\tilde{l}_1^{\max}$  and  $\tilde{l}_1^{\min}$  are calculated using the GAUNT program according to Eqs. (6.3.15) and (6.3.16), respectively. Thus, because of the symmetric properties of the Gaunt coefficients, a lot of terms in the original expression, Eq. (6.3.18), of  $\mathcal{H}_1^\mu$  have a vanishing contribution to the summation and the inability to avoid the computation of such zero terms results in longer execution time. The latter expression, Eq. (6.3.20), of  $\mathcal{H}_1^\mu$  is meant to address such computational problems by using the symmetric conditions of the Gaunt coefficients that help to constraint the GAUNT program to compute only non-vanishing contributions.

The four-dimensional summation of  $\mathcal{H}_1^\mu$  in Eq. (6.3.20) cannot be converted to a single-index summation at once as there are dependent indices,  $l_3$  and  $m_3$ , that need to be resolved in advance.

Hence we resort to performing step-by-step conversion to one-dimensional summation. The remedy for two dependent summation indices, with particular reference to angular momentum and its projection, is given in Eqs. (D.2.4) and (D.2.5) of Appendix D. Hence we can have the following conversion

$$\sum_{l_3=0}^{l_3^{\max}} \sum_{m_3=-l}^l \longrightarrow \sum_{s_3=0}^{N_{s_3}^{\max}}. \quad (6.3.22)$$

Subsequently, Eq. (6.3.20) of  $\mathcal{H}_1^\mu$  is reduced to a three-dimensional summation:

$$\mathcal{H}_1^\mu = \sum_{\bar{l}_1=0}^{\bar{l}_1^{\max}} \sum_{s_3=0}^{N_{s_3}^{\max}} \sum_{\tilde{s}_z=0}^1 H_{1,l_2,m_2}^\mu \left( \tilde{l}_1^{\min} + 2\bar{l}_1, \tilde{m}_3 - l_3(s_3) - m_2, l_3(s_3), \tilde{m}_3(s_3) - l_3(s_3), \tilde{s}_z - 1/2 \right). \quad (6.3.23)$$

Now therefore, we employ Eqs. (D.1.8) - (D.1.11) of Appendix D to convert this three-dimensional summation to one-dimensional summation. That is,

$$\mathcal{H}_1^\mu = \sum_{s=0}^{N_s^{\max}} H_{1,l_2,m_2}^\mu \left( \tilde{l}_1^{\min} + 2\bar{l}_1(s), \tilde{m}_3 - l_3(s_3(s)) - m_2, l_3(s_3(s)), \tilde{m}_3(s_3(s)) - l_3(s_3(s)), \tilde{s}_z(s) - 1/2 \right), \quad (6.3.24)$$

where

$$\bar{l}_1(s) = \frac{s - s \pmod{2(N_{s_3}^{\max} + 1)}}{2(N_{s_3}^{\max} + 1)}, \quad (6.3.25)$$

$$\tilde{s}_z(s) = s \pmod{2}, \quad (6.3.26)$$

$$s_3(s) = \frac{s - \tilde{s}_z(s)}{2} \pmod{N_{s_3}^{\max} + 1}, \quad (6.3.27)$$

$$l_3(s_3(s)) = \lfloor \sqrt{s_3(s)} \rfloor, \quad (6.3.28)$$

$$m_3(s_3(s)) = s - \lfloor \sqrt{s_3(s)} \rfloor \left( \lfloor \sqrt{s_3(s)} \rfloor + 1 \right), \quad (6.3.29)$$

and

$$N_s^{\max} = 2(\bar{l}_1^{\max} + 1)(N_{s_3}^{\max} + 1) - 1. \quad (6.3.30)$$

Similarly,  $\mathcal{H}_2^\mu$  can be rewritten in one-dimensional summation format and it has an identical structure as the expression of  $\mathcal{H}_1^\mu$  given in Eq. (6.3.24). That is,

$$\mathcal{H}_2^\mu = \sum_{t=0}^{N_t^{\max}} H_{2,l'_2,m_2}^\mu \left( \tilde{l}_1^{\min} + 2\bar{l}_1(t), \tilde{m}_3 - l_3(s_3(t)) - m_2, l_3(s_3(t)), \tilde{m}_3(s_3(t)) - l_3(s_3(t)), \tilde{s}_z(t) - 1/2 \right), \quad (6.3.31)$$

and all of the indices are determined expressed as functions of  $t$  using Eqs (6.3.25) - (6.3.30). with the only exception that  $l_2$  must be replaced by  $l'_2 = 2j - l_2$ .

In cluster computing the parallelization of serial programs is typically a manual task, which is time consuming, complex, and prone to error. The original expression, Eq. (5.4.44), of the weak nuclear transition current  $\mathcal{H}^\mu$  can be programmed serially by using nested loops to execute multi-dimensional summation. But one soon realizes that such simplicity with designing the serial program results in longer execution times than what is normally expected. In response to that, we partition the data set of the problem such that the parallelized serial program can be partially executed on individual processors on the cluster.



There are at least two ways to partition the data associated with the problems block and cyclic partition patterns[121]. In the MPI environment each processor in a cluster is associated with a unique integer identifier called rank. Thus processors use ranks  $r = 0, 1, 2, \dots, p - 1$  to identify each other for communication while executing MPI program. The multi-index to single-index summation formalism has created the platform to operate on multi-dimensional data structures as though it is single-dimensional. In order to implement data partitioning in the block-by-block pattern, one often needs to write a separate subroutine that may use certain arithmetic operations to break the data into smaller blocks upon being called by the main MPI program. Then these blocks are distributed among processors for partial execution

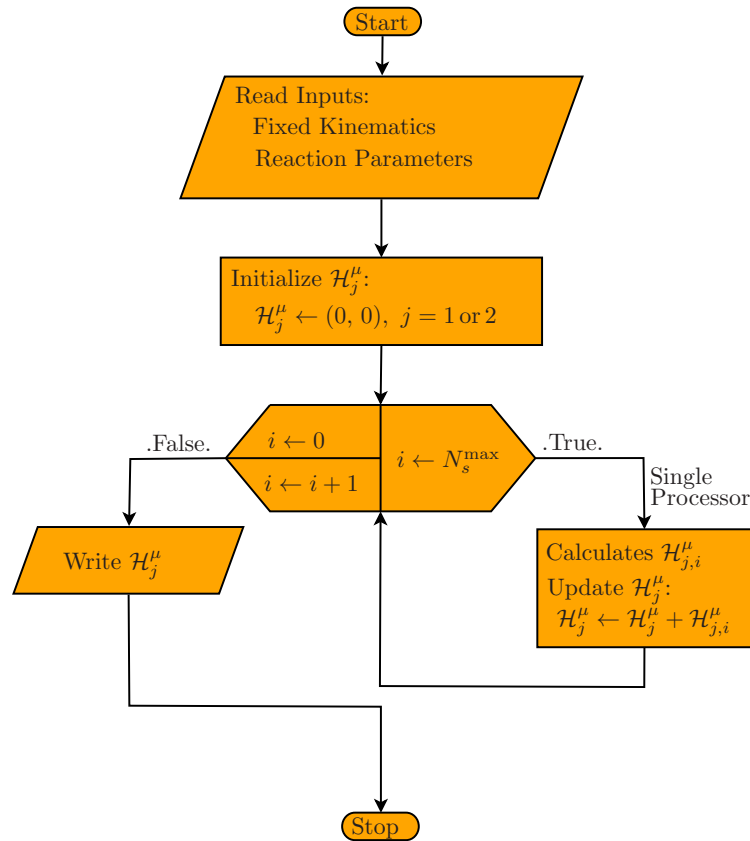


**Figure 6.3:** Flow diagram of what a serial execution of the weak nuclear transition currents  $\mathcal{H}_1^\mu$  and  $\mathcal{H}_2^\mu$  on a single processor looks like. Here we only intend to illustrate the parallelizable parts without bothered by the detail of the actual calculation. Since the summation is performed over very large number of terms on a single processor, such computations using the standard personal computer have been proven to be time consuming.

of the computational problem. This approach, however, can be very troublesome, because (i) it requires an additional subroutine for partitioning the main data into blocks; (ii) it may not necessary ensure the even distribution of data among processors, and hence one of them may end up executing instructions of the problem on very large or very small portions of the data; and (iii) it can also contribute to time consumption due to the previous two reasons. Therefore, we resort to the data partitioning in a cyclic pattern, because of its simplistic yet fast and reliable way to parallelize a serial program. By default, the primary node (p-node) of the computer cluster is identified as rank  $r = 0$ ; and this leaves the rest of the  $p - 1$  nodes to be IDed by ranks ranging from  $r = 1$  to  $r = p - 1$ , and they are collectively named as secondary nodes (s-nodes).

The one-dimensional summations in Eq. (6.3.24) of  $\mathcal{H}_1^\mu$  and Eq. (6.3.31) of  $\mathcal{H}_2^\mu$  can easily be coded into serial programs using Fortran 95. These summations over a very large number of terms, which present their own computational challenges, are performed using a do loop as it is

more suitable in handling repeated executions. Traditionally, the do loop syntax consists of the following parameters: initial value, final value, and step size of a loop control variable. Data partitioning in a cyclic pattern can directly be coded into the do loop by carefully re-specifying the initial value and step size in terms of ranks and number of processors. In doing so, we employ the concept of equivalent class of congruence relation  $\equiv (\text{mod } q)$  on  $\mathbb{Z}$ , where  $q \in \mathbb{Z}_{\geq 0}$ .

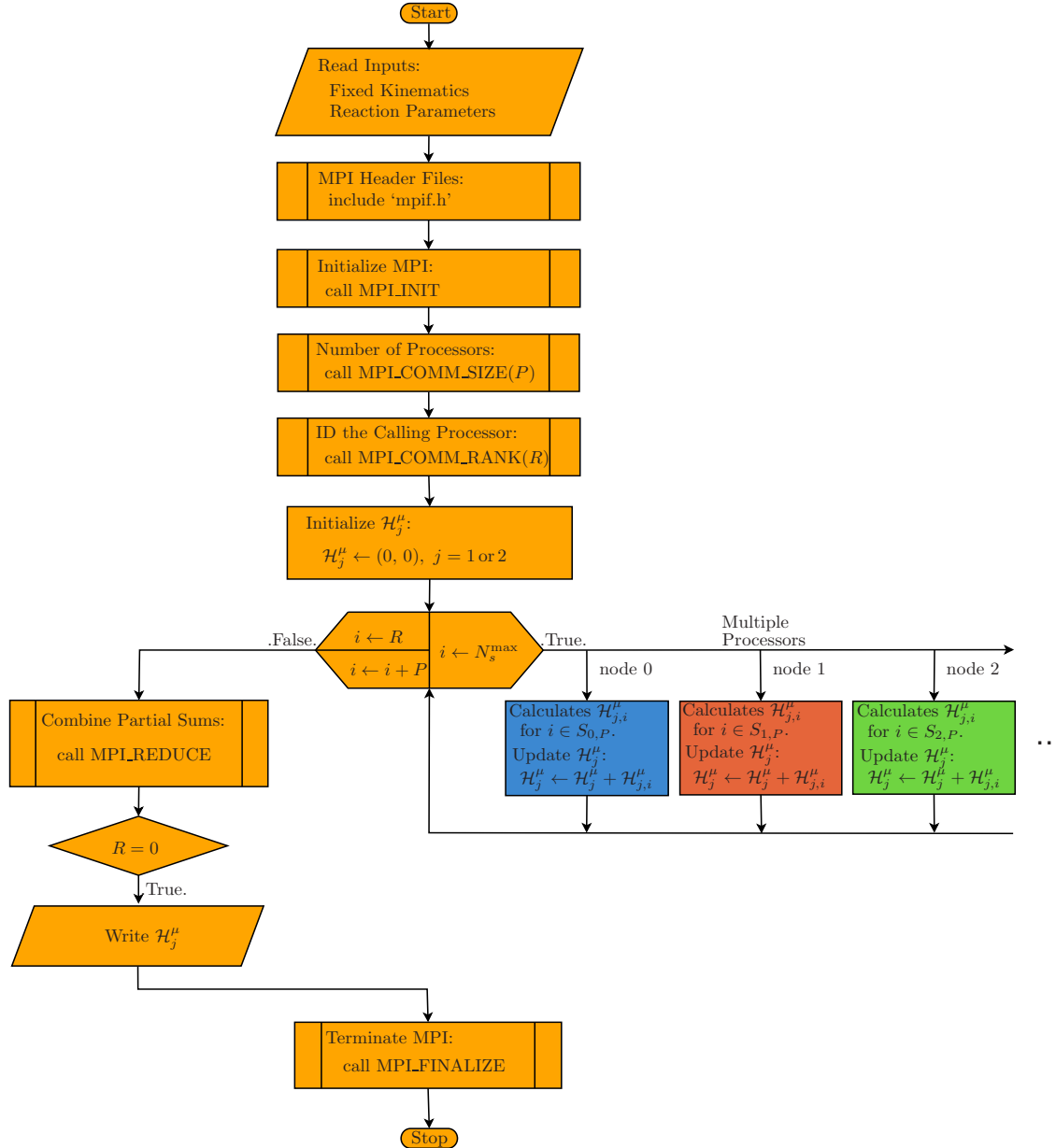


**Figure 6.4:** Flow diagram providing a rough illustration as to how the parallel computations of the nuclear transition currents  $\mathcal{H}_1^\mu$  and  $\mathcal{H}_2^\mu$  on a computer cluster are carried out. Note that this illustration does not show the detailed calculations, instead it emphasizes on the parallelization mechanism based on distributed-memory architecture. Here very large number of terms are partially summed over by individual processors of the cluster, simultaneously; hence resolving the problem of long execution time of the corresponding serial program.

In this particular case, for example, the congruence relation  $\equiv (\text{mod } q)$  has equivalent classes:  $[0]_q, [1]_q, [2]_q, \dots, [q-1]_q$ , where

$$[n]_q = \{m \in \mathbb{Z} : m \equiv n (\text{mod } q)\} = \{\dots, n-2q, n-q, n, n+q, n+2q, \dots\}, \quad (6.3.32)$$

for  $n \in \{0, 1, 2, \dots, q-1\}$ . The index of summation  $s(t)$  in the expression of  $\mathcal{H}_1^\mu(\mathcal{H}_2^\mu)$  is nonnegative and it always starts at zero and ends at  $N_s^{\max}(N_t^{\max})$ . If we now define a set  $S$  as

$$S = \{0, 1, 2, \dots, N_s^{\max}\}, \quad (6.3.33)$$

then we can partition set  $S$  in a cyclic pattern using the congruence classes defined in Eq. (6.3.32) as follows:

$$S_{n,q} = [n]_q \cap S = \{n, n+q, \dots, N_n\}, \quad (6.3.34)$$

where  $N_n = \max(S_{n,q})$ ; and these sets of the partition must satisfy the condition:

$$S = S_{0,q} \cup S_{1,q} \cup \dots \cup S_{q-1,q}. \quad (6.3.35)$$

Note, however, that such a partition of the set indices, with which the data elements are identified and retrieved, does not make any sense until some sort of associations are established between the parameters of the partition scheme and that of the MPI environment on which we intend to run the parallel program. In so doing, we now set the number of processors on the cluster machine to be  $p = q$ , and the rank of a processor  $r = n$ . Thus, with slight modification of the do loop of the serial programs of  $\mathcal{H}_1^\mu$  and  $\mathcal{H}_2^\mu$ , we can invoke the processors to execute partial sums simultaneously once the MPI environment is booted on the cluster.

The flow diagrams have been used to illustrate the rough structure of the serial and parallel programs of the same problem. The flowchart in Fig. 6.3 gives the sense of how the serial program of either  $\mathcal{H}_1^\mu$  or  $\mathcal{H}_2^\mu$  is executed on a single personal computer. Here the do loop sequentiality executes addition of terms, one term at a time, with constant increase of summation index by unity. This program is marked by slow execution time as the entire task is exhaustively taken care of by a single processor. On the other hand, Fig. 6.4 displays the ideal flowchart of the MPI programs, which are the parallelized version of the serial programs of  $\mathcal{H}_1^\mu$  and  $\mathcal{H}_2^\mu$ . As it can be seen in the figure, the do loop uses rank of the calling processor as initial value and the total number of processors as step size of the loop control variable. Soon after the MPI communicator is initialized, all participating processors simultaneously start partial execution starting from terms with indices identical to their ranks and then repeat the operation by moving on to the next terms with step of  $p$ .

The cluster that we have assembled for the computational part of our study is a six-node system of interconnected processors. Each node has its own hard disk drive and network connection. The p-node is Intel E7505 Chipset-based Tower Server running Intel Xeon Processor (dual-core, 3.06GHz, 2GB of RAM, 186GB disk, Gigabit ethernet); whereas the five s-nodes are desktop computers each running Intel Pentium Processor (single-core, 3.0GHz, 1GB of RAM, 74GB disk, Gigabit ethernet). Each node runs the Linux Mandriva 2008 operating system (server flavor for p-node and desktop flavor for s-nodes). The nodes in the cluster are interconnected via GSW-1601, a 16-port 10/100/1000Mbps Gigabit Ethernet Switch. This communication network provides access to individual nodes such that they can be configured, booted, and diagnosed to result in optimum execution of MPI programs on the cluster. There are two different ways by which all nodes on the cluster identify each other: (i) using their ranks in the MPI environment, (ii) using their static IP address on the cluster. The latter case becomes even more relevant when a user wants to have secured access to the cluster via ssh applications. For example, we can use the `ssh` command to securely login onto any node in the cluster; and data movement among the nodes must also be carried out using secured command `scp`.

LAM is a simple yet powerful environment for running and monitoring MPI applications on clusters [123, 124]. Once LAM goes live on a cluster, all nodes act as parts of a single parallel computing multicomputer system. In order to boot the LAM environment on a cluster, we must run “`lamboot`” on command line as: `lamboot -v lamhosts`. Here “`lamhosts`” is a simple shell script containing the list of hostnames or static IP addresses of all participating machines. MPI programs are compiled by `mpif77`, which is a wrapper for the underlying Fortran 77 compiler, as: `mpif77 -O -o foo.exe foo.f`, where “`foo.f`” is the MPI program and “`foo.exe`” is the

executable file that will be created by the MPI compiler. Next, in order to execute the MPI program we use the `mpirun` command: `mpirun -np 6 foo.exe`. In addition to the executable file of the MPI program, the data files of pre-calculated kaon distorted wave function, Gaunt coefficients, and multidimensional summation indices must be transferred using `scp` from p-node to s-nodes before executing the MPI program. Note that these data files must have identical local directory paths on all dedicated nodes to be accessed by the running MPI program. We have created an all-in-one shell script that (i) boots LAM, (ii) compiles the MPI program, (iii) transfers executable and data files, and (iv) runs executable files on the cluster.

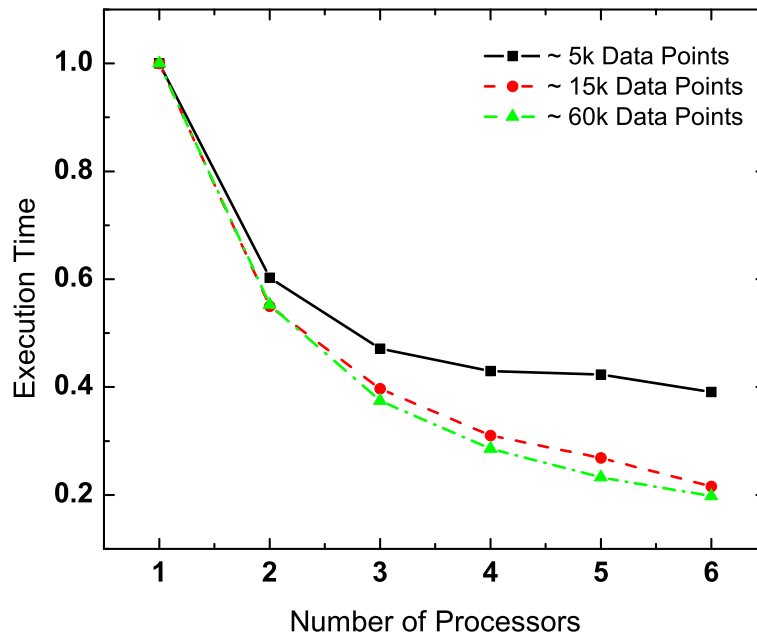


**Figure 6.5:** Execution time as a function of number of processors for three data sets. Here we only considered special cases for the sake of examining the improvement of the MPI program in terms of computational speed. These plots are generated after adding together the execution times and data sizes of MPI routines of  $\mathcal{H}_1^\mu$  and  $\mathcal{H}_2^\mu$ . For each data set the list of execution times is scaled down by a factor of the inverse of the execution time on a single processor.

In Fig. 6.5 we illustrate how the execution speed improves, when running the MPI routines of  $\mathcal{H}_1^\mu$  and  $\mathcal{H}_2^\mu$ , as the number of processors increases. Three curves represent three different cases of the MPI program: (i) the black curve (solid line and square symbol) represents a case when close to  $5 \times 10^3$  terms (data points) are summed over on the cluster; (ii) the red curve (dash line and circle symbol) depicts a case when close to  $1.5 \times 10^4$  items are summed over on the cluster; and (iii) the green curve (dash-dot line and triangle symbol) illustrates the case when close to  $6.0 \times 10^4$  data points are summed over on the cluster. In each case, the execution times for various numbers of processors are normalized by multiplying them with a factor of the inverse of the execution time recorded when the MPI program is run on a single processor. Thus, it is quite evident from the curves of Fig. 6.5 that the execution time is readily minimized as we increase the cluster size. The results of the relativistic distorted wave analysis of the exclusive reaction are presented and discussed in chapter 7.

## Chapter 7

# Results and Discussion

In this chapter, results of the relativistic plane and distorted wave analyses of the quasifree reaction are presented and discussed. Within both approximations, the differential cross sections are calculated under two kinematic settings: quasifree and open kinematics. Here we restrict ourselves to the CC and  $\Delta S = 0$  processes to explore the theoretical predictions of this study. We average over initial spin states and sum over all possible final spin states; and hence we only present unpolarized differential cross sections. Note, however, that our formalism is also suitable to investigate the polarization observables of the quasifree process. As for the spin quantization axis,  $\hat{i}'_2$ , it is fixed along the direction of the three-momentum of the outgoing hyperon, i.e.,  $\hat{i}'_2 \equiv \hat{i}'_2(\theta_{p'_2}, \phi_{p'_2})$ . This particular choice is aimed at staying consistent with the fact that the weak interaction naturally favors particles with longitudinal spin polarization (i.e., polarization along the direction of motion), in particular the ones with negative helicity states to account for its violation of one of the fundamental symmetries, parity.

We limit the incident neutrino energy in the threshold region of the underlying free process  $\nu N \rightarrow \ell KY$ . The three-momenta of the outgoing kaon and hyperon are set to lie on the same plane, named, production plane by imposing the constraint:  $\phi'_1 = \phi'_2 - 180 = \phi$ . Further, we limit ourselves to the coplanar geometric setup whereby the scattering and production planes coincide:  $\phi = 0$ . It has been pointed out in the study of kaon photo-production[47], the coplanar setup generates larger cross sections relative to the out-of-plane setups. Therefore, because of

**Table 7.1:** Relativistic shell structure of  $^{12}\text{C}$  as calculated from the QHD model with the NL3 parameter set.

Orbital	$j$	$l$	$\kappa$	Nucleons	$E_b$ (MeV)	
					Proton	Neutron
$1s^{1/2}$	1/2	0	-1	2	49.70	53.47
$1p^{3/2}$	3/2	1	-2	4	16.04	19.38

our choice of the kinematic setup, the following kinematic quantities:  $\hat{\mathbf{q}}$ ,  $\phi_{p'_1}$  and  $\phi_{p'_2}$  are fixed at the start. On the other hand,  $^4\text{He}$ ,  $^{12}\text{C}$ ,  $^{16}\text{O}$ ,  $^{40}\text{Ca}$ , and  $^{208}\text{Pb}$  are our candidates as target nuclei in the study of neutrino-induced associated production of strange particles. There are at least four CC and  $\Delta S = 0$  channels:  $\text{K}^+\Sigma^+$ ,  $\text{K}^+\Sigma^0$ ,  $\text{K}^0\Sigma^+$ , and  $\text{K}^+\Lambda$  that can be explored, but for the numerical investigation we limit ourselves to  $\text{K}^+\Lambda$  channel as it is not only reported to have a larger cross section but also is experimentally feasible to measure the polarization of the  $\Lambda$ -hyperon.

### 7.1 RPWIA Analysis Results of the $\text{K}^+\Lambda$ Production

In chapter 3, we have developed the RPWIA framework to calculate the differential cross section for describing the quasifree reaction  $A(\nu, \ell KY)B$ . In this section, we present the results of our plane wave limit analysis of the exclusive reaction. The RPWIA calculation is performed for  $\text{K}^+\Lambda$

production process on the  $^{12}\text{C}$  in the laboratory frame. Various distributions of the differential cross section are plotted for a number of sets of kinematic inputs in both quasifree and open arrangements. We have serially coded the expression of the five-fold differential cross section defined in chapter 3, Eq. (3.1.18), using Fortran 95 in such a way that it would be suitable to

**Table 7.2:** Relativistic shell structure of  $^{16}\text{O}$ , including the binding energies of both proton and neutron orbitals, as calculated from the Walecka model with the NL3 parameter sets.

Orbital	$j$	$l$	$\kappa$	Nucleons	$E_b$ (MeV)	
					Proton	Neutron
$1s^{1/2}$	1/2	0	-1	2	37.11	41.28
$1p^{3/2}$	3/2	1	-2	4	17.83	21.71
$1p^{1/2}$	1/2	1	+1	2	11.42	15.21

generate angular, missing momentum and energy distributions for four values of the incident neutrino energy. Since we are interested in presenting the unpolarized differential cross sections,

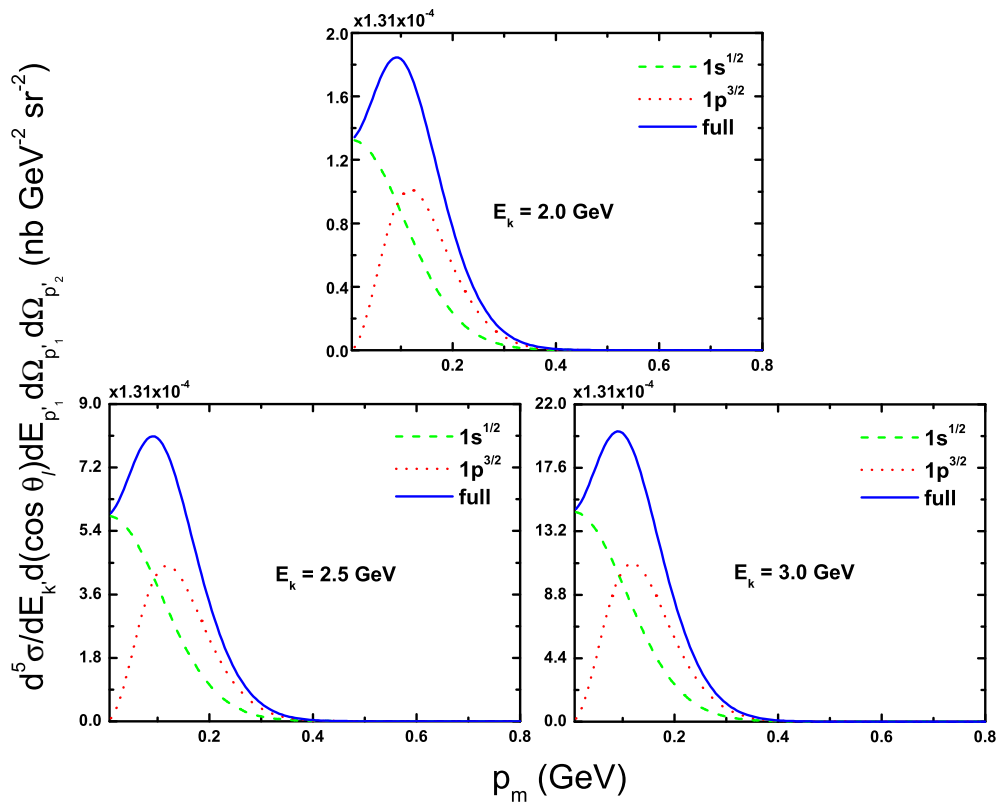


**Figure 7.1:** Missing momentum distribution of the RPWIA differential cross section for the neutrino-induced  $K^+\Lambda$  production on  $^{12}\text{C}$ . The short-dashed (short-dash-dotted) line is the contribution from the neutrons in  $1s^{1/2}$  ( $1p^{3/2}$ ) orbital, and the solid line is their total sum. The quasifree kinematic inputs are fixed at  $\omega = 1.46$  GeV,  $Q^2 = 0.05$  GeV $^2$ , and  $\theta_{p'_1} = 10$  deg.

we must use the expression of the nuclear transition matrix element given in chapter 3, Eq. (3.2.8). In Table 7.1 and 7.2 we have listed down the parameters of the relativistic shell model of  $^{12}\text{C}$  and  $^{16}\text{O}$  nuclei, respective, along with the binding energies of nucleon orbitals. We would like to point out that our results of the RPWIA analysis for the neutrino-induced associated production of strange particles on nuclei have also been published in the International Journal of Modern Physics E[125].

### 7.1.1 Quasifree Kinematic Setting

The detail of the quasifree kinematic setting has been given in chapter 3, section 3.1.2. As mentioned earlier, this kinematics setting has a close resemblance to the kinematics of the underlying elementary process on free nucleon. This setting allows the investigation the missing momentum and kaon angle distributions of the differential cross section for the neutrino energy range  $2.0 \leq E_k \leq 3.0$  GeV. Here we present the RPWIA model results which are calculated under the quasifree kinematic setting, whereby we fix  $\omega$  at 1.46 GeV and  $Q^2$  at  $0.05 \text{ GeV}^2$  to generate the missing momentum and angular distributions.

Fig. 7.1 shows the missing momentum dependence of the RPWIA differential cross section of neutrino-induced associated  $K^+ \Lambda$  production on  $^{12}\text{C}$  at  $\theta_{p'_1} = 10$  deg. The graphs illustrate the contributions from neutrons in the  $1s^{1/2}$  and  $1p^{3/2}$  orbitals of  $^{12}\text{C}$  and their sum for the  $K^+ \Lambda$  production. Based on the plots of the radial wave functions  $g_{E_{K^+}}(p_m)$  and  $f_{E_{K^+}}(p_m)$  of the bound nucleon given in chapter 3, Fig. 3.4, these results clearly indicate the proportionality

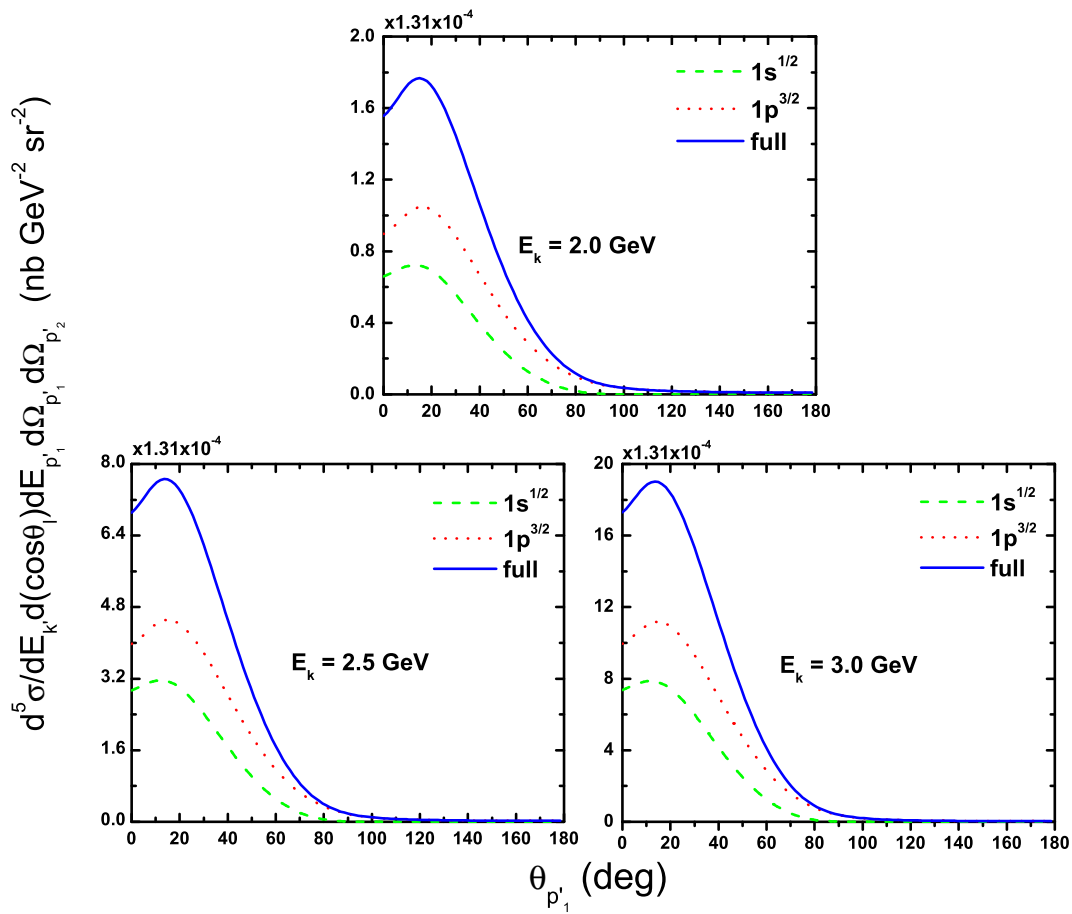


**Figure 7.2:** Angular distribution of the RPWIA differential cross section with respect to the kaon angle for the exclusive reaction  $A(\nu, \mu^- K^+ \Lambda)B$  on  $^{12}\text{C}$ . The quasifree kinematic inputs are fixed at  $\omega = 1.46 \text{ GeV}$ ,  $Q^2 = 0.05 \text{ GeV}^2$ , and  $p_m = 0.12 \text{ GeV}$ . The short-dashed (short-dash-dotted) line is the contribution from the neutrons in  $1s^{1/2}$  ( $1p^{3/2}$ ) orbital, and the solid line is their total contribution.

that may exist between momentum distributions of the differential cross section and the bound neutron inside the nucleus. The contribution from the  $1s^{1/2}$  dominates over the  $1p^{3/2}$  orbital for the missing momentum in the range  $p_m < 0.1 \text{ GeV}$ , whereas for the rest of the range the latter one dominates the former. Therefore, we can guarantee the generation of a significantly larger angular distribution of the differential cross section with respect to the kaon angle  $\theta_{p'_1}$  by



fixing the missing momentum in the range  $p_m \leq 0.3$  GeV. This was, in fact, the main purpose we planned to achieve with the missing momentum distribution plots.

Fig. 7.2 shows the angular distribution plots of the RPWIA differential cross section with respect to the kaon angle  $\theta_{p'_1}$ , and calculated within the quasifree kinematics, whereby the missing momentum is fixed at  $p_m = 0.12$  GeV. The contribution from the  $1p^{3/2}$  orbital is dominant for the whole range of the kaon angle, and the peak occurs for both  $1s^{1/2}$  and  $1p^{3/2}$  curves at forward angle. Moreover, the curves of the cross section level off slowly as we increase the kaon angle suggesting that there is a good chance to detect the produced  $K^+$  even in the wider nearby region of the very forward angle. It has been noted in other work[126, 127] that the RIA model offers more reliable analysis of the reaction with the produced kaon exiting in the direction of forward angles. It is also worth noting that the cross sections appear to increase with the incident energy of the neutrino even as we go far from the threshold region.

### 7.1.2 Open Kinematic Setting

We now present the numerical results of our plane wave limit analysis for the CC production process  $A(\nu, \mu^- K^+ \Lambda)B$  on  $^{12}\text{C}$  within the open kinematics arrangement. As was done for the case of the quasifree kinematics, the calculation of the laboratory frame four-momenta of the reaction was also performed in chapter 3, section 3.1.2, within the open kinematic setting. This

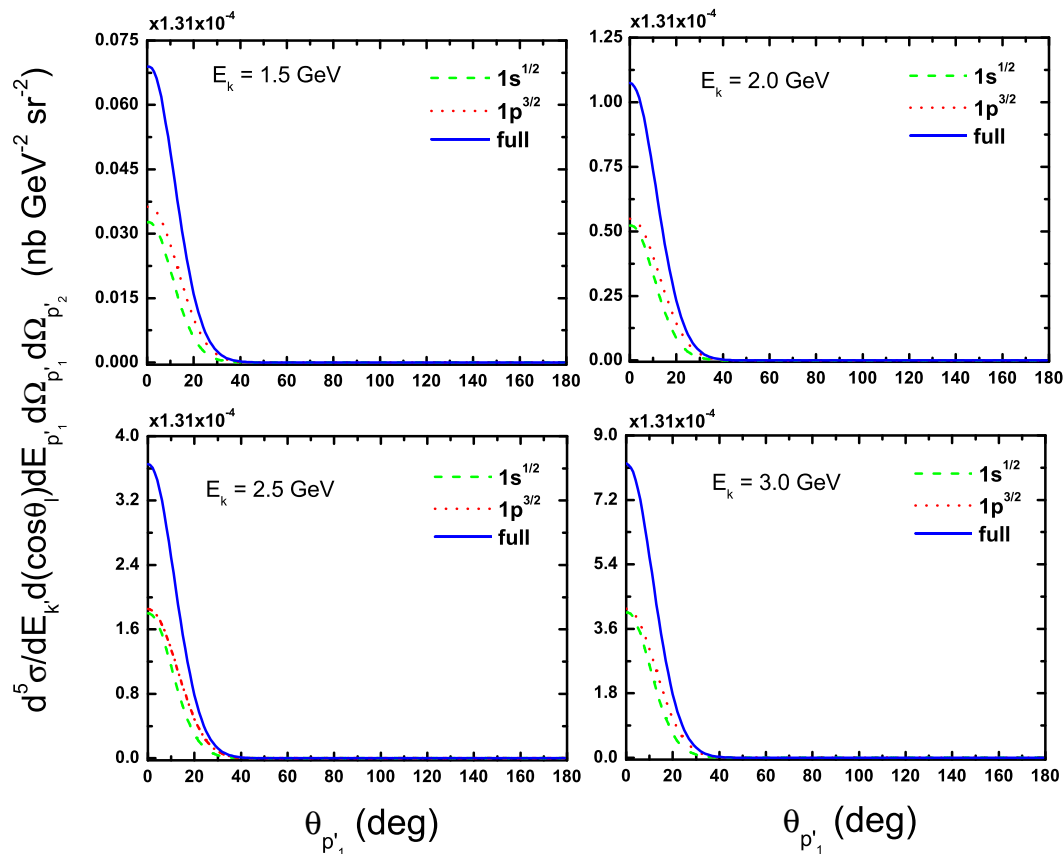


**Figure 7.3:** Angular distribution of the RPWIA differential cross section with respect to the kaon angle for neutrino-induced  $K^+ \Lambda$  production on  $^{12}\text{C}$  in energy range  $1.5 \leq E_k \leq 3$  GeV calculated under open kinematics. The curves correspond to the individual contributions of the orbitals and their sum at  $\omega = 1.32$  GeV,  $Q^2 = 0.12$  GeV<sup>2</sup>,  $T_K = 300$  MeV, and  $\theta_{p'_2} = 0.5$  deg.

setting appears to be more natural in that it lets  $p_m$  vary over a wide range; and thus making the entire momentum distribution of the bound nucleon accessible for the study of the exclusive

reaction. The angular and energy distributions of the differential cross section are generated at four incident energies of the neutrino in the range  $1.5 \leq E_k \leq 3.0$  GeV, whereas the energy transition and the norm-square of the four-momentum transfer are fixed at  $\omega = 1.32$  GeV and  $Q^2 = 0.12$  GeV<sup>2</sup>, respectively, for all cases. With this kinematic setting we will extensively explore the angular distributions with respect to kaon and hyperon angles as well as the energy distribution with respect to kinetic energies of the outgoing kaon. One of the remaining input variables,  $\theta_{p'_1}$ ,  $\theta_{p'_2}$ , and  $E_{p'_1}$ , can become a plotting variable while the other two remain fixed under open kinematic arrangement. Note, however, that for the study of the energy distribution of the differential cross section we use the kinetic energy  $T_K \simeq E_{p'_1} - M_K$  of the outgoing kaon as a plotting variable instead of the total energy  $E_{p'_1}$ .

Fig. 7.3 shows the kaon angle distribution of the RPWIA differential cross section for the neutrino-induced CC  $K^+ \Lambda$  production on  $^{12}\text{C}$  target. In this case, since  $\theta_{p'_1}$  is being used as the plotting variable, we now fix the kaon kinetic energy and hyperon angle at  $T_K = 300$  MeV and  $\theta_{p'_2} = 0.5$  deg, respectively. Working within the NL3 parametrization scheme to the relativistic shell model, we demonstrate the individual contributions of the bound neutrons in the  $1s^{1/2}$

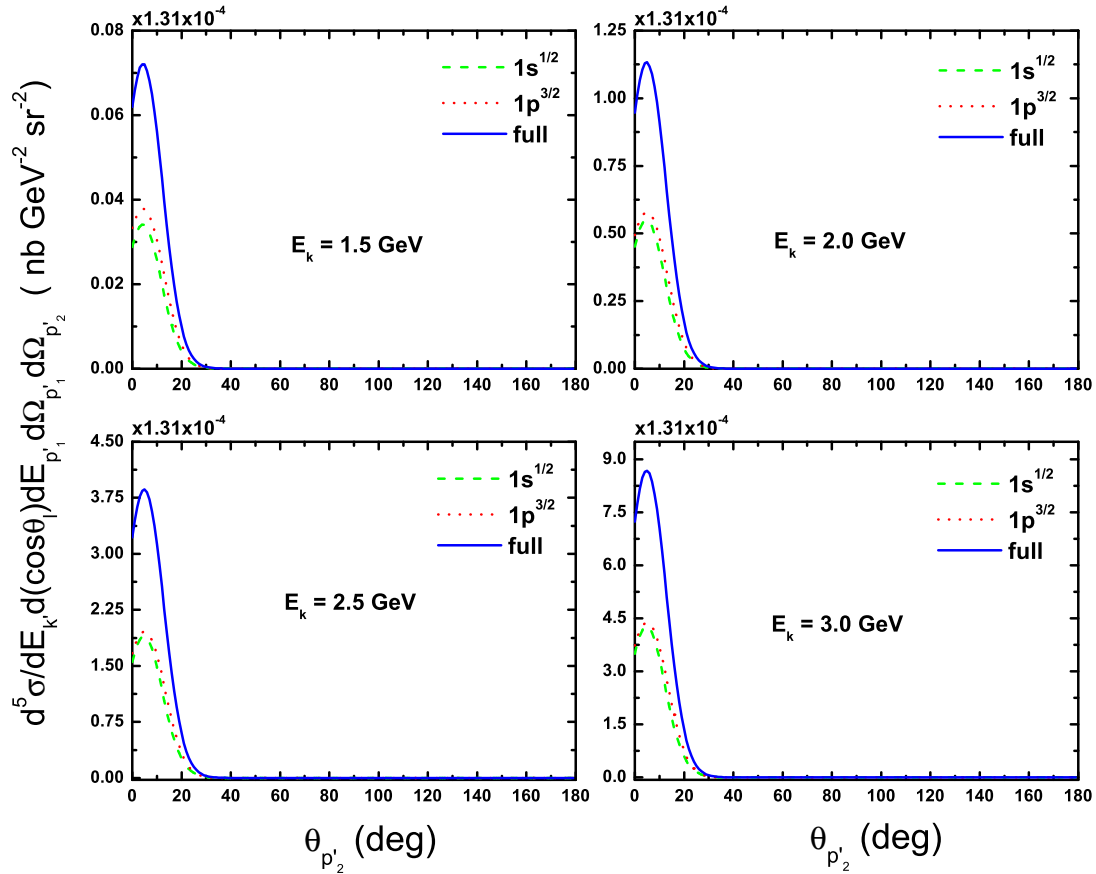


**Figure 7.4:** Angular distribution of the RPWIA differential cross section with respect to the  $\Lambda$ -hyperon angle for neutrino-induced  $K^+ \Lambda$  production on neutron orbital of  $^{12}\text{C}$  target under open kinematics at  $\theta_{p'_1} = 5$  deg and  $T_K = 300$  MeV.

and  $1p^{3/2}$  orbitals of  $^{12}\text{C}$  along with the overall contribution to the RPWIA differential cross section of the  $K^+ \Lambda$  production. The contributions from the two orbitals are nearly the same up to some scaling factor. The distribution curves are peaked in the forward angles and they level off faster than the curves for the quasifree production. As pointed out in the study of CC neutrino-nucleus scattering in Ref. [50], the shapes and peaks of the cross sections mirror the missing momentum distribution of the stuck nucleon inside the nucleus.

In a similar fashion, we show, in Fig. 7.4, the angular distribution of the RPWIA differential cross section with respect to the  $\Lambda$ -hyperon angle for neutrino-induced associated production of  $K^+\Lambda$  on neutron orbitals of  $^{12}\text{C}$ . Since  $\theta_{p'_2}$  is the plotting variable, we fix the angle and kinetic energy of the outgoing kaon at  $\theta_{p'_1} = 5$  deg and  $T_K = 300$  MeV, respectively. The contributions from both  $1s^{1/2}$  and  $1p^{3/2}$  orbitals attain their peaks at the most forward angles indicating the similar characteristic that the kaon and hyperon angular distributions may have in common. But one can also easily notice the slight shift of the hyperon angular distribution away from the most forward angle. Moreover, hyperon angular distributions fall off sharply before reaching 30 deg as is also the case for the outgoing kaon. In fact, we can tune the kinetic energy and angle of the kaon to be able to not only shift the cross section peak but also obtain a double-peaked  $\Lambda$ -hyperon angular distributions.

The open kinematic setting can also be used to explore the kaon energy dependence of the differential cross section of the reaction  $A(\nu, \ell KY)B$  calculated within the RPWIA framework. Thus, Fig. 7.5 shows the energy distributions of the RPWIA differential cross section with respect to the kinetic energy of the outgoing kaon for the reaction  $A(\nu, \mu^- K^+ \Lambda)B$  on  $^{12}\text{C}$ . Here we fix the angles of the outgoing kaon and hyperon at  $\theta_{p'_1} = 10$  deg and  $\theta_{p'_2} = 2.5$  deg,

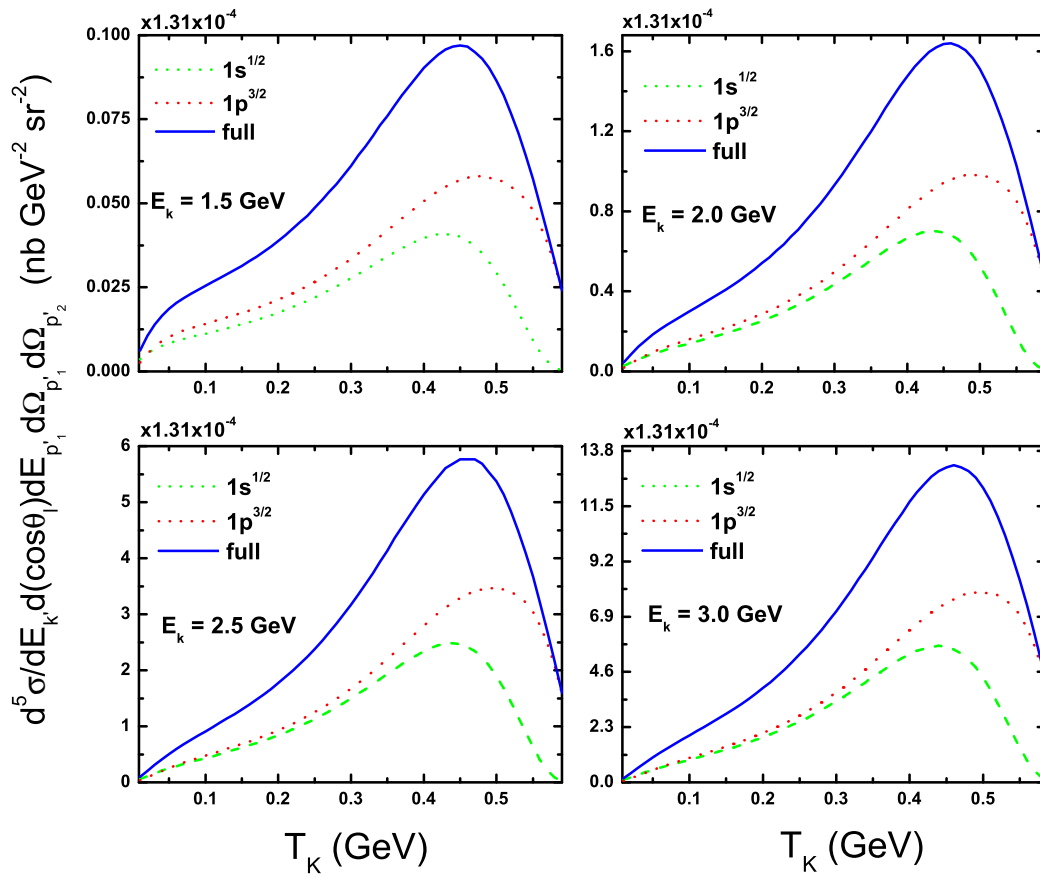


**Figure 7.5:** Energy distribution of the RPWIA differential cross section with respect to the kaon kinetic energy for the process  $^{12}\text{C}(\nu, \mu^- K^+ \Lambda)$  under open kinematic setting at  $\omega = 1.32$  GeV,  $Q^2 = 0.12$  GeV<sup>2</sup>,  $\theta_{p'_1} = 10$  deg, and  $\theta_{p'_2} = 2.5$  deg.

respectively, owing to the fact that  $T_K$  is the plotting variable. Upon fixing the angles of the outgoing kaon and hyperon at forward angles, the kaon energy distribution peaks from the  $^{12}\text{C}$  orbitals occur near  $T_K \simeq 450$  MeV for all of the neutrino energy values used. Moreover, above  $T_K = 300$  MeV the contribution from the  $1p^{3/2}$  orbital shows a significant dominance over the contribution from the neutron in the  $1s^{1/2}$  orbital of  $^{12}\text{C}$ .

## 7.2 RDWIA Analysis Results of the $K^+ \Lambda$ Production

In the previous chapter, we have developed the RDWIA formalism in order to describe the neutrino-induced associated production of strange particles on nuclei in terms of the five-fold differential cross section, Eq. (5.3.10), in the c.m. frame. In this section, we present results of the relativistic distorted wave analysis of the  $K^+ \Lambda$  production on  ${}^4\text{He}$ ,  ${}^{12}\text{C}$ ,  ${}^{16}\text{O}$ ,  ${}^{40}\text{Ca}$ , and  ${}^{208}\text{Pb}$ , at the neutrino incident energy  $E_k = 2.5$  GeV. The analysis is done using the coplanar kinematic setting. The c.m. frame four-momenta of the exclusive reaction are determined

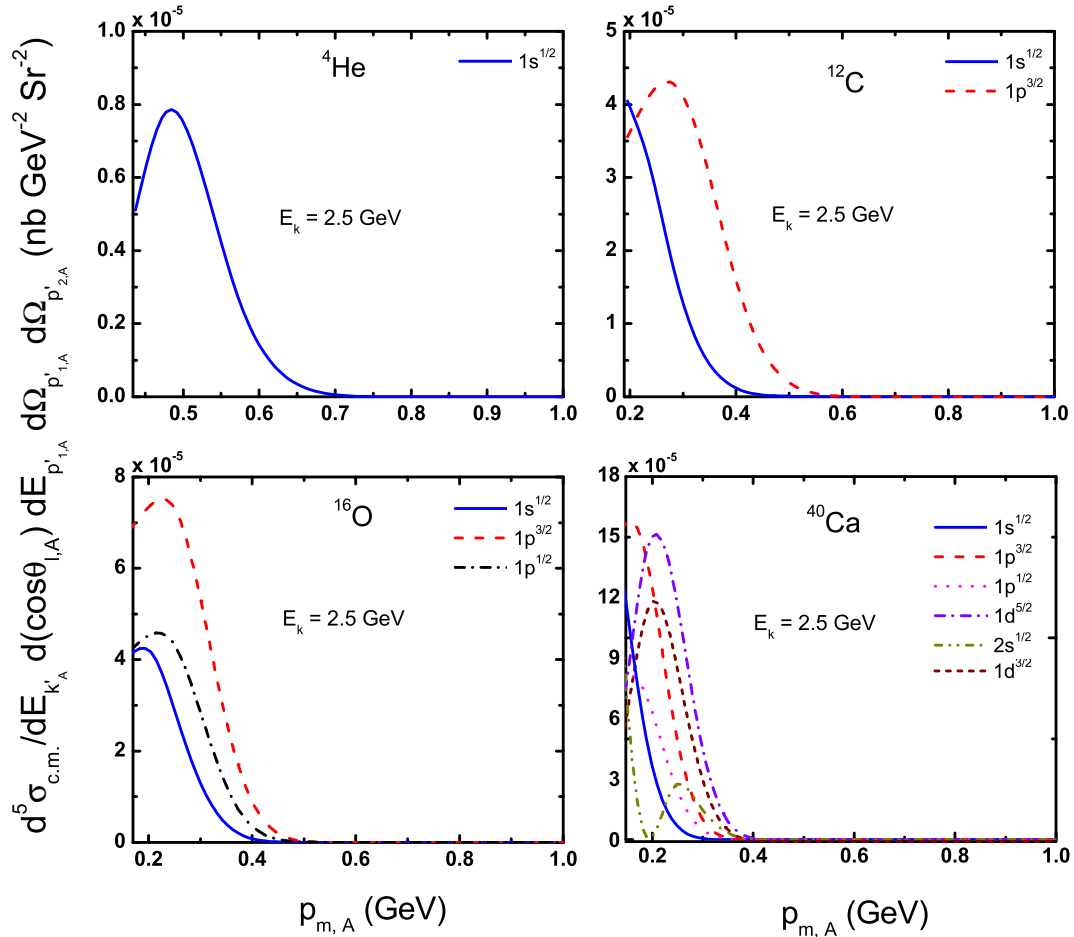


**Figure 7.6:** Missing momentum distribution of the RDWIA differential cross section for the neutrino-induced CC  $K^+ \Lambda$  production on  ${}^4\text{He}$  (top-left panel),  ${}^{12}\text{C}$  (top-right panel),  ${}^{16}\text{O}$  (bottom-left panel),  ${}^{40}\text{Ca}$  (bottom-right panel) nuclei in the c.m. frame under quasifree kinematics. Under this setting, the neutrino incident energy, energy transfer, and norm-square of four-momentum transfer, angle of outgoing kaon are fixed in laboratory frame at  $E_k = 2.5$  GeV,  $\omega = 1.4$  GeV,  $Q^2 = 0.12$  GeV<sup>2</sup>, and  $\theta_{p'_1} = 15$  deg, respectively.

by means of the Lorentz transformation, as described in last chapter, of the corresponding laboratory four-momenta which are calculated using the formulae we have developed in chapter 3. The serial Fortran 95 code for numerically computing the c.m. frame differential cross section was developed and then converted into MPI program for parallel computing on a cluster of computers each running Linux operating system as clearly illustrated in chapter 6. In what follows, the angle and energy dependence of the RDWIA differential cross section of the reaction will be shown and discussed in detail via quasifree and open kinematic settings. Under quasifree kinematics, we also compare results of the plane and distorted wave analyses of the neutrino-induced CC  $K^+ \Lambda$  production on  ${}^4\text{He}$ ,  ${}^{12}\text{C}$  and  ${}^{40}\text{Ca}$  nuclei.

In our RDWIA analysis of the exclusive reaction, we take into account only the outgoing kaon FSI effects by turning the hyperon FSI off. Thus, we can refer to this particular analysis as RDWIA-I as explained in chapter 4, Table 4.1; and as of now, however, we may use either RDWIA or RDWIA-I to mean the same thing. We have incorporated the distortion effects via the kaon wave function obtained by solving the Klein-Gordon equation, Eq. (4.5.3), modified to include the relativistic optical potential. In chapter 4, we have covered the theoretical and numerical aspects of this topic in great details. Owing to the nature of the problem, the kaon

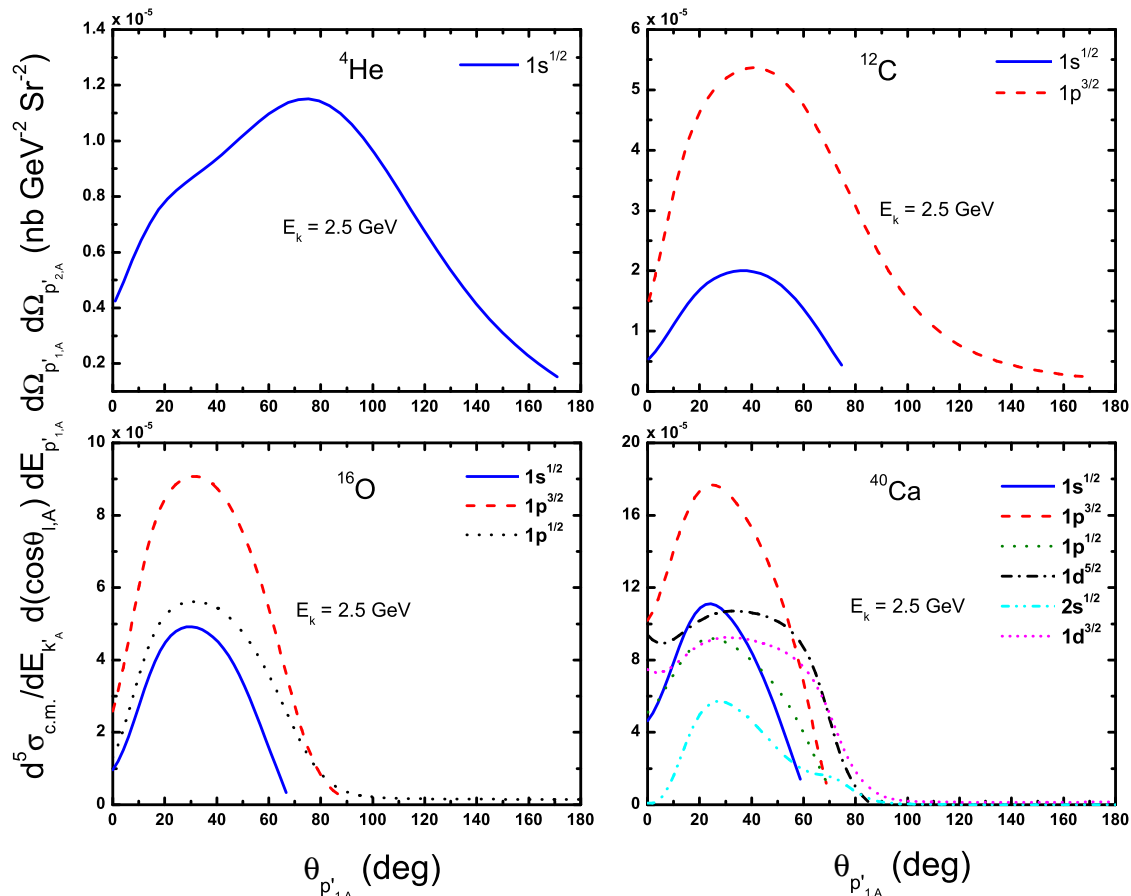


**Figure 7.7:** Kaon angle dependence of the RDWIA differential cross section for the exclusive reaction  $A(\nu, \mu^- K^+ \Lambda)B$  on  ${}^4\text{He}$  (top-left panel),  ${}^{12}\text{C}$  (top-right panel),  ${}^{16}\text{O}$  (bottom-left panel),  ${}^{40}\text{Ca}$  (bottom-right panel) nuclei in the c.m. frame under quasifree kinematics. Under this setting, the neutrino incident energy, missing momentum, energy transfer, and norm-square of four-momentum transfer are fixed at  $E_k = 2.5$  GeV,  $p_m = 0.12$  GeV,  $\omega = 1.4$  GeV, and  $Q^2 = 0.12$  GeV $^2$ , respectively, in laboratory frame.

distorted wave function is evaluated in terms of partial waves; and in our numerical study, this wave function is approximated by a total of  $l_3^{\max} + 1$  partial waves where we fix  $l_3^{\max}$  at 50. These partial waves are pre-calculated, at 200 points in a radial distance ranging from  $r_{\min} = 0.05$  fm to  $r_{\max} = 10$  fm for each partial wave, using the fourth-order Runge-Kutta algorithm in the c.m. frame of the outgoing kaon and residual nucleus and then stored as arrays to a datafile for later retrieval. We have employed the Gaussian quadrature to perform the numerical integration of the radial parts, which were defined in chapter 5, Eqs. (5.4.47) and (5.4.48), of the weak nuclear transition current. For both radial parts we have used  $N = 50$  integration points since the quadrature has shown excellent convergence above 40 points.

### 7.2.1 Quasifree Kinematic Setting

Under this kinematic setting, we present the missing momentum and kaon angle dependence of the c.m. frame RDWIA differential cross section describing the exclusive neutrino-induced CC  $K^+ \Lambda$  associated production on  ${}^4\text{He}$ ,  ${}^{12}\text{C}$ ,  ${}^{16}\text{O}$ , and  ${}^{40}\text{Ca}$ . We first fix the kinematic inputs and calculate the four-momenta of the interaction in the laboratory frame, and then determine the corresponding c.m. frame quantities using the Lorentz boost  $\beta_{\nu\Lambda}$  given in chapter 5, Eq. (5.2.2). In the laboratory frame, the neutrino incident energy, energy transfer, and norm-square of four-momentum transfer are fixed at  $E_k = 2.5$  GeV,  $\omega = 1.4$  GeV, and  $Q^2 = 0.12$  GeV<sup>2</sup>, respectively, to compute the c.m. frame missing momentum and angular distributions of the differential cross section using the MPI program running on a cluster of six computers.

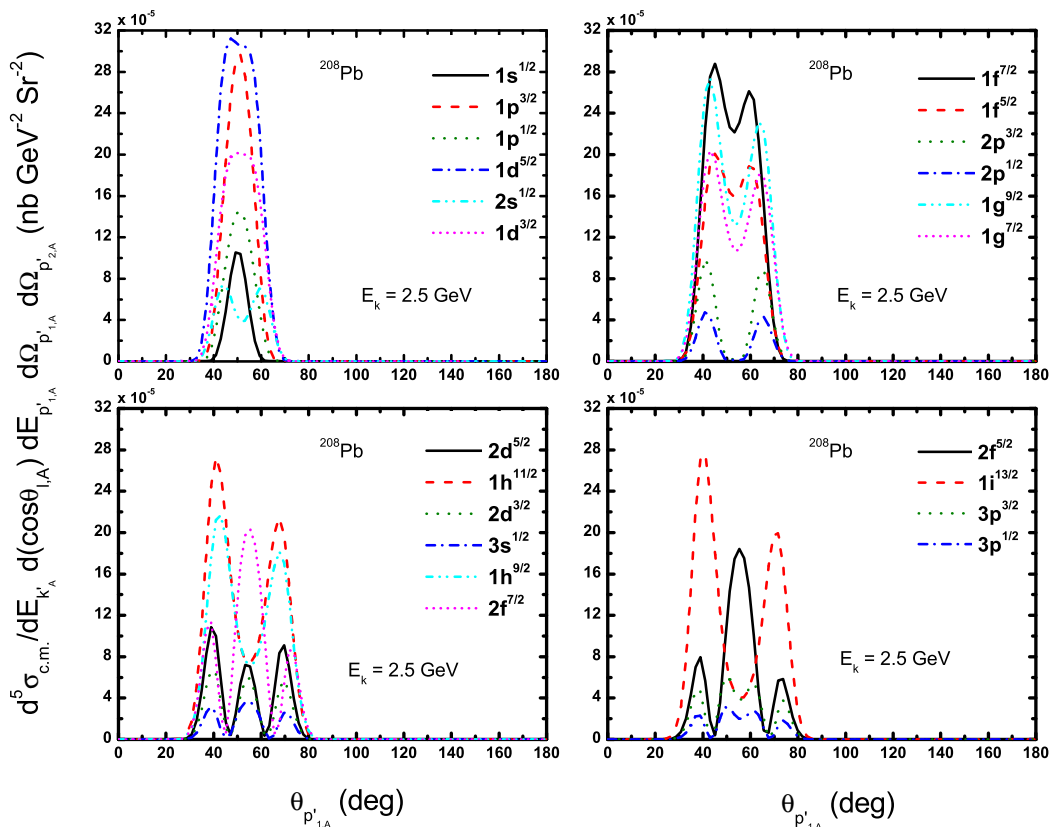


**Figure 7.8:** Kaon angle dependence of the RDWIA differential cross section, which is calculated via the open kinematics in the c.m. frame, for the neutrino-induced CC  $K^+ \Lambda$  production on neutron orbitals of  ${}^{208}\text{Pb}$ . Under this kinematic setting, the laboratory frame kinematic inputs are fixed at  $E_k = 2.5$  GeV,  $\omega = 2.0$  GeV,  $Q^2 = 0.12$  GeV<sup>2</sup>,  $T_K = 350$  MeV, and  $\theta_{p'_2} = 15$  deg.

Fig. 7.6 shows the c.m. frame missing momentum of the RDWIA differential cross section of neutrino-induced associated  $K^+ \Lambda$  production on  ${}^4\text{He}$ ,  ${}^{12}\text{C}$ ,  ${}^{16}\text{O}$  and  ${}^{40}\text{Ca}$ , whereby the outgoing kaon angle is fixed at  $\theta_{p'_1} = 15$  deg in laboratory frame which is equivalent to  $\theta_{p'_{1,A}} \simeq 16.42$  deg in the c.m. frame. At the neutrino incident energy  $E_k = 2.5$  GeV, (i) the missing momentum distribution for the exclusive process on the neutron in the  $1s^{1/2}$  orbital of  ${}^4\text{He}$  (top-left panel) peaks near  $p_{m,A} = 0.5$  GeV, and then levels off starting from  $p_{m,A} = 0.65$  GeV; (ii) above  $p_{m,A} = 0.25$  GeV, the contribution of  $1p^{3/2}$  orbital to the overall cross section of the reaction on  ${}^{12}\text{C}$  (top-right panel) is significantly dominates the one on the  $1s^{1/2}$  orbital, and the contribution of latter dies out more rapidly than that of the former; (iii) the missing momentum distribution

from the  $1s^{1/2}$ ,  $1p^{3/2}$ , and  $1p^{1/2}$  orbitals of  $^{16}\text{O}$  (bottom-left panel) attain their peaks in the range:  $0.20 \leq p_{m,A} \leq 0.25$  GeV with that of the  $1p^{3/2}$  orbital being the most dominant one though non-negligible contributions come to the overall cross section from all orbitals; and (iv) for the missing momentum distribution of the neutrino-induced CC production process on  $^{40}\text{Ca}$  (bottom-right panel), almost all orbitals have their cross sections peaked in the range:  $0.15 \leq p_{m,A} \leq 0.30$ .

Fig. 7.7 shows the c.m. frame kaon angle distributions of the RDWIA differential cross section of the CC reaction process  $A(\nu, \mu^- K^+ \Lambda)B$  on  $^4\text{He}$ ,  $^{12}\text{C}$ ,  $^{16}\text{O}$  and  $^{40}\text{Ca}$ , whereby the incident neutrino energy and missing momentum is fixed at  $E_k = 2.5$  GeV and  $p_m = 0.12$  GeV, respectively, in laboratory frame which are equivalent to  $E_{k,A} \simeq 2.08$  GeV and  $p_{m,A} \simeq 0.27$  GeV in the c.m. frame. The top-left panel displays the kaon angle distribution of the production process on  $^4\text{He}$ . For such a target the only contribution to differential cross section of the CC associated production comes from the neutron in  $1s^{1/2}$  orbital. Note also that the cross section does not have a narrow peak instead it appears to be broader, slowly increasing until  $\theta_{p'_{1,A}} \simeq 75$  deg and then shows slow decrease all the way up to the most backward angle. The top-right panel displays the  $1s^{1/2}$  and  $1p^{3/2}$  contributions to the kaon angle distribution of differential

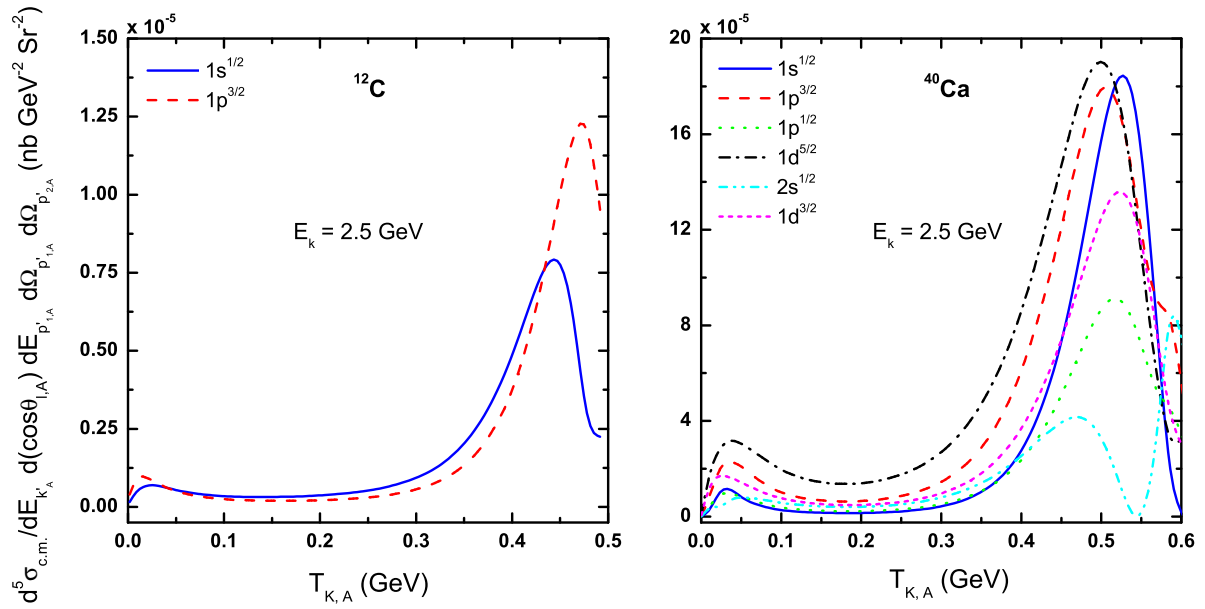


**Figure 7.9:** Kaon kinetic energy dependence of the RDWIA differential cross section, which is calculated via the open kinematics in the c.m. frame, for the neutrino-induced CC  $K^+ \Lambda$  production on neutron orbitals of  $^{12}\text{C}$  (left panel) and  $^{40}\text{Ca}$  (right panel). Under this kinematic setting, the laboratory frame kinematic inputs are fixed at  $E_k = 2.5$  GeV,  $\omega = 1.4$  GeV,  $Q^2 = 0.12$  GeV<sup>2</sup>, and  $\theta_{p'_1} = \theta_{p'_2} = 5$  deg.

cross section for the  $K^+ \Lambda$  production process on  $^{12}\text{C}$  under the quasifree kinematic setting. The curves clearly show the dominance of the  $1p^{3/2}$  orbital over the whole range of the c.m. frame kaon angle; and this dominance is more magnified in the angle range where both curves attain their peaks, i.e., near  $\theta_{p'_{1,A}} \simeq 40$  deg. The bottom-left panel shows angular distributions of the production process on  $1s^{1/2}$ ,  $1p^{3/2}$  and  $1p^{1/2}$  orbitals of  $^{16}\text{O}$ . The results from this target do not give any peculiar shape different from the  $^{12}\text{C}$  target except that the cross section peaks occur at relatively smaller kaon angle, i.e.,  $\theta_{p'_{1,A}} \simeq 30$  deg. The bottom-right panel displays the contribution of all orbitals to the overall differential cross section describing the CC production process on  $^{40}\text{Ca}$ . The contributions from  $s$ - and  $p$ -shell neutrons are relatively sharp-peaked at forward angles as opposed to those from  $d$ -shell neutrons which are broad-peaked over a wide



range of forward angles. Here also the dominance of the  $1p^{3/2}$  orbital contribution is highly pronounced at its beak.

In general, if one compares the contributions of  $1s^{1/2}$  orbitals of the four nuclei, the peak of the missing momentum distribution increases and shifts toward smaller missing momentum region as we go from  $^4\text{He}$  to  $^{40}\text{Ca}$ ; and the same can be inferred for the rest of the orbitals. Moreover, similar characteristics can be observed if one compares angular distributions from individual orbitals across the four nuclei used in this study. Note also that under quasifree kinematics, owing to the relatively larger binding energy,  $E_b \geq 20$  MeV, which is the case for low-lying neutron orbitals, the associated cross section plots are forced to have cutoff points. This is evident from the quadratic equation: Eq. (3.1.23) of chapter 2, which was derived in order to determine kaon energy  $E_{p'_1}$  as its physical solution. Thus, an attempt to solve such an equation for larger binding energies leads to a negative discriminator of the corresponding quadratic formula as one keeps increasing  $\theta_{p'_1}$  beyond some critical angle.

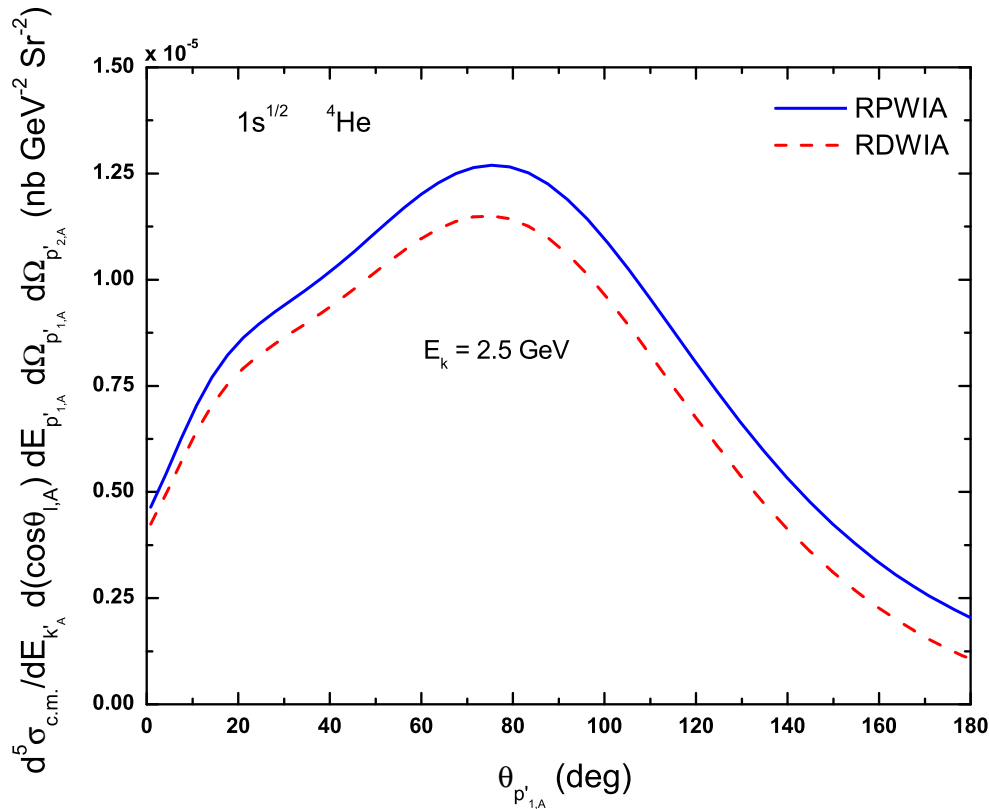


**Figure 7.10:** Comparison between the kaon angle dependence of the RPWIA (solid blue line) and RDWIA (dashed red line) differential cross sections, which are calculated via the quasifree kinematics in the c.m. frame, of the neutrino-induced CC  $K^+\Lambda$  production on  $^4\text{He}$ . The laboratory frame kinematic inputs are fixed at  $E_k = 2.5$  GeV,  $p_m = 0.12$  GeV,  $\omega = 1.4$  GeV, and  $Q^2 = 0.12$  GeV $^2$ .

### 7.2.2 Open Kinematic Setting

Under this kinematic setting, we illustrate kaon angle and energy dependences of the RDWIA differential cross section of the neutrino-induced CC  $K^+\Lambda$  production on nuclei. The calculation procedure of this kinematic setting is significantly different from quasifree kinematic setting; and that includes the use of different sets of kinematic quantities as inputs which ultimately results in different values of the output four-momenta of the reaction. For both angular and energy distributions of the differential cross section the following two laboratory frame quantities remain fixed at  $E_k = 2.5$  and  $Q^2 = 0.12$  GeV $^2$ . Then all necessary specifications are fed into the parallel

program to calculate the five-fold differential cross section of the reaction  $A(\nu, \mu^- K^+ \Lambda)B$  as a function of either angle or kinetic energy of the outgoing kaon.

Fig. 7.8 depicts the angular distribution of the c.m. frame RDWIA differential cross section with respect to the outgoing kaon angle for the reaction  $A(\nu, \mu^- K^+ \Lambda)B$  on  $^{208}\text{Pb}$  under open kinematics at  $\omega = 2.0$  GeV,  $T_K = 350$  MeV and  $\theta_{p'_2} = 15$  deg. The top-left panel displays the contributions from the first six neutron orbitals of  $^{208}\text{Pb}$ , the top-right panel displays the next six neutron orbitals, and so on. The angular distribution curves have their peaks shifted away from the most forward angle, and almost no contribution comes from ranges:  $\theta_{p'_{1,A}} \lesssim 25$  deg and  $\theta_{p'_{1,A}} \gtrsim 80$  deg of the kaon angle for all orbitals. It is also worth noting that the shapes of the cross section have their origin in the dynamic part of the exclusive reaction, and the kinematic part with a very smooth angle dependence almost appears as a constant factor in the whole range of the kaon angle. The kaon angle range, whereby the cross section peaks occur, corresponds to the laboratory frame missing momentum range:  $p_m \lesssim 300$  MeV. As we go from the lower to the upper  $s$ -shells of  $^{208}\text{Pb}$ , the number of cross section peaks increases by certainly compromising their peak height. The same can be inferred for the rest of the  $^{208}\text{Pb}$  shells.

Fig. 7.9 shows the energy dependence of the c.m. frame RDWIA differential cross section with respect to the kinetic energy of the outgoing kaon for the reaction  $A(\nu, \mu^- K^+ \Lambda)B$  on  $^{12}\text{C}$  (left panel) and  $^{40}\text{Ca}$  (right panel) under open kinematic setting at  $\omega = 1.4$  GeV, and  $\theta_{p'_1} = \theta_{p'_2} = 5$  deg. We first focus on the left panel. The energy distributions of the RDWIA

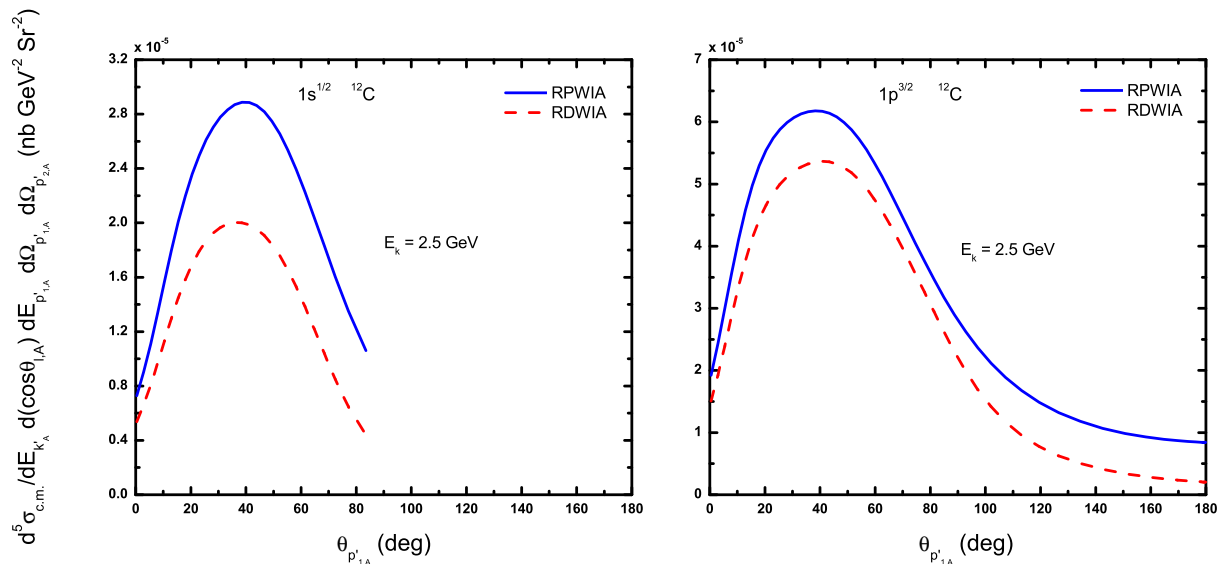


**Figure 7.11:** Comparison between the kaon angle dependence of the RPWIA (solid blue line) and RDWIA (dashed red line) differential cross sections, which are calculated via the quasifree kinematics in the c.m. frame, of the neutrino-induced CC  $K^+ \Lambda$  production on  $^{12}\text{C}$ . The laboratory frame kinematic inputs are fixed at  $E_k = 2.5$  GeV,  $p_m = 0.12$  GeV,  $\omega = 1.4$  GeV, and  $Q^2 = 0.12$  GeV<sup>2</sup>.

differential cross section of the reaction from  $1s^{1/2}$  and  $1p^{3/2}$  orbitals of  $^{12}\text{C}$  attain their peaks at  $T_{K,A} \simeq 450$  MeV and  $T_{K,A} = 475$  MeV, respectively. On the other hand, below  $T_{K,A} \simeq 300$  MeV the two energy distributions appear to show only smooth dependence on the kinetic energy of the outgoing kaon. We can also notice that, the contribution of the  $1p^{3/2}$  orbital of  $^{12}\text{C}$  prominently dominates that of the  $1s^{1/2}$  orbital above  $T_{K,A} \simeq 450$  MeV. Moving on to the right panel, we have the contributions of the  $^{40}\text{Ca}$  orbitals to the overall energy distribution the neutrino incident energy  $E_k = 2.5$  GeV. The prominent contributions of all orbitals comes for the kaon kinetic energy in the range  $400 \leq T_{K,A} \leq 600$  MeV, where they all attain their respective peaks with  $1s^{1/2}$ ,  $1p^{3/2}$  and  $1d^{5/2}$  contributions dominating the pack.

### 7.3 Comparison between RPWIA and RDWIA-I Results

In this section, we will demonstrate what effect the consideration of the FSI of the outgoing kaon with the residual nucleus has on the differential cross section of the CC reaction  $A(\nu, \mu^- K^+ \Lambda)B$  under both kinematic settings. Under quasifree kinematics the exclusive differential cross sections obtained within the two frameworks are compared for  ${}^4\text{He}$ ,  ${}^{12}\text{C}$ , and  ${}^{40}\text{Ca}$  targets, whereas under open kinematic setting the comparison is done using  ${}^{208}\text{Pb}$  nuclear target. We will accomplish this task by comparing RDWIA-I analysis results against those from the baseline calculations done in the plane wave limit. Note that, in the case of RDWIA-I analysis the calculations are carried out with the assumption that the hyperon FSI is switched off at all time. For individual nuclei considered we have performed orbital-wise comparison.

The c.m. frame expression for the RPWIA differential cross section is exactly the same as that of the RDWIA model given in Eq. (5.3.10) with only one exception, that is, the transition matrix element should be re-calculated by replacing the kaon distorted wave with the kaon plane wave

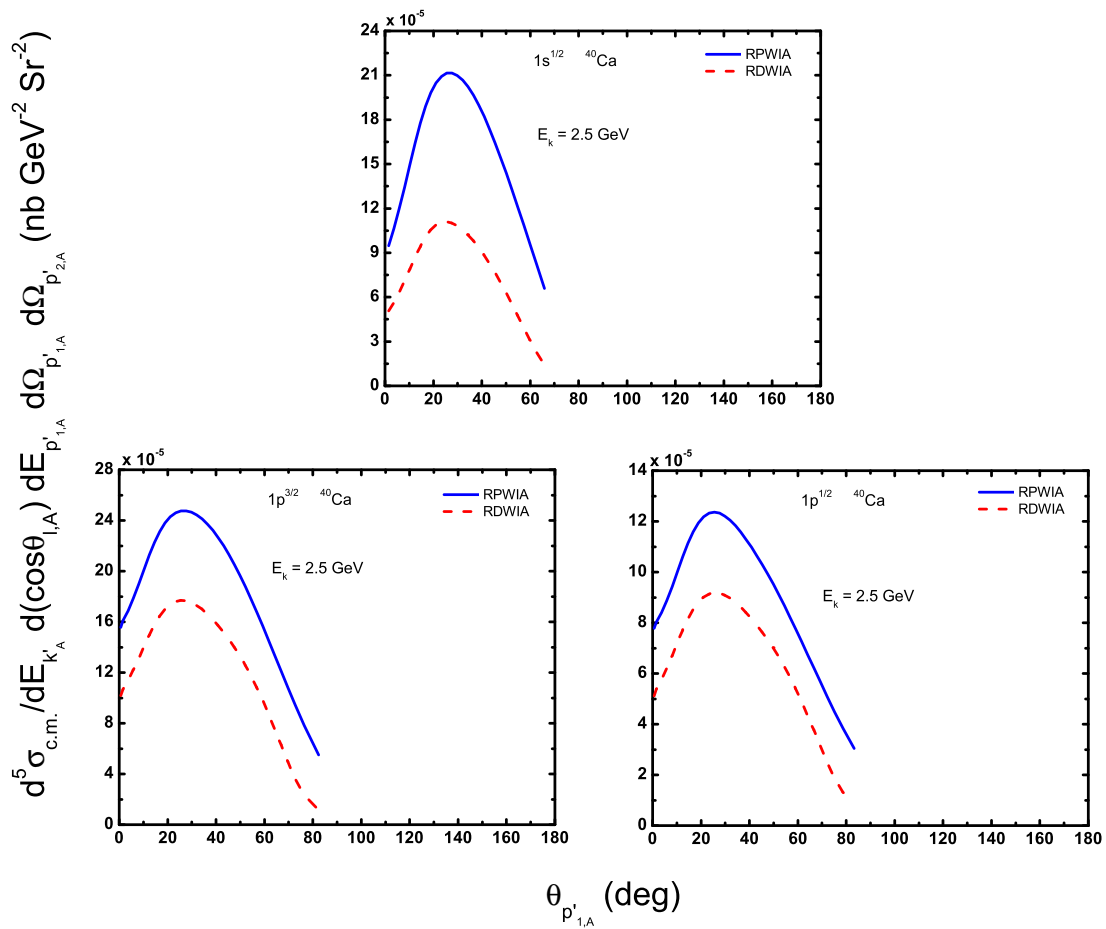


**Figure 7.12:** Comparison between the kaon angle dependence of the RPWIA (solid blue line) and RDWIA (dashed red line) differential cross sections, which are calculated via the quasifree kinematics in the c.m. frame, of the neutrino-induced CC  $K^+ \Lambda$  production on  $1s^{1/2}$  (top panel),  $1p^{3/2}$  (bottom-left panel), and  $1p^{1/2}$  (bottom-right panel) orbitals of  ${}^{40}\text{Ca}$ . The laboratory frame kinematic inputs are fixed at  $E_k = 2.5$  GeV,  $p_m = 0.12$  GeV,  $\omega = 1.4$  GeV, and  $Q^2 = 0.12$  GeV $^2$ .

according to Eq. (5.4.52) defined in chapter 2. In other words, we only need to substitute the complex-valued and numerical functions  $R_{l_3, p'_{1,B}}^{(+)}(x)$  with the real-valued and analytical spherical Bessel functions  $j_{l_3}(xp'_{1,B})$ , which are the radial parts in the partial wave expansion of the kaon

plane wave function. Thus, in the plane wave limit the radial parts of  $\mathcal{H}^\mu$ : Eqs. (5.4.47) and (5.4.48), are modified as follows:

$$\mathcal{G}_E^\kappa \begin{matrix} l_1 & l_3 \\ p'_A & p'_{1,B} \end{matrix} \longrightarrow \int dx x j_{l_1}(xp'_A) j_{l_3}(xp'_{1,B}) g_{E\kappa}(x), \quad (7.3.1)$$

$$\mathcal{F}_E^\kappa \begin{matrix} l_1 & l_3 \\ p'_A & p'_{1,B} \end{matrix} \longrightarrow \int dx x j_{l_1}(xp'_A) j_{l_3}(xp'_{1,B}) f_{E\kappa}(x). \quad (7.3.2)$$

Under quasifree kinematics, for all calculations the laboratory frame input quantities, neutrino incident energy, missing momentum, energy transfer, and norm-square of four-momentum transfer, remain fixed at  $E_k = 2.5$  GeV,  $p_m = 0.12$  GeV,  $\omega = 1.4$  GeV, and  $Q^2 = 0.12$  GeV<sup>2</sup>, respectively. Fig. 7.10 shows the kaon angle dependence of the RPWIA (solid blue line) and

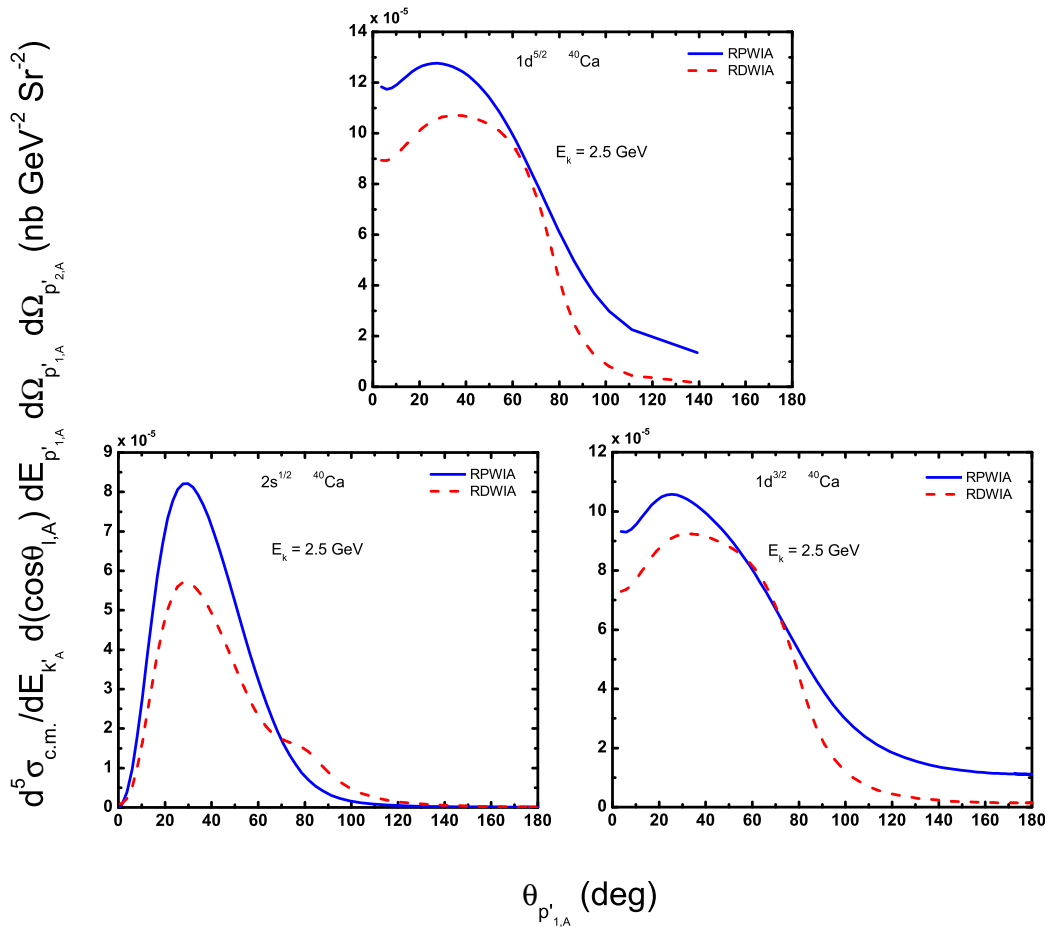


**Figure 7.13:** Comparison between the kaon angle dependence of the RPWIA (solid blue line) and RDWIA (dashed red line) differential cross sections, which are calculated via the quasifree kinematics in the c.m. frame, of the neutrino-induced CC  $K^+ \Lambda$  production on  $1d^{5/2}$  (top panel),  $2s^{1/2}$  (bottom-left panel), and  $1d^{3/2}$  (bottom-right panel) orbitals of  $^{40}\text{Ca}$ . The laboratory frame kinematic inputs are fixed at  $E_k = 2.5$  GeV,  $p_m = 0.12$  GeV,  $\omega = 1.4$  GeV, and  $Q^2 = 0.12$  GeV<sup>2</sup>.

RDWIA (dashed red line) differential cross sections of the exclusive reaction  $A(\nu, \mu^- K^+ \Lambda)B$  on  $^4\text{He}$ . The RDWIA-I prediction of the reaction cross section is characterized by a reduced angular distribution for all range of the kaon angle in comparison to the RPWIA result. This feature is more pronounced far from the very forward angle. The reduction caused by the kaon FSI is about 8% (54%) in the nearby region of the very forward (backward) angle. Note, however, that we do not see any significant alteration to the overall shape of the RPWIA differential cross section due to the consideration of the kaon FSI.

Fig. 7.11 shows the effect of the kaon final state interaction on the angular distributions of the cross section for the neutrino-induced  $K^+ \Lambda$  production process on  $1s^{1/2}$  and  $1p^{3/2}$  orbitals of  $^{12}\text{C}$ . Here also we observe that at neutrino incident energy  $E_k = 2.5$  GeV the kaon FSI does not substantially affect the shape of the angular distributions though it results in a significant reduction of the overall differential cross section. At a given kaon angle, the kaon FSI effect is slightly stronger on the  $1s^{1/2}$  contribution than that of the  $1p^{3/2}$ . But for both contributions, the kaon FSI has stronger influence in the region far away from the very forward angle.

Fig. 7.12 shows the comparison between the RPWIA and RDWIA differential cross sections of the neutrino-induced CC  $K^+ \Lambda$  production on  $^{40}\text{Ca}$  orbitals:  $1s^{1/2}$  (top panel),  $1p^{3/2}$  (bottom left panel), and  $1p^{1/2}$  (bottom right panel), whereas Fig. 7.13 displays the similar comparison

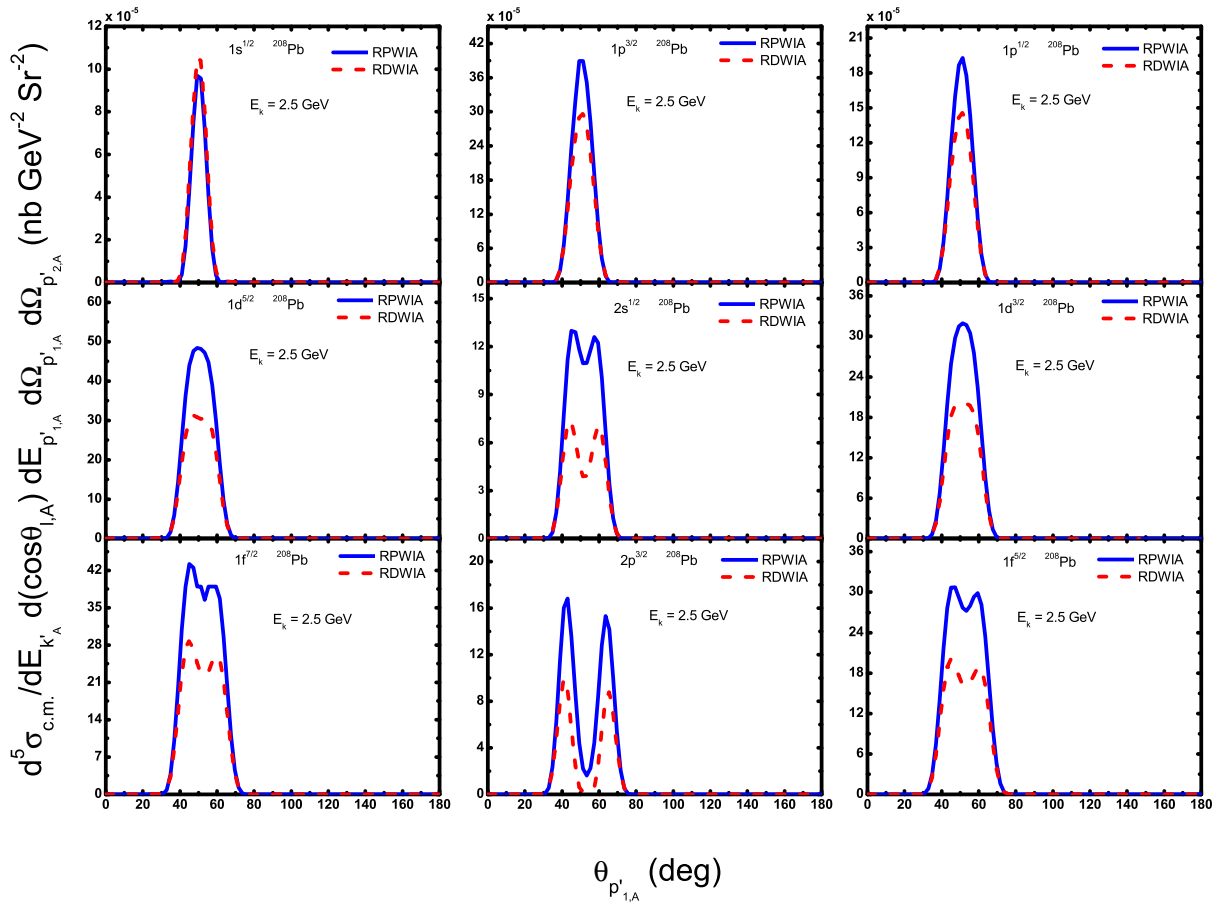


**Figure 7.14:** Angular distributions of the differential cross section with respect to the kaon angle for the exclusive reaction  $A(\nu, \mu^- K^+ \Lambda)B$  on bound neutrons in  $1s^{1/2}$ ,  $1p^{3/2}$ ,  $1p^{1/2}$ ,  $1d^{5/2}$ ,  $2s^{1/2}$ ,  $1d^{3/2}$ ,  $1f^{7/2}$ ,  $2p^{3/2}$ , and  $1f^{5/2}$  orbitals of  $^{208}\text{Pb}$  calculated in the RPWIA (solid blue line) and RDWIA (dashed red line) frameworks.

for the contributions coming from the rest of the orbitals:  $1d^{5/2}$  (top panel),  $2s^{1/2}$  (bottom left panel), and  $1d^{3/2}$  (bottom right panel). The kaon FSI effect on the differential cross sections of the neutrino-induced CC  $K^+ \Lambda$  production on individual orbitals of  $^{40}\text{Ca}$  is quite visible in almost the same way as it has influenced the results of the reaction on  $^4\text{He}$  and  $^{12}\text{C}$  discussed earlier. The contributions from the  $1s^{1/2}$ ,  $1p^{3/2}$  and  $1p^{1/2}$  orbitals of  $^{40}\text{Ca}$ , respectively, show about 45%, 30% and 25% reductions in the nearby region of the very forward angle due to the kaon optical potential. The last three orbitals of  $^{40}\text{Ca}$  also display similar reductions at the very forward angle. The kaon distortion also alters the shape of the reaction cross sections as the kaon angle increases. As a result, the kaon FSI gives rise to a significant enhancement of the angular distribution coming from the  $2s^{1/2}$  orbital above 70 deg of kaon angle.

Under open kinematics, we investigate the effect of the kaon FSI on the neutrino-induced associated production from heavy nuclei with particular interest in  $^{208}\text{Pb}$ . The RPWIA and RDWIA angular distributions are compared by fixing the laboratory frame quantities,  $E_k$ ,  $Q^2$ ,  $\omega$ ,  $T_K$  and  $\theta_{p'_2}$  at 2.5 GeV, 0.12 GeV<sup>2</sup>, 2.0 GeV, 350 MeV and 15 deg, respectively. Figs. 7.14,

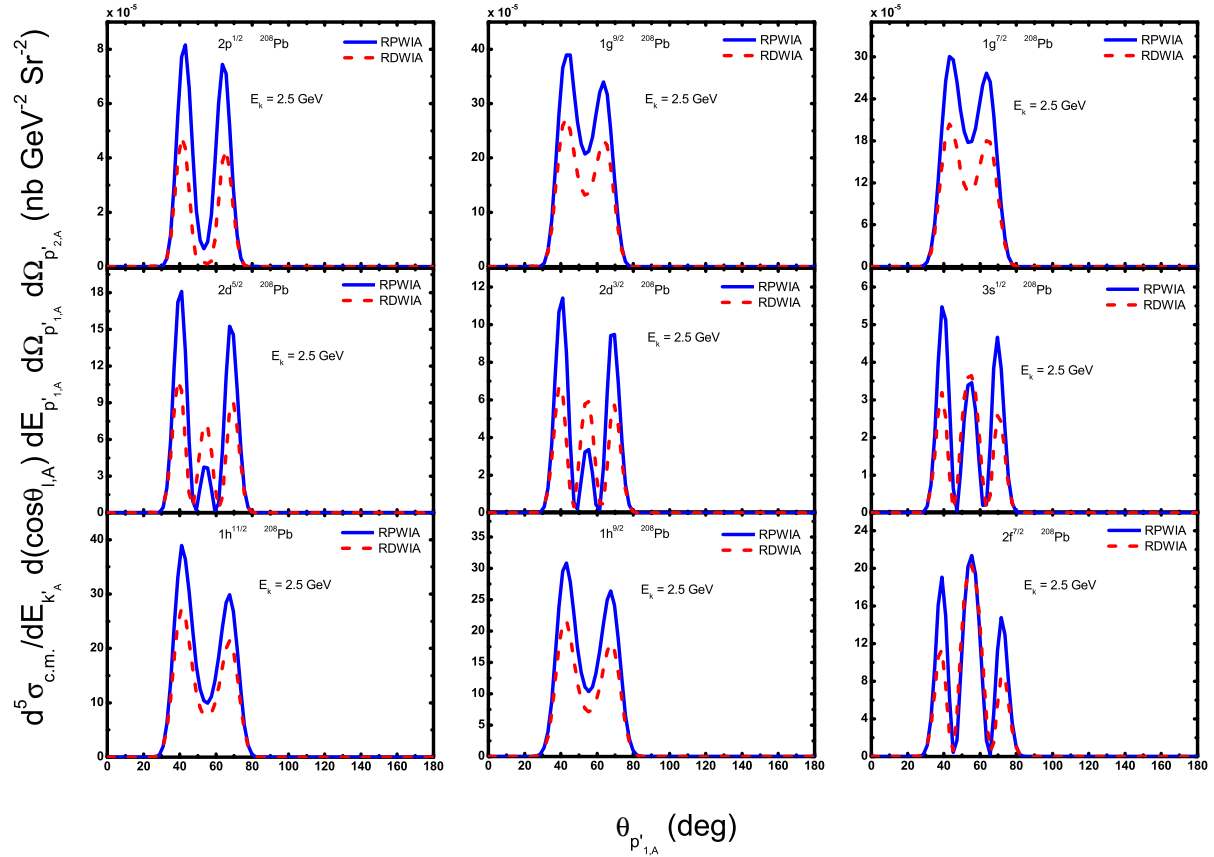


**Figure 7.15:** Angular distributions of the differential cross section with respect to the kaon angle for the exclusive reaction  $A(\nu, \mu^- K^+ \Lambda)B$  on bound neutrons in  $2p^{1/2}$ ,  $1g^{9/2}$ ,  $1g^{7/2}$ ,  $2d^{5/2}$ ,  $2d^{3/2}$ ,  $3s^{1/2}$ ,  $1h^{11/2}$ ,  $1h^{9/2}$ , and  $2f^{7/2}$  orbitals of  $^{208}\text{Pb}$  calculated in the RPWIA (solid blue line) and RDWIA (dashed red line) frameworks.

7.15, and 7.16 depict the c.m. frame kaon angular dependence of the RPWIA and RDWIA differential cross sections for the neutrino-induced CC  $K^+ \Lambda$  production on twenty-two neutron orbitals of  $^{208}\text{Pb}$ . In general, the consideration of the kaon FSI results in the reduction the angular distributions of the differential cross section over the entire range of kaon angle with the exception of the contributions coming from the  $1s^{1/2}$ ,  $2d^{5/2}$ ,  $2d^{3/2}$  and  $3s^{1/2}$  orbitals. Under this kinematic setting, the influence of kaon distortion is more prominent near the peaks of the angular distributions without causing a substantial alteration of their shapes.

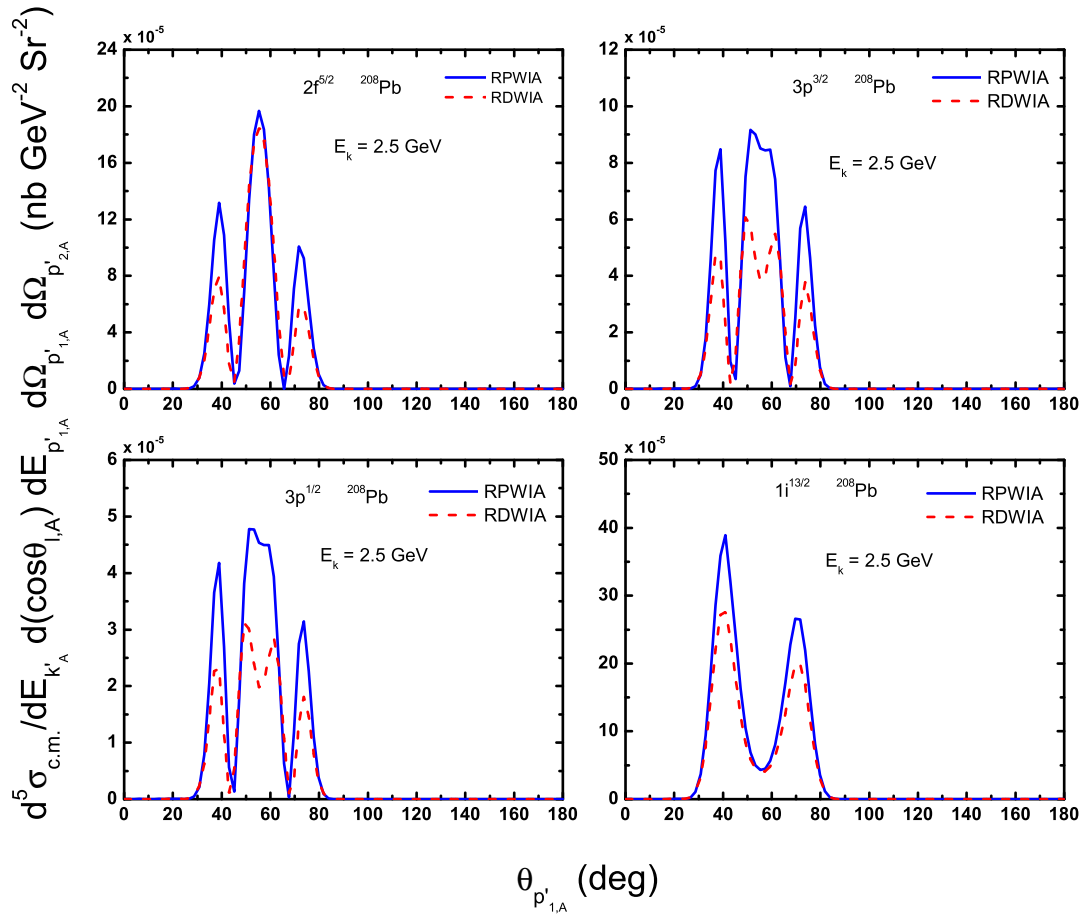


**Figure 7.16:** Angular distributions of the differential cross section with respect to the kaon angle for the exclusive reaction  $A(\nu, \mu^- K^+ \Lambda)B$  on bound neutrons in  $2f^{5/2}$ ,  $3p^{3/2}$ ,  $3p^{1/2}$ , and  $1i^{13/2}$  orbitals of  $^{208}\text{Pb}$  calculated in the RPWIA (solid blue line) and RDWIA (dashed red line) frameworks.



## Chapter 8

# Summary and Conclusion

We have studied the neutrino-induced associated production of strange particles on nuclei using a fully relativistic formalism within both the RPWIA and RDWIA frameworks in the energy region between 1 GeV to 3 GeV. We have developed these models to be of a general nature which is suitable for the investigation of at least twelve production channels listed in Table 1.1, but we have focused our discussion on the numerical predictions of the charged current and strangeness conserving  $K^+\Lambda$  production channel because of not only its relatively larger cross section as reported by Refs. [25, 29] but also its experimental feasibility to measure the polarization of the  $\Lambda$ -hyperon. Moreover, we have selected five closed shell nuclei:  ${}^4\text{He}$ ,  ${}^{12}\text{C}$ ,  ${}^{16}\text{O}$ ,  ${}^{40}\text{Ca}$ , and  ${}^{208}\text{Pb}$  as targets on which the exclusive reaction process occurs. The four-momenta of the reaction have been calculated in the laboratory frame under coplanar geometric setting; and they can always be transformed into the c.m. frame using the Lorentz boost when necessary.

The successful implementation of relativistic impulse approximation in the theoretical description of the production process  $A(\nu, \ell KY)B$  has led us to assume that neutrino-nucleus scattering proceeds via a single-boson-exchange which would subsequently interact with a single bound nucleon inside the nucleus rather than the nucleus as a whole. In other words, the rest of the bound nucleons are assumed to behave as spectators in the scattering process. In addition, the elementary weak current operator remains unaltered as the underlying process on free nucleon [34, 35] is embedded in the nuclear medium. The nuclear medium effects such as Fermi motion, Pauli blocking, and nuclear binding have been incorporated via the nucleon bound state wave function calculated from the relativistic mean field approximation to the the Walecka model with NL3 parameter set. Although we have presented the numerical results of the unpolarized differential cross section, our RPWIA formalism can easily be extended to extensively study of polarization observables which, by analogy, are considered to be sensitive to the fundamental physics behind the elementary process and nuclear modification effects while mostly insensitive to the final state interaction effects [82].

As a starting point, we have first numerically studied missing momentum, angular and energy distributions of the RPWIA differential cross section describing the neutrino-induced CC  $K^+\Lambda$  production on neutron orbitals of  ${}^{12}\text{C}$  in the laboratory frame under both quasifree and open kinematic settings. Under quasifree kinematic setting, the missing momentum distribution gives an indication that the bound state wave functions maintain a qualitative influence over the  $1s^{1/2}$  and  $1p^{3/2}$  contributions. Thus, the missing momentum distributions suggest that relatively larger angular and energy distributions can be obtained by tuning the missing momentum in the range:  $p_m \leq 0.3$  GeV. Upon fixing the missing momentum at  $p_m = 0.12$  GeV, (i) the angular distribution with respect to the outgoing kaon angle attains its peak at forward angle and (ii) the  $1p^{3/2}$  orbital provides the dominant contribution to the overall RPWIA differential cross section in the laboratory frame. Under the open kinematic setting, the angular distributions of the RPWIA differential cross sections with respect to the outgoing kaon and hyperon angles become the most forward-peaked in the energy region of our interest. This kinematic setting also allows the study of energy dependence of the reaction cross section, and the result of our

plane wave calculation shows that kaon energy distribution has its peak near  $T_K = 450$  MeV for all neutrino energies used.

In conclusion, the great merits of the RPWIA formalism are the following: (i) it offers a model which incorporates a number of important aspects of the reaction, (ii) it provides a first-order indication of the behavior of the cross sections for these types of reactions, (iii) from a theoretical perspective it allows a measure of analytical manipulation which greatly facilitates the numerical implementation, (iv) it provides the baseline calculations for any RDWIA models which seek to incorporate various FSI effects, and (v) it is the best tool to carry out an investigation into the polarization observables of the exclusive reaction  $A(\nu, \ell KY)B$ . Moreover, in the Born approximation of the weak hadronic vertex, the inclusion of the relevant resonance contributions in the evaluation of the elementary matrix element near the threshold region also enhances the importance of such a study. One can also take into account the Coulomb distortion of the scattered muon in the CC associated production reactions.

As opposed to the RPWIA framework, the RDWIA formalism is of a very sophisticated nature even though it starts from the baseline calculation developed in the plane wave limit. Theoretically, this has to do with the fact that there are no easy ways of incorporating the distortion effects coming from FSI of either kaon, hyperon, or both with the residual nucleus. As a consequence, we have faced a number of difficulties during the numerical implementation of the problem which has been proven (i) to be highly error-prone and (ii) to take very long execution times to generate the results. As a remedy, we have resorted to a technique called high performance computing in order to minimize the execution time by converting the sequential program to its parallelized version which runs on a computer cluster having a shared memory architecture. Nevertheless, the time we have saved by running the MPI equivalent of the serial program has been compromised by the time wasted on designing and implementing the code, particularly in identifying and correcting errors related to the code and cluster setup.

The RDWIA model for the neutrino-induced associated production of strange particles on nuclei has also been developed with particular interest in the kaon FSI effects by turning off the hyperon FSI. We have incorporated the kaon distortion effects through its wave function which is a numerical solution of the modified Klein-Gordon equation containing the Kisslinger form of the relativistic optical potential. The kaon optical potential, which is the simplified version of kaon-nucleus many-body problem, has been constructed from a phase shift analysis of  $K^+N$  scattering amplitudes by Martin. The fourth-order Runge-Kutta algorithm has been used to numerically integrate the radial Klein-Gordon equation - a linear second-order differential equation; and then the computed kaon distorted wave function has been normalized by taking into account its asymptotic behavior at larger distance where the optical potential is expected to vanish. For numerical study of our RDWIA model, the distorted partial waves of the outgoing kaon have been generated in advance and then stored in a datafile for later retrieval when calculating the cross section of the production process.

The relativistic distorted wave analysis of the CC process  $A(\nu, \mu^- K^+ \Lambda)B$  has been carried out in the c.m. frame. Under quasifree kinematics, we have examined the missing momentum and angular distributions of the RDWIA differential cross section of the production process on  ${}^4\text{He}$ ,  ${}^{12}\text{C}$ ,  ${}^{16}\text{O}$ , and  ${}^{40}\text{Ca}$  nuclei. In the case of the missing momentum distribution of the overall differential cross section describing the reaction on individual nuclei, the dominant contribution comes from relatively smaller missing momentum region. The angular distributions with respect to the outgoing kaon angle have indicated the dominant contribution of the  $1p^{3/2}$  orbital, which is even more pronounced in the angle range whereby the peaks occur, for the case of  ${}^{12}\text{C}$ ,  ${}^{16}\text{O}$ , and  ${}^{40}\text{Ca}$  targets. Under open kinematics, the kaon angular and energy distributions of the RDWIA differential cross section have been investigated. The angular distribution with respect to the kaon angle has been presented for the production process on  ${}^{208}\text{Pb}$ ; and the orbital contributions are characterized by sharp and/or multiple peaks occurring between  $\theta_{p'_{1,A}} = 30$  and  $\theta_{p'_{1,A}} = 80$  deg. On the other hand, the kaon energy distributions of the differential cross section for the process on  ${}^{12}\text{C}$  and  ${}^{40}\text{Ca}$  have shown for both targets that the peaks of the contributions

from individual orbitals occur within the kaon kinetic energy range between  $T_{K,A} = 400$  and  $T_{K,A} = 600$  MeV.

The angular distributions from the RDWIA calculation for the neutrino-induced CC  $K^+ \Lambda$  have been compared to the RPWIA results under both quasifree and open kinematic settings. Under quasifree kinematic, the kaon FSI decreases the magnitude of the angular distributions for the whole range of the kaon angle in the case of  ${}^4\text{He}$  and  ${}^{12}\text{C}$  nuclei, and the same holds for the contributions coming from the first four orbitals of the  ${}^{40}\text{Ca}$ . The  $2s^{1/2}$  and  $1d^{3/2}$  orbitals of  ${}^{40}\text{Ca}$  have their contributions characterized by both reduction and enhancement caused by the kaon FSI over different ranges of the kaon angle. Under open kinematic, the orbital angular distributions for the  ${}^{208}\text{Pb}$  target show sensitivity to the kaon distortion in the kaon angle range where their peaks occur, and most of those orbital contributions display a significant reduction of the reaction cross section caused by the kaon FSI in the peak region.

Our current calculations are timely in a sense that the ongoing neutrino-oscillation experiments such as MiniBooNE, K2K, and MINER $\nu$ A, as well as other experiments dedicated to proton decay searches like Super-KamioKande, demand an improved knowledge of the exclusive reaction channels such as strangeness associated productions. Therefore, our RPWIA and RDWIA results may play a significant role in the analysis of data from those experiments, and also in the separation process of backgrounds from the proton decay signal. It is very important to point out that a full distorted wave analysis of the neutrino-induced associated production on nuclei will be possible when both the outgoing kaon and hyperon FSI effects are incorporated in our formalism, simultaneously. Along this line, the RDWIA model we have developed can be extended to study (i) the effect of hyperon FSI by turning the kaon FSI off, and (ii) the effects of both kaon and hyperon FSIs on the production process.

# Appendices

## Appendix A

# Computing the Kinematics

To carry out the numerical analysis of the exclusive reaction  $A(\nu, \ell KY)B$ , the four-momenta of all participating particles and nuclei must be specified before proceeding to computing the differential cross section. We have already chosen to develop our theory under two kinematic settings: quasifree and open kinematics, and hence we design separate algorithms for each of them. Thus, we use flowcharts to illustrate how the step-by-step executions are performed within individual algorithms leading up to the computation of the laboratory frame four-momenta. Then these separate algorithms are converted into Fortran 95 programs which will then merge into a single subroutine, KINLAB1, to allow us to compute the kinematic quantities. Note that the detailed kinematic description is given in chapter 3 section 3.1.2.

### A.1 Flow Diagram for Quasifree Kinematics

In the quasifree kinematics, the algorithm takes  $\omega$ ,  $Q^2$ ,  $\theta_{p'_1}$ , and  $p_m$  as kinematic input variables, and then it computes and returns all four-momenta of participating particles. The calculation of the four-vectors under this kinematic setting proceeds in two steps: (i) set the missing momentum to zero such that the kaon and hyperon energies take their values of the underlying process on free nucleon, and (ii) use the nonzero  $p_m$  value of the missing momentum along with  $E_{p'_1}$  and  $E_{p'_2}$  to determine the rest of unknown quantities. The flowchart in Fig. A.1 illustrates the sequence of calculating the laboratory frame four-momenta under the quasifree kinematic setting using the Fortran 95 subroutine, KINLAB1.

### A.2 Flow Diagram for Open Kinematics

In the open kinematic setting, the algorithm requires input values of  $\omega$ ,  $Q^2$ ,  $E_{p'_2}$ ,  $\theta_{p'_1}$ , and  $\theta_{p'_2}$ , and then computes and returns the four-momenta. Unlike the quasifree kinematic, the calculation of the four-momenta of the reaction is straightforward. The flowchart in Fig. A.2 shows how the KINLAB1 subroutine performs step-by-step calculation of four-momenta under open kinematics.

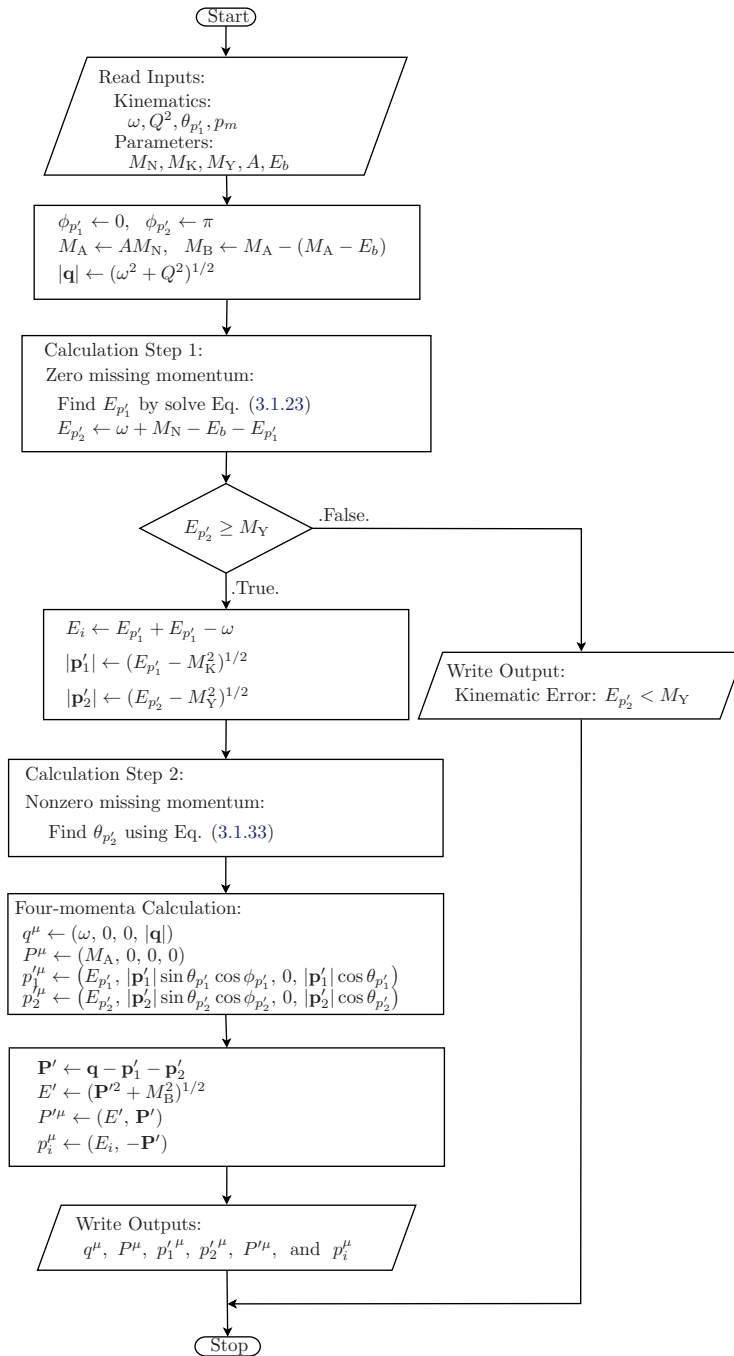


**Figure A.1:** Flow diagram illustrates how the quasifree kinematics part of KINLAB1 subroutine calculates the laboratory frame four-momenta. The four-momenta at the production vertex are determined in two steps as this setting requires that the energies of the outgoing kaon and hyperon to be the same as their two-body values and the use of a finite value for the missing momentum can be set to only shift the hyperon angle from its free space value.

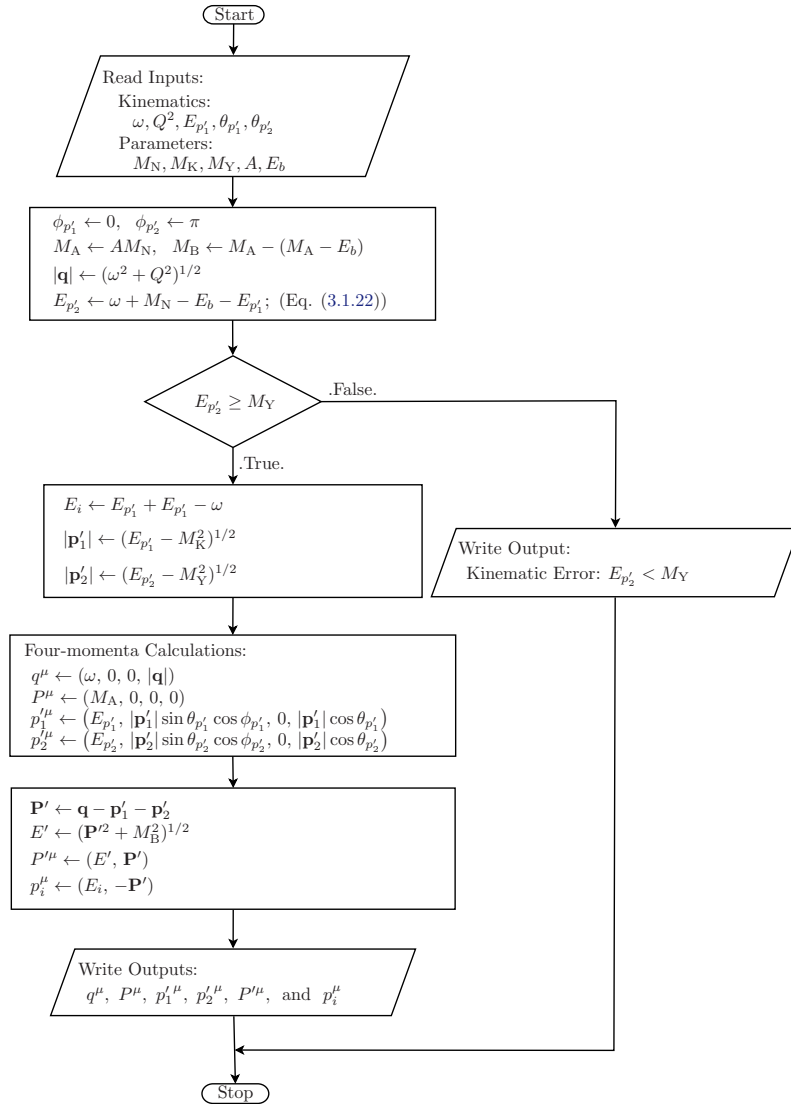


**Figure A.2:** Flow diagram illustrates how the open kinematics part of KINLAB1 subroutine calculates the laboratory frame four-momenta. This setting calculates all unknown quantities in straightforward manner by assigning nine kinematic inputs at the start and letting  $p_m$  vary over the entire range of the momentum distribution of the bound nucleon.



## Appendix B

### Block-matrix Form of $\hat{J}^\mu(q)$

As briefly summarized in chapter 2, by making use of the bilinear covariant basis and independent four-momenta along with the Dirac algebra we have derived the most general weak hadronic current:

$$\begin{aligned} \hat{J}^\mu(q) &= \tilde{A}^\mu I + \tilde{B}^\mu \gamma_5 + \tilde{C}_1 \gamma^\mu + \tilde{C}^\mu \not{q} + \tilde{D}_1 \gamma_5 \gamma^\mu \\ &+ \tilde{D}^\mu \gamma_5 \not{q} + \tilde{D}_5 \not{q} \gamma^\mu + \tilde{D}_6 \gamma_5 \not{q} \gamma^\mu, \end{aligned} \quad (\text{B.0.1})$$

where

$$\begin{aligned} \tilde{A}^\mu &= \tilde{A}_1 q^\mu + \tilde{A}_2 p^\mu + \tilde{A}_3 p_2'^\mu + \tilde{A}_4 \varepsilon^{\mu\nu\alpha\beta} q_\nu p_\alpha p_{2\beta}', \\ \tilde{B}^\mu &= \tilde{B}_1 q^\mu + \tilde{B}_2 p^\mu + \tilde{B}_3 p_2'^\mu + \tilde{B}_4 \varepsilon^{\mu\nu\alpha\beta} q_\nu p_\alpha p_{2\beta}', \\ \tilde{C}^\mu &= \tilde{C}_2 q^\mu + \tilde{C}_3 p^\mu + \tilde{C}_4 p_2'^\mu, \\ \tilde{D}^\mu &= \tilde{D}_2 q^\mu + \tilde{D}_3 p^\mu + \tilde{D}_4 p_2'^\mu. \end{aligned} \quad (\text{B.0.2})$$

In general there are eighteen unknown amplitudes yet to be determined from tree diagram based models. The conventions of Bjorken and Drell have been maintained for the Dirac matrices and the four-vector notations.

The main purpose of this investigation is to re-derive  $\hat{J}^\mu(q)$  in the block matrix form. In other words we extract the general forms of  $\hat{J}_{ij}^\mu$ . In so doing, we kick off by closely examining the basis of the bilinear covariant expansion terms except the antisymmetric term  $\sigma^{\mu\nu}$  which is absent in the general form of  $\hat{J}^\mu(q)$ . In most cases, however, the demand for symmetric terms led to dropping such terms. We also take a look at the secondary basis as well:

$$\Gamma_0 = \{I, \gamma^5, \gamma^\mu, \gamma^5 \gamma^\mu\} \quad (\text{B.0.3})$$

$$\Gamma_1 = \{\not{q}, \gamma^5 \not{q}, \not{q} \gamma^\mu, \gamma^5 \not{q} \gamma^\mu\} \quad (\text{B.0.4})$$

where  $\Gamma_0$  is a set of the primary basis from bilinear covariant set and  $\Gamma_1$  is the secondary basis which are the extracts of the primary basis combined with four-momentum transfer. Note also that the absence of the explicit form of  $\sigma^{\mu\nu} q_\nu$  in the general expression of  $\hat{J}^\mu(q)$  because of the fact that it is absorbed by other terms such as  $\not{q} \gamma^\mu$ .

The block-matrix representations of  $I$  and  $\gamma^5$  are given in a straightforward manner as:

$$I = \begin{pmatrix} I_2 & 0 \\ 0 & I_2 \end{pmatrix}, \quad \gamma^5 = \begin{pmatrix} 0 & I_2 \\ I_2 & 0 \end{pmatrix}, \quad (\text{B.0.5})$$

where  $I_2$  is a 2 dimensional identity matrix. The block-matrix representation of the Dirac gamma matrix  $\gamma^\mu$ , however, comes at heavy cost unlike the previous. Component wise it can be written as

$$\gamma^0 = \begin{pmatrix} I_2 & 0 \\ 0 & -I_2 \end{pmatrix}, \quad \gamma^i = -\gamma_i = \begin{pmatrix} 0 & \sigma^i \\ -\sigma^i & 0 \end{pmatrix}, \quad (\text{B.0.6})$$

where  $i = 1, 2, 3$  and  $\sigma^i$  are the two dimensional Pauli matrices defined as

$$\sigma^1 = \begin{pmatrix} 0 & 1 \\ 1 & 0 \end{pmatrix}, \quad \sigma^2 = \begin{pmatrix} 0 & -i \\ i & 0 \end{pmatrix}, \quad \sigma^3 = \begin{pmatrix} 1 & 0 \\ 0 & -1 \end{pmatrix}, \quad (\text{B.0.7})$$

and each of them obeys the following identity:  $\sigma^i = \sigma_i$ . It is clear that the Dirac gamma matrix presents a complication that we choose to simplify by redefining the  $4 \times 4$  matrix and first rank tensor  $\gamma^\mu$  by making use of its components in Eq. (B.0.6) and the delta function as follows:

$$\gamma^\mu = \delta_0^\mu \gamma^0 + \delta_i^\mu \gamma^i, \quad i = 1, 2, 3, \quad (\text{B.0.8})$$

and it can be written even in a more explicit form as:

$$\gamma^\mu = \begin{pmatrix} \delta_0^\mu I_2 & 0 \\ 0 & -\delta_0^\mu I_2 \end{pmatrix} + \begin{pmatrix} 0 & \delta_i^\mu \sigma^i \\ -\delta_i^\mu \sigma^i & 0 \end{pmatrix} = \begin{pmatrix} \delta_0^\mu I_2 & \delta_i^\mu \sigma^i \\ -\delta_i^\mu \sigma^i & -\delta_0^\mu I_2 \end{pmatrix}. \quad (\text{B.0.9})$$

This expression plays a pivotal role owing to the fact that the block-matrix representations of the rest of the basis in  $\Gamma_0$  and  $\Gamma_1$  can be derived using this block-matrix form of  $\gamma^\mu$  as well as the first two basis:  $I$  and  $\gamma_5$  as given in Eq. (B.0.5). We begin by expressing  $\not{q}$  as follows:

$$\not{q} = q_\nu \gamma^\nu = \begin{pmatrix} \delta_0^\nu q_\nu I_2 & \delta_i^\nu q_\nu \sigma^i \\ -\delta_i^\nu q_\nu \sigma^i & -\delta_0^\nu q_\nu I_2 \end{pmatrix} = \begin{pmatrix} q_0 I_2 & -q^i \sigma^i \\ q^i \sigma^i & -q_0 I_2 \end{pmatrix}. \quad (\text{B.0.10})$$

Note that the relativistic notation with metric tensor gives  $q_i = -q^i$  for the space-like component, and the four-vector notation conventions are maintained throughout. Now we proceed to express  $\gamma^5 \gamma^\mu$  as

$$\gamma^5 \gamma^\nu = \begin{pmatrix} -\delta_i^\nu \sigma^i & -\delta_0^\nu I_2 \\ \delta_0^\nu I_2 & \delta_i^\nu \sigma^i \end{pmatrix}. \quad (\text{B.0.11})$$

The block-matrix representation of  $\gamma^5 \not{q}$  also becomes

$$\gamma^5 \not{q} = \begin{pmatrix} -\delta_i^\nu q_\nu \sigma^i & -\delta_0^\nu q_\nu I_2 \\ \delta_0^\nu q_\nu I_2 & \delta_i^\nu q_\nu \sigma^i \end{pmatrix} = \begin{pmatrix} q^i \sigma^i & -q_0 I_2 \\ q_0 I_2 & -q^i \sigma^i \end{pmatrix}. \quad (\text{B.0.12})$$

We are almost through, but we are left with two basis terms that are yet to be expressed in the block-matrix form, these are  $\not{q} \gamma^\mu$  and  $\gamma^5 \not{q} \gamma^\mu$ . The latter one becomes trivial once we determine the former basis. Hence we first look at  $\not{q} \gamma^\mu$ :

$$\not{q} \gamma^\mu = \begin{pmatrix} q_0 I_2 & -q^i \sigma^i \\ q^i \sigma^i & -q_0 I_2 \end{pmatrix} \begin{pmatrix} \delta_0^\mu I_2 & \delta_j^\mu \sigma^j \\ -\delta_j^\mu \sigma^j & -\delta_0^\mu I_2 \end{pmatrix}, \quad (\text{B.0.13})$$

explicitly performing the matrix product we get

$$\not{q} \gamma^\mu = \begin{pmatrix} \delta_0^\mu q_0 I_2 + \delta_j^\mu q^i \sigma^i \sigma^j & \delta_0^\mu q^i \sigma^i + \delta_j^\mu q_0 \sigma^j \\ \delta_0^\mu q^i \sigma^i + \delta_j^\mu q_0 \sigma^j & \delta_0^\mu q_0 I_2 + \delta_j^\mu q^i \sigma^i \sigma^j \end{pmatrix}. \quad (\text{B.0.14})$$

It is worth noting that we have chosen to stay consistent in that the four-vectors are remain in the contravariant form. Eq. (B.0.14) needs further simplification by invoking the conditions of the SU(2) symmetry on the Pauli matrices  $\sigma_i$ . Suppose the entries of the matrix in Eq. (B.0.14) can be labeled as  $a_{nm}^\mu$ ,  $n, m = 1, 2$ . Now we focus on the first entry,  $a_{11}^\mu$ :

$$a_{11}^\mu = \delta_0^\mu q_0 I_2 + \delta_j^\mu q^i \sigma^i \sigma^j. \quad (\text{B.0.15})$$

In the language of group theory, we can introduce the following symmetric condition:

$$\sigma^i \sigma^j = \delta_{ij} I_2 + i \epsilon_{ijk} \sigma^k, \quad (\text{B.0.16})$$

where  $\epsilon_{ijk}$  is the three dimensional antisymmetric Levi-Civita tensor:

$$\epsilon_{ijk} = \begin{cases} +1, & \text{for even permutation of } 1, 2, 3, \\ -1, & \text{for odd permutation of } 1, 2, 3, \\ 0, & \text{otherwise,} \end{cases} \quad (\text{B.0.17})$$

and it is also know as the structure function of the Lie-algebra representation of SU(2) group:

$$[\sigma^i, \sigma^j] = 2i \epsilon_{ijk} \sigma^k. \quad (\text{B.0.18})$$

For coding purpose it can also be written in expanded form as

$$\epsilon_{ijk} = \delta_1^i [\delta_2^j \delta_3^k - \delta_3^j \delta_2^k] - \delta_2^i [\delta_1^j \delta_3^k - \delta_3^j \delta_1^k] + \delta_3^i [\delta_1^j \delta_2^k - \delta_2^j \delta_1^k]. \quad (\text{B.0.19})$$

It is worth mentioning that the Einstein summation convention has been invoked throughout. After replacing the above identity one can show that

$$a_{11}^\mu = \delta_\alpha^\mu q^\alpha I_2 - i \delta_i^\mu \epsilon_{ijk} q^j \sigma^k. \quad (\text{B.0.20})$$

Use is also made of the interchangeability of dummy indices. We must avoid any possible confusion that may arise with the notation used for  $\delta_\alpha^\mu q^\alpha$  which is nothing more than an ordinary summation:

$$\delta_\alpha^\mu q^\alpha = \sum_{\alpha=0}^4 \delta_\alpha^\mu q^\alpha = q^\mu, \quad (\text{B.0.21})$$

instead of being a contraction between two tensors or four-vectors:  $k_\nu p^\nu = k^0 p^0 - \mathbf{k} \cdot \mathbf{p}$ . Note that the off-diagonal entries of Eq. (B.0.14) do not need further analysis; the diagonal entries are the same and so are off-diagonal entries.

$$\not{q} \gamma^\mu = \begin{pmatrix} \delta_\alpha^\mu q^\alpha I_2 - i \delta_i^\mu \epsilon_{ijk} q^j \sigma^k & \delta_0^\mu q^i \sigma^i + \delta_j^\mu q_0 \sigma^j \\ \delta_0^\mu q^i \sigma^i + \delta_j^\mu q_0 \sigma^j & \delta_\alpha^\mu q^\alpha I_2 - i \delta_i^\mu \epsilon_{ijk} q^j \sigma^k \end{pmatrix}. \quad (\text{B.0.22})$$

Following this, the block-matrix format of  $\gamma^5 \not{q} \gamma^\mu$  can be obtained as follows:

$$\gamma^5 \not{q} \gamma^\mu = \begin{pmatrix} \delta_0^\mu q^i \sigma^i + \delta_j^\mu q_0 \sigma^j & \delta_\alpha^\mu q^\alpha I_2 - i \delta_i^\mu \epsilon_{ijk} q^j \sigma^k \\ \delta_\alpha^\mu q^\alpha I_2 - i \delta_i^\mu \epsilon_{ijk} q^j \sigma^k & \delta_0^\mu q^i \sigma^i + \delta_j^\mu q_0 \sigma^j \end{pmatrix}. \quad (\text{B.0.23})$$

Now therefore, we replace the block-matrix forms of all basis terms of the weak hadronic

current operator to find that

$$\hat{J}^\mu(q) = \begin{pmatrix} \hat{J}_{11}^\mu(q) & \hat{J}_{12}^\mu(q) \\ \hat{J}_{21}^\mu(q) & \hat{J}_{22}^\mu(q) \end{pmatrix}, \quad (\text{B.0.24})$$

$$\begin{aligned} &= \tilde{A}^\mu \begin{pmatrix} I_2 & 0 \\ 0 & I_2 \end{pmatrix} + \tilde{B}^\mu \begin{pmatrix} 0 & I_2 \\ I_2 & 0 \end{pmatrix} + \tilde{C}_1 \begin{pmatrix} \delta_0^\mu I_2 & \delta_i^\mu \sigma^i \\ -\delta_i^\mu \sigma^i & -\delta_0^\mu I_2 \end{pmatrix} \\ &+ \tilde{C}^\mu \begin{pmatrix} q_0 I_2 & -q^i \sigma^i \\ q^i \sigma^i & -q_0 I_2 \end{pmatrix} + \tilde{D}_1 \begin{pmatrix} -\delta_i^\mu \sigma^i & -\delta_0^\mu I_2 \\ \delta_0^\mu I_2 & \delta_i^\mu \sigma^i \end{pmatrix} + \tilde{D}^\mu \begin{pmatrix} q^i \sigma^i & -q_0 I_2 \\ q_0 I_2 & -q^i \sigma^i \end{pmatrix} \\ &+ \tilde{D}_5 \begin{pmatrix} q^\mu I_2 - i\delta_i^\mu \epsilon_{ijk} q^j \sigma^k & \delta_0^\mu q^i \sigma^i + \delta_j^\mu q_0 \sigma^j \\ \delta_0^\mu q^i \sigma^i + \delta_j^\mu q_0 \sigma^j & q^\mu I_2 - i\delta_i^\mu \epsilon_{ijk} q^j \sigma^k \end{pmatrix} \\ &+ \tilde{D}_6 \begin{pmatrix} \delta_0^\mu q^i \sigma^i + \delta_j^\mu q_0 \sigma^j & q^\mu I_2 - i\delta_i^\mu \epsilon_{ijk} q^j \sigma^k \\ q^\mu I_2 - i\delta_i^\mu \epsilon_{ijk} q^j \sigma^k & \delta_0^\mu q^i \sigma^i + \delta_j^\mu q_0 \sigma^j \end{pmatrix}, \quad (\text{B.0.25}) \end{aligned}$$

where the entries of block-matrix are

$$\begin{aligned} \hat{J}_{11}^\mu(q) &= \tilde{A}^\mu I_2 + \tilde{C}_1 \delta_0^\mu I_2 + \tilde{C}^\mu q_0 I_2 - \tilde{D}_1 \delta_i^\mu \sigma^i + \tilde{D}^\mu q^i \sigma^i \\ &+ \tilde{D}_5 \left( \delta_\alpha^\mu q^\alpha I_2 - i\delta_i^\mu \epsilon_{ijk} q^j \sigma^k \right) + \tilde{D}_6 \left( \delta_0^\mu q^i \sigma^i + \delta_j^\mu q_0 \sigma^j \right) \end{aligned} \quad (\text{B.0.26})$$

$$\begin{aligned} \hat{J}_{12}^\mu(q) &= \tilde{B}^\mu I_2 + \tilde{C}_1 \delta_i^\mu \sigma^i - \tilde{C}^\mu q^i \sigma^i - \tilde{D}_1 \delta_0^\mu I_2 - \tilde{D}^\mu q_0 I_2 \\ &+ \tilde{D}_5 \left( \delta_0^\mu q^i \sigma^i + \delta_j^\mu q_0 \sigma^j \right) + \tilde{D}_6 \left( \delta_\alpha^\mu q^\alpha I_2 - i\delta_i^\mu \epsilon_{ijk} q^j \sigma^k \right) \end{aligned} \quad (\text{B.0.27})$$

$$\begin{aligned} \hat{J}_{21}^\mu(q) &= \tilde{B}^\mu I_2 - \tilde{C}_1 \delta_i^\mu \sigma^i + \tilde{C}^\mu q^i \sigma^i + \tilde{D}_1 \delta_0^\mu I_2 + \tilde{D}^\mu q_0 I_2 \\ &+ \tilde{D}_5 \left( \delta_0^\mu q^i \sigma^i + \delta_j^\mu q_0 \sigma^j \right) + \tilde{D}_6 \left( \delta_\alpha^\mu q^\alpha I_2 - i\delta_i^\mu \epsilon_{ijk} q^j \sigma^k \right) \end{aligned} \quad (\text{B.0.28})$$

$$\begin{aligned} \hat{J}_{22}^\mu(q) &= \tilde{A}^\mu I_2 - \tilde{C}_1 \delta_0^\mu I_2 - \tilde{C}^\mu q_0 I_2 + \tilde{D}_1 \delta_i^\mu \sigma^i - \tilde{D}^\mu q^i \sigma^i \\ &+ \tilde{D}_5 \left( \delta_\alpha^\mu q^\alpha I_2 - i\delta_i^\mu \epsilon_{ijk} q^j \sigma^k \right) + \tilde{D}_6 \left( \delta_0^\mu q^i \sigma^i + \delta_j^\mu q_0 \sigma^j \right) \end{aligned} \quad (\text{B.0.29})$$

The more convenient form of these block-matrices can be given compactly as follows:

$$\hat{J}_{11}^\mu(q) = \tilde{A}_{11}^\mu I_2 + \tilde{B}_{11}^\mu q^i \sigma^i + \tilde{C}_{11} \delta_i^\mu \sigma^i + \tilde{D}_{11} \delta_i^\mu \epsilon_{ijk} q^j \sigma^k \quad (\text{B.0.30})$$

where

$$\tilde{A}_{11}^\mu = \tilde{A}^\mu + \tilde{C}_1 \delta_0^\mu + \tilde{C}^\mu q_0 + \tilde{D}_5 q^\mu \quad (\text{B.0.31})$$

$$\tilde{B}_{11}^\mu = \tilde{D}^\mu + \tilde{D}_6 \delta_0^\mu \quad (\text{B.0.32})$$

$$\tilde{C}_{11} = -\tilde{D}_1 + \tilde{D}_6 q_0 \quad (\text{B.0.33})$$

$$\tilde{D}_{11} = -i\tilde{D}_5 \quad (\text{B.0.34})$$

$$\hat{J}_{12}^\mu(q) = \tilde{A}_{12}^\mu I_2 + \tilde{B}_{12}^\mu q^i \sigma^i + \tilde{C}_{12} \delta_i^\mu \sigma^i + \tilde{D}_{12} \delta_i^\mu \epsilon_{ijk} q^j \sigma^k \quad (\text{B.0.35})$$

where

$$\tilde{A}_{12}^\mu = \tilde{B}^\mu - \tilde{D}_1 \delta_0^\mu - \tilde{D}^\mu q_0 + \tilde{D}_6 q^\mu \quad (\text{B.0.36})$$

$$\tilde{B}_{12}^\mu = -\tilde{C}^\mu + \tilde{D}_5 \delta_0^\mu \quad (\text{B.0.37})$$

$$\tilde{C}_{12} = \tilde{C}_1 + \tilde{D}_5 q_0 \quad (\text{B.0.38})$$

$$\tilde{D}_{12} = -i\tilde{D}_6 \quad (\text{B.0.39})$$

$$\hat{J}_{21}^\mu(q) = \tilde{A}_{21}^\mu I_2 + \tilde{B}_{21}^\mu q^i \sigma^i + \tilde{C}_{21} \delta_i^\mu \sigma^i + \tilde{D}_{21} \delta_i^\mu \epsilon_{ijk} q^j \sigma^k \quad (\text{B.0.40})$$

where

$$\tilde{A}_{21}^\mu = \tilde{B}^\mu + \tilde{D}_1 \delta_0^\mu + \tilde{D}^\mu q_0 + \tilde{D}_6 q^\mu \quad (\text{B.0.41})$$

$$\tilde{B}_{21}^\mu = \tilde{C}^\mu + \tilde{D}_5 \delta_0^\mu \quad (\text{B.0.42})$$

$$\tilde{C}_{21} = -\tilde{C}_1 + \tilde{D}_5 q_0 \quad (\text{B.0.43})$$

$$\tilde{D}_{21} = -i\tilde{D}_6 \quad (\text{B.0.44})$$

$$\hat{J}_{22}^\mu(q) = \tilde{A}_{22}^\mu I_2 + \tilde{B}_{22}^\mu q^i \sigma^i + \tilde{C}_{22} \delta_i^\mu \sigma^i + \tilde{D}_{22} \delta_i^\mu \epsilon_{ijk} q^j \sigma^k \quad (\text{B.0.45})$$

where

$$\tilde{A}_{22}^\mu = \tilde{A}^\mu - \tilde{C}_1 \delta_0^\mu - \tilde{C}^\mu q_0 + \tilde{D}_5 q^\mu \quad (\text{B.0.46})$$

$$\tilde{B}_{22}^\mu = -\tilde{D}^\mu + \tilde{D}_6 \delta_0^\mu \quad (\text{B.0.47})$$

$$\tilde{C}_{22} = \tilde{D}_1 + \tilde{D}_6 q_0 \quad (\text{B.0.48})$$

$$\tilde{D}_{22} = -i\tilde{D}_5 \quad (\text{B.0.49})$$

## Appendix C

# Numerical Methods

In our formalisms, we have come across integral and differential equations for which analytical calculations become formidable. Here we give a brief overview of numerical methods that are vital for dealing with our analytical shortcomings in solving those problems. First, we introduce the Gaussian quadrature, which is one of the numerical methods we can use to handle difficult integral equations. Second, we discuss the fourth-order Runge-Kutta method, which allows us to deal with first- and second-order differential equations with well-defined initial conditions.

### C.1 Gaussian Quadrature

In numerical analysis, a Gaussian quadrature offers an accurate approximation of the integral of a given function over a finite interval. The conventional choice of integration range is  $[-1, 1]$ , whereas in this study we choose a slightly different but convenient interval, that is,  $[0, 1]$ . Thus according to this scheme an arbitrary function  $f(x)$  is integrated as

$$\int_0^1 dx f(x) = \sum_{k=1}^N \omega_k f(x_k), \quad (\text{C.1.1})$$

where  $x_k$  and  $\omega_k$  are Gaussian integration points (or roots of Legendre polynomials) and weighting coefficients, respectively. One of the attractive aspects of the Gaussian quadrature is that it can be extended to evaluate the integral of a function to other limits different from the conventional choice. This is often accomplished by transforming variables. That is,

$$\begin{aligned} \int_{x_a}^{x_b} dx f(x) &= (x_b - x_a) \int_0^1 dt f((x_b - x_a)t + x_a) \\ &= (x_b - x_a) \sum_{k=1}^N \omega_k f((x_b - x_a)x_k + x_a). \end{aligned} \quad (\text{C.1.2})$$

Moreover, this numerical integration method can be generalized to multiple integral problems. Suppose an arbitrary function  $f$  that depends on  $n$  variables:  $x_1, x_2, \dots, x_n$ , and we want to integrate this function over all of its  $n$  variables. Thus, such  $n$ -dimensional integration can be evaluated numerically by using the extended version of 1-dimensional Gaussian quadrature

formula in Eq. (C.1.2):

$$\begin{aligned}
 & \int_{x_{a,1}}^{x_{b,1}} \int_{x_{a,2}}^{x_{b,2}} \cdots \int_{x_{a,n}}^{x_{b,n}} dx_1 dx_2 \cdots dx_n f(x_1, x_2, \cdots, x_n) \\
 &= \prod_{i=1}^n \int_{x_{a,i}}^{x_{b,i}} dx_i f(x_1, x_2, \cdots, x_n) \\
 &= \prod_{i=1}^n (x_{b,i} - x_{a,i}) \int_0^1 dt_i f((x_{b,1} - x_{a,1})t_1 + x_{a,1}, \cdots, (x_{b,n} - x_{a,n})t_n + x_{a,n}) \\
 &= \prod_{i=1}^n (x_{b,i} - x_{a,i}) \sum_{k_i}^N \omega_{k_i} f((x_{b,1} - x_{a,1})x_{k_1} + x_{a,1}, \cdots, (x_{b,n} - x_{a,n})x_{k_n} + x_{a,n}), \quad (\text{C.1.3})
 \end{aligned}$$

where  $x_{k_i}$  and  $\omega_{k_i}$  ( $i = 1, 2, \cdots, n$ ) are the usual roots and weights, respectively, of the Gaussian quadrature solving the  $n$ -dimensional integration.

## C.2 Fourth-order Runge-Kutta Method

The fourth-order Runge-Kutta method is one of the powerful iterative methods which can be used to numerically solve differential equations. This iterative algorithm is the most accurate numerical method with better convergence and stability in comparison to other methods such as Euler and midpoint numerical integrations. Now consider an initial value problem of the following form:

$$y' = F(x, y(x)), \quad y(x_0) = y_0. \quad (\text{C.2.1})$$

Thus, the RK4 solution of the above first-order differential equation is obtained by iterating the equations:

$$y_{n+1} = y_n + \frac{h}{6}(k_1 + 2k_2 + 2k_3 + k_4), \quad (\text{C.2.2})$$

$$x_{n+1} = x_n + h, \quad (\text{C.2.3})$$

for  $n = 0, 1, 2, \dots$  and with step size  $h > 0$ , and the coefficients  $k_1, k_2, k_3$ , and  $k_4$  defined as

$$k_1 = F(x_n, y_n), \quad (\text{C.2.4})$$

$$k_2 = F(x_n + \frac{h}{2}, y_n + \frac{h}{2}k_1), \quad (\text{C.2.5})$$

$$k_3 = F(x_n + \frac{h}{2}, y_n + \frac{h}{2}k_2), \quad (\text{C.2.6})$$

$$k_4 = F(x_n + h, y_n + hk_3). \quad (\text{C.2.7})$$

The RK4 method cannot directly solve a second-order differential equations of the form:

$$y'' = F(x, y(x), y'(x)), \quad y(x_0) = y_0, \quad y'(x_0) = y'_0, \quad (\text{C.2.8})$$

as the method is traditionally designed to deal with first-order differential equations. One way of tackling this shortcoming is to start by converting the second-order differential equation into a system of coupled first-order equations. For convenience, we now introduce two arbitrary functions  $\xi(x)$  and  $\zeta(x)$  such that,

$$\xi(x) = y(x), \quad (\text{C.2.9})$$

$$\zeta(x) = y'(x). \quad (\text{C.2.10})$$



Thus, the second-order equation, Eq. (C.2.8), can be written as the following coupled first-order equations:

$$\frac{d\xi(x)}{dx} = F_1(x, \xi(x), \zeta(x)) = \zeta(x), \quad (\text{C.2.11})$$

$$\frac{d\zeta(x)}{dx} = F_2(x, \xi(x), \zeta(x)) = F(x, \xi(x), \zeta(x)). \quad (\text{C.2.12})$$

The RK4 method for solving such coupled equations is slightly different from its standard definition, Eq. (C.2.2); and a single iteration step of  $h$  can now be written as [128, 129]:

$$\xi_{n+1} = \xi_n + \frac{h}{6}[k_1 + 2k_2 + 2k_3 + k_4], \quad (\text{C.2.13})$$

$$\zeta_{n+1} = \zeta_n + \frac{h}{6}[m_1 + 2m_2 + 2m_3 + m_4], \quad (\text{C.2.14})$$

$$x_{n+1} = x_n + h, \quad (\text{C.2.15})$$

where

$$k_1 = F_1(r_n, \xi_n, \zeta_n), \quad m_1 = F_2(r_n, \xi_n, \zeta_n), \quad (\text{C.2.16})$$

$$k_2 = F_1\left(r_n + \frac{h}{2}, \xi_n + \frac{h}{2}k_1, \zeta_n + \frac{h}{2}m_1\right), \quad m_2 = F_2\left(r_n + \frac{h}{2}, \xi_n + \frac{h}{2}k_1, \zeta_n + \frac{h}{2}m_1\right), \quad (\text{C.2.17})$$

$$k_3 = F_1\left(r_n + \frac{h}{2}, \xi_n + \frac{h}{2}k_2, \zeta_n + \frac{h}{2}m_2\right), \quad m_3 = F_2\left(r_n + \frac{h}{2}, \xi_n + \frac{h}{2}k_2, \zeta_n + \frac{h}{2}m_2\right), \quad (\text{C.2.18})$$

$$k_4 = F_1(r_n + h, \xi_n + hk_3, \zeta_n + hm_3), \quad m_4 = F_2(r_n + h, \xi_n + hk_3, \zeta_n + hm_3). \quad (\text{C.2.19})$$

Note that the RK4 method solves for both  $\xi(x)$  and  $\zeta(x)$ , simultaneously. This exact method is used to numerically solve for the radial Klein-Gordon (complex second-order differential) equation by converting the algorithm to a Fortran 95 program.

## Appendix D

# Conversion of Multidimensional Summation

Our effort to implement parallel computing has faced strong challenges due to the fact that the weak nuclear transition current happens to be a complex expression with multidimensional summations of terms which are very large in number. Thus, before directly applying parallel computing for such a problem, we go on to re-define the original expression by developing a technique that converts an  $n$ -dimensional summation problem to a one-dimensional summation problem. In other words, we will find a summation index  $s$  such that all  $n$  number of summation indices can be expressed as a function of the new index. In a technical sense, we basically deal with a summation problem with only single index, hence making possible the implementation of the parallel computation for any given serial program.

Now we develop such a technique to be able to convert a multidimensional summation to a one-dimensional summation. Note that, by multidimensional summation we mean summation over multiple indices with which individual terms or functions are specified. For example, we consider the following operation:

$$I_n = \prod_{m=1}^n \sum_{i_m} F_{i_1, i_2, \dots, i_n} = \sum_{i_1} \sum_{i_1} \cdots \sum_{i_n} F_{i_1, i_2, \dots, i_n}, \quad (\text{D.0.1})$$

as an  $n$ -dimensional or  $n$ -index summation of  $F_{i_1, i_2, \dots, i_n}$ . Here, our main focus is to construct a total of  $n$  functions that can relate individual indices of the original summation to a new index, say,  $s$  such that  $n$ -dimensional summation can be rewrite as a summation that only depends on a single index, and thus converting the multidimensional summation to a one-dimensional summation. To begin with, we now consider a two-dimensional summation of an arbitrary function  $F_{i_1, i_2}$ :

$$I_2 = \sum_{i_1=0}^{N_1} \sum_{i_2=0}^{N_2} F_{i_1, i_2}. \quad (\text{D.0.2})$$

### D.1 Independent Summation Indices

We now assume that there is no dependency between the two indices; and we claim that there exists an index  $s$  such that Eq. (D.0.2) can be written as

$$I_2 = \sum_{s=0}^{s_{N_s}} F_{i_1(s), i_2(s)} = F_{i_1(0), i_2(0)} + F_{i_1(1), i_2(1)}(x) + \cdots + F_{i_1(s_{N_s}), i_2(s_{N_s})}. \quad (\text{D.1.1})$$

We can redefine  $F_{i_1(s), i_2(s)}$  as a single index function  $G_s$  such that

$$I_2 = \sum_{i_1=0}^{N_1} \sum_{i_2=0}^{N_2} F_{i_1, i_2} = \sum_{s=0}^{s_{N_s}} G_s. \quad (\text{D.1.2})$$

Now we fix the values of the upper limits  $N_1$  and  $N_2$  of the original summation of Eq. (D.0.2) at 2. Thus, upon explicitly expressing the summations over  $F_{i_1, i_2}$  and  $G_s$ , we can establish the following convenient relations by means of direct identification:

$$G_1 = F_{0,0}, \quad G_2 = F_{0,1}, \quad G_3 = F_{0,2}, \quad \dots, \quad G_9 = F_{2,2}. \quad (\text{D.1.3})$$

Note, however, that this is not a unique set of relations we can establish between single-index and multi-index summations, since such an indentation method depends solely on personal preferences. Now careful inspection of Eq. (D.1.3) suggests that we can apply the concept of modular arithmetic to construct functions with which the dependence of the two indices  $i_1$  and  $i_2$  on the new index  $s$  can be established. Such an approach allows us to simplify the complicated problem using only indices without having to deal with the details of the problem. Table D.1 lists down the old indices and the associated new index for visual inspection.

**Table D.1:** Lists of integer values of indices: (i) when sequential summation is performed upon a function using two indices:  $i_1$  and  $i_2$ ; and (ii) when the same operation is carried out using a single index  $s$ . Here  $N_1$  and  $N_2$  are set to 2. This table illustrates how simply one can deduce the two indices from their single-index representation  $s$ . The upper limit for the indices are fixed at the beginning and hence their determination becomes dependant on  $s$ ,  $N_1$  and  $N_2$ . Note that the dependence on both  $s$  and  $N_2$  visibly notable but one may ask the what is the importance of  $i_1^{\max}$ . The answer is simple. The maximum value of  $s$  depends on both upper limits.

$i_1$	$i_2$	$s$
0	0	0
0	1	1
0	2	2
1	0	3
1	1	4
1	2	5
2	0	6
2	1	7
2	2	8

If we now compare the lists of  $i_2$  (second column) and  $s$  (third column) of Table D.1, we can easily see an equivalent relation - congruence mod  $N_2 + 1$ :

$$i_2(s) = s \pmod{N_2 + 1}. \quad (\text{D.1.4})$$

Now we need to express  $i_1$  as a function of  $s$  as well. In doing so, once again we must make use of the definition of the congruence relation, which states that given integers  $a$ ,  $b$ , and  $m$ ,  $a$  is congruent to  $b$  modulo  $m$ , if  $a - b = km$  for some integer  $k$ . In other words, if we know  $a$ ,  $b$ , and  $m$ , we can easily specify  $k$ . That is,  $k = (a - b)/m$ . Thus, for this particular problem if we identify  $a$ ,  $b$ , and  $m$  with  $s$ ,  $i_2$ , and  $N_2 + 1$ , respectively, then  $k$  is none other than  $i_1$ :

$$i_1(s) = \frac{s - i_2}{N_2 + 1}. \quad (\text{D.1.5})$$

Note also that since  $N_1$  and  $N_2$  are fixed at the start, the upper limit  $N_s$  of summation over the new index  $s$  can be determined as

$$N_s = \prod_{k=1}^2 (N_k + 1) - 1. \quad (\text{D.1.6})$$

We now proceed to look at the case of three-dimensional summation before we are able to generalize such a concept to higher dimensional summations. Consider a triple-index summation

of a function  $F_{i_1, i_2, i_3}$ :

$$I_3 = \sum_{i_1=0}^{N_1} \sum_{i_2=0}^{N_2} \sum_{i_3=0}^{N_3} F_{i_1, i_2, i_3} = \sum_{s=0}^{N_s} F_{i_1(s), i_2(s), i_3(s)}. \quad (\text{D.1.7})$$

These three indices can be expressed as functions of  $s$  as follows

$$i_3(s) = s \pmod{N_3 + 1}, \quad (\text{D.1.8})$$

$$i_2(s) = \tilde{i}_2 \pmod{N_2 + 1}, \quad \tilde{i}_2 = \frac{s - i_3}{N_3 + 1}, \quad (\text{D.1.9})$$

$$i_1(s) = \frac{s - s \pmod{\prod_{k=2}^3 (N_k + 1)}}{\prod_{k=2}^3 (N_k + 1)}, \quad (\text{D.1.10})$$

and the upper limit of  $s$  is defined as

$$N_s = \prod_{k=1}^3 (N_k + 1) - 1. \quad (\text{D.1.11})$$

Therefore, we can see that these special cases can be generalized to higher dimensional summations. Now consider  $n$ -dimensional summation with indices  $i_1, i_2, \dots, i_n$  having  $N_1, N_2, \dots, N_n$  summation upper bounds, respectively. If  $F_{i_1, i_2, \dots, i_n}$  is a function specified by  $n$  number of indices, then its  $n$ -dimensional summation can be written as

$$I_n = \prod_{k=1}^n \sum_{i_k=0}^{N_k} F_{i_1, i_2, \dots, i_n} = \sum_{i_1=0}^{N_1} \sum_{i_2=0}^{N_2} \cdots \sum_{i_n=0}^{N_n} F_{i_1, i_2, \dots, i_n} = \sum_{s=0}^{N_s} F_{i_1(s), i_2(s), \dots, i_n(s)}, \quad (\text{D.1.12})$$

where

$$i_n(s) = s \pmod{N_n + 1}, \quad (\text{D.1.13})$$

$$i_{n-1}(s) = \tilde{i}_{n-1} \pmod{N_{n-1} + 1}, \quad \tilde{i}_{n-1} = \frac{s - i_n}{N_n + 1}, \quad (\text{D.1.14})$$

$$i_{n-2}(s) = \tilde{i}_{n-2} \pmod{N_{n-2} + 1}, \quad \tilde{i}_{n-2} = \frac{s - s \pmod{\prod_{k=n-1}^n (N_k + 1)}}{\prod_{k=n-1}^n (N_k + 1)}, \quad (\text{D.1.15})$$

⋮

$$i_m(s) = \tilde{i}_m \pmod{N_m + 1}, \quad \tilde{i}_m = \frac{s - s \pmod{\prod_{k=m+1}^n (N_k + 1)}}{\prod_{k=m+1}^n (N_k + 1)}, \quad (\text{D.1.16})$$

⋮

$$i_1(s) = \frac{s - s \pmod{\prod_{k=2}^n (N_k + 1)}}{\prod_{k=2}^n (N_k + 1)}, \quad (\text{D.1.17})$$

and

$$N_s = \prod_{k=1}^n (N_k + 1) - 1. \quad (\text{D.1.18})$$

## D.2 Dependent Summation Indices

Here, we consider a case in which the indices display some sort of dependence between themselves, with particular interest in two-dimensional summation over orbital angular momentum  $l$  and its projection  $m$ . To begin with, we consider a summation of an arbitrary function  $\mathcal{Y}_{l,m}$ :

$$I_2 = \sum_{l=0}^{l_{\max}} \sum_{m=-l}^l \mathcal{Y}_{l,m}. \quad (\text{D.2.1})$$

We should set lower limits of all summation indices to zero. In doing so, the index  $m$  can linearly be transformed into  $\tilde{m}$  as  $m = \tilde{m} - l$  which then gives

$$I_2 = \sum_{l=0}^{l_{\max}} \sum_{\tilde{m}=0}^{2l} \mathcal{Y}_{l,\tilde{m}-l}. \quad (\text{D.2.2})$$

Now we must be able to find a single index  $s$  such that the two-dimensional summation in Eq. (D.2.1) with two dependent indices can be written as

$$I_2 = \sum_{s=0}^{N_s} \mathcal{Y}_{l(s),\tilde{m}(s)-l(s)}. \quad (\text{D.2.3})$$

In doing so,  $l$  and  $\tilde{m}$  (or  $m$ ) must be expressed as functions of index  $s$ . In such a situation we only need to fix  $l_{\max}$  at the start. Thus, by explicitly writing down Eqs. (D.2.2) and (D.2.3), for which we have listed the values of indices for illustration purpose in Table D.2 for small value of  $l_{\max} = 2$ , we can establish the best possible, if not unique, relations between the original indices

**Table D.2:** List of successive values of indices: angular momentum and its projection, when summing over a function that is specified by both. This list gives a guidance as to how we can express the two original indices as a function of the new index  $s$  such that the two-dimensional summation is converted to one-dimensional summation. The upper limit of  $s$  can be determined from  $l_{\max}$ .

$l$	$m$	$\tilde{m}$	$s$
0	0	0	0
1	-1	0	1
1	0	1	2
1	1	2	3
2	-2	0	4
2	-1	1	5
2	0	2	6
2	1	3	7
2	2	4	8

$l$  and  $m$  and the new index  $s$ . That is,

$$l(s) = \lfloor \sqrt{s} \rfloor, \quad (\text{D.2.4})$$

$$m(s) = s - \lfloor \sqrt{s} \rfloor (\lfloor \sqrt{s} \rfloor + 1), \quad (\text{D.2.5})$$

where use is made of a notation  $\lfloor x \rfloor$  which is known as a floor function of real numbers that returns the largest integer not greater than  $x$ . The upper limit  $N_s$  for the summation over the new index  $s$  can as well be calculated as

$$N_s = (l_{\max} + 1)^2 - 1. \quad (\text{D.2.6})$$

# Bibliography

- [1] Y. Fukuda *et al.* (Super-KamioKande Collaboration), Phys. Rev. Lett. **81**, 1562 (1998).
- [2] J. Monroe (MiniBooNE Collaboration), hep-ex/0406048 (2004).
- [3] Y. Ashie (Super-KamioKande Collaboration), Phys. Rev. Lett. **93**, 101801 (2004).
- [4] E. Alie (K2K Collaboration), Phys. Rev. Lett. **94**, 081802 (2005).
- [5] J. Ashman *et al.*, Nucl. Phys. B **328**, 1 (1989).
- [6] L. A. Ahrens *et al.*, Phys. Rev. D **35**, 785 (1987).
- [7] S. Brice *et al.* (FINeSE Collaboration), hep-ex/0402007 (2004).
- [8] A. Meucci, C. Giusti and F. D. Pacati, Nucl. Phys. A **744**, 307 (2004).
- [9] B. I. S. van der Ventel and J. Piekarewicz, Phys. Rev. C **69**, 035501 (2004).
- [10] B. I. S. van der Ventel and J. Piekarewicz, Phys. Rev. C **73**, 025501 (2006).
- [11] S. Boyd (MINER $\nu$ A Collaboration), Nucl. Phys. (Proc. Suppl.) **139**, 311 (2005), Available at: <http://minerva.fnal.gov/>.
- [12] M. H. Ahn *et al.* (K2K Collaboration), Phys. Rev. D. **74**, 072003 (2006).
- [13] H. C. Kim, J. Piekarewicz and C. J. Horowitz, Phys. Rev. C **51**, 2739 (1995).
- [14] S. K. Singh, M. J. Vicente Vacas and E. Oset, Phys. Rev. C **416**, 23 (1998).
- [15] T. Sato, D. Uno and T. S. H. Lee, Phys. Rev. C **67**, 065201 (2003).
- [16] T. Leitner, L. Alvarez-Ruso and U. Mosel, Phys. Rev. C **74**, 065502 (2006).
- [17] S. Ahmad, M. S. Athar and S. K. Singh, Phys. Rev. D **74**, 973008 (2006).
- [18] D. Drakoulakos *et al.* (MINER $\nu$ A Collaboration), hep-ex/0405002 (2004).
- [19] W. A. Mann, NuMI-NOTE-GEN (2003).
- [20] N. Solomey, Nucl. Phys. B **142**, 74 (2005).
- [21] Super-KamioKande Official website, Available at: <http://www-sk.icrr.u-tokyo.ac.jp/sk/physics/pdecay-e.html/>.
- [22] LAGUNA Official website, Available at: <http://www.laguna-science.eu/>.
- [23] K. Abe *et al.*, hep-ex/1109.3262 (2011).
- [24] UNO Official website, Available at: <http://nngroup.physics.sunysb.edu/uno/>.
- [25] S. J. Barish *et al.*, Phys. Rev. Lett. **33**, 448 (1974).
- [26] H. Deden *et al.*, Phys. Lett. B **58**, 361 (1975).
- [27] O. Erriques *et al.*, Phys. Lett. B **70**, 385 (1977).
- [28] O. Erriques *et al.*, Nucl. Phys. B **140**, 123 (1978).
- [29] N. J. Baker *et al.*, Phys. Rev. D **24**, 2779 (1981).

- [30] R. E. Shrock, Phys. Rev. D **12**, 2049 (1975).
- [31] W. Mecklenburg, Acta Phys. Austriaca **48**, 293 (1978).
- [32] A. A. Amer, Phys. Rev. D **18**, 2290 (1978).
- [33] H. K. Dewan, Phys. Rev. D **24**, 2369 (1981).
- [34] G. B. Adera. *Strange Particle Production via the Weak Interaction*. Master's thesis, Stellenbosch University (2009).
- [35] G. B. Adera, B. I. S. van der Ventel, D. D. van Niekerk and T. Mart, Phys. Rev. C **82**, 025501 (2010).
- [36] M. Rafi Alam, I. Ruiz Simo, M. Sajjad Athar and M. J. Vicente Vacas, Phys. Rev. C **82**, 033001 (2010).
- [37] L. Ray and G. W. Hoffmann, Phys. Rev. C **31**, 538 (1985).
- [38] R. D. Smith and S. J. Wallace, Phys. Rev. C **32**, 1654 (1985).
- [39] B. C. Clark, R. L. Mercer, D. G. Ravenhall and A. M. Saperstein, Phys. Rev. C **7**, 466 (1973).
- [40] L. G. Arnold, B. C. Clark, R. L. Mercer, D. G. Ravenhall and A. M. Saperstein, Phys. Rev. C **14**, 1878 (1976).
- [41] J. A. McNeil, L. Ray and S. J. Wallace, Phys. Rev. C **27**, 2123 (1983).
- [42] J. A. McNeil, J. R. Shepard and S. J. Wallace, Phys. Rev. Lett. **50**, 1439 (1983).
- [43] D. D. van Niekerk, B. I. S. van der Ventel, N. P. Titus and G. C. Hillhouse, Phys. Rev. C **83**, 044607 (2011).
- [44] N. P. Titus, B. I. S. van der Ventel, D. D. van Niekerk and G. C. Hillhouse, Phys. Rev. C **83**, 044616 (2011).
- [45] C. Bennhold and L. E. Wright, Phys. Lett. B **191**, 11 (1987).
- [46] L. J. Abu-Raddad and J. Piekarewicz, Phys. Rev. C **61**, 014604 (2000).
- [47] F. X. Lee, T. Mart, C. Bennhold, H. Haberzettl and L. E. Wright, Nucl. Phys. A **659**, 237 (2001).
- [48] F. X. Lee, C. Bennhold and L. E. Wright, Phys. Rev. C **55**, 318 (1997).
- [49] C. Bennhold, F. X. Lee, T. Mart and L. E. Wright, Nucl. Phys. A **639**, 227c (1998).
- [50] C. Maieron, C. M. Martínez, J. A. Caro and J. M. Udías, Phys. Rev. C **68**, 048501 (2003).
- [51] C. M. Martínez, P. Lava, N. Jachowicz, J. Ryckebusch, K. Vantournhout and J. M. Udías, Phys. Rev. C **73**, 024607 (2006).
- [52] J. D. Walecka, Ann. Phys. **83**, 491 (1974).
- [53] Y. K. Gambhir, P. Ring and A. Thimet, Ann. Phys. **189**, 132 (1990).
- [54] P. Ring, Prog. Part. Nucl. Phys. **193**, 37 (1996).
- [55] G. A. Lalazissis, J. König and P. Ring, Phys. Rev. C **55**, 540 (1997).
- [56] H. Kim, J. Piekarewicz and C. J. Horowitz, Phys. Rev. C **51**, 2739 (1995).
- [57] B. D. Serot, Phys. Lett. B **86**, 146 (1979).
- [58] J. P. Blaizot, D. Gogny and B. Grammaticos, Nucl. Phys. A **265**, 317 (1975).
- [59] J. Boguta and A. R. Bodmer, Nucl. Phys. A **292**, 414 (1977).
- [60] C. E. Price and G. E. Walker, Phys. Rev. C **36**, 1354 (1987).
- [61] W. Pannart, P. Ring and J. Boguta, Phys. Rev. Lett. **59**, 2420 (1987).
- [62] Y. K. Gambhir and P. Ring, Phys. Lett. B **202**, 5 (1988).
- [63] B. D. Serot and J. D. Walecka, Adv. Nucl. Phys. **16**, 1 (1986).
- [64] B. D. Serot and J. D. Walecka, Int. J. Mod. Phys. E **6**, 515 (1977).
- [65] B. D. Serot and J. D. Walecka, Phys. Lett. B **87**, 172 (1979).

- [66] B. G. Todd-Rutel and J. Piekarewicz, Phys. Rev. Lett. **95**, 122501 (2005).
- [67] H. Toki, D. Hirata, Y. Sugahara, Sumiyoshi and I. Tanihata, Nucl. Phys. A **588**, c357 (1995).
- [68] J. B. Bjorken and S. D. Drell, *Relativistic Quantum Mechanics* (McGraw-Hill, New York, 1964).
- [69] M. Nowakowski, E. A. Passchos and J. M. Rodríguez, Eur. J. Phys. **26**, 545 (2005).
- [70] W. Greiner and J. Reinhardt, *Quantum Electrodynamics* (Springer, Berlin, 2009).
- [71] G. F. Chew, M. L. Goldberger, R. E. Low and Y. Nambu, Phys. Rev. **106**, 1345 (1957).
- [72] M. Gell-mann, Phys. Lett. **8**, 214 (1964).
- [73] G. Zweig, CERN-8182-TH-401 (1964).
- [74] M. Gell-mann, Phys. Rev. **125**, 1067 (1962).
- [75] N. Cabibbo, Phys. Rev. Lett. **10**, 531 (1963).
- [76] P. Renton, *Electroweak Interactions: An Introduction to the Physics of Quarks and Leptons* (Cambridge Univ. Press, Cambridge, 1990).
- [77] D. P. Murdock, C. J. Horowitz, H. Kim and S. Pollock, Phys. Rev. C **48**, 6 (1993).
- [78] P. A. Carruthers, *Introduction to Unitary Symmetry* (John Wiley & Sons, Inc., New York, 1966).
- [79] O. Dumbrajs *et al.*, Nucl. Phys. B **216**, 277 (1983).
- [80] J. F. Donoghue and B. R. Holstein, Phys. Rev. D **25**, 2015 (1982).
- [81] S. J. Barish, Phys. Rep. **39C**, 281 (1978).
- [82] L. J. Abu-Raddad. *Photoproduction of Pseudoscalar Mesons from Nuclei*. Ph.D. thesis, The Florida State University (2000).
- [83] M. C. Martínez, J. A. Caballero, T. W. Donnelly and J. M. Udías, Phys. Rev. C **77**, 064604 (2008).
- [84] O. Nachtmann, Nucl. Phys. **B22**, 385 (1970).
- [85] W. M. Alberico, M. B. Barbaro, S. M. Bilenky, J. A. Caballero, C. Giunti, C. Maieron, E. Moya de Guerra and J. M. Udías, Nucl. Phys. A **623**, 471 (1997).
- [86] S. K. Singh and M. J. Vicente Vacas, Phys. Rev. D **74**, 053009 (2006).
- [87] E. D. Cooper, S. Hama, B. C. Clark and R. L. Mercer, Phys. Rev. C **47**, 297 (1993).
- [88] E. D. Cooper, B. K. Jennings and J. Mareš, Nucl. Phys. A **580**, 419 (1994).
- [89] E. D. Cooper, B. K. Jennings and J. Mareš, Nucl. Phys. A **585**, 157 (1995).
- [90] C. B. Dover and P. J. Moffa, Phys. Rev. C **16**, 1087 (1977).
- [91] P. B. Siegel, W. B. Kaufmann and W. R. Gibbs, Phys. Rev. C **30**, 1256 (1984).
- [92] S. R. Cotanch and F. Tabakin, Phys. Rev. C **15**, 1379 (1977).
- [93] A. K. Kerman, H. McManus and R. M. Thaler, Ann. Phys. (N.Y.) **8**, 551 (1959).
- [94] R. H. Landau, S. C. Phatak and F. Tabakin, Ann. Phys. (N.Y.) **78**, 299 (1973).
- [95] B. R. Martin, Nucl. Phys. B **94**, 413 (1975).
- [96] G. Giacomelli *et al.*, Nucl. Phys. B **20**, 301 (1970).
- [97] G. Giacomelli *et al.*, Nucl. Phys. B **71**, 138 (1974).
- [98] S. R. Cotanch, Nucl. Phys. A **308**, 253 (1978).
- [99] L. S. Kisslinger, Phys. Rev. **98**, 761 (1955).
- [100] H. K. Lee and H. McManus, Nucl. Phys. A **167**, 257 (1971).
- [101] J. H. Koch and M. Sternheim, Phys. Rev. C **6**, 1118 (1972).



- [102] L. S. Kisslinger and F. Tabakin, *Phys. Rev. C* **9**, 188 (1974).
- [103] R. Mach, *Nucl. Phys. A* **205**, 56 (1973).
- [104] C. Bennhold and L. E. Wright, *Phys. Rev. C* **39**, 927 (1989).
- [105] R. A. Eisenstein and G. A. Miller, *Comp. Phys. Comm.* **8**, 130 (1974).
- [106] E. H. Auerbach, D. M. Fleming and M. M. Sternheim, *Phys. Rev.* **162**, 1683 (1967).
- [107] L. Tiator and L. E. Wright, *Phys. Rev. C* **30**, 989 (1984).
- [108] M. L. Goldberger and K. M. Watson, *Collision Theory* (John Wiley & Sons. Inc., New York, 1964).
- [109] G. E. Forsythe, M. A. Malcolm and C. B. Moler, *Computer Methods for Mathematical Computations* (Prentice-Hall, 1976).
- [110] R. W. B. Ardill and K. J. M. Moriarty, *Comp. Phys. Comm.* **14**, 261 (1978).
- [111] M. Abramowitz and I. A. Stegun, *Handbook of Mathematical Functions with Formulas, Graphs and Mathematical Tables* (Dover Publications, Inc., New York, 1965).
- [112] Y. Ikebata, *Phys. Rev. C* **52**, 890 (1995).
- [113] J. Mano and Y. Kudo, *Prog. Theor. Phys.* **100**, 91 (1998).
- [114] D. Dinchon and P. E. Hoggan, *Int. J. Quantum Chem.* **107**, 2186 (2007).
- [115] W. H. Press, S. A. Teukolsky, T. Vetterling and B. P. Flannery, *Numerical Recipes in Fortran* (Cambridge University Press, Cambridge, 1992), 2nd ed.
- [116] S. T. Lai and Y. N. Chiu, *Comput. Phys. Comm.* **61**, 350 (1990).
- [117] D. F. Fang and J. F. Shriner Jr., *Comput. Phys. Comm.* **70**, 147 (1992).
- [118] J. Rasch, and A. C. H. Yu, *SIAM J. Sci. Comput.* **25**, 1416 (2003).
- [119] E. J. Weniger and E. A. Steinborn, *Comp. Phys. Comm.* **25**, 149 (1982).
- [120] M. Rotenberg, R. Bivins, N. Metropolis, and J. K. Wootery Jr., *The 3-j and 6-j Symbols* (Crosby Lockwoods, London, 1959).
- [121] B. Barney, *Introduction to parallel computing*,  
Available at: [https://computing.llnl.gov/tutorials/parallel\\_comp/#Whatis](https://computing.llnl.gov/tutorials/parallel_comp/#Whatis).
- [122] P. S. Pacheco, *An Introduction to parallel Programming* (Elsevier Science, 2011).
- [123] G. Burns, R. Daoud and J. Vaigl, in *Proceedings of Supercomputing Symposium* (1994), p. 379,  
Available at: <http://www.lam-mpi.org/download/files/lam-papers.tar.gz>.
- [124] J. M. Squyres and A. Lumsdaine, in *Proceedings, 10th European PVM/MPI Users' Group Meeting* (Springer-Verlag, 2003), p. 379.
- [125] G. B. Adera and B. I. S. van der Ventel, *Int. J. Mod. Phys. E* **20**, 2475 (2011).
- [126] A. Salam and H. Arenhövel, *Phys. Rev. C* **70**, 044008 (2004).
- [127] P. Bydžovský, *Int. J. Mod. Phys. E* **19**, 2169 (2010).
- [128] J. M. J. Kooy and L. W. H. Uytenbogaart, *Ballistic of the Future* (McGraw-Hill Book Company. Inc., New York, 1946).
- [129] S. S. Kuo, *Computer Applications of Numerical Methods* (Addison-Wesley, Reading, Mass., 1972).